Investigation of Gas Transport Rates Through a Covered Waste Rock Pile and Synchrotron Studies on the Sulfide Oxidation Reaction

by

Mark Steinepreis

A thesis

presented to the University of Waterloo

in fulfilment of the

thesis requirements for the degree of

Master of Science

in

Earth Sciences

Waterloo, Ontario, Canada, 2017

Author’s Declaration

I hereby declare that I am the sole author of this thesis. This is a true copy of the thesis, including any required final revisions, as accepted by my examiners.

I understand that my thesis may be made electronically available to the public.

Abstract

This thesis presents a field based investigation into gas transport mechanisms and rates through a waste-rock pile with a low permeable cover, and a synchrotron based study into intermediate sulfidic species that are produced as iron-sulfide grains oxidise to sulfate. The two studies are at different size scales, however both improve the understanding of the processes that affect the production of acid rock drainage and the release of metals to the hydrosphere at mine sites.

The study site for the gas transport investigation was waste-rock stockpile #3 at Detour Gold Corporation mine (Detour), operating in northern Ontario, Canada. Field monitoring was carried out during late 2014 and through 2015. Wind vector, air pressure and temperature were recorded around the exterior of the pile; pore-gas pressure, pore-gas concentration of O_2 and CO_2 and temperature were recorded within the pile. Correlations between external and internal pressure indicated that transport through the cover and waste-rock was laminar and therefore followed Darcy's law. Fluctuations in ambient temperature were dampened through the cover and within the waste-rock; internal pile temperatures were higher than average daily ambient temperature during the winter and lower in the summer. The O_2 concentrations in the pore-gas were higher and more variable in the summer (5-15% v/v at approximately 2.5m into the pile) than in the winter (consistently below 3% v/v at 2.5m depth). Design efforts to reduce the O_2 level within the pile should therefore be optimised for summer time conditions. The CO_2 concentrations were higher and more variable in the summer (0.5-6% v/v at approximately 2.5m into the pile) than in the winter (between 7-8% v/v at 2.5m depth).

Numerical simulations were carried out in COMSOL version 5.1 to prepare a calibrated model for gas transport through the pile. Field measured parameters were used as boundary conditions

for the exterior of the pile, and field measured parameters for the interior of the pile were compared with model outputs to consider calibration. Numerical simulations indicated that the advective flux of O_2 through the cover and into the interior of the pile is approximately 100 times higher than diffusive fluxes during the summer. Increasing the thickness of the cover and using a cover material that has a lower permeability would further reduce the O_2 concentration within the pile.

Two sulfide grains (one chalcopyrite and one pyrrhotite) that were collected from crushed waste-rock samples from Detour were analysed at the synchrotron at the Advanced Photon Source at Argonne, Illinois, USA. It is understood that sulfate is the ultimate oxidation product of sulfides, however less is known about intermediate sulfidic species that are produced. Linear combination analysis of the X-ray absorption near edge spectra (XANES) for the grains and standard sulfidic species indicated that variable combinations of chalcopyrite ($CuFeS_2$), pyrrhotite/troilite (Fe_xS_{1-x}/FeS), marcasite (FeS_2), elemental sulfur (S^0) thiosulfate ($S_2O_3^{2-}$), tetrathionate ($S_4O_6^{2-}$), sulfite (SO_3^{2-}) and sulfate (SO_4^{2-}) are present over the grains. It is not currently known if the inclusion of these species in predictive simulation of sulfide oxidation rates is warranted.

Acknowledgements

A special thanks is extended to Jim Robertson and Detour Gold Corporation for supporting scientific research by offering their facilities for this study. Funding was provided partially by Detour, the Natural Sciences and Engineering Research Council of Canada (NSERC) and the Ontario Research Fund (ORF), without which this research would not have been possible.

Many thanks to my supervisor, Dr David Blowes for taking a chance on me and providing me the opportunity to expand my technical knowledge. I would like to express my gratitude to Richard Amos from Carelton University, who designed and built the apparatus that recorded the bulk of my field data and was always available to provide assistance. A thank you is also extended to my other committee members, Dr Carol Ptacek and Dr Marek Stastna at the University of Waterloo, for ongoing technical support and advice.

Site personnel at Detour have provided me with a lot of assistance and have always been available when asked for favours. These people include Marie-Helen Turgeon, Travis Desormeaux, Ryan Johnson and Melissa LeClair. I have also received support from several other graduate students and UW personnel including Jeff Bain, Brayden McNeill, Lianna Smith and Allison Reynolds.

Synchrotron analyses were performed at GeoSoilEnviroCARS (The University of Chicago, Sector 13), Advanced Photon Source (APS), Argonne National Laboratory. GeoSoilEnviroCARS is supported by the National Science Foundation - Earth Sciences (EAR-1128799) and Department of Energy- GeoSciences (DE-FG02-94ER14466). This research used resources of the Advanced Photon Source, a U.S. Department of Energy (DOE) Office of Science User Facility operated for the DOE Office of Science by Argonne National Laboratory

under Contract No. DE-AC02-06CH11357. I am grateful for the assistance that Drs. Matt Newville and Tony Lanzirotti provided during the visits to the APS.

I thank my parents, David and Linda for their endless encouragement. Finally, I cannot overstate the support that I have received from my wife Jude, who has moved across the world to help me pursue my career goals. Jude has had to take on extra responsibility with our daughter Emma while I have been occupied at all hours completing my thesis. I dedicate this thesis to them.

Table of Contents

List of Tables

List of Figures

List of Symbols

Gas Transport

u – gas velocity [m s^{-1}]

p – air/gas pressure [Pa]

κ – gas permeability [m^2]

μ – gas viscosity [Pa.s]

ρ – gas or solid density (kg m^{-3})

θ_p – the porosity of the porous media [1]

c – mass concentration [1]

M – the molar mass [kg mol^{-1}]

D – diffusion coefficient [m^2 s^{-1}]

j – diffusive flux [kg m^{-2} s^{-1}]

N – total flux [kg m^{-2} s^{-1}]

Q – consumption or production of species [kg m^{-3} s^{-1}]

β – coefficient of thermal expansion of the pore-gas [K^{-1}]

Heat Transport

k – thermal conductivity [W m^{-1} K^{-1}]

c_p – volumetric heat capacity at constant pressure [J kg^{-1} K^{-1}]

q – heat flux [W m^{-1}]

d_z – assumed out-of-plane thickness (1m for 2-dimensional models)

Q – production of heat due to sulfide oxidation [W m^{-3}].

Sulfide Oxidation

S – oxidation rate [kg m^{-3} s^{-1}]

D_2 – Diffusion coefficient of oxygen into particle [m^2 s^{-1}]

ε_s – molar ratio of sulfur consumption to O_2 consumption [1]

ϕ^g – mass fraction of O_2 in pore gas [1]

ϕ^s – mass fraction of S in porous media [1]

ρ_{rs} – density of sulfur [kg m^{-3}]

H – Henry's Law [1]

a – average particle size [m]

Fourier Analysis

X(ω) – Fourier transform of function x(t)

ω – sinusoidal frequency [s^{-1}]

T - sinusoidal period [s]

N – number of points from the data set [1]

nfft – length of the data time series [s]

F_s – sampling frequency [s^{-1}]

Chapter 1 – Introduction

Mining activity generates significant amounts of waste material that must be stored indefinitely. The two main forms of waste are tailings and waste rock. The former is a fine grained slurry that is a by-product of ore processing, and is stored within purpose-built facilities typically referred to as tailings storage facilities (TSFs). Waste-rock is uneconomic rock material excavated to gain access to the economic ore that ranges from clay-sized fines to boulder-sized particles and is stored as unsaturated waste-rock stockpiles (WRS').

Infiltration of precipitation can produce poor quality water at both TSFs and WRS'. The oxidation of sulfides within the waste materials may lead to low pH and elevated concentrations of sulfate and metals in groundwater and surface water (Blowes et al., 2003). This poor quality water is often termed acid mine drainage (AMD) or acid rock drainage (ARD).

Sulfide minerals that have been identified in waste-rock at other mine sites include pyrite (FeS), pyrrhotite ($Fe_{1-x}S_x$), sphalerite (Zn,Fe)S, chalcopyrite ($CuFeS_2$), pentlandite $(Fe,Ni)_9S_8$, covallite (CuS) and arsenopyrite (FeAsS); as described by Jambor (2003). The oxidation reaction for pyrite can be described as follows:

$$FeS_{2(s)} + \frac{7}{2}O_2 + H_2O \rightarrow Fe^{2+} + 2SO_4^{2-} + 2H^+ \quad \text{1-1}$$

$$Fe^{2+} + 0.25O_2 \rightarrow Fe^{3+} + 0.5H_2O \quad \text{1-2}$$

$$4Fe^{2+} + O_2 + 10H_2O \rightarrow 4Fe(OH)_{3(s)} + 8H^+ \quad \text{1-3}$$

Reaction 1-1 describes the first step in the oxidation of pyrite, to release ferrous iron, sulfate and acidity. Other metals within the sulfides will also be liberated during this reaction step. The

released ferrous iron may also oxidise to ferric iron according to Reaction 1-2. Iron (oxyhydr)oxides, typically ferrihydrite and goethite (Belzille et al., 2004), may precipitate near neutral pH, according to Reaction 1-3. The overall reaction for pyrite is as follows:

$$FeS_{2(s)} + \frac{15}{4}O_2 + \frac{7}{2}H_2O \rightarrow 2SO_4^{2-} + Fe(OH)_{3(s)} + 4H^+ \quad 1\text{-}4$$

Ferric iron may also be an oxidant under acidic conditions (pH<4) and will proceed at a faster rate than oxidation by gaseous O_2 (Janzen, 2000):

$$FeS_{2(s)} + 14Fe^{3+} + 8H_2O \rightarrow 15Fe^{2+} + 2SO_4^{2-} + 16H^+ \quad 1\text{-}5$$

Reactions 1-1 through 1-3 all require a supply of gaseous O_2 to persist (Lefebvre et al., 2001a) and Reaction 1-5 requires that a source of Fe^{3+} be maintained by Reaction 1-2. It follows that a reasonable design strategy for the storage of mine waste could be to limit the availability of O_2 within the system to inhibit sulfide oxidation and reduce the production of AMD. Understanding and quantifying of the mechanisms for supply of O_2 into and through waste material are therefore important fields of study in the management of mine wastes. Gas is readily transported through WRS' by advective (pressure driven) and diffusive (concentration driven) mechanisms (Pantelis and Ritchie, 1992), whereas transport of gas through TSFs is limited by the fine nature of the material and is dominated by diffusion (Wunderly et al., 1996).

Reactions 1-4 and 1-5 describe the reaction of S from an oxidation state of -2 to +6. The kinetics of these reactions have been studied extensively, however the intermediate sulfidic species that are formed as the reactions goes to completion are less well understood. Langman et al. (2015) identified marcasite (FeS_2), elemental S (S^0), thiosulfate ($S_2O_3^{2-}$), sulfite (SO_3^{2-}) and sulfate

(SO_4^{2-}) within weathered sulfide grains, however few studies have been carried out in this field and it is not known whether these findings are universal.

The production and movement of CO_2 is another important component to gas transport where carbonate minerals are present. The oxidation of sulfide results in the production of acidity and subsequent acid-neutralisation in the presence of carbonate minerals (Lee et al., 2003). The dissolution of carbonate minerals within waste-rock can sustain near-neutral pH levels in solution, according to the following neutralisation reaction with calcite ($CaCO_3$):

$$CaCO_3 + H^+ \rightarrow Ca^{2+} + HCO_3^- \quad 1\text{-}6$$

$$HCO_3^- + H^+ \rightarrow CO_2 + H_2O \quad 1\text{-}7$$

Other carbonate minerals that may be present include dolomite ($CaMg(CO_3)_2$), ankerite ($CaFe(CO_3)_2$) and siderite ($FeCO_3$) (Blowes et al., 2003). The dissolution of carbonate minerals may help to maintain a near-neutral pH for pore water and effluent that enters the hydrosphere, which will inhibit the oxidation of sulfide minerals by ferric iron according to reaction 1-5, however it will play a lesser role in the attenuation of metals and sulfate. Additionally, the dissolution of the carbonates will also release the constituent metals to solution. This contaminated, yet near-neutral pH, water is often termed neutral mine drainage.

Depletion of carbonate minerals will result in a decrease in the pH of pore water. Aluminium hydroxides including aluminium hydroxide ($Al(OH)_3$) and gibbsite (crystalline $Al(OH)_3$) will buffer to a pH between 4-4.5 (Johnson et al., 2000) until depletion. The iron (oxyhydr)oxides that precipitated around the weathering sulfide grain at neutral pH will buffer the pH between 2.5 – 3.5 (Blowes et al., 2003). Alumino-silicate minerals may also provide some acid neutralisation

capacity, however the rate of reaction is considered to be too low to maintain a constant pH (Blowes et al., 2003).

The consumption of O_2 and production of CO_2 through the acid producing and neutralising reactions initially result in sub-atmospheric O_2 levels, and replenishment of O_2 can occur through gas transport into the pile. The timeframe to consume O_2 is in the range of hours to days and depletion of sulfur in sulfides is in the range of years to hundreds of years (Pantelis et al., 2002), indicating that a long term design strategy to limit sulfide oxidation is required. One possible strategy is to utilise low permeability soil covers; which were installed on WRS' at the Detour Gold Mine (Detour) at the cessation of operations in the late 1990s. Most geochemistry studies have been carried out on freshly placed waste-rock, and the waste-rock stockpiles at Detour provide a unique opportunity to consider waste that has been oxidising for approximately 30 years. The WRS' at Detour contain variable pyrite, pyrrhotite, chalcopyrite and covellite (McNeill, 2016).

1.1 Detour Lake Research Program

1.1.1 Research Program Scope and Objective

The multidisciplinary research at Detour aims to increase the understanding of the production and transport of acid mine drainage and other poor quality water through waste-rock material at the Detour. The areas of study are in the areas of geochemistry, hydrology, microbiology and gas and heat transport. The results of the research will be used in the planning for storage strategies of waste-rock that will be produced through ongoing production.

The long term objectives of the project are as follows:

1. Study the hydrology of the existing waste-rock piles;

2. Identify the sulfide and carbonate minerals that are present within the waste-rock, and study the reactivity with respect to the production of acid mine drainage and acid neutralisation;
3. Identify processes that affect the liberation, transport and attenuation of all species, including secondary minerals, that are produced by the oxidative and neutralisation processes;
4. Investigate gas, water and heat transport mechanisms and rates as well as the water chemistry within the cover and the waste-rock; and
5. Understand the role of sulfide oxidising bacteria in the production of acid rock drainage.

Two MSc theses have been completed on the Detour WRS' to date. Cash (2014) provided a physical characterisation of the waste-rock material, including grain size distribution. This work was primarily focussed on achieving goal 1. McNeill (2016) provided a comprehensive geochemical and mineralogical and bacterial characterisation of the waste-rock material. This work continued on from Cash (2014) to progress with goal 1, and commenced work on goals 2 and 4.

1.1.2 Goal of this Thesis

Gas and heat transport mechanisms and rates have been studied for this thesis (research program goal 4). The aim of this work has been to identify gas transport mechanisms and rates through the existing covered WRS' at Detour, and consider possible design features that could be applied to future WRS' to reduce O_2 ingress into the waste-rock.

The evolution of the speciation of sulfur as the ARD oxidation progresses from sulfide to sulfate has also been studied for this thesis, using the synchrotron at the Advanced Photon Source at

Argonne, Illinois, USA (research program goal 3). The aim of this work is to identify intermediate sulfur species that are produced as sulfide (S^{2-}) oxidises to sulfate (SO_4^{2-}) within Fe-sulfides at Detour. This work can be expanded in future studies to consider the need to include these intermediate species in predictive simulations for the production of ARD and release of metals to the hydrosphere.

1.2 Thesis Organisation

This thesis contains four chapters. Chapter 1 outlines the aims of this thesis. Chapter 2 outlines the monitoring and numerical simulation of gas transport at Waste-Rock Stockpile #3 at Detour. Data plots from the work discussed in this chapter are contained in Appendix A. Chapter 3 discusses the results of testing at the Advanced Photon Source (synchrotron) of select sulfide grains from Detour. Data plots from this chapter are contained in Appendix B. Chapter 4 presents the conclusions of the thesis and provides recommendations for additional work.

1.3 Site Description

Detour Lake mine is located in Northern Ontario, Canada, approximately 185km north-east by road from the town of Cochrane (Figure 1-1). Production of gold through open pit mining commenced in 1983 and was ceased in 1999 (Detour Gold Corporation, 2010) due to the low price of gold and exhaustion of higher grade deposits. Mining recommenced in 2013 under the current owners, Detour Gold Corporation.

Figure 1-1 – Detour Gold Mine location (from Detour Gold Corporation, 2012)

Waste-rock from the original (1983-1999) production was placed in four stockpiles (denoted WRS#1 – WRS#4; Figure 1-2) around the crest of the pit. A low permeability cover was installed on two waste-rock piles, WRS#3 and WRS#4, at the end of operations in 1999. WRS#3

has remained relatively undisturbed since. WRS#4 was partially excavated over the winter of 2011-12 and the western face is now open to the atmosphere (McNeill, 2016).

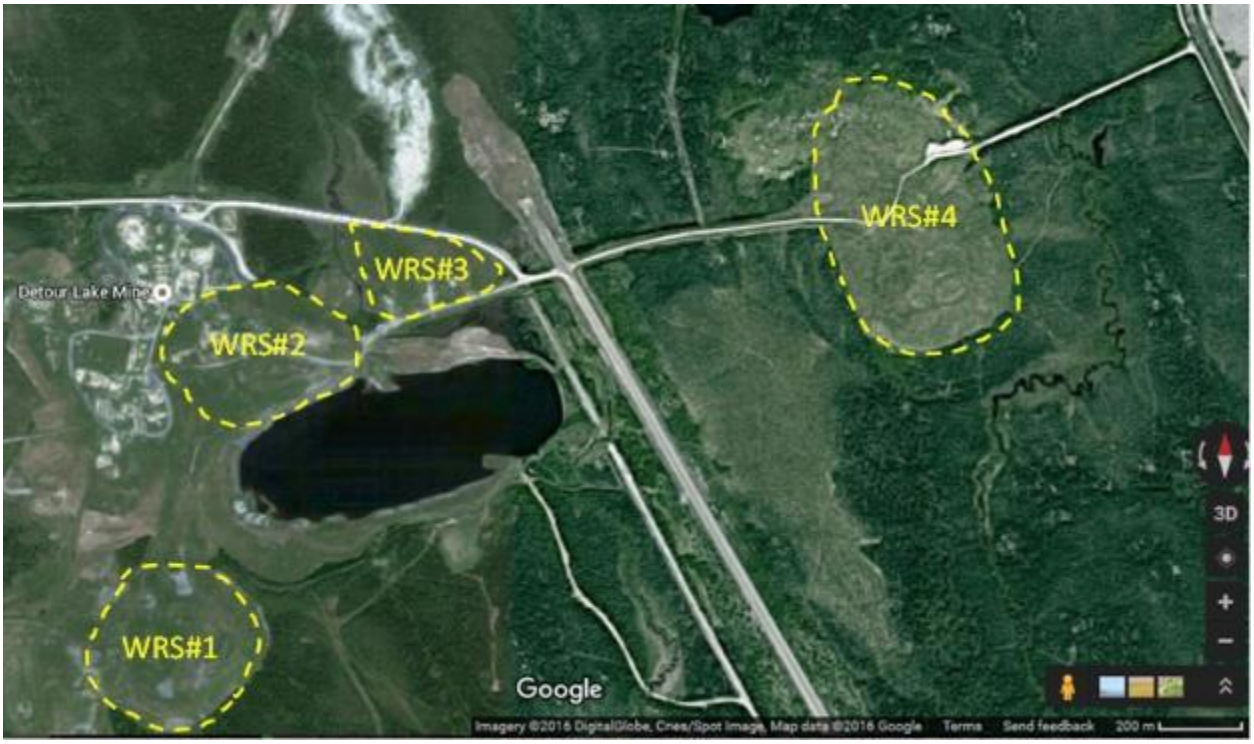

Figure 1-2 – Location of waste-rock stockpile #1 to waste-rock stockpile #4 at Detour Gold Mine

DGC has made WRS#1 - WRS#4 available for geochemistry studies, and instrumentation was installed within boreholes in WRS#3 and WRS#4 in 2011, for automatic monitoring of temperature and moisture content and routine pore-gas and water-quality monitoring. A test-pitting program was carried out in 2013 to install similar instrumentation within the cover of WRS#3. Additional instrumentation was installed in 2014 for automatic monitoring of air pressure around and within WRS#3, gas concentrations within the pile and the wind vector.

Chapter 2 – Gas Transport Through a Covered Waste-rock Pile

2.1 Introduction

Oxygen is transported into a waste-rock pile through gas and water movement. There are three principal mechanisms for gas transport through porous media, which provides a direct method of supplying O_2 into waste-rock piles (Scanlon et al., 2002):

- Advection of gas – resulting from air pressure gradients between the exterior and interior of the pile. The gradients develop due to the action of wind, barometric pressure fluctuations, loss or gain of gaseous mass from sulfide oxidation (loss of O_2) and acid neutralisation (gain of CO_2) and temperature gradients. The latter is due to the variability of atmospheric temperature and heat production within the waste-rock. Advective transport of gas is typically affected by the permeability of the material. Resistance to advective gas transport also develops due to the viscosity of the gas (Scanlon et al., 2002).
- Diffusion of gas – driven by concentration gradients of the components of air and typically affected by the diffusion coefficient of each component through air and water; diffusion through air is more efficient than diffusion through water (Kim and Benson, 2004). Sulfide oxidation reduces the concentration of gaseous O_2 within the body of the pile, and CO_2 may be produced where carbonate neutralisation occurs, resulting in concentration gradients of these two species between the atmosphere and the body of the pile. A gradient in the concentration of gaseous N_2 also develops as a result of these processes.

- Advective and dispersive transport of dissolved O_2 and CO_2 in the fluid phase - The supply of dissolved O_2 through water infiltration is considered to be minor (Amos et al., 2015), and has not been considered further in this research.

Soil covers will typically have a lower permeability and diffusion coefficient than the underlying waste-rock, and will therefore impede gas transport through both advection and diffusion. Furthermore, soil materials typically have lower thermal conductivity values than waste-rock (Pham, 2013) and will also impede heat transport. The lower thermal conductivity of the cover will subdue temperature variations within the waste-rock pile, maintaining lower temperatures within the waste-rock when ambient temperatures exceed internal temperatures, and retaining heat within the pile in the reverse situation.

Previous studies considered the benefit of using low permeability soil covers on waste rock piles to limit oxygen ingress. Harries and Ritchie (1987) observed a decrease in heat production, and therefore oxidation rate, after emplacement of a low permeability soil cover on White's Dump at Rum Jungle, Northern Territory, Australia. O'Kane et al. (1998) observed a decreasing trend in O_2 content with time at 1m below the base of the compacted cover on a waste rock dump network at the Equity Silver Mine in British Columbia, Canada. The possible benefits of the soil covers at Detour are considered in this study.

2.2 Gas Transport Theory

2.2.1 Advective Transport – Pressure Induced

Gas transport into mine wastes is induced where pressure differences develop between the exterior and interior of the pile.

Different relationships of varying complexity have been developed, however advective gas transport within porous media can be most simply described using Darcy's Law (conservation of momentum) where flow is uncomplicated by turbulent and buoyant effects:

$$u = -\frac{\kappa}{\mu}(\nabla P) \qquad 2\text{-}1$$

where u is the gas velocity from advective transport [m s^{-1}], κ is the gas permeability of the waste-rock material [m^2], μ is the gas dynamic viscosity [Pa s] of the pore-gas and ∇P is the gas pressure gradient [Pa].The pressure regime around the exterior of the pile is influenced by the following factors:

- Barometric pressure changes;
- Wind flow over the pile; and
- Atmospheric temperatures.

Barometric pressure fluctuates due to diurnal temperature variations and transient weather fronts (Auer et al., 1996). The role of barometric pressure fluctuations has been considered in previous studies (Auer et al., 1996; and Massmann et al., 1992); however, the focus has been on the release of volatile contaminants from porous media and replacement with clean air, commonly referred to as 'Barometric Pumping'. Both studies indicate that barometric pumping may occur over the depth range of just several metres, even though air pressures within porous media respond to fluctuations in barometric pressure over large vertical distances (>30m). The role of barometric pressure fluctuations in the overall transport of gas into and through a waste-rock pile has not been well studied in waste-rock (Amos et al., 2015). One study by Harries and Ritchie (1981) indicated a clear trend between barometric pressure and O_2 content of waste-rock pore-

gas, however this relationship was only observed at one of their monitoring locations. Nonetheless, it is clear that a good understanding of local barometric pressure regimes is important to understand the pressure distribution within waste-rock piles.

The influence of barometric pressure in the development of pressure gradients is described in Figure 2-1a. The scenario provided assumes an initial equal air pressure between the exterior and interior of the pile and that all other parameters are equal. An instantaneous increase in barometric pressure will result in a corresponding increase in the pressure around the pile, however the pressure inside the pile would rise gradually due to the finite permeability of the materials (Elberling et al., 1998). The pressure gradient would be into the pile until the external and internal pressures equilibrate. An instantaneous decrease in barometric pressure would result in a pressure gradient out of the pile.

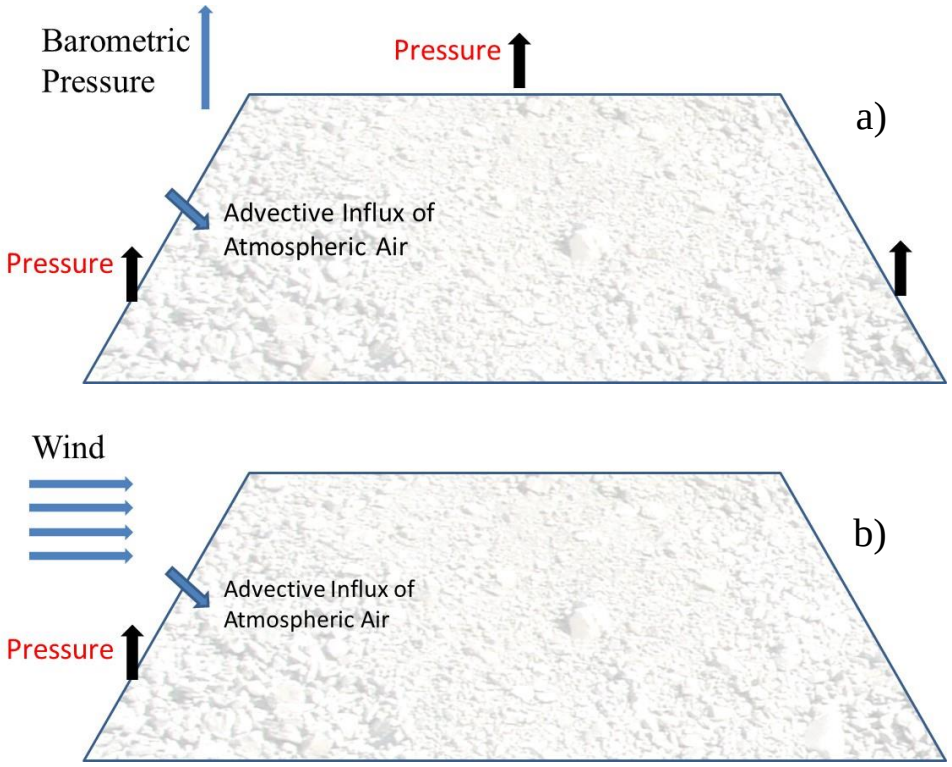

Figure 2-1 – Idealised pressure distribution around a waste-rock stockpile from a) an increasing barometric pressure and b) wind flow

The flow of wind around the pile will induce varying pressure around the perimeter, the magnitude of which will be affected by the pile geometry. The influence of wind in the development of pressure gradients is described in Figure 2-1b. The scenario provided assumes a wind flow of left-right, leading to increased pressure on the left (windward) side of the pile. Induced pressures on the top and leeward side of the pile are less clear as a result of 3-dimensional effects.

Processes that will affect the pressure regime within the interior of the pile include gaseous mass changes from sulfide oxidation (mass loss of O_2) and acid neutralisation from carbonate minerals (mass gain of CO_2), and thermal changes within the pile.

The composition of the gas within waste-rock is different to the atmosphere and will vary within the waste-rock due to the consumption of O_2 through oxidation and production of CO_2 through acid neutralisation. The relative proportions of each species will affect the density and pressure of the gas within the pile according to the relative molar masses of the species. Thermal gradients will develop within the pile and between the exterior and interior of the pile due to the production of heat from oxidation reactions and heat transport between the exterior and interior. The density and pressure regime within the pile will also be affected by the temperatures according to the ideal gas law (Scanlon et al., 2002).

2.2.2 Diffusive Transport

Diffusive transport is driven by concentration differences in any component of the pore-gas within the pile. The components that are most relevant in waste-rock are O_2, CO_2 and N_2. Diffusion is considered to be a less rapid gas-transport process than advection (Lefebvre et al., 2001a).

Sulfide oxidation and subsequent carbonate neutralisation affect the concentration, and therefore partial pressure, of O_2 and CO_2 within the pore-gas. The partial pressure of N_2 within the pore-gas will also fluctuate with changes in total pressure, resulting in concentration gradient for that species as well.

Diffusive gas transport for constituent i (O_2, CO_2 and N_2) is described as:

$$j_i = -\left(\rho D_i^f \nabla c_i + \rho c_i D_i^f \frac{\nabla M_n}{M_n}\right) \qquad 2\text{-}2$$

where i indicates the component of the gas (O_2, CO_2 and N_2), j_i is the diffusive flux of component i [kg m^{-2} s^{-1}], ρ is the gas density [kg m^{-3}], c_i is the mass percentage [1], D_i^f is the diffusion coefficient [m^2 s^{-1}], M_i is the molar mass [kg mol^{-1}] and M_n is the molar mass of the gas mixture [kg mol^{-1}].

The direction of the diffusive transport of O_2 will always be into the pile, as the sulfide reaction is O_2 consuming and no other reactions exist that are O_2 producing. Conversely, the diffusive transport of CO_2 will always be out of the pile at Detour, as carbonate dissolution through acid neutralisation produced this gas.

The flow regime for diffusive gas transport is represented on Figure 2-2:

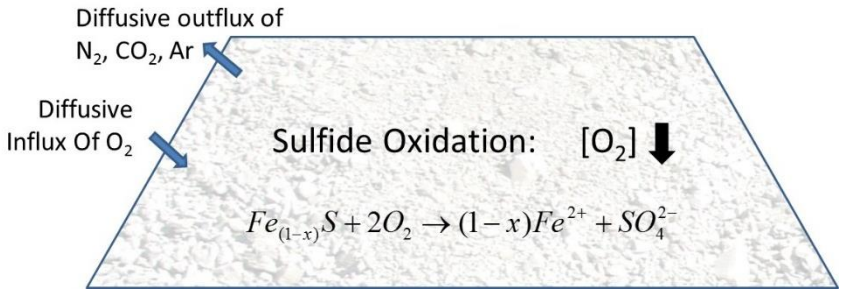

Figure 2-2 – Typical diffusive flux direction for O_2, N_2, CO_2 and Ar within a waste-rock stockpile

2.2.3 Coupled Transport

A flowchart showing the mechanisms for O_2 transport into and out from the pile is shown as Figure 2-3. The wind vector, barometric pressure and heat production directly affect advective transport rates of O_2, and the consumption of O_2 through oxidation will affect both advective and diffusive transport rates. The integrated nature of the gas transport processes necessitates a coupled expression for advective and diffusive gas transport, as well as heat transport.

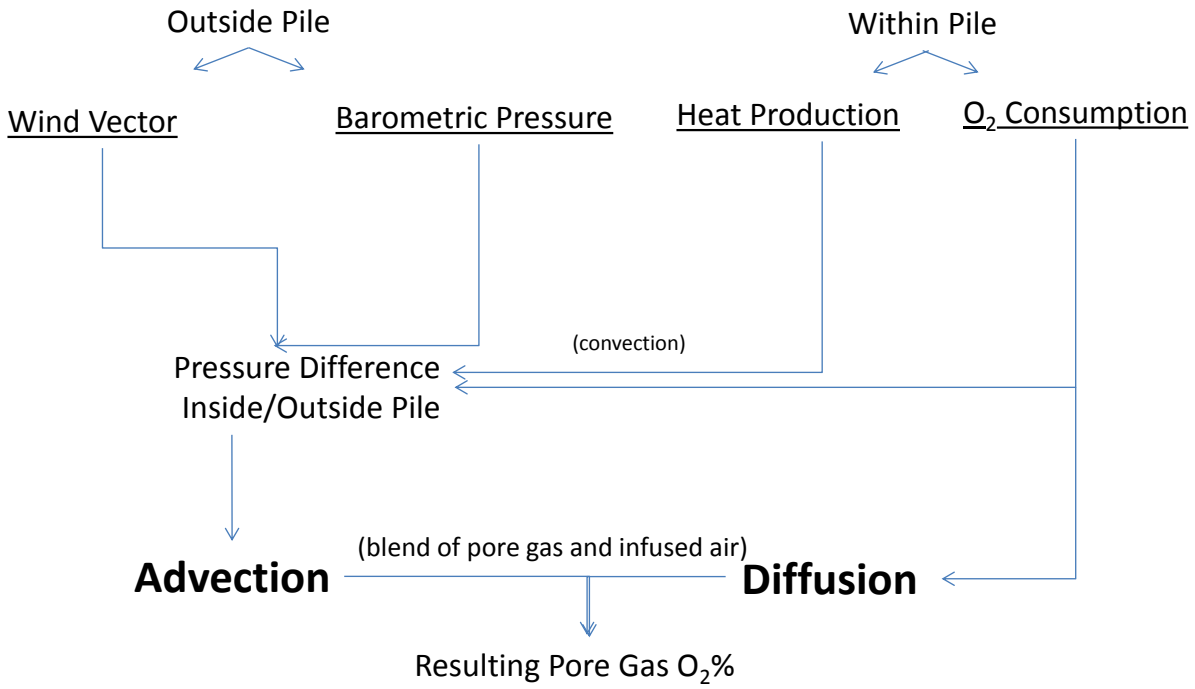

Figure 2-3 – Flow diagram for the advective and diffusive transport of oxygen through a waste-rock stockpile

The flow equations for advection are typically expressed with respect to bulk air flow, and those for diffusion are typically expressed with respect to the transport of a component of air. The focus of the current study is the transport of O_2 through the pile, and therefore the advection equations are adapted to couple the flow equations.

Combining 2-1 and 2-2, the resulting transport of constituent is through advection and diffusion may be most simply described as:

$$N_i = j_i + \rho u c_i \quad \text{2-3}$$

where N_i is total flux of species i [kg m^{-2} s^{-1}].

2.3 Heat Transport Theory

Temperature gradients within the waste-rock and between the exterior and interior of the pile affect pressure gradients. Heat transport is in the direction of the decreasing temperature gradient, and the component of gas transport from temperature effects is in the direction of the increasing temperature gradient, which corresponds to the decreasing density gradient. Gas pressure within the pile is related to temperature according to the ideal gas law (Scanlon et al., 2002). An understanding of heat transport is therefore required to adequately characterise pressure and thereby quantify gas transport.

The sulfide oxidation reaction is exothermic (Lowson, 1982) and energy storage would therefore be expected in waste-rock as porous media are poor conductors of heat (Harries and Ritchie, 1981). Furthermore, oxidation rates will increase further as temperatures increase.

Heat of reactions for the oxidation of sulfides and subsequent carbonate neutralisation are shown for pyrite below:

Table 2-1 – Heat of reaction for sulfide oxidation and carbonate neutralisation processes

Reaction Step	ΔH (kJ mol^{-1})	Reference
$FeS_{2(s)} + \frac{7}{2}O_2 + H_2O \rightarrow Fe^{2+} + 2SO_4^{2-} + 2H^+$	-1,440	Harries and Ritchie (1981); Lowson (1982)
$Fe^{2+} + 0.25O_2 \rightarrow Fe^{3+} + 0.5H_2O$	-102	Harries and Ritchie (1981); Lowson (1982)
$2FeS_2 + 14Fe^{3+} + 8H_2O \rightarrow 15Fe^{2+} + 2SO_4^{2-} + 16H^+$	-11	Harries and Ritchie (1981); Lowson (1982)
$CaCO_3 + 2H^+ \rightarrow Ca^{2+} + H_2O + CO_2$	-14	Nordstrom and Munoz (1994)

Temperature gradients develop within the pile and between the exterior and interior of the pile depending on the relative contribution of oxidation and seasonal changes in ambient temperatures.

The conductive transport of heat within porous media is typically described by:

$$q = -d_z k_{eff} \nabla T \qquad 2\text{-}4$$

where q is heat flux due to conduction [W m^{-1}], $d_z$is the assumed out-of-plane thickness (1m for 2-dimensional models), k_{eff} is the effective thermal conductivity of the pore-gas and porous media [W m^{-1} K^{-1}], ∇T is the thermal gradient [K m^{-1}].

The coupling of conductive and convective heat transport is described by:

$$d_z(\rho C_\rho)_{eff}\frac{\partial T}{\partial t} + d_z \rho C_\rho u.\nabla T + \nabla.q = d_z Q \qquad 2\text{-}5$$

where $(\rho C_\rho)_{eff}$ is the effective heat capacity [J K^{-1} m^{-3}] of the pore-gas and porous media, u is the Darcy velocity of the pore-gas [m s^{-1}] and Q is the production of heat due to sulfide oxidation [W m^{-3}]. Thermodynamic equilibrium, and therefore temperature equivalency, is typically assumed for all phases (Pantelis et al., 2002).

2.3.1 Sulfide Reaction Rates

Sulfide oxidation is considered to be a first order reaction for the purpose of quantitative simulation (Lahmira and Lefebvre, 2014). The rate of reaction within sulfide grains is commonly modelled using fixed rate models (Ritchie, 1994; and Lefebvre et al., 2001b) or the shrinking core model (Levenspiel, 1972). The latter models the decrease in the rate of oxidation over time as an alteration coating replaces the primary sulfide mineral; the radius of the sulfide component within grains decreases, and O_2 must diffuse through the alteration rim to react with the inner sulfide residual.

The waste-rock within WRS#3 had been oxidising for approximately 30 years prior to this study, and the time period for data collection has been approximately 18 months. A fixed rate model for sulfide oxidation is therefore appropriate as the alteration coatings on individual grains are unlikely to increase significantly in size over that period. One such model was proposed by Ritchie (2003).

$$S(\omega^g, \omega^s, T) = 9.02\frac{3D_2\varepsilon_s\phi^g\phi^s\rho_{rs}}{HR^2} \qquad 2\text{-}6$$

where S is the oxidation rate [kg m^{-3} s^{-1}], D_2 is the diffusion coefficient of O_2 through the particle [m^2 s^{-1}], ε_s is the molar ratio of sulfur consumption to O_2 consumption based on the stoichiometry of the reaction [1], ϕ^g is the mass fraction of O_2 in the pore-gas [1], ϕ^s is the mass fraction of sulfur in the waste-rock [1], ρ_{rs} is the density of sulfur [kg m^{-3}] , H is Henry's constant [1], R is the average particle size [m].

2.4 Methods

Two boreholes were drilled within WRS#3 during 2011, to collect drill cutting samples of the waste-rock and to install instrumentation. Soil moisture and temperature measurement probes (ECH_2O probes and thermistors) were installed at several depths during the completion of the boreholes (McNeill, 2016). Lengths of ¼" LDPE tubing were installed from the surface to several depths for monitoring of pore-gas concentrations. The nomenclature of the monitoring locations includes the name of the borehole and the depth at which it was installed, for example BH2011-3-1-9.2m indicates 9.2 m depth beneath the surface at borehole BH2011-3-1 (Figure 2-4b).

Additional ECH_2O probes and ¼" LDPE tubing were installed within the 1-m thick soil cover on WRS#3 during a test pitting program in 2013. The BH nomenclature has been retained for these monitoring locations, and have been denoted BH2013-3-3 to BH2013-3-7 (Figure 2-4a).

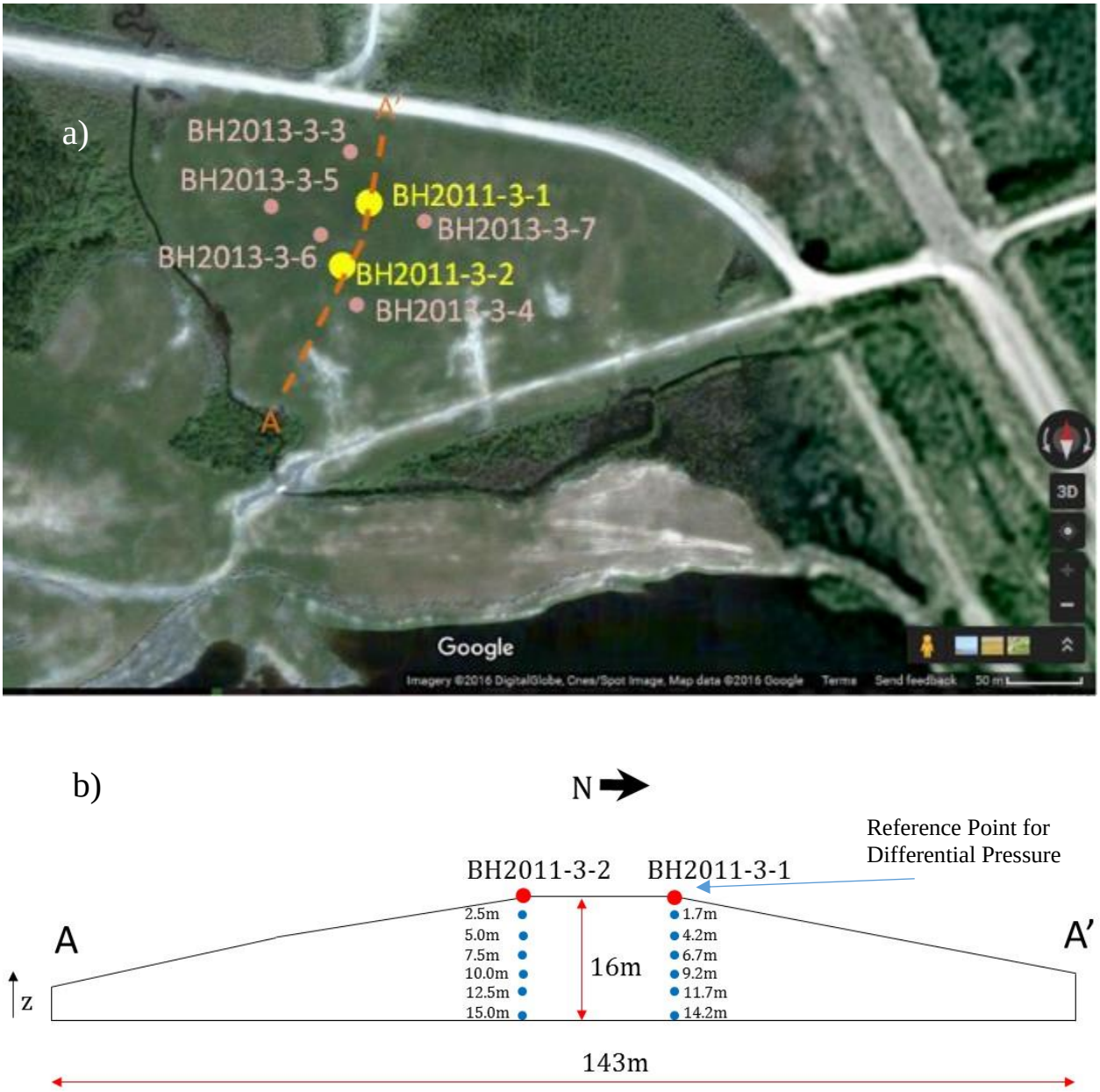

Figure 2-4 – a) Location of boreholes BH2011-3-1 and BH2011-3-2 and test-pits BH2013-3-3 to BH2011-3-7 on WRS#3 (Modified From Google Maps, 2016) and b) cross section along A-A'

2.5 Pressure, Gas Concentration and Wind Vector Monitoring

An automated system for monitoring of exterior and interior gas pressures and pore-gas concentrations was installed at the surficial location of BH2011-3-1 in May, 2014 (Figure 2-5). The ¼'' tubing that was installed in 2011 within the boreholes was used to record measurements at 12 locations within the interior of the pile (Figure 2-4b) and additional tubing was extended

within 25 mm PVC to 12 locations around the exterior of the pile to record exterior air pressure (Figure 2-6). Monitoring locations for the latter were named according to the position on the side slope (batter) of the pile and the directional location. For example, N1 refers to the location near the crest of the pile and on the north side and E3 refers to the base (toe) of the pile on the east side.

A wind sensor was installed on the apparatus to record the wind vector (speed and direction). The instrumentation was similar to that installed in a test waste-rock pile by Amos et al. (2009b).

Figure 2-5 – Instrumentation on WRS#3 used to record and log pressure and gas-concentration data

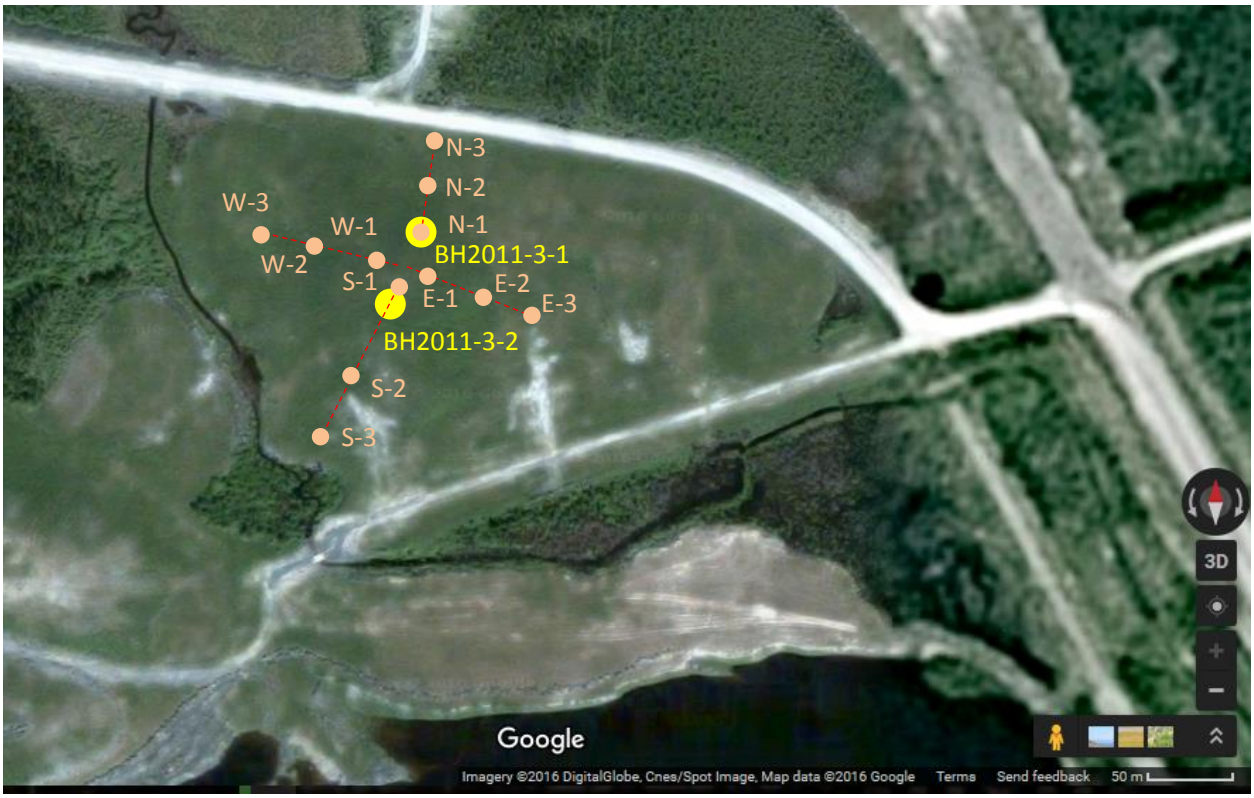

Figure 2-6 – Exterior pressure monitoring locations around the exterior of the WRS#3 (Modified from Google Maps, 2016)

Air pressure around the exterior and interior of the pile was recorded as differential measurements relative to the location of the apparatus, i.e. the surficial location of BH2011-3-1 invariably had a differential pressure of zero (Figure 2-4b). The barometric air pressure at the location of the apparatus was recorded using a Setra 278 sensor (range of 800-1100 hPa, accuracy of 0.075%) and the differential measurements were recorded at the end of the interior and exterior LDPE tubing using Ashcroft CXLdp sensors (range of ±0.25 inch H_2O/62 Pa, accuracy of 0.25%). Wind vector (speed and direction) measurements were recorded with a Campbell Scientific 05103AP-10 wind monitor. Measurements for the concentration of O_2 were recorded with an Advanced Micro Instruments Model 65 sensor (range of 0-25% v/v) and CO_2 with an Edinburgh Instruments Gascard II sensor (range of 0-30% v/v). The apparatus recorded

and retained measurements with a Campbell Scientific CR1000 data logger and was powered by two, 1000W Solar Panels.

The interior tubing was connected to the pressure and gas-concentration sensors using 3-way valves. The tubing was extended from the surface of the pile to the upstream connection of a three way valve. The downstream pneumatic connection was to the pressure sensors when power to the valve was off, and connection to the gas-concentration sensor was when power was on.

Measurements for wind vector and exterior and interior pressure were taken at 4 second intervals. The program recorded average measurements at 1 minute intervals, to average out erratic data. A measurement was recorded for gas O_2 and CO_2 once per day. The power to each valve was switched on for about 2 minutes to obtain the sample for testing, and during this time the corresponding pressure reading was invalid. The program averaged the pressure reading immediately before and after the power was switched on to the valve, and applied that figure for the time frame. Data was downloaded from April-October in 2014 and 2015.

A review of the external and internal pressure data was carried out by the preparation of pressure contour animations for approximate 2D representations of the pile along the north-south plane and the east-west plane. The animations were reviewed for unexpected contours to identify periods of erroneous data.

An example of a reasonable contour plot is Figure 2-7a to c.

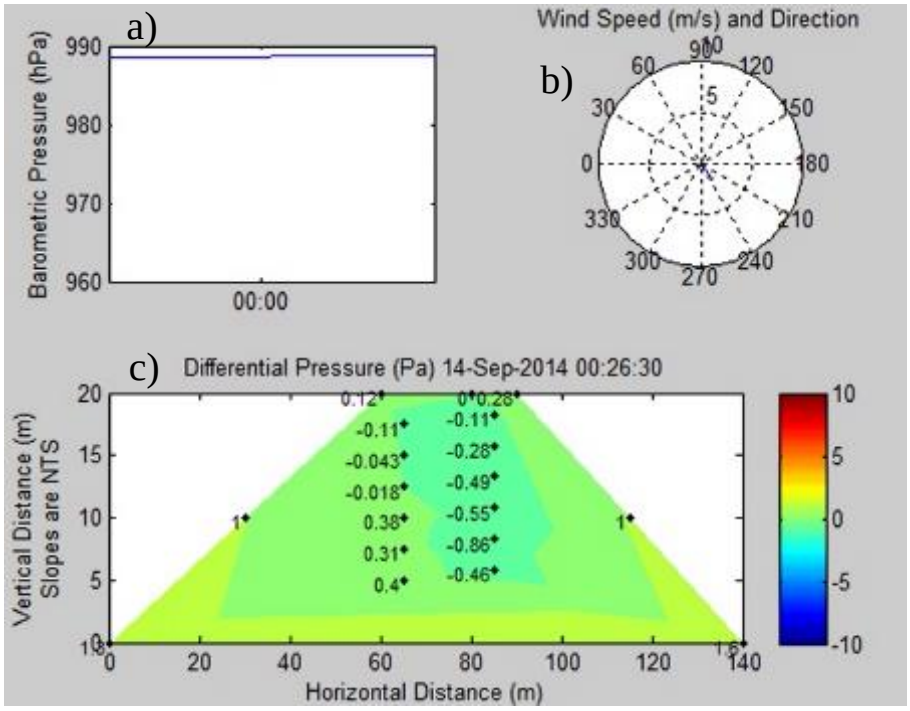

Figure 2-7 – Expected pressure contour plot, a) barometric pressure from 23:36 – 12:26am on 14 September 2014, b) wind speed and direction, c) pressure contours

An example of a questionable pressure contour plot is Figure 2-8a to c:

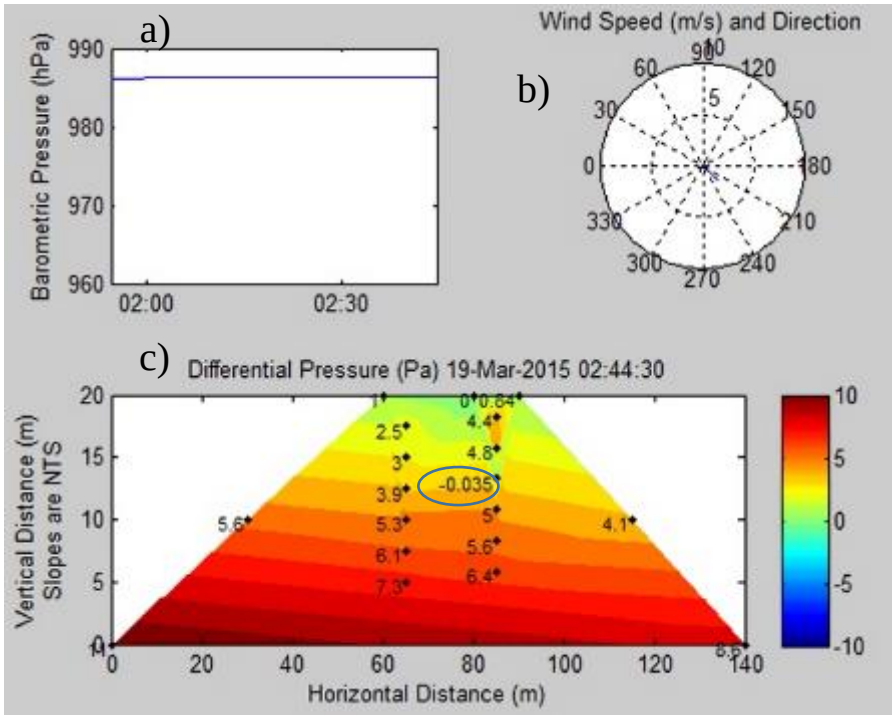

Figure 2-8 – Unexpected pressure contour plot, a) barometric pressure from 01:56 – 02:46am on 14 September 2014, b) wind speed and direction, c) pressure contours

The data point that was judged to be erroneous is encircled in Figure 2-8c. Erroneous data were excluded from the data set for all analysis. Erroneous data were primarily caused by issues with the apparatus, i.e. loose connections or wildlife damage, however some data were erroneous by seemingly random occurrence. Such data were identified with large and instantaneous fluctuations, oftentimes from the lower range of the sensor directly to the upper range, that weren't replicated at adjacent points.

The system was maintained during the site visits subsequent to the data download and analysis. The following checks on the integrity of the system were carried out as part of the routine of the site visits.

- Walkover the lengths of PVC that house the pressure tubing to check for damage. Damage sometimes occurred due to wildlife or drag effects on the tubing;
- Inspection of the ends of the pressure tubing to check for blockage; and
- Inspection of all connections and replacement as necessary.

The source of any errors in the pressure data was generally identifiable. For example, a leaky valve would often produce a result for O_2 content at a subsurface location that was equal to the composition of atmospheric air. Some pressure sensors had to be replaced during the course of the monitoring period.

Pore-gas concentration measurements required a greater power demand than the pressure measurements and were taken once a day, according to the following processes:

- Power was provided to the O_2 and CO_2 sensors at 12pm, and left to warm up for 30 minutes. The start time was selected to allow sufficient daylight to recharge the batteries after the pore-gas concentration measurements;

- The valve for a sample port was powered up and the pore-gas was sampled for 2 minutes using a KNF micro diaphragm gas sampling pump prior to the recording of a measurement. This time frame was considered adequate to purge the previous sample and supply sufficient new volume for pore-gas concentration measurement; and
- The power for the sampled gas port was disconnected and was provided to the next port. The gas sampling procedure is repeated for 12 sampling locations.

Calibration of the gas sampling system was carried out at each site visit, according to the following process:

- Disconnection of a gas sample tube from the system, and connection of calibration gas in its place. The gas sampling system was then run with calibration gas and the voltage output from the O_2 and CO_2 sensors recorded manually; and
- Confirmation of the readings from the automated system with the portable Quantum Model 902P sensor.

Discrepancies with readings from either of these two checks prompted an investigation. The source of any leaks was identified and repaired and the above processes repeated to confirm the repairs.

2.5.1 Temperature and Moisture Content Monitoring

ECH_2O probes (temperature and moisture content) and thermistors (temperature) were installed in WRS#3 in 2011 as described by McNeill, (2016). Measurements were recorded at 6 hour intervals and recorded on data loggers.

2.6 Results

The objective for the monitoring of WRS#3 was to understand the movement of gas and heat through the system, which was considered through comparisons and correlations between different monitoring locations.

Data are available once a minute for pressures and wind vector, once every 6 hours for temperatures and moisture content and daily for gas-concentrations. Pressure and wind data was calculated for 10 minute averages to save on processing time and smooth erratic trends; the accuracy of this assumption was evaluated using statistical analysis. Daily averages were calculated for all data sets to allow comparison with the daily gas-concentration data. The accuracy of using daily averaged data sets was evaluated by statistical analysis.

Coincident measurements for different data sets were compared to determine Pearson's correlation coefficients. Qualitative thresholds for correlation coefficients are introduced for this study (Table 2-2).

Table 2-2 – Introduced thresholds for qualitative descriptions that correspond with calculated correlation coefficients

Pearson's Correlation Coefficient (absolute value)	**Description**
0 – 0.2	Very Poor
0.2 – 0.4	Poor
0.4 – 0.6	Moderate
0.6 – 0.8	Good
0.8 – 1.0	Very Good

Correlation analysis method is complicated in this case by time lags in mass and energy transport within the system. Gas transport is inhibited by material parameters such as the permeability, diffusivity and thermal conductivity of the cover and waste-rock materials. Comparisons

between data sets from internal and external monitoring points may or may not show strong correlations when compared in this way.

All data sets exhibit sinusoidal behaviour in the time range of minutes to days. The sinusoidal data sets are well suited for Fourier analysis, which transforms the data sets from the time scale to the frequency scale.

The premise behind Fourier analysis is that a sinusoidal curve can be expressed as the sum of individual sine and cosine curve components, each of which has a unique frequency (Stade, 2011). The magnitude of each component is calculated through the Fourier transform. The data sets for the monitored parameters are non-periodic (non-repetitive), for which the following general expression for the Fourier transform applies (Leaver and Unsworth, 2007):

$$X(\omega) = \frac{1}{2\pi}\int_{-\infty}^{\infty} x(t)e^{-i\omega t}dt \qquad 2\text{-}7$$

$$e^{-i\omega t} = \cos(\omega t) - isin(\omega t) \qquad 2\text{-}8$$

$$\omega_k = \frac{2\pi k}{T}\ ;\ \omega_k = 2\pi k f \qquad 2\text{-}9$$

where $X(\omega)$ is the Fourier transform of function x(t), ω is the angular frequency of the individual sinusoid curves [rads s^{-1}], f is the temporal frequency [Hz], T is the period [s], k is a real number [k=0,1,2…∞]. The desired frequencies of the individual component curve are designated by the user and the amplitude of each is the calculated according to the above relationship.

The expression is modified for discrete (non-infinite) data sets, such as those available in this case.

$$X_K = \sum_{n=1}^{N-1} x_n e^{-i2\pi kn/N} \qquad 2\text{-}10$$

where N is the number of data points that form the original curve. Other terms that are commonly used are nfft, the length of the data time series [s], F_s, the sampling frequency [s^{-1}; not to be confused with the frequency of the sinusoidal curves, ω *or* f] and B, the sampling interval [$B = \frac{1}{F_s}$; s]. Therefore, N=nfft*Fs. Sampling intervals of B = 10 min (pressure, wind data), B = 6 h (temperature and moisture content) and B = 1 day (gas-concentrations) were considered for this study.

The discrete Fourier transform (DFT) was calculated for the available discrete data sets by MATLAB using the Fast Fourier Transform, (FFT) algorithm (Mathworks, 2016). The FFT calculates the DFT at a faster rate than would be achievable by calculating the DFT directly. It is noted in the documentation for the software that the FFT is applicable for sinusoidal periods $T > 2B$ [s]. The corresponding frequency of $F_s = 1/2B$ [s^{-1}] is known as the Nyquist frequency. Therefore, the analysis is applicable for t > 2days with respect to the daily averaged data sets, t > 12 hours for the 6 hour data sets and t > 20minutes for the 10 minute averaged data sets. The output DFT output may also not reflect the original signal in the higher frequency/lower period region (Elliott and Rao, 1983). A 'window', or 'weighting' function is often applied (multiplied) to the input data set to reduce this effect of the FFT. Window functions are a waveform function within the interval of the data set, and are zero outside the interval. The Hamming window was applied to the data set prior to calculation of the DFT.

The Fourier transform is typically plotted as an amplitude-frequency (angular or temporal) curve or amplitude-period curve. The latter was used for this thesis. The peaks in the amplitude-period curve indicate the dominant periods in the original time series.

2.6.1 Data set availability

High-quality data for air pressure and pore-gas concentrations are available intermittently from early September, 2014 until mid-November, 2015. The gas logger did not function over the winter, from mid-December, 2014 until mid-March, 2015. Some monitoring ports were damaged by ice or water ingress and were not repaired until the end of April, 2015.

Temperature monitoring from the thermistors was consistent from 2012 to 2015, except for July 2015 due to the action of wildlife. Data availability from the ECH$_2$O probes installed in the cover and waste-rock was above 75% from October, 2013 to November, 2015.

2.6.2 Wind Speed and Direction

Mean wind speed over the data collection period was 3.56 m s^{-1}, with a median of 3.32 m s^{-1} and a standard deviation of 1.97 m s^{-1}. The maximum observed wind speed over the time period was 15.55 m s^{-1} (Table 2-3).

Table 2-3 – Wind speed statistics for the 10 minute average data set from the WRS#3 logger

Wind Speed Parameter	**Value**
Mean	3.56 m s^{-1} (12.82 km hr^{-1})
Median	3.32 m s^{-1} (11.95 km hr^{-1})
Standard Deviation	1.97 m s^{-1} (7.09 km hr^{-1})
Maximum	15.55 m s^{-1} (55.98 km hr^{-1})
Minimum	0

The mean wind speed measured from the field collected data set at one minute intervals (3.6 km hr^{-1}) is equal to the 10 minute averaged data (3.6 km hr^{-1}) and within 10% of the mean of the daily averaged data (3.3 km hr^{-1}, Figure 2-9a). Correlation analysis with other pressure parameters has been carried out with the 10 minute average data. The wind speed histogram is skewed below the mean relative to the normal distribution (Figure 2-9b).

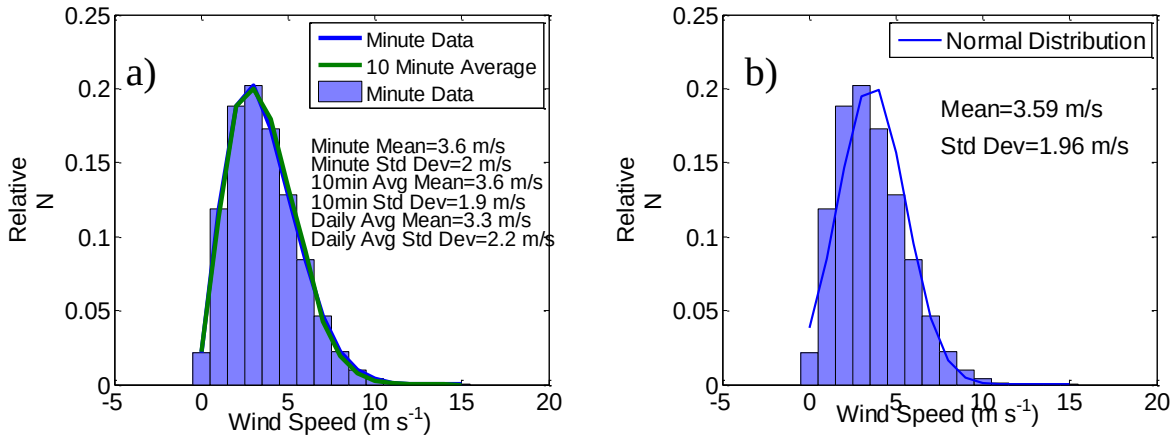

Figure 2-9 – Histograms of wind speed from WRS#3 logger, a) 1 minute data and 10 minute averaged data b) comparison of the 10 minute averaged data with the normal distribution

A histogram of wind direction indicates that the wind was generally blowing from 175-325 degrees from North within the analysis period, which represents a dominant wind direction from the south to the west (Figure 2-10). There is a secondary peak in the histogram between 25-50 degrees from North. It was observed during the fieldwork that the wind would generally be from a southerly direction during calmer times, however would often turn to the north when a precipitous weather system was approaching. These observations are reflected in the wind direction histogram.

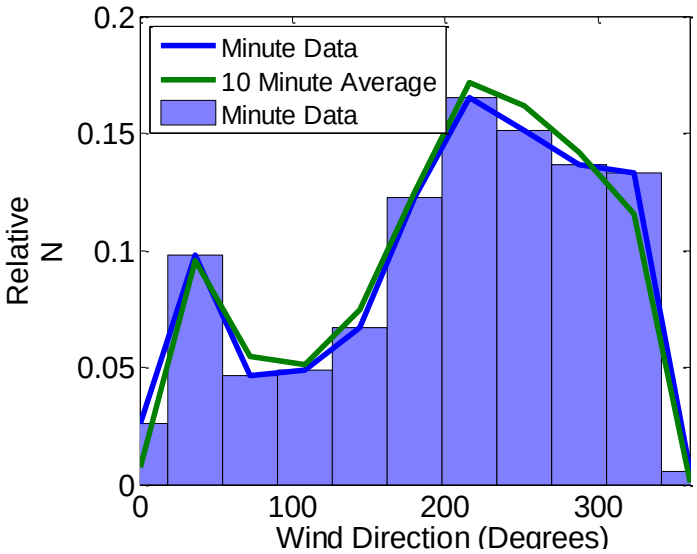

Figure 2-10 – Histogram of wind direction from the WRS#3 logger

Data collection was sporadic during the winter of 2014-15 and 2015-16. A wind monitoring system recording hourly measurements of wind speed (Figure 2-11a) and direction (Figure 2-11b) was maintained by mine personnel elsewhere on site. The average wind speed from the sensor on WRS#3 (summer, 2015) is 3.59 m s^{-1} and is 2.62 m s^{-1} from the mine operated sensor during the winter of 2014-15. Both wind direction histograms indicate that the wind was mostly from 175-325 degrees from North.

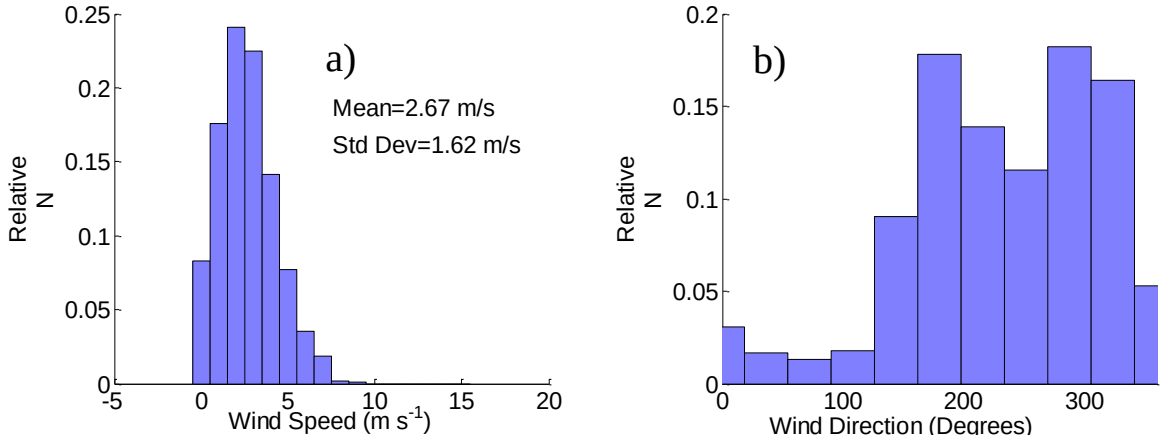

Figure 2-11 – Histograms of wind vector from the mine operated monitoring system from 01-December-2014 to 31-March-2014, a) wind speed, b) wind direction

The DFT of the 10-minute averaged data set for wind speed indicate that the dominant period is t=1 day (Figure 2-12a1). Secondary peaks are evident at approximately 0.5 and 7 days. The plot for the DFT of the data from the mine operated monitoring system (including summer and winter data) also indicates peaks at t=0.5 and 1 days (Figure 2-12b1), however the period at t = 7 days is less dominant. The data sets have been plotted for the time period less than 1 day (Figure 2-12a2 and b2) and an additional dominant period at approximately 0.3 days is indicated in the data from the mine operated monitoring system. A peak is also present at that same period in the WRS#3 data, however numerous other peaks are present for periods between 0.1 – 0.4 days.

It is notable that the wind sensor on WRS#3 was installed approximately 2.5 m above ground level at the location of borehole BH2011-3-1 and turbulent effects may influence the data at that height.

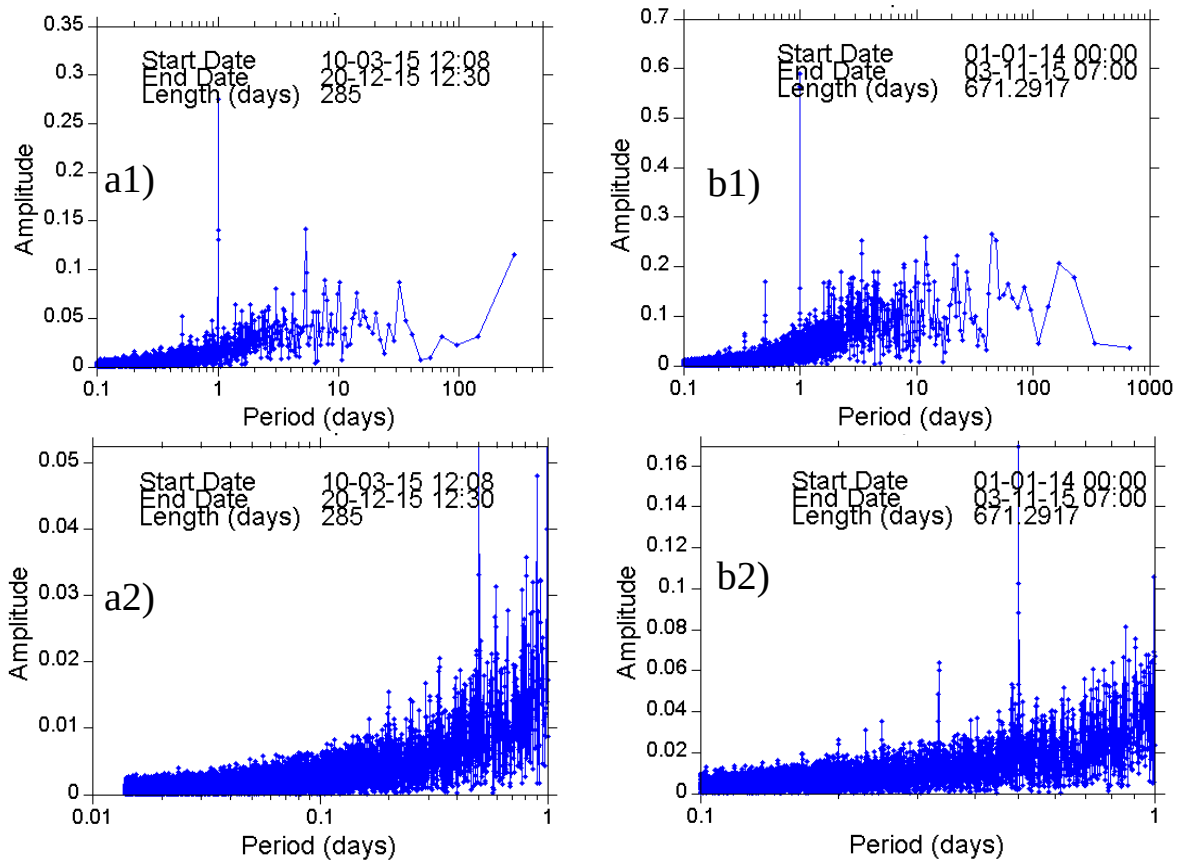

Figure 2-12 – Discrete Fourier transform for a1) the 10 minute average data for wind speed from the WRS#3 logger, a2) for periods less than 1 day, b1) the hourly data from the mine operated monitoring system and b2) for periods less than 1 day

2.6.3 Barometric Pressure

Barometric pressure typically reduces with increased elevation above sea level and the average barometric pressure at sea level is considered to be 101.3 kPa. The following relationship can be used to estimate a typical average for a point at any elevation above sea level (NOAA, NASA and USAF, 1976):

$$P = P_b \left[\frac{T_b}{T_b + L_b(h - h_b)} \right]^{\frac{g_o M}{R * L_b}} \qquad 2\text{-}11$$

where P_b is the static pressure at sea level [101,325 Pa], T_b is standard temperature [288.15 K], L_b is standard temperature lapse rate [-0065 K m^{-1}], h is the height above sea level [m], h_b is the

height at the base of the atmospheric layer [0 m], R is the universal gas constant [8.315 J K^{-1} mol^{-1}], g_o is the acceleration due to gravity [9.81 m s^{-2}] and M is the molar mass of Earth's air [$28.96x10^{-3}$ kg mol^{-1}]. The crest of WRS#3 was surveyed to be at approximately 292 masl. Therefore, a reasonable estimate for atmospheric pressure at the crest of WRS#3 is 978.5 hPa.

The mean barometric pressure as measured on WRS#3 is in agreement with the calculated estimate, within 0.1% (Table 2-4). The minimum barometric pressure of 942.2 hPa was recorded during a precipitation event on 24th November, 2014. A total of 25.0 mm of rain was recorded that day by a rain gauge operated by Detour personnel.

Table 2-4 – Barometric pressure statistics from the WRS#3 logger for the 10minute average data set

Barometric Pressure Parameter	**Value**
Mean	979.3 hPa
Median	979.7 hPa
Standard Deviation	9.6 hPa
Maximum	1000.9 hPa
Minimum	942.2 hPa

The mean barometric pressure from the field collected data set at one minute intervals, 10 minute average data and daily averaged data are in relative agreement at 979.3 hPa (Figure 2-13a). The histogram for barometric pressure is slightly skewed above the mean, compared with the normal distribution (Figure 2-13b).

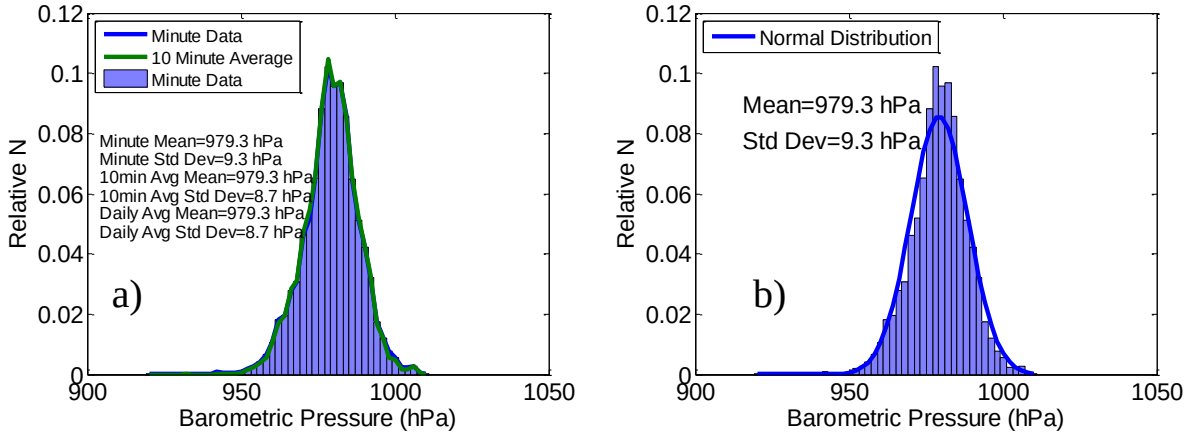

Figure 2-13 – Histograms of barometric pressure from the WRS#3 logger, a) 1 minute data, 10 minute averaged data and daily averaged data, b) comparison of the 10 minute averaged data with the normal distribution

Mine personnel operate a monitoring system for barometric pressure (hourly measurements) and a histogram for the winter months (01-December-2014 to 31-March-2014) was prepared to consider the time frame that was not captured by monitoring on WRS#3 (Figure 2-14).

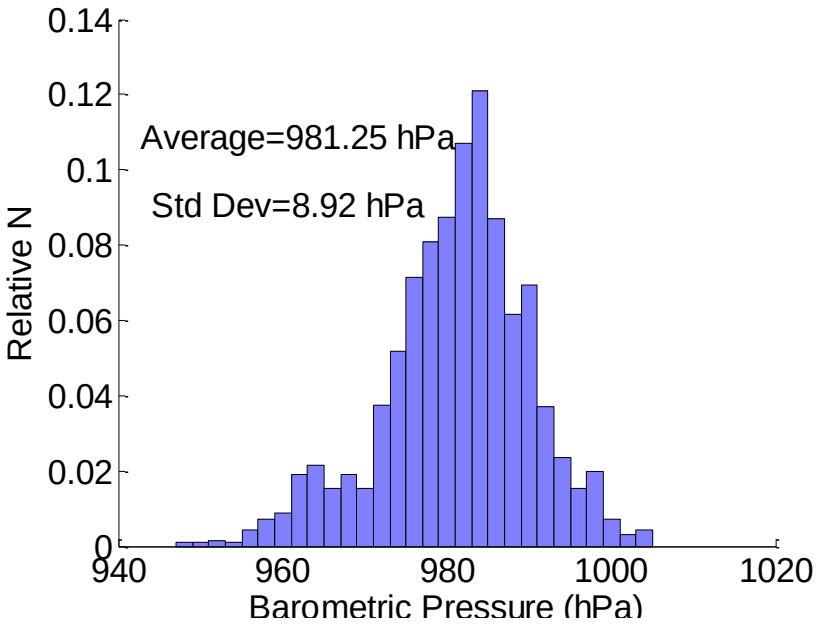

Figure 2-14 – Histogram of barometric pressure from hourly data the mine operated monitoring system during winter, 2014-15

The average barometric pressure from the sensor on WRS#3 (summer, 2015) is 979.3 hPa and is 981.2hPa from the mine operated sensor during the winter of 2014-15.

The DFT for the 10 minute averaged data set for barometric pressure indicates a local peak at t = 1 day (Figure 2-15a1), however it not as dominant as the peak at the same period for wind speed (Figure 2-12). The periods in the range of approximately t = 7 - 20 days are broadly dominant. A peak is indicated at approximately t = 100 days, which is likely the result of calculation bias and is therefore not significant. The peaks at t = 1 day and 7 - 20 days are indicated on the DFT for the data from the mine monitoring system (including summer and winter data), however the 100 day period is not dominant (Figure 2-15b1). A peak at t = 0.5 days is indicated in the data from the mine operated system but is relatively minor from the data on WRS#3.

The data sets have been plotted for the time period less than 1 day (Figure 2-13a2 and b2) and an additional dominant period at approximately 0.3 days is indicated in the data from the mine operated monitoring system. The DFT of the WRS#3 data is highly variable in this period range, however some dominant peaks are indicated at 0.3, 0.5 and 0.8 – 1 days.

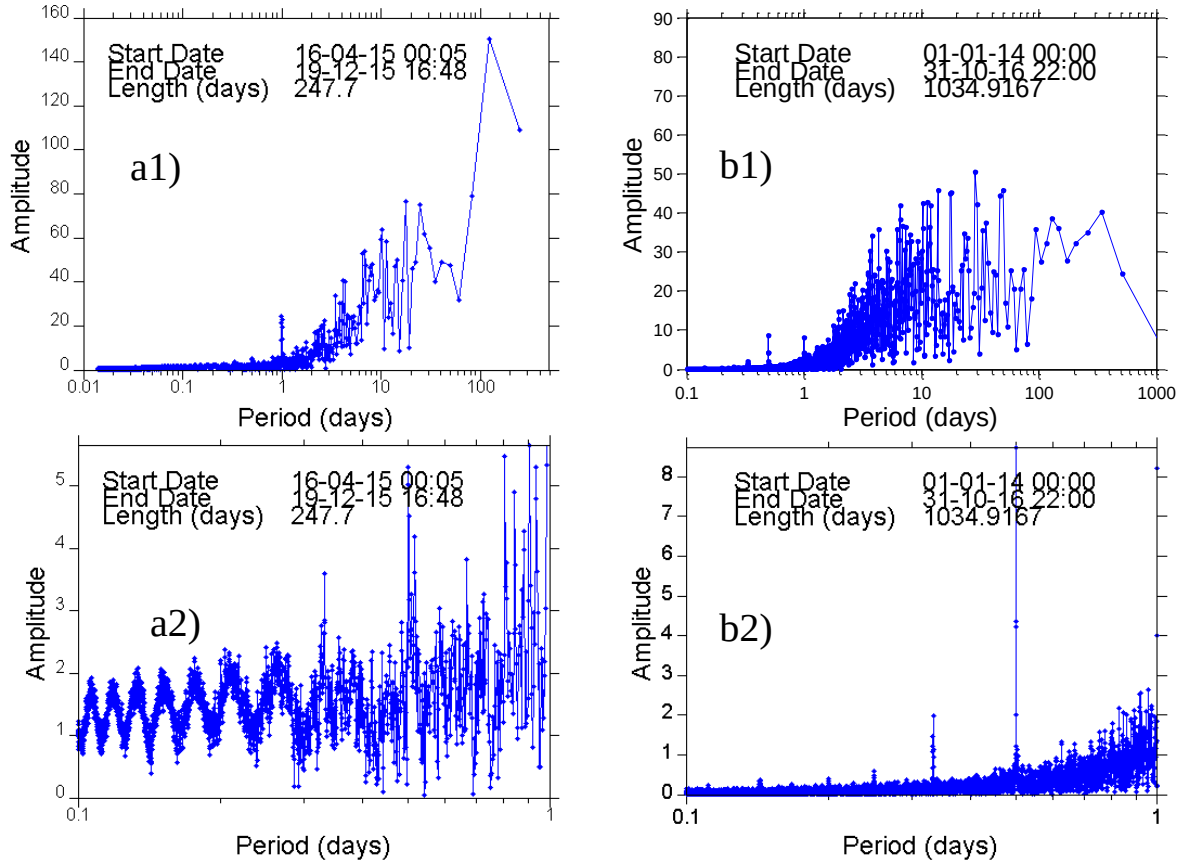

Figure 2-15 – Discrete Fourier transform for barometric pressure, a1) 10 minute average data from WRS#3, a2) for periods less than 1 day, b1) hourly data from the mine operated monitoring system, b2) for periods less than 1 day

2.6.4 External Differential Air Pressure

The air pressure around the perimeter of the pile responds to changes in the barometric pressure and wind vector. Average differential air pressures increase towards the toe of the pile (Table 2-5), due to turbulent effects from wind flow or otherwise increased path lengths for the flow to pass over the pile. The exception was the western side of the pile, which had an average differential pressure of 2.4 Pa towards the middle of the batter and 1.7 Pa at the toe. Otherwise, average differential pressures was around 0.5 Pa near the crest of the pile and between 4-5.9 Pa at the toe.

Table 2-5 – External pressure statistics from the WRS#3 logger for the 10minute average data set

Monitoring Face	**Average Differential Pressure (Pa)**		
	1 (Crest)	2 (middle)	3 (Toe)
South	0.48	3.55	5.69
East	0.55	3.08	3.97
West	0.63	2.37	1.71
North	0.68	2.92	5.89

The DFT for external air pressure show broad dominance for the range of period between t = 7 – 20 days, which is indicative of the influence of barometric pressure. The peak at the daily period is more dominant for the locations at the toe of the pile (Figure 2-16c and f) compared with the locations at the crest and middle (Figure 2-16a, b, d and e), reflecting the increasing influence of wind from the crest to the toe. There is also a peak at t = 0.5 days at the toe, except at location E3, that is an indicator of the action of wind. The peaks at t > 100 days are due to calculation bias and are not indicative.

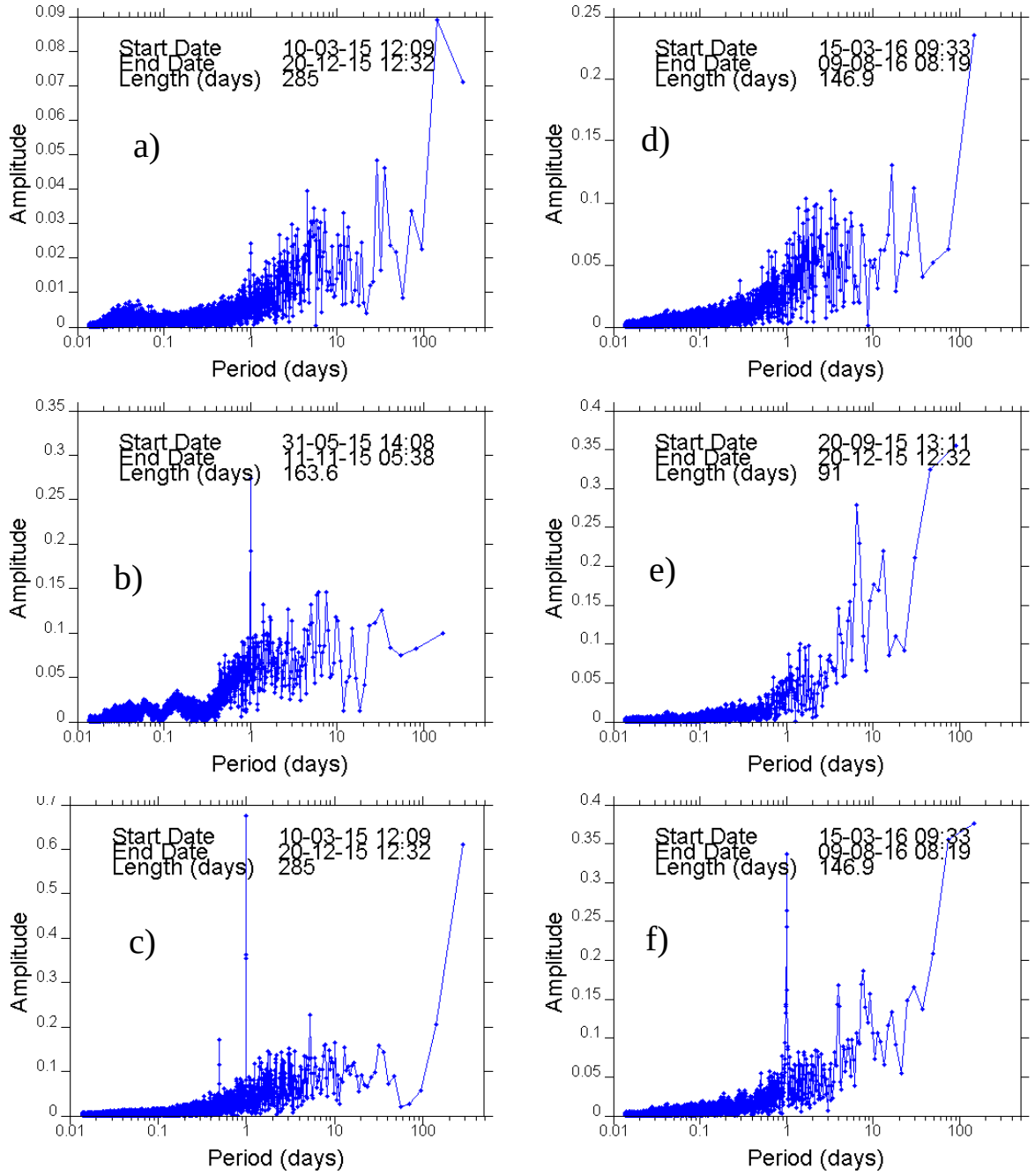

Figure 2-16 – Discrete Fourier transform for the 10 minute data set for external pressure, a) north side, near the crest, b) north side, middle, c) north side, near the toe, d) east side, near the crest, e) east side, middle and f) east side, near the toe

Example data sets for the north side, near the crest (Figure 2-17a) and the toe (Figure 2-17b) have been plotted for the time periods less than 1 day. No additional peaks are indicated within

this time frame, apart from the peak at t = 0.5 days for the location at the toe that was clearly identified for the entire data set.

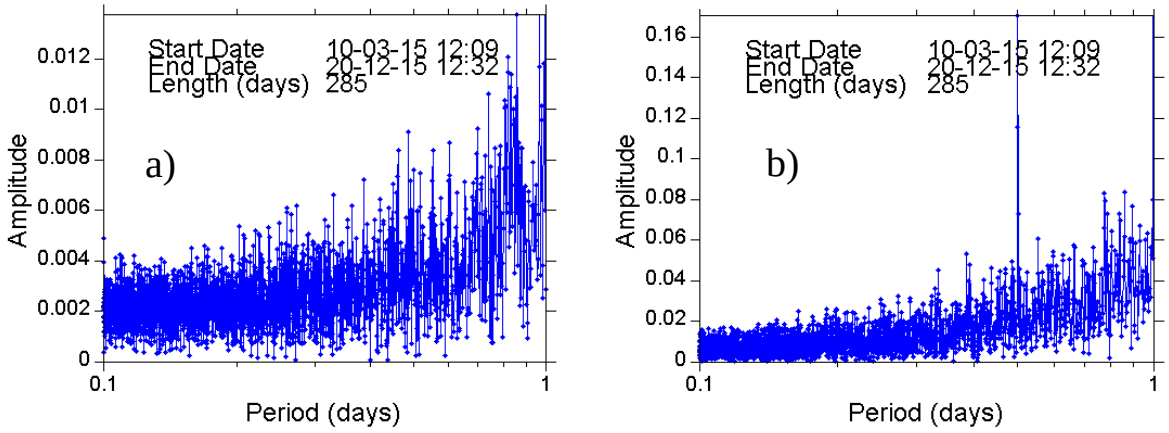

Figure 2-17 – Discrete Fourier transform for the 10 minute data set for external pressure, a) north side near crest, for periods less than 1 day and b) north side, near toe, for periods less than 1 day

2.6.5 Internal Air Pressure

It is notable that the barometric pressure can vary by up to 2000 Pa (20 hPa) over the course of a day, however the measured differential air pressure around the exterior of the pile and within the interior of the pile (relative to the pressure at the crest) generally stays within the range of ±10Pa. The differential pressures are at least three orders of magnitude less than the magnitude of the barometric pressure, indicating the effect that barometric has on the pressure regime within the pile, even at depths beyond 15m.

Negative values for differential pressure at the internal monitoring points indicate that the direction of advective transport is into the pile at that time, and positive pressures indicate outward flow. Positive internal differential pressures are indicative of decreasing barometric pressure (Figure 2-18). The differential pressure within the pile is positive for a greater amount of time during the winter than the summer (Table 2-6).

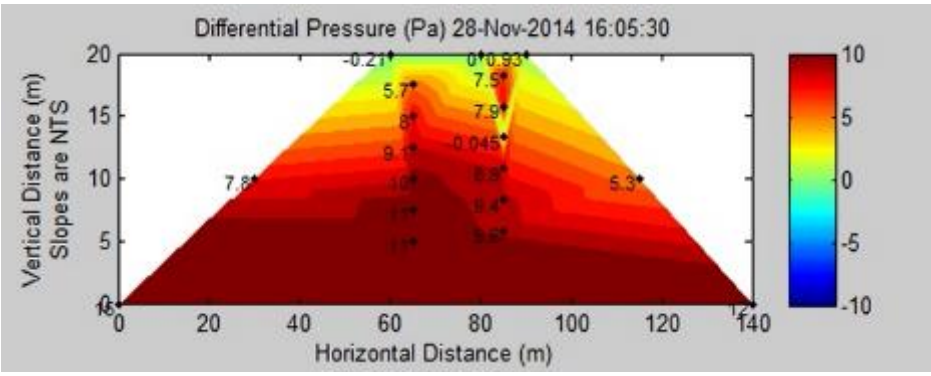

Figure 2-18 – Contour plot representing a positive differential gas pressure distribution within the interior of WRS#3

Table 2-6 – Internal pressure statistics from the WRS#3 logger for the 10minute average data set

Monitoring Location	**% Time of Positive Differential Pressure (Summer)**	**% Time of Positive Differential Pressure (Winter)**
BH2011-3-1-1.7m	37	74
BH2011-3-1-4.2m	35	75
BH2011-3-1-6.7m	22	75
BH2011-3-1-9.2m	29	84
BH2011-3-1-11.2m	37	74
BH2011-3-1-14.2m	27	81
BH2011-3-2-2.5m	44	73
BH2011-3-2-5m	41	74
BH2011-3-2-7.5m	52	82
BH2011-3-2-10m	47	84
BH2011-3-2-12.5m	39	91
BH2011-3-2-15m	40	85

The DFT for internal air pressure is similar to that of barometric pressure, due to the relatively small differential pressures measured within the pile. The peak at the daily period does not

appear to become more or less dominant at shallow (Figure 2-19a1) or deeper locations (Figure 2-19b2).

Plots for the time period less than 1 day (Figure 2-19a2 and b2) indicate that there are several peaks within this range that are not identifiable in the entire data set. Peaks are indicated at approximately 0.15, 0.2, 0.3 and 0.8 days in both data sets.

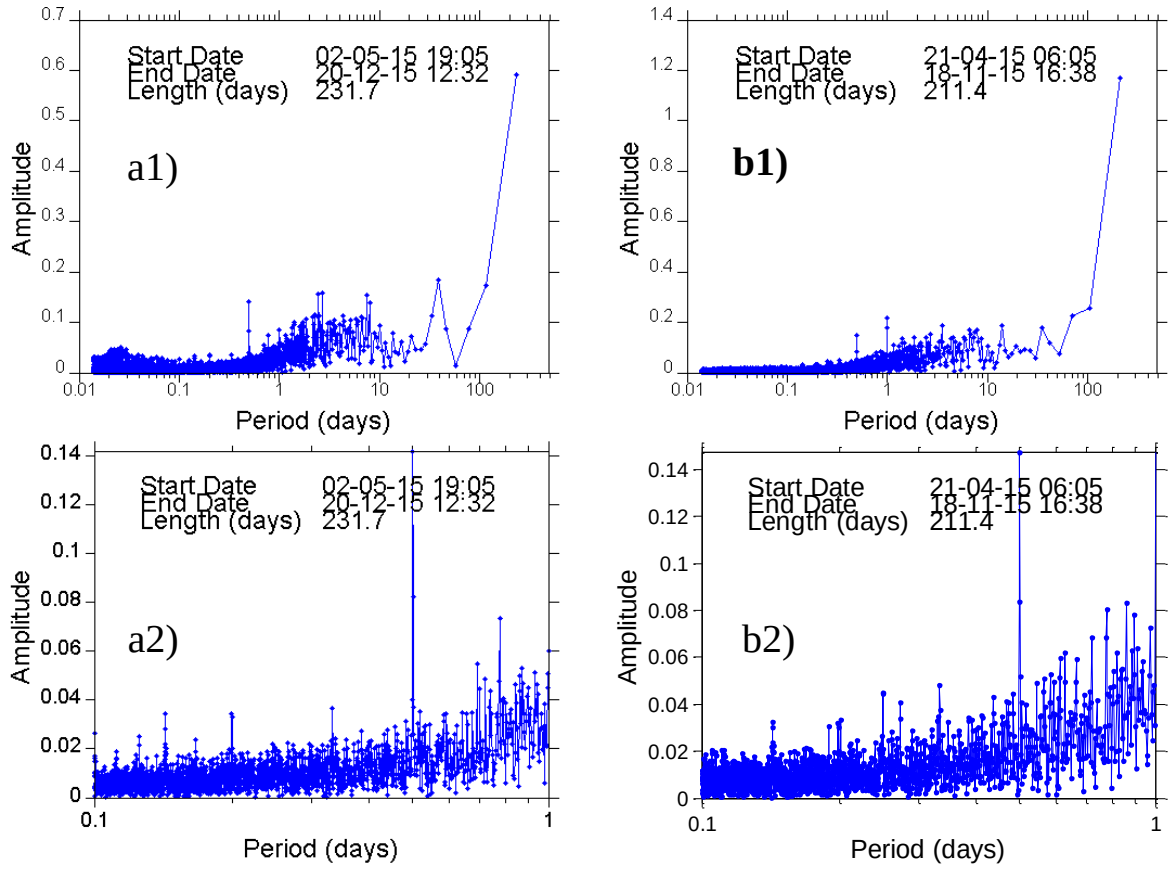

Figure 2-19 – Discrete Fourier transform for the 10 minute data set for internal pressure, a1) BH2011-3-1 at 1.7m depth, a2) for periods less than 1 day , b1) BH2011-3-1 at 14.2m and b2) for periods less than 1 day

2.6.6 Internal Temperature

Heat is released with sulfide oxidation, and this heat is retained within waste-rock piles due to the poor thermal conductivity of waste-rock (Harries and Ritchie, 1981). Elevated temperatures

could therefore be anticipated within waste-rock piles, and sulfide oxidation rates will increase with rising temperature.

Heat is transported into and within waste-rock piles through conduction and convection. Soil covers are a poor conductor of heat in comparison to the waste-rock (Pham, 2013). Covers will therefore reduce heat influx into the waste-rock pile during those times when the exterior temperature is higher than the internal temperature, and will retain heat within the pile when the internal temperature is greater than the external temperature. Heat retention within waste-rock is not desirable, however it will occur during the winter in northern environmental such as Detour, when the permeability of the cover is likely to be reduced due to freezing.

The temperature was monitored within the cover and the waste-rock at WRS#3. The temperature profile at BH2013-3-5 (Figure 2-20a and b), entirely within the cover, clearly indicates dampening of the seasonal fluctuations in ambient temperature. The dampening of the ambient temperature fluctuations is more pronounced during the winter than the summer as indicated by the lower rate of change of temperature. The frozen cover in the winter has a relatively higher insulating capacity and lower permeability. The amplitude of the temperature fluctuations reduces further into the pile (Figure 2-21).

It is notable that the timing of the maximum and minimum temperatures within the pile does not necessarily correspond with the summer and winter seasons due to time factors in heat transport and the insulating nature of the cover. Interestingly, the peak temperature at 9.18 m depth is around mid-January, which is in the middle of winter.

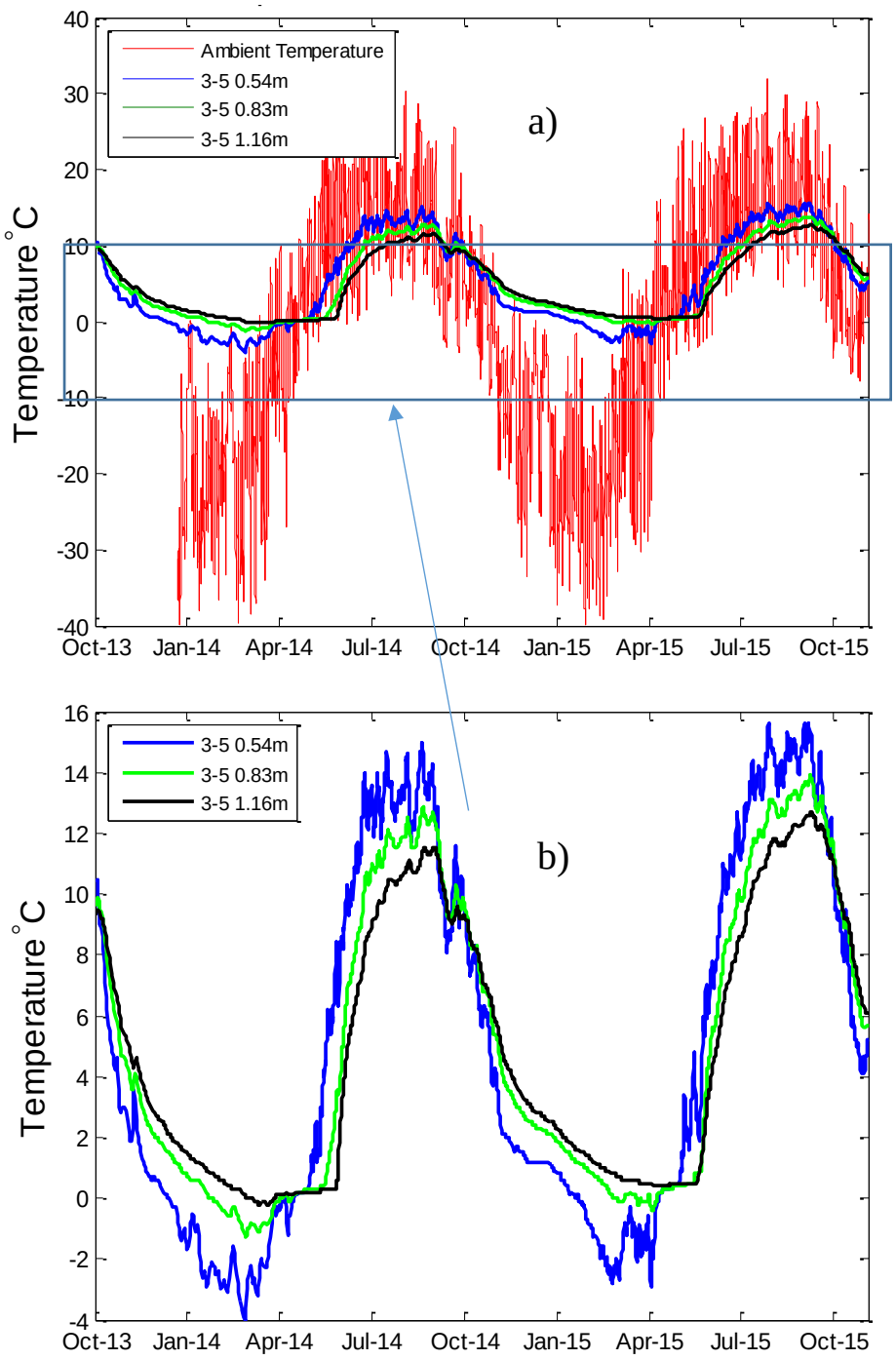

Figure 2-20 – Time series for temperature within the cover at BH2011-3-5, a) including ambient temperature, b) cover data only

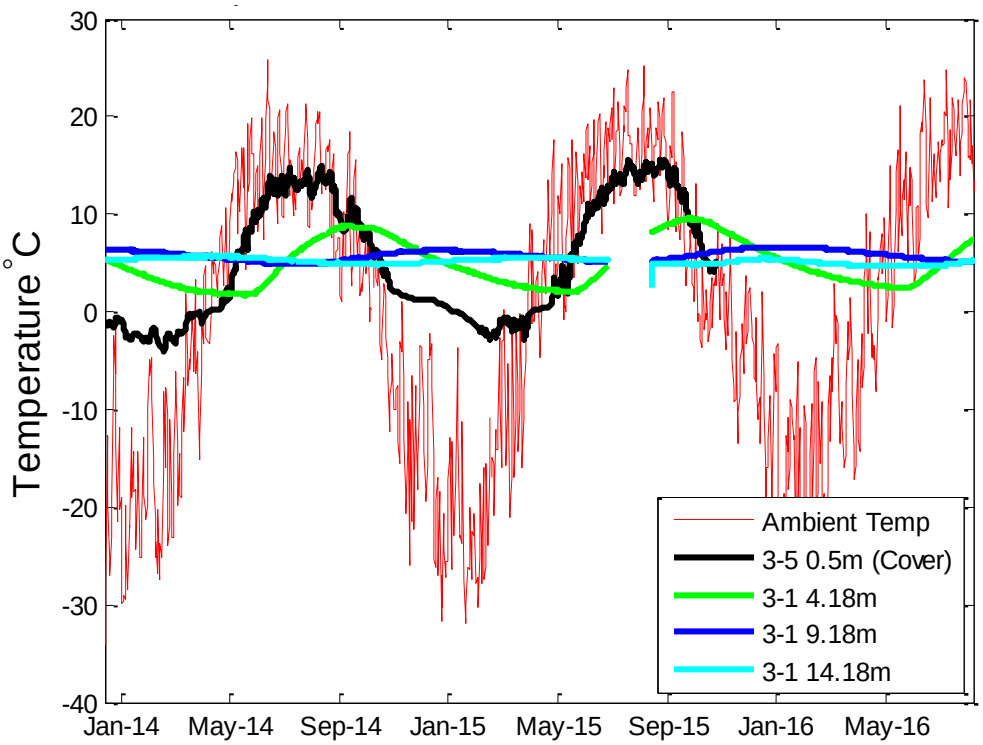

Figure 2-21 – Time series for the ambient temperature and temperature within the cover and waste-rock at WRS#3

The water table is considered to be the base of the pile and was generally measured between 16-17m below the crest. Temperature measurements were recorded at four locations beneath this depth, two each at BH2011-3-1 and BH2011-3-2 (Figure 2-22).

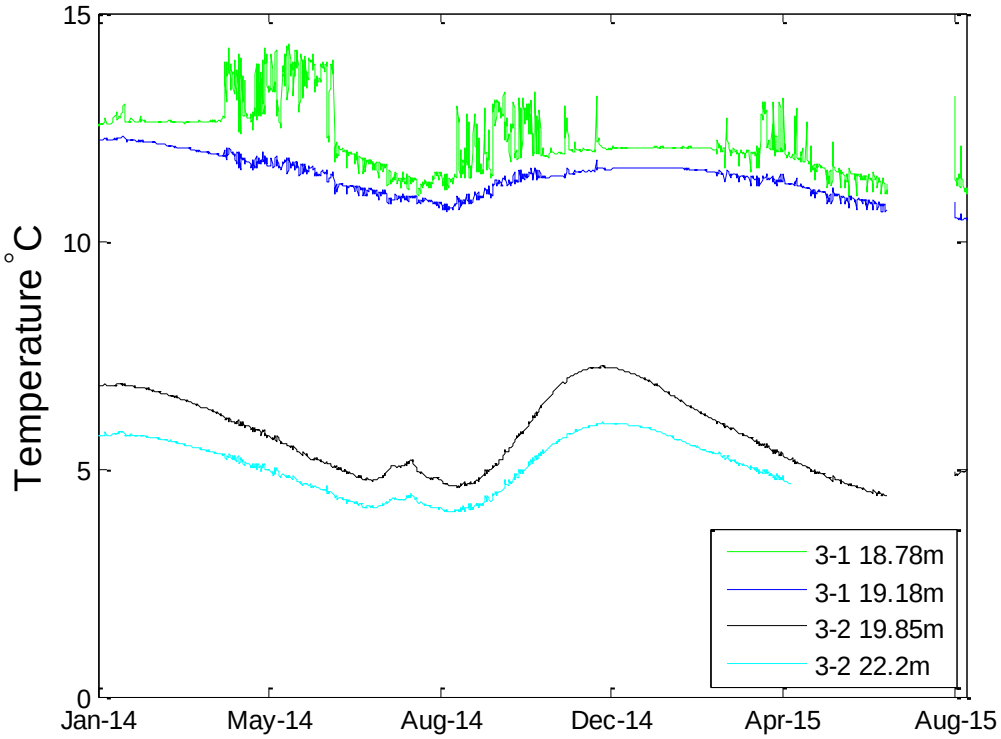

Figure 2-22 – Time series for the temperature beneath the water table at WRS#3

Loss of heat through the base of waste-rock piles has been observed in other studies (Lefebvre et al., 2001a). There was a difference in temperature of approximately 6°C between BH2011-3-1-19.18/18.78 m and BH2011-3-2-19.85 m, which is a larger difference than would be expected for two points that are only 20 m apart and at similar elevations. The minimum annual temperature beneath the base at BH2011-3-2 is approximately equal to the minimum at BH2011-3-1-14.18m, which is the nearest measuring point with respect to elevation. However, the maximum temperature beneath the base is higher than the maximum temperature at BH2011-3-1-14.18 (Figure 2-23). This indicates that the basal temperature is not directly determined by ambient temperature fluctuations and heat transport through the pile. Factors outside of the pile footprint that may influence the basal temperature, including regional groundwater flow and heat production from peat strata in the natural subsurface. The base is a source of heat when the temperatures are higher than that immediately above it, which coincides approximately with the

winter. The base becomes a sink for heat during the summer, like the waste-rock immediately above it.

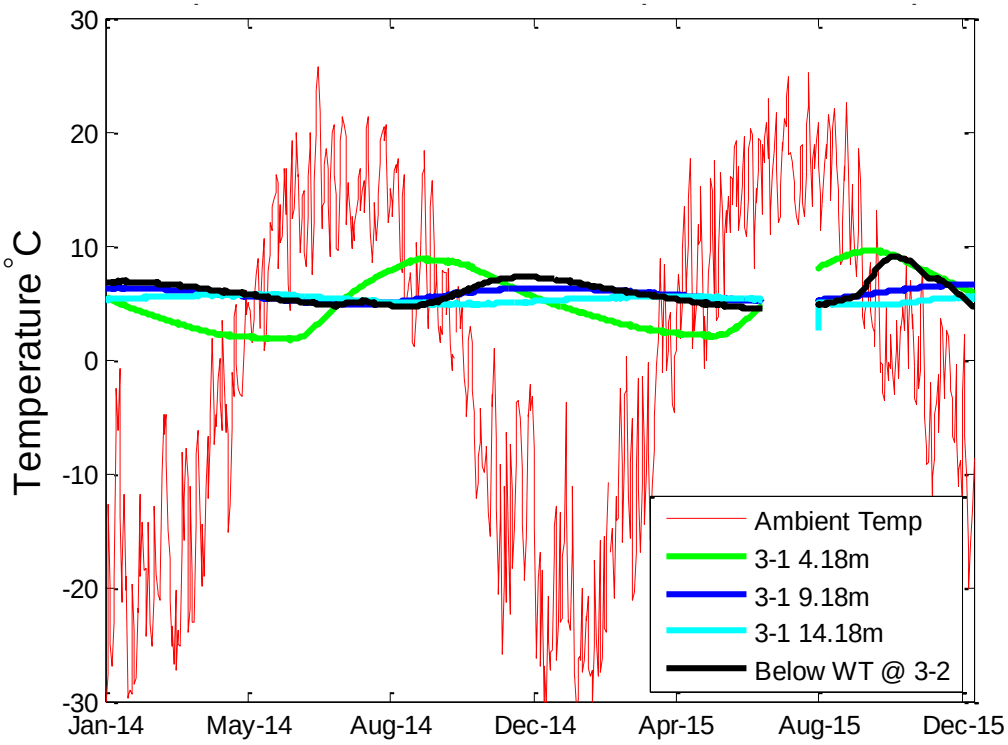

Figure 2-23 – Time series for the ambient temperature, temperature within the waste-rock and beneath the water table

The recorded temperatures are not as high as have been observed at other mines. Temperatures up to 56°C have been observed at localised points at Rum Jungle in Northern Territory, Australia (Harries and Ritchie, 1981) and up to 65°C at Mine Doyon in Quebec (Lefebvre et al., 2001a). Thermally driven advection was considered to be the dominating mechanism for gas transport at these locations.

The pile internal temperatures are typically higher than the atmospheric temperature during the winter (Figure 2-24a) and typically lower than the atmospheric temperatures during the summer (Figure 2-24b).

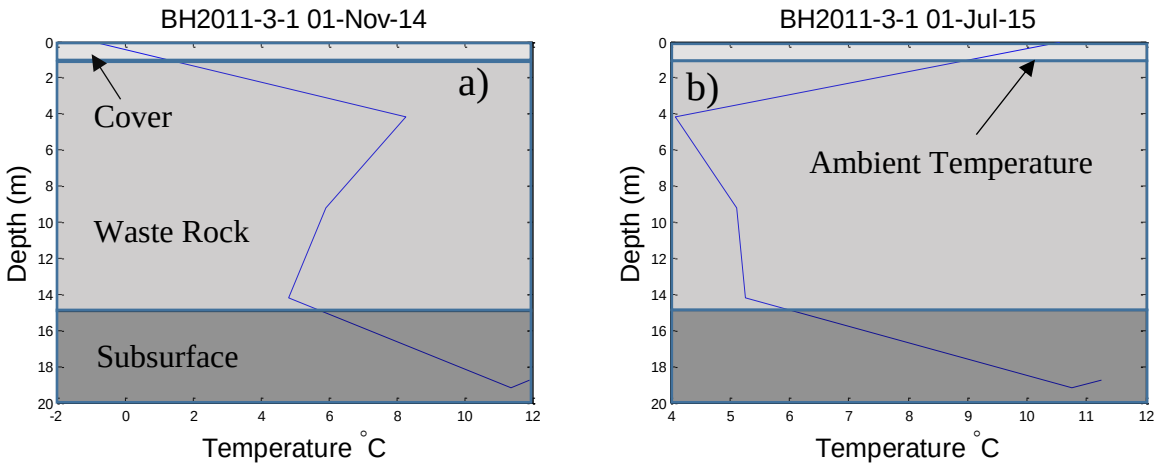

Figure 2-24 – Temperature profile with depth on a day in a) the winter, 1st November 2014, b) the summer, 1st July 2015

The dominant period in the DFT for both surficial and internal temperature is coincident with the calendar year (Figure 2-25a1 and b1). The magnitude of this peak overshadows the other peaks in the amplitude-period plot, and plotting the data for time periods less than 10 days (Figure 2-25a2 and b2) indicates that there are numerous other local peaks, including at 0.3, 0.5 and 5 days, that are captured in the surface measurement profile but are not observed in the interior locations. The cover is acting as a thermal barrier, and surficial temperature fluctuations are dampened within the waste-rock.

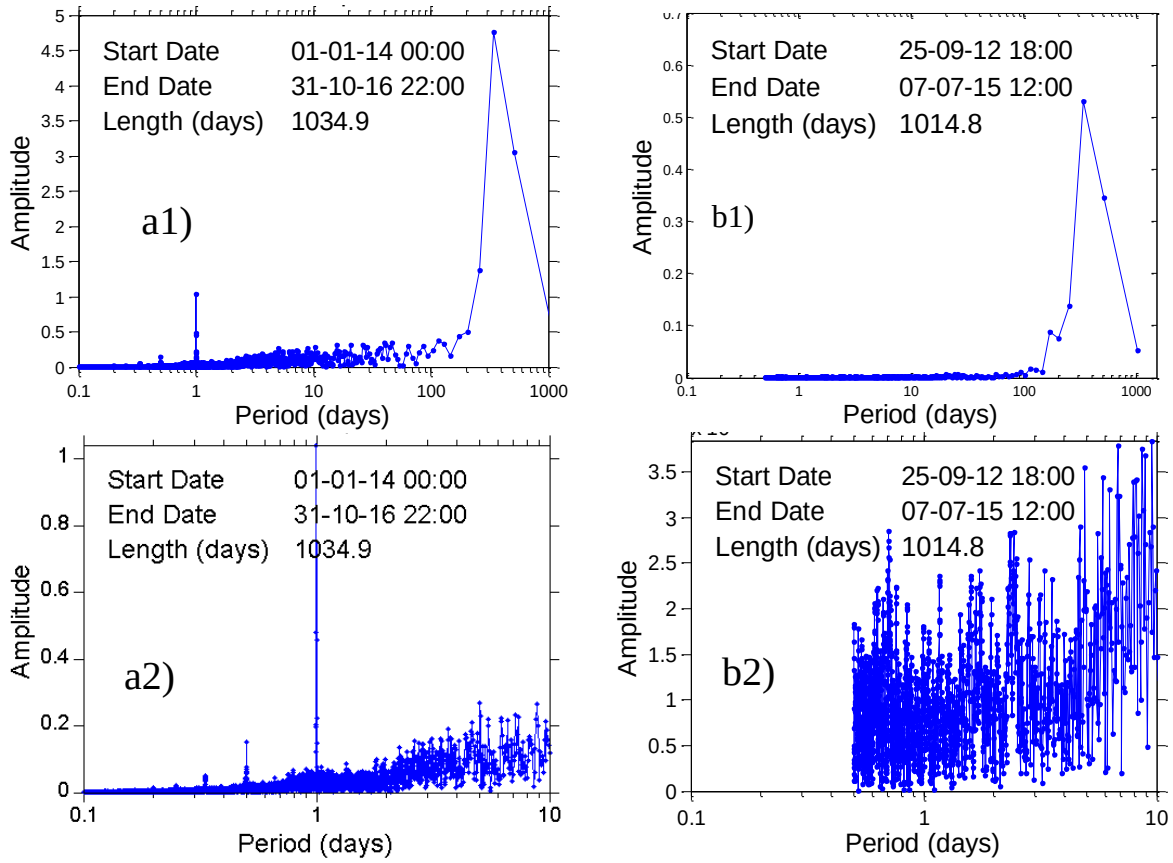

Figure 2-25 – Discrete Fourier transform for a1) ambient temperature, a2) for periods less than 1 day, b1) temperature within the waste-rock at BH2011-3-1-4.85m and b2) for periods less than 1 day

2.6.7 Pore-gas Oxygen Content

The pore-gas O_2 content within the cover was higher than that within the waste-rock, as expected, however some O_2 depletion was observed within the cover (Figure 2-26a and b). It is possible that sulfide oxidation occurred within the cover and O_2 depleted gas was transported from within the waste-rock. The O_2 content of the pore-gas was generally at atmospheric levels within the top 0.2 m of the cover but the extent of O_2 depletion below this depth is variable.

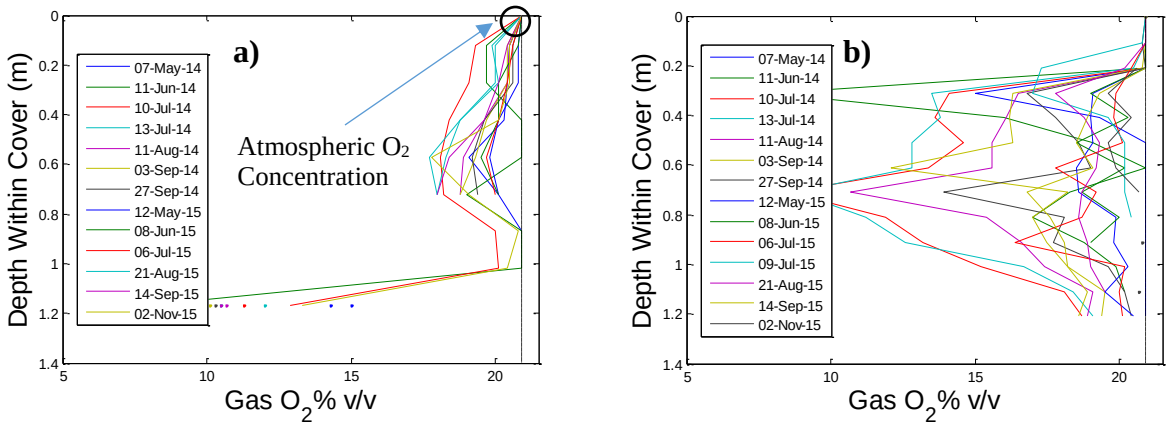

Figure 2-26 – Measured pore-gas oxygen content within the cover at WRS#3, a) BH2013-3-4 and b) BH2013-3-7. Manual readings recorded with a Quantum Model 902P sensor

Pore-gas O_2 content within the waste-rock was more variable during the summer (Figure 2-27a) than the winter (Figure 2-27b). Fluctuations in the O_2 content of up to 8% v/v were observed over the course of 24 hours during the summer. Oxygen content generally decreases with depth during the summer and the trends of the time series are similar. The O_2 content at the base of the pile was relatively constant in the winter and summer, below 5% v/v.

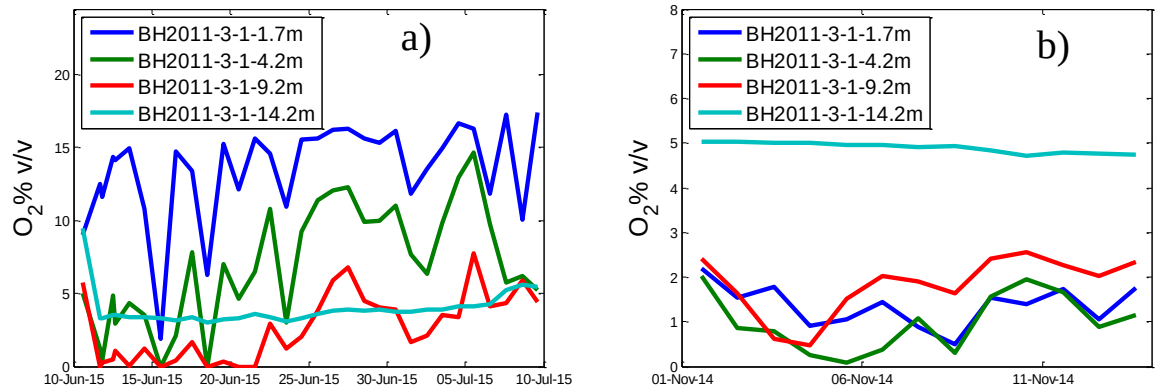

Figure 2-27 – Time series for pore-gas oxygen content during a) a period in the summer and b) the winter. Recorded with the WRS#3 Automated Logger

The O_2 concentration profile with depth drops exponentially during the winter (Figure 2-28a and b), defined for this study as November through June, which is indicative of a diffusion dominated gas transport system. The upper bound threshold for material permeability to ensure diffusion dominated transport is generally considered to be $1x10^{-10}$ m^2 (Lefebvre et al., 2001a).

The profile with depth follows a more linear trend with depth during the summer (Figure 2-28c and d), defined for this study as August through October, which is indicative of an advection dominated gas transport system (Lefebvre et al., 2001a). Particle size distribution test results provided in Cash (2014) indicate that the percentage fines (passing the 75µm sieve) was less than 20% for most samples of the cover material, which in this case was not sufficient to provide a sufficient barrier to advective transport.

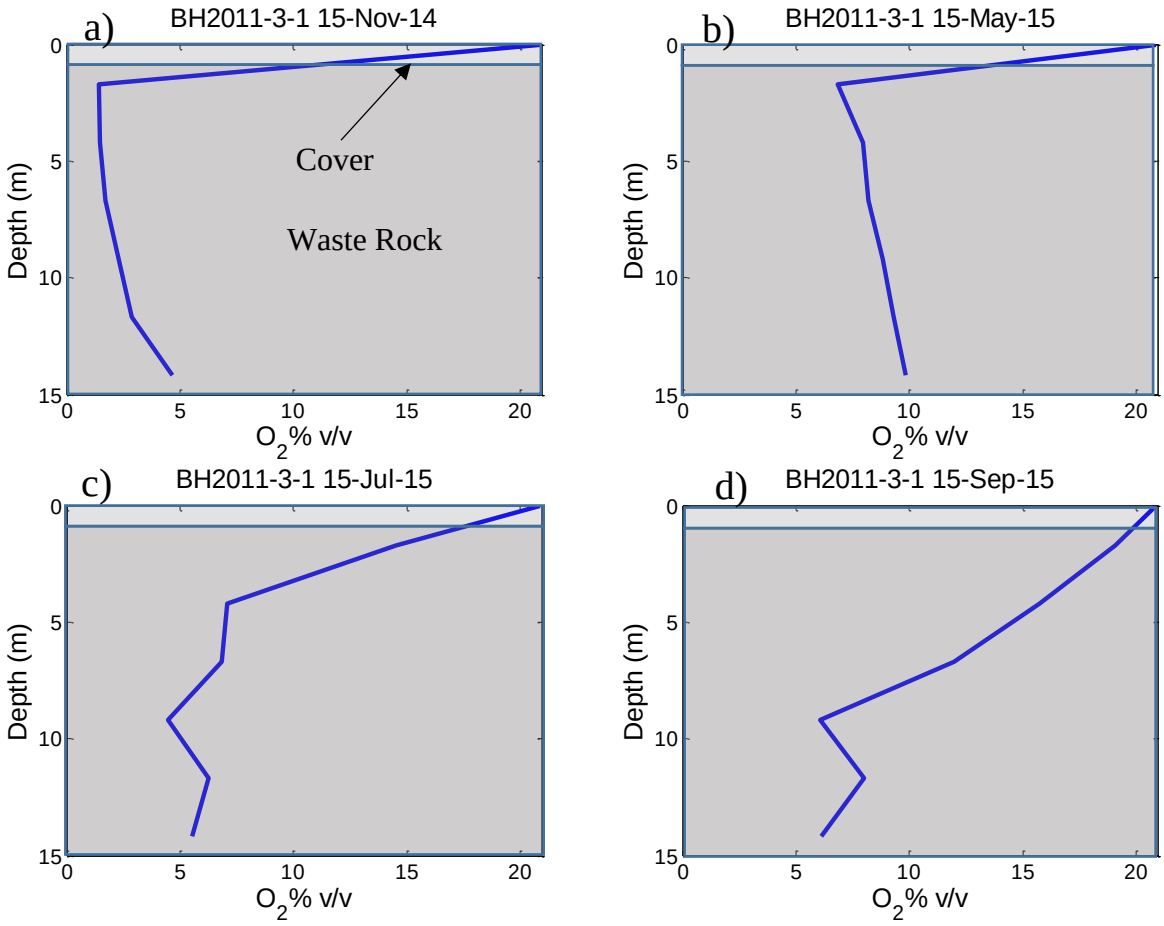

Figure 2-28 – Pore-gas oxygen content with depth for a) typical diffusive profile during the winter on a) 15^{t} November, 2014, b) 15th May, 2015, c) transition period including both the advective and diffusive profile on 15st July, 2015 and d) typical advective profile during the summer on 15st September, 2015

Temperature monitoring indicated that the cover was only partially saturated throughout most of the year and that the cover partially froze during the winter. Freezing during the winter likely

reduced the permeability of the cover significantly and therefore the magnitude of advective transport. The cover was thawed during the summer, and was not sufficiently impervious to fully cut off the contribution of advective gas transport. The typical profile from July 2015 (Figure 2-28c) indicates advective transport (typical for a summer profile) in the upper 7.5 m and diffusive transport (typical of a winter profile) beneath this depth, indicating that this month is transitory between the winter to summer profiles.

No local peaks are observed in the DFT for pore-gas O_2 content (Figure 2-29a and b). The peak at t=74 days, the extent of the data set, is likely due to calculation bias and not indicative of an actual trend. Sampling for pore-gas concentrations at BH2011-3-1 and BH2011-3-2 are completed daily so it is not possible to resolve periodic fluctuations less than two days.

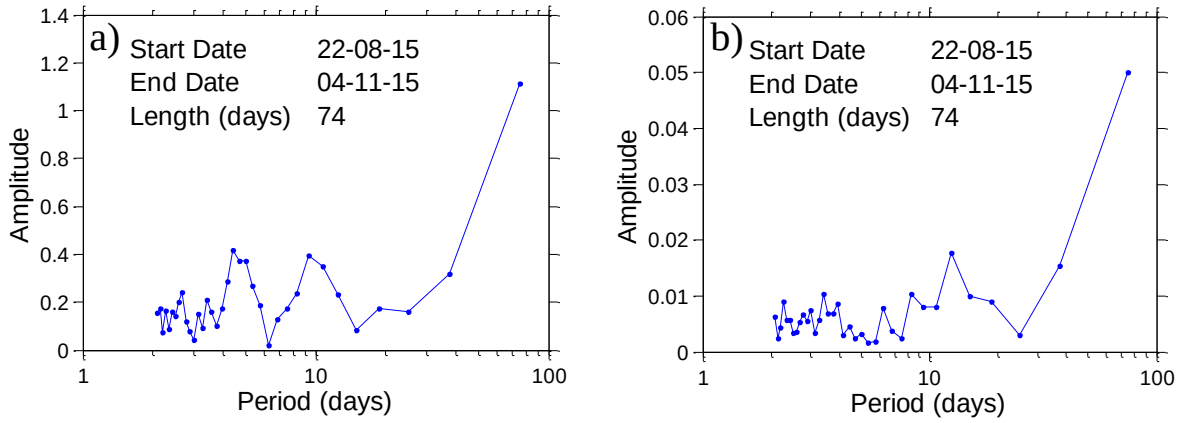

Figure 2-29 – Discrete Fourier transform for pore-gas oxygen content at a) BH2011-3-1-4.2m and b) BH2011-3-1-14.2m

Field monitoring of O_2 within waste rock at the daily frequency or better has seldom been carried out. Continual daily monitoring of the O_2 level within covered piles was carried out by Amos et al. (2009a) within waste rock with a sufficiently low sulfur content (>0.08% wt) that the measured O_2 level was always close to atmospheric (minimum recording of approximately 20% v/v). Singurindy et al. (2012) recorded the O_2 concentrations daily within an uncovered

experimental pile at the Antamina mine in Peru daily. Measurements were taken for one year, within waste rock with a sulfur content of between 0.2 – 4.26 % wt. The O_2 level was between 16% v/v and atmospheric levels (20.9%) at most monitoring locations, which is higher than observed at Detour. The O_2 level at one monitoring point at Antamina was between 7% and 15% over the year of monitoring.

Monitoring has been carried out at discrete times has been carried out at other sites (Garvie et al., 1999; Lundgren, 2001; Birkham et al., 2003). Seasonal fluctuations were generally observed, highlighting the importance of a site specific characterisation. Observations at the Nordhalde waste-rock pile in Germany (Smolensky et al., 1999; Lefebvre et al., 2001a) indicated diffusion dominated transport in the summer and advection dominated transport in the winter, *i.e.* the opposite trends observed at Detour. The pile from the Nordhalde study did not have a low permeability cover; however the permeability of the waste-rock itself is indicated to be low, in the range of $8x10^{-12}$ m^2. Diffusion is typically the dominant mechanism with this magnitude of permeability; however, significant temperature gradients within the Nordhalde pile developed during the winter, inducing some thermally driven convection.

2.6.8 Pore-gas CO_2 Content

Pore-gas CO_2 content within the cover was generally between 0-1% above 0.2m depth and variable enrichment of CO_2 was observed below this depth (Figure 2-30a and b). The CO_2 content in the cover is variable with depth and with time. The average sulfur content of the cover material was 0.05% from carbon/sulfur testing carried out by McNeill (2016). Sulfide oxidation could be occurring within the cover, and carbon dioxide may therefore also be produced in the cover through carbonate neutralisation. Carbon dioxide may also be produced within the waste-rock and transported through the cover by advective and diffusive means.

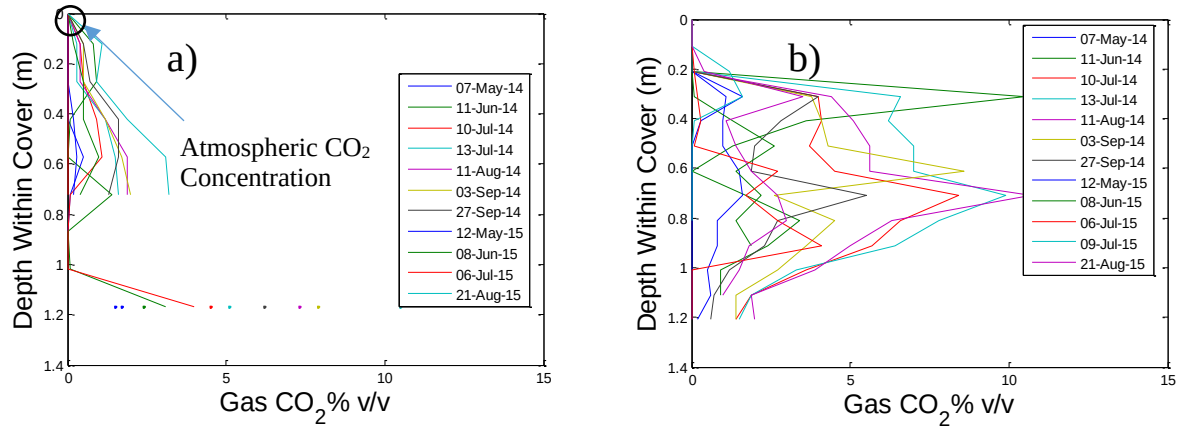

Figure 2-30 – Measured pore-gas carbon dioxide content within the cover at WRS#3, a) BH2013-3-4 and b) BH2013-3-7. Manually recorded with a Quantum 902P sensor

The pore-gas CO_2 content within the waste-rock is variable during the summer (Figure 2-31a) and relatively constant during the winter (Figure 2-31b), as has been observed with the O_2 content during the same time periods.

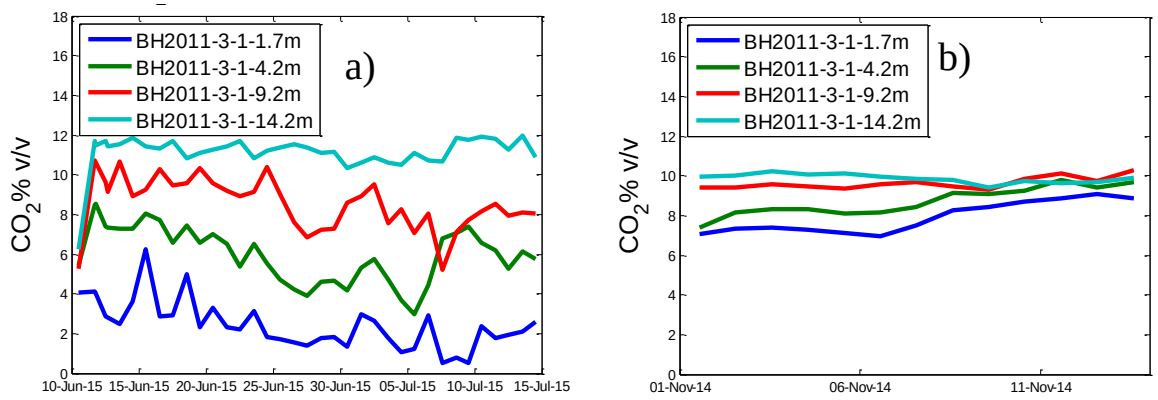

Figure 2-31 – Time series for pore-gas carbon dioxide content during a) a period in the summer and b) the winter. Recorded with the WRS#3 automated logger

An increasing trend for CO_2 content is evident with depth. The trend in the winter could be qualitatively described as 'inverse exponential' (Figure 2-32a) and the trend in summer is linearly increasing with depth (Figure 2-32b).

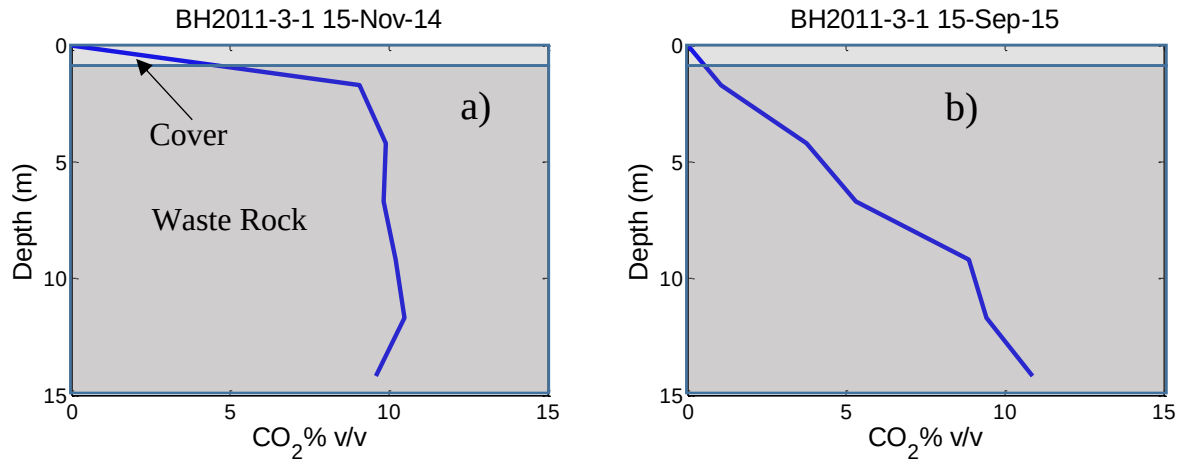

Figure 2-32 – Pore-gas carbon dioxide content with depth for a) typical diffusive profile during the winter on 15th November b) typical advective profile during the summer on 15th September, 2015

No local peaks are evident in the DFT for pore-gas CO_2 content within the time frame of the available data (Figure 2-33a and b). The peak at t=74 day is likely due to calculation bias and cannot be considered representative.

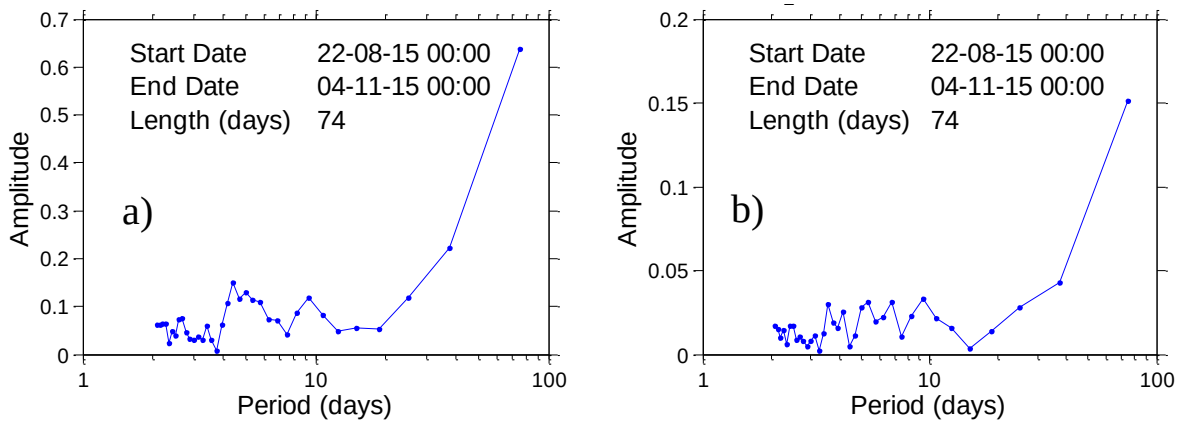

Figure 2-33 – Discrete Fourier transform for pore-gas carbon dioxide content at a) BH2011-3-1-4.2m and b) BH2011-3-1-14.2m

Field monitoring of CO_2 within waste rock has been carried out in fewer studies than O_2. Continual daily monitoring of CO_2 was carried out at by Amos et al. (2009), and levels of up to 0.6% v/v were recorded, which is an order of magnitude above atmospheric levels. Singurindy et al. (2012) recorded CO_2 levels up 2% v/v, which is the limit of the sensor used, in daily

measurements at the Antamina mine in Peru. It is not known if the CO_2 level within that pile is comparable to the levels (up to 12% v/v) that have been recorded at Detour.

2.6.9 Moisture Content

The moisture content of the cover is highly variable both laterally and with increasing depth (Figure 2-34a and b). Several wetting fronts are evident in the plots, as indicated with a sudden increase in moisture content. For example, the peak in moisture content on the 11th of June, 2015, occurred after a 16.9mm rainfall event (Figure 2-34a). Locally variable material properties are indicated, particularly in the data sets for BH2013-3-4, given the variable moisture content with similar depth (0.83m and 0.85m) and variable response to wetting fronts. An overall decrease in moisture content is evident at all monitoring locations as the summer progresses.

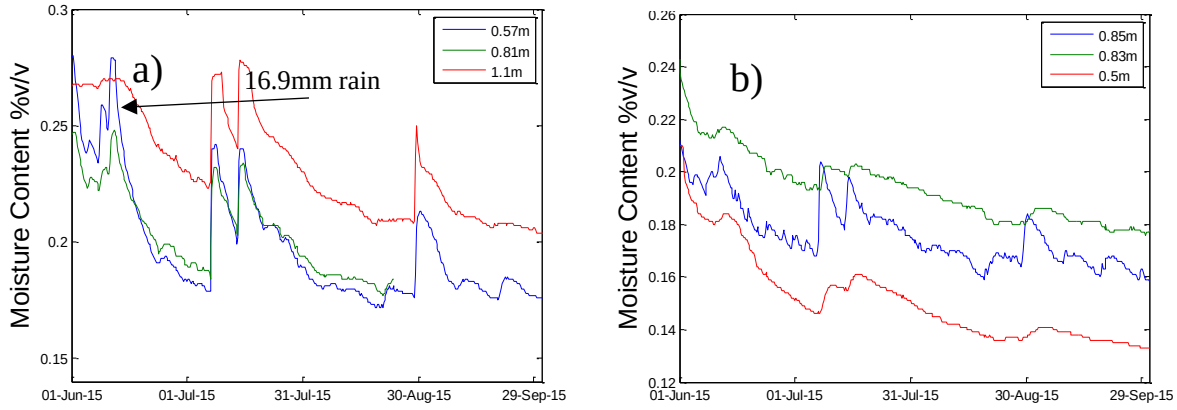

Figure 2-34 – Time series for moisture content within the cover at a) BH2013-3-3 and b) BH2013-3-4. Recorded with ECH2O Probes

The moisture content of the waste-rock is highly variable both laterally and with depth (Figure 2-35a and b). Many wetting fronts are evident during the summer months at the shallow monitoring locations at both BH2011-3-1 and BH2011-3-2. The time that it takes to drain to a moisture content that is likely to be close to the residual is approximately 6 weeks at BH2011-3-1-1.18m and 4 weeks for BH2011-3-2-1.8m. Only one wetting front is indicated at the deeper

(3.18m) monitoring location at BH2011-3-1 (Figure 2-35a and b), and this occurred in the late fall. The freshet in May of 2015 was not observed at this deeper (3.18 m) location. In contrast, the freshet was observed at the deeper (7.85 m) monitoring location at BH2011-3-2; however, it is still clear that there is not a response at this depth to all the wetting fronts that pass the shallow location. The waste-rock is considered to be relatively free draining, so it is possible that preferential flow paths have formed between the shallow and deeper monitoring locations that drained away the bulk of the infiltration.

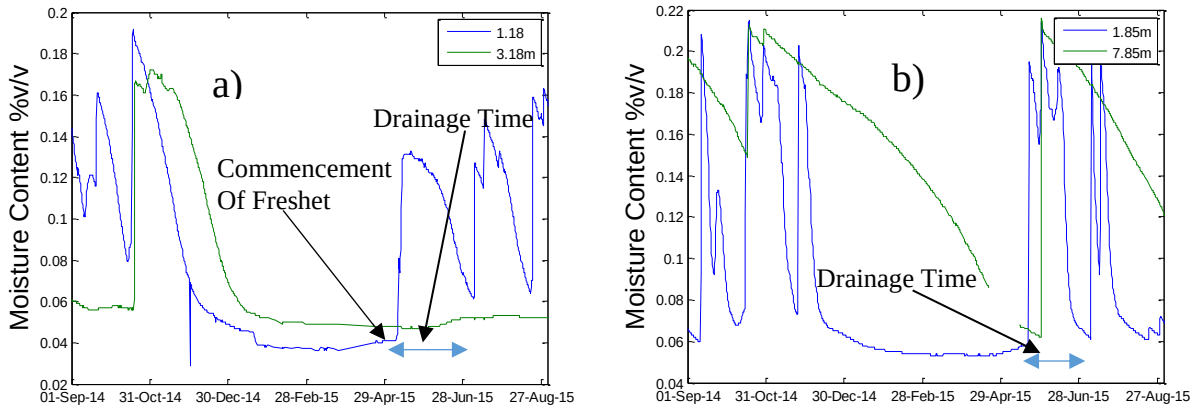

Figure 2-35 – Time series for moisture content within the waste-rock at a) BH2011-3-1 and b) BH2011-3-2

2.7 Data Analysis

A visual inspection of the time series plots for air pressure, pore-gas content, barometric pressure, wind vector and temperature indicate that they are generally sinusoidal, however phase differences (time lags) between different data sets are evident. Determining correlation coefficients between the wind, air pressure and pore-gas data sets is therefore complicated by time considerations. For example, a change in wind speed and air pressure at the surface of the pile will affect both the air pressure and O_2 content of the gas within the pile after a time delay that is related to the permeability and diffusion characteristics of the pile materials. The

correlation between data sets will not be properly reflected by considering data points taken at the same time.

The DFT of the data sets were also reviewed to consider the relationship between data sets. The dominant peaks in the plot give a qualitative indication of the relationship of one data set to the other.

2.7.1 Wind Vector/Barometric Pressure and External Air Pressures

The relationship between wind speed and external air pressure is typically parabolic, when both the wind speed (Figure 2-36a) and the northern (Figure 2-36b) and eastern wind velocity are considered. Wind speed is an invariably positive parameter, however the magnitude of the northern and eastern vector are negative where the direction is from the south and west respectively.

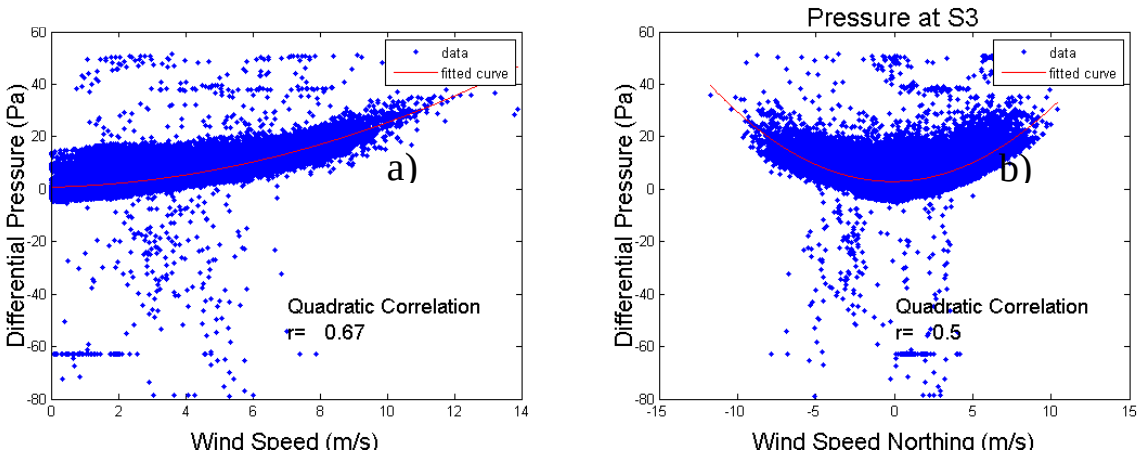

Figure 2-36 – Correlation between a) wind speed and differential pressure at the southern toe, b) northing of the wind velocity and differential pressure. 10 minute average data sets

The parabolic relationship between wind speed and air pressure is expected according to Bernoulli's fluid flow principal (Bird, 1960):

$$\frac{u^2}{2} + gz + \frac{p}{\rho} = constant \qquad 2\text{-}12$$

where u is the flow velocity [m s^{-1}], g is the acceleration due to gravity [m s^{-2}], z is the reference elevation [m], p is the pressure [Pa] and ρ is the density [kg m^{-3}]. Equation 2-12 is only applicable for incompressible flow, however the parabolic relationship between wind speed and air pressure is still indicated by the relationship.

The greater influence of wind at the toe is reflected in the DFT for wind speed and external pressure. The peak at the daily period (characteristic of wind) is more dominant for the locations at the toe of the pile (Figure 2-16a) compared with the locations at the crest and the middle (Figure 2-16b). This relationship is also reflected in the Pearson's correlation coefficients for a parabolic relationship between wind speed and external air pressure (Table 2-7). Moderate correlations are generally indicated for wind speed and external pressure at the toe, poor to moderate at the middle of the batter and very poor at the crest. Correlations are sometimes higher for wind speed than directional velocities, even where pressures on the east and north side of the pile are compared with the easting and northing vector of the wind vector respectively (monitoring location E2).

Barometric pressure and differential air pressure around the exterior of the pile show very poor correlation when coincident measurements for both are considered. Nonetheless, it is known that barometric pressure influences the development of the pressure regime around the pile. External differential pressures generally only fluctuate by $\pm$10 Pa over the course of the day, even though barometric pressure may fluctuate by several thousands of Pascals over the same time period.

Table 2-7 – Correlation coefficients for wind speed vs external pressure

Monitoring Location	Pearson's Correlation Coefficient – Wind Speed	Pearson's Correlation Coefficient – North Vector	Pearson's Correlation Coefficient – East Vector
S1 (crest)	0.06	0.33	0.27
S2	0.60	0.46	0.44
S3 (toe)	0.67	0.50	0.48
E1 (crest)	0.03	0.06	0.04
E2	0.48	0.56	0.20
E3 (toe)	0.58	0.54	0.31
W1 (crest)	0.12	0.26	0.10
W2	0.28	0.28	0.12
W3 (toe)	0.39	0.30	0.26
N1 (crest)	0.15	0.15	0.06
N2	0.51	0.51	0.26
N3 (toe)	0.49	0.47	0.26

2.7.2 Wind Vector/Barometric Pressure and Internal Air Pressures

The relationship between wind vector and internal air pressure is typically parabolic (Figure 2-37a and b), as has been observed with wind vector and external air pressure (Figure 2-36a and b). The correlation coefficients for wind vector and internal air pressure are generally very poor to poor for the locations at BH2011-3-1 and BH2011-3-2, however it is likely that scatter and outliers are reducing the coefficients. The sharp discrepancy between correlation coefficients from adjacent monitoring locations may be due to preferential high permeability pathways within the waste-rock. Higher external pressures were recorded in the north-south direction than the

east-west direction (Table 2-5), and consequently the correlation coefficients are higher for the northing vector than the easting vector.

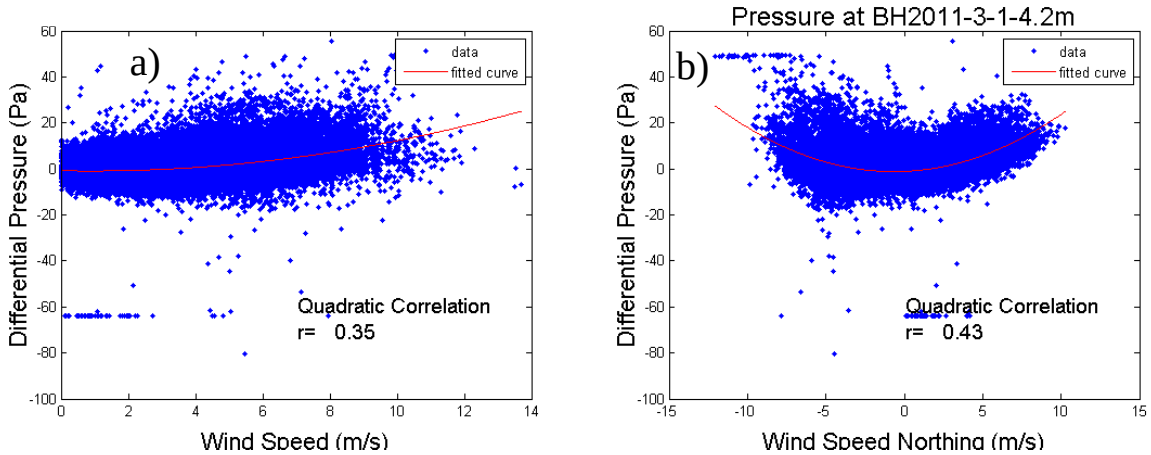

Figure 2-37 – Correlation between a) wind speed and differential pressure at BH2011-3-1-4.2m, b) northing of the wind velocity and differential pressure. 10 minute average data sets

Table 2-8 – Correlation coefficients for wind speed vs internal pressure

Monitoring Location	Pearson's Correlation Coefficient	Correlation Coefficient – North Vector	Correlation Coefficient – East Vector
BH2011-3-1-1.7m	0.28	0.37	0.22
BH2011-3-1-4.2m	0.35	0.42	0.29
BH2011-3-1-6.7m	0.40	0.49	0.21
BH2011-3-1-9.2m	0.36	0.46	0.18
BH2011-3-1-11.2m	0.29	0.36	0.10
BH2011-3-1-14.2m	0.39	0.44	0.20
BH2011-3-2-2.5m	0.22	0.20	0.23
BH2011-3-2-5m	0.35	0.33	0.35
BH2011-3-2-7.5m	0.23	0.21	0.22
BH2011-3-2-10m	0.30	0.25	0.24
BH2011-3-2-12.5m	0.26	0.22	0.18
BH2011-3-2-15m	0.27	0.23	0.19

Barometric pressure and ambient air temperature show very poor correlation with internal gas pressure when coincident measurements for both are considered; however, it is known that barometric pressure affects the internal pressure regime.

2.7.3 External and Internal Air Pressures

A moderate linear correlation is indicated between the daily averaged data for internal differential pressure measurements and external measurements at the toe (Figure 2-38a to c), grading to a very poor correlation at the crest. The correlation is better for the daily averaged data than the 10 minute averaged data. The linear relationships between external and internal pressure indicate that gas transport through the cover and waste-rock is laminar and follows Darcy's law. This observation is in agreement with the observations of Chi et al. (2013).

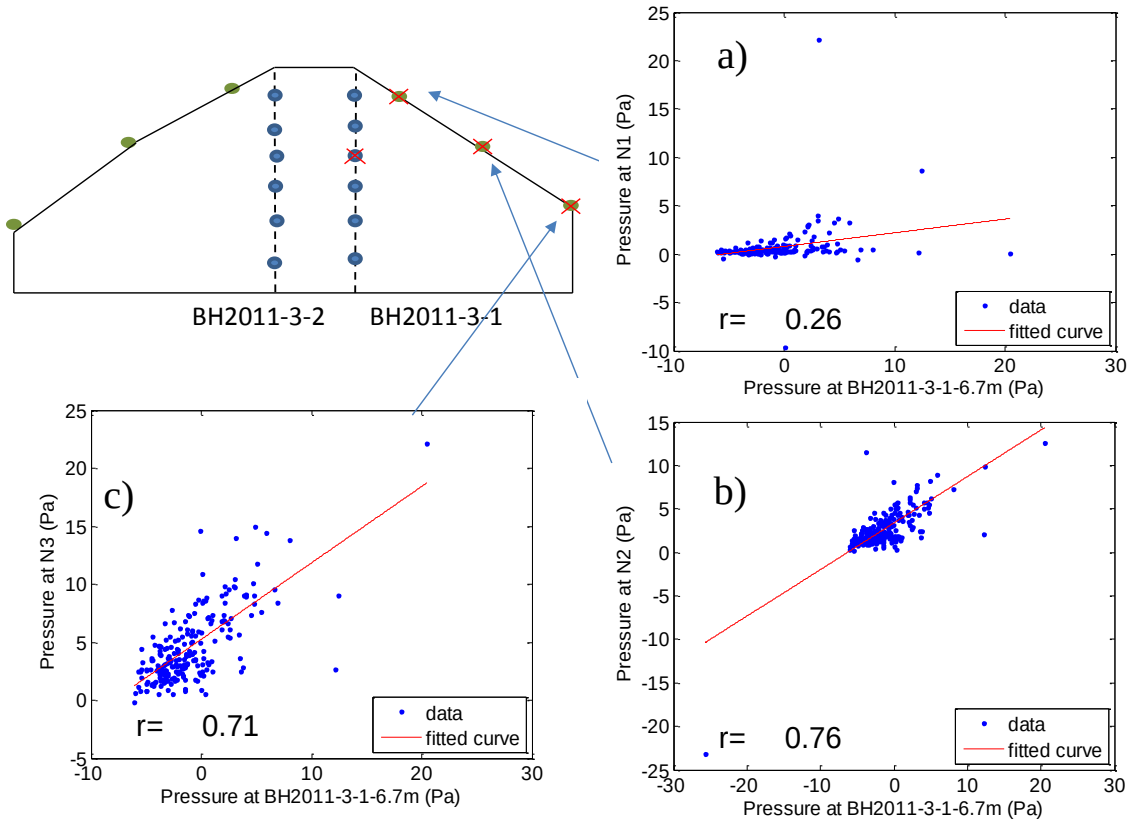

Figure 2-38 – Correlation between the internal pressure at BH2011-3-1-4.2m and a) external location N1 (crest), b) external location N2 and c) external location N3 (toe). Daily averaged data sets

2.7.4 Interior Air pressure / Interior Air Pressure From the Monitoring Location Directly Below or Above

A very good linear relationship is indicated for daily averaged data for pressure when compared with those from the monitoring location directly below it (Figure 2-39a to c and Table 2-9). The correlation coefficients are typically higher than those for the comparisons between external and internal monitoring locations, possibly due to the relatively similar permeability characteristics within the waste-rock as compared with transport through the low permeability cover and the higher permeable waste-rock. This linear relationship confirms that the transport of gas within the waste-rock is laminar and it can be reasonably described by Darcy's law. This finding agrees with that from Chi et al. (2013).

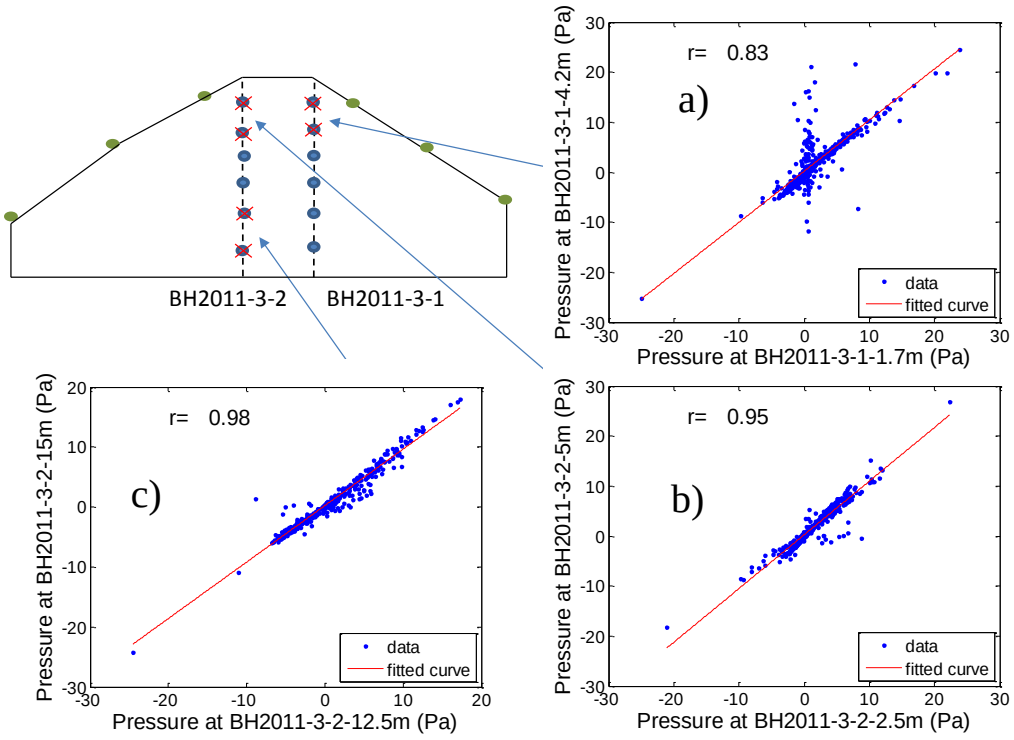

Figure 2-39 – Correlation between internal pressure and the location directly below it, a) BH2013-3-1-1.7/4.2m, b) BH2013-3-2-2.5/5m and c) BH2013-3-2-12.5/15m. Daily averaged data sets

Table 2-9 – Correlation coefficients for interior pressure vs monitoring point directly below

Monitoring Location	Correlation Coefficient
BH2011-3-1-1.7/4.2 m	0.83
BH2011-3-1-4.2/6.7 m	0.97
BH2011-3-1-6.7/9.2 m	0.93
BH2011-3-1-9.2/12.7 m	0.86
BH2011-3-1-12.7/14.2 m	0.87
BH2011-3-2-2.5/5 m	0.95
BH2011-3-2-5/7.5 m	0.87
BH2011-3-2-7.5/10 m	0.95
BH2011-3-2-10/12.5 m	0.93
BH2011-3-2-12.5/15 m	0.98

2.7.5 Interior Air Pressure / Interior Air Pressure From the Location Across at Similar Depth

A good to very good linear relationship is indicated for daily averaged data for pressure when compared with those from the monitoring location directly across from it (Figure 2-40a to c and Table 2-10). The horizontal distance between horizontally adjacent monitoring locations is approximately 20m.

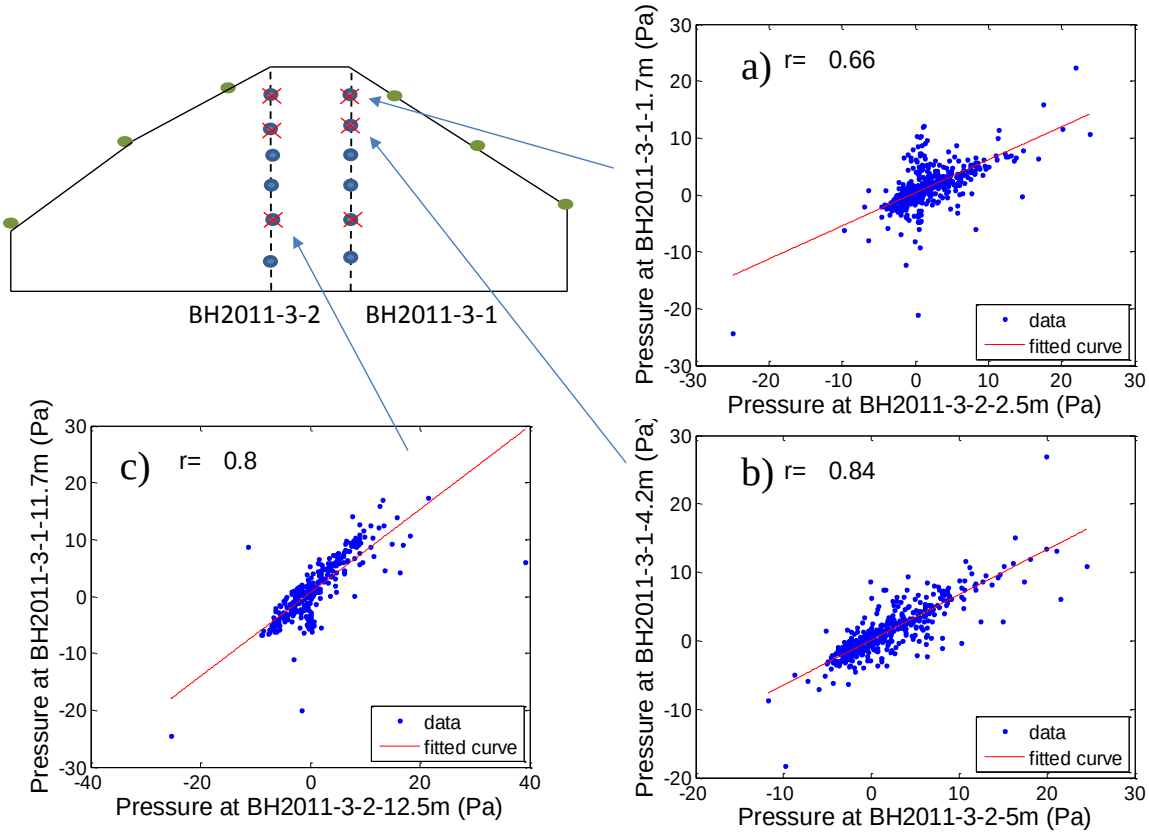

Figure 2-40 – Correlation between internal pressure and the location directly across from it, a) BH2013-3-1-1.7/BH2013-3-2-5m, b) BH2013-3-1-4.2m/BH2013-3-2-5m and c) BH2013-3-1-11.7m/BH2013-3-2-15m. Daily averaged data sets

Table 2-10 – Correlation coefficients for interior pressure vs monitoring point directly across

Monitoring Location	**Correlation Coefficient**
BH2011-3-1-1.7/ BH2011-3-2-2.5m	0.66
BH2011-3-1-4.2/ BH2011-3-2-5m	0.84
BH2011-3-1-6.7/ BH2011-3-2-7.5m	0.75
BH2011-3-1-9.2/ BH2011-3-2-10m	0.89
BH2011-3-1-11.7/ BH2011-3-2-12.5m	0.80
BH2011-3-1-14.2/ BH2011-3-2-15m	0.94

2.7.6 Ambient Temperature / Interior Temperature

The measured exterior and interior temperatures do not correlate well when coincident measurements are plotted (Figure 2-41a), except for the fit between the ambient temperature and the temperature at BH2011-3-1-9.18m (Figure 2-41b) and BH2011-3-2-9.85m. The temperature regime within WRS#3 is influenced by the ambient temperature, the temperature at the base and the production of heat due to sulfide oxidation. A good correlation between ambient temperature and internal temperature would not be expected due to the time component of heat transport through the cover and pile. However, a review of the time series plots in Figure 2-21 indicates that the maximum ambient temperature is during the summer and the maximum temperature at BH2011-3-1-9.18m is in the winter. The temperatures at this depth are approximately 6 months out of phase, half the time of the annual peak period, and a negative correlation in temperature is apparent.

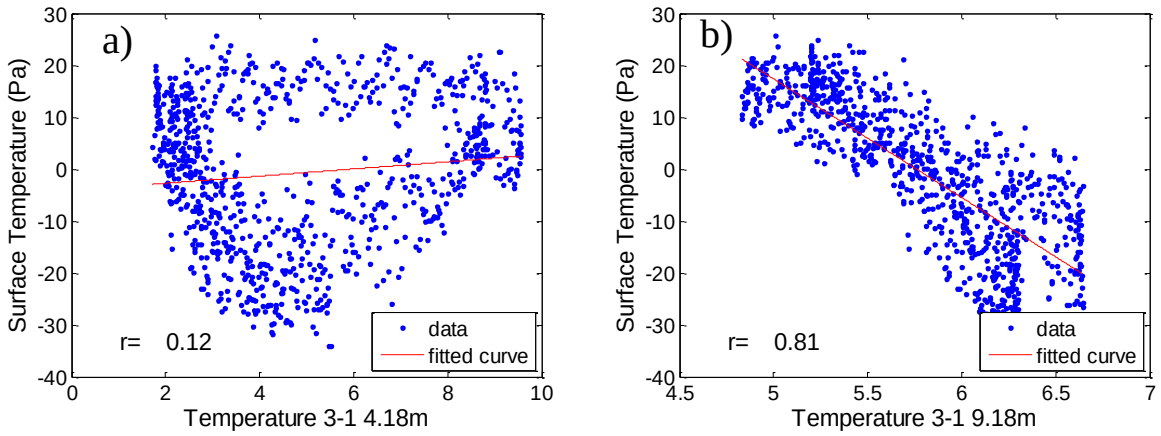

Figure 2-41 – Correlation between ambient temperature and internal temperature at a) BH2013-3-1-4.18m and b) BH2013-3-1-9.18m. Daily averaged data sets

2.7.7 Pore-gas O_2 content / Pore-gas O_2 Content from a Monitoring Location Directly Below or Above

A variable (from moderate to very good, except for one location that was poor) linear relationship is indicated for gas O_2 content from a monitoring point and the point directly below it is when coincident measurements are compared (Figure 2-42a to c and Table 2-11). It is possible that the development of high permeability zones will preferentially transport O_2 away from some locations and towards others. The distribution of sulfides within the pile is likely to be variable, causing disproportionate consumption of O_2 where sulfide content is higher. The regressions in O_2 content are affected by outlying data, an example of this is shown in Figure 2-42c. For one data point, the O_2 reading at BH2011-3-2-15m was over 19% v/v, however the reading at BH2011-3-2-12.5m remained low at less than 1% v/v. Similar examples are in the data sets in Figure 2-42a and b, and are likely due to gusts of wind that preferentially induced gas transport through a particular path within the waste rock. These observations indicate the limited benefits from regression analysis in this complex gas transport system. Numerical simulations are preferred to obtain improved understanding of the flow mechanisms.

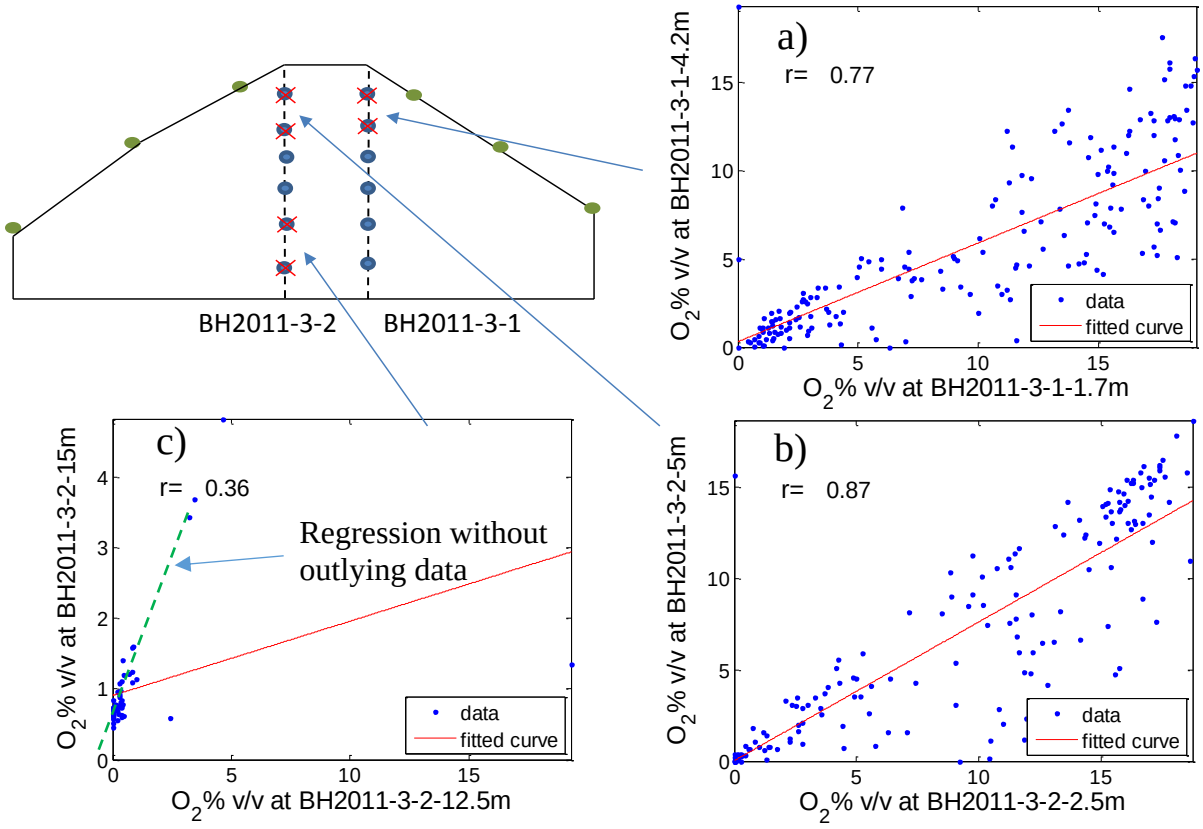

Figure 2-42 – Correlation between pore-gas oxygen concentration and the location directly below it, a) BH2013-3-1-1.7/4.2m, b) BH2013-3-2-2.5/5m and c) BH2013-3-2-12.5/15m. Daily averaged data sets

Table 2-11 – Correlation coefficients for pore-gas oxygen content vs the monitoring point directly below

Monitoring Location	**Correlation Coefficient**
BH2011-3-1-1.7/4.2m	0.77
BH2011-3-1-4.2/6.7m	0.88
BH2011-3-1-6.7/9.2m	0.65
BH2011-3-1-9.2/11.7m	0.67
BH2011-3-1-11.7/14.2m	0.75
BH2011-3-2-2.5/5m	0.87
BH2011-3-2-5/7.5m	0.88
BH2011-3-2-7.5/10m	0.92
BH2011-3-2-10/12.5m	0.99
BH2011-3-2-12.5/15m	0.36

2.7.8 Pore-gas O_2 Content/ Pore-gas O_2 Content from a Monitoring Location Directly Across at Similar Depth

The correlation between the gas O_2 content from a monitoring point and the point at the adjacent borehole at similar depth is moderate to very good when coincident measurements are compared, except for the basal monitoring locations that was very poor (Figure 2-43a to c and Table 2-12). A variable correlation would be anticipated due to the likely development of preferential pathways for gas transport, particularly in the horizontal direction. The regression were affected by outlying data, as was observed for the regressions for adjacent monitoring points in the vertical direction.

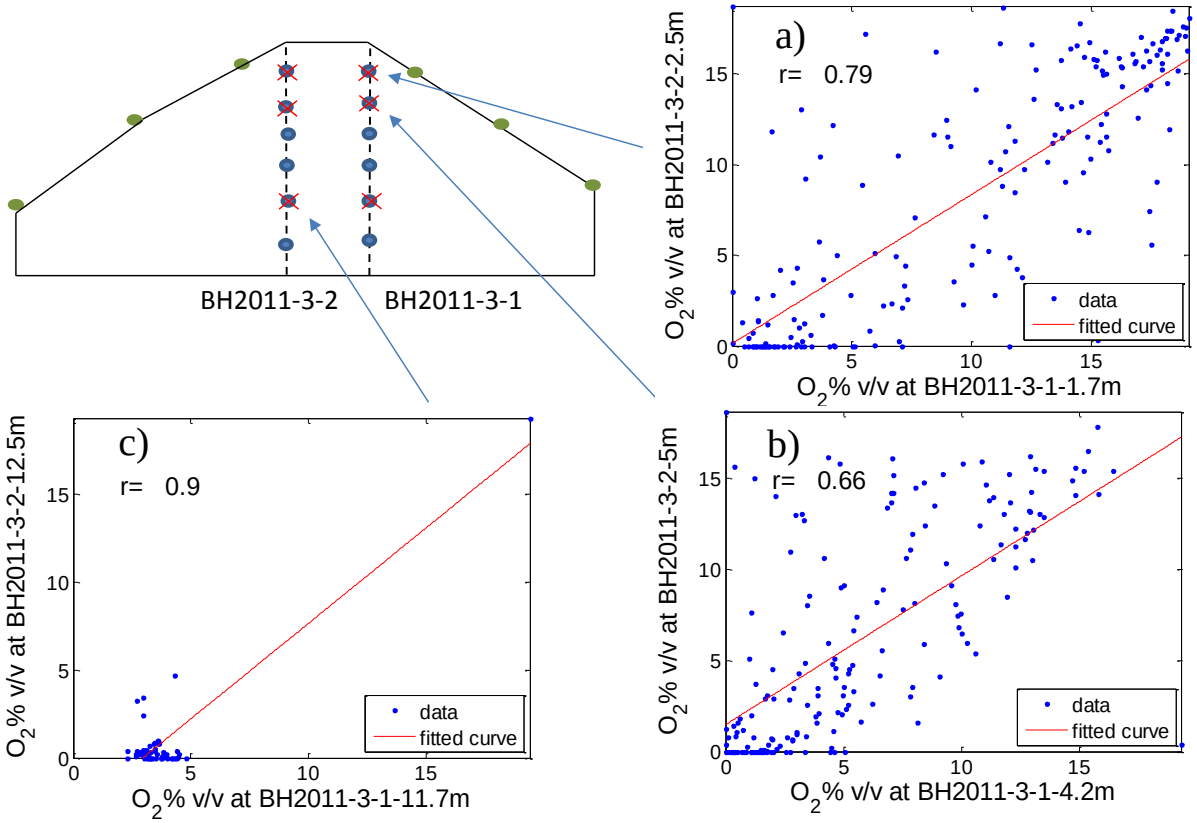

Figure 2-43 – Correlation between pore-gas oxygen content and the location directly across from it, a) BH2013-3-1-1.7/BH2013-3-2-5m, b) BH2013-3-1-4.2m/BH2013-3-2-5m and c) BH2013-3-1-11.7m/BH2013-3-2-15m. Daily averaged data sets

Table 2-12 – Correlation coefficients for pore-gas oxygen content vs the monitoring point directly across

Monitoring Location	**Correlation Coefficient**
BH2011-3-1-1.7/ BH2011-3-2-2.5m	0.79
BH2011-3-1-4.2/ BH2011-3-2-5m	0.66
BH2011-3-1-6.7/ BH2011-3-2-7.5m	0.65
BH2011-3-1-9.2/ BH2011-3-2-10m	0.52
BH2011-3-1-11.7/ BH2011-3-2-12.5m	0.9
BH2011-3-1-14.2/ BH2011-3-2-15m	0.068

2.7.9 Pore-gas [O_2] / Pore-gas [CO_2]

Pore-gas O_2 and CO_2 content show a poor to very good correlation when concurrent measurements at the same location are compared (Figure 2-44a and b). However, the strength of the correlation is noted to decrease with depth into the pile and a poor relationship is indicated below 10m depth. The oxidising action of the sulfide grains to produce O_2 and the neutralising action of the carbonates to produce CO_2 may not occur at the same location in the pile, which may be reflected in the poorer correlations (Table 2-13); in addition biogenic production of CO_2 at the base of the pile may affect the O_2:CO_2 proportions.

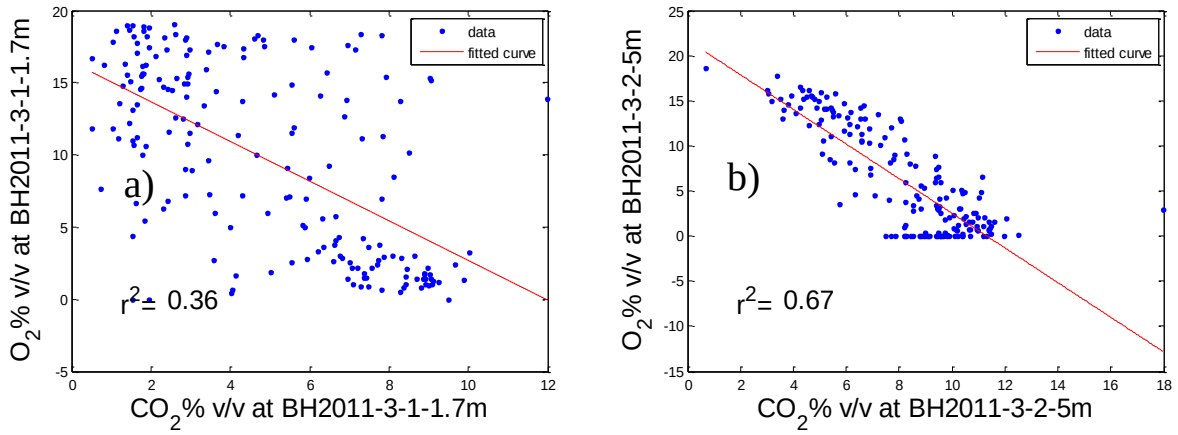

Figure 2-44 – Correlation between pore-gas oxygen content and carbon dioxide content at a)BH2011-3-1-1.7m and b) BH2011-3-2-5m

Table 2-13 – Correlation coefficients for pore-gas oxygen content vs carbon dioxide content

Monitoring Location	Correlation Coefficient
BH2011-3-1-1.7m	0.60
BH2011-3-1-4.2m	0.65
BH2011-3-1-6.7m	0.22
BH2011-3-1-9.2m	0.31
BH2011-3-1-12.7m	0.60
BH2011-3-1-14.2m	0.28
BH2011-3-2-2.5m	0.57
BH2011-3-2-5m	0.82
BH2011-3-2-7.5m	0.75
BH2011-3-2-10m	0.66
BH2011-3-2-12.5m	0.59
BH2011-3-2-15m	0.09

2.8 Numerical Simulation of Coupled Transport Processes

Numerical simulations were carried out to quantify gas and heat transport rates for the current WRS#3 and for hypothetical predictive scenarios to consider possible methods to reduce O_2 ingress into the pile. The results for the predictive scenarios can be extrapolated for the design of future waste-rock piles. Calibrated models were prepared and the input parameters were used as the basis for the predictive models.

Analysis was focused on field data collected during the summer of 2015, when the measured O_2 levels in the pore-gas were at their highest. It is likely that design considerations for future waste-rock piles at Detour will be optimised for summer-time conditions, as the cover is likely to freeze during the winter and O_2 transport rates into the pile will be relatively lower.

The software COMSOL Multiphysics version 5.2 (COMSOL Multiphysics, 2015) was used for the simulations. The 'Darcy's Law' and 'Transport of Concentrated Species' model interfaces within COMSOL were used to couple the advective and diffusive transport of gas through the system. These interfaces were coupled with the 'Heat Transport in Porous Media' interface to model heat flow through the system.

2.8.1 Previous Studies for Numerical Simulation of Gas Transport in Waste Rock

Relatively few studies have considered simulations for the transport of gas and heat through waste rock. Lefebvre et al. (2001a and b) carried out a comprehensive study on the transport of water as well as gas and heat through the South Dump at Doyon mine in Quebec, Canada and Nordhalde waste rock pile in Germany. Temperatures up to 65°C were observed at Doyon and numerical simulations indicated that thermally driven advection was the predominant mechanism for gas transport. Temperatures were up to 20°C lower at the Nordhalde waste rock pile, and the pile had a lower permeability than at Doyon. Numerical simulations indicated that thermally driven advection and diffusion were both significant contributors to gas transport within this pile. The boundary conditions for the gas and heat transport models were constant temperature (5°C) and pressure (100kPa) around the exterior of the pile for the Doyon pile and annual cyclic temperatures and constant pressures for the Nordhalde pile. Smolensky (1999) had earlier considered the effect of barometric pressure fluctuations in the Nordhalde pile. These authors observed that the O_2 content within the waste rock pile varied with cyclical fluctuations in barometric pressure, however comparisons with field data was not carried out.

Pham, (2013) carried out a heat transport study for test waste rock piles. Simulation scenarios considered surficial temperature fluctuations and calibrations to internal pile temperature, and considerations of pressure regimes within the piles from assumed wind velocities and material

permeability. The S content of the waste rock is low at this location, and O_2 depletion (below 20% v/v) was not observed. Reasonable calibration of gas transport models would have been difficult in this location, as a wide range of input parameters could output these well oxygenated conditions.

Other numerical simulation studies for gas transport in waste rock include Pantelis and Ritchie (1992), who modelled the transport of water, gas and heat through an assumed waste rock pile geometry and surficial temperature and pressure profile, and concluded that diffusion transport dominates for permeabilities less than $10^{-10}m^2$. Molson et al. (2005) and Linklater et al. (2005) also coupled water, gas and heat flow, however steady state and diffusion dominated gas transport was assumed. Comparisons to field measured oxygen profiles with depth was carried out for the latter. Binning et al. (2007) considered the transport of gas through a 1-D model of a pyritic waste rock pile. Advection and diffusion was considered and constant atmospheric pressures were applied. Advection was observed to comprise approximately 23% of the flux of oxygen into the waste rock.

The effect of wind in gas transport within waste rock was considered by Ritchie and Miskelly (2000) and Anne and Pantelis (1997) in gas transport models. These studies considered steady state values for wind flow and barometric pressure over a waste rock pile, and differential pressures within the piles were within the range of single Pascals.

Elberling (1998) considered the movement of O_2 gas with atmospheric pressure cycles. Comparison of modelled output and field measured pore gas O_2 gas was carried out. The study was not in the waste rock scenario, and wind was not included.

The field data that are available for pressure (including barometric and wind driven), temperature, O_2 and CO_2 concentrations for this study was used as boundary conditions for numerical simulations of gas transport in waste rock, or as comparative data for model calibration. Previous numerical simulation studies have either been carried out at steady state, have not included one of the gas transport components or have not included comparisons with field data.

2.8.2 Governing Relationships – Gas Transport

The 'Darcy's Law' interface calculates the advective transport of air and gas (Equation 2-13). Data analysis in Section 2.7.3 through 2.7.5 indicates that gas transport through the cover and waste-rock is laminar and therefore that Darcy's law is applicable. An extension to Darcy's law is required for compressible fluids, such as pore gas, to consider buoyancy effects (Nield and Bejan, 2013). The governing relationship for advective gas transport is given by:

$$u = -\frac{\kappa}{\mu}(\nabla \mathrm{P} + \rho g(\beta(T - T_o))) \qquad 2\text{-}13$$

where u is the gas velocity from advective transport [m s^{-1}], κ is the gas permeability of the waste-rock material [m^2], μ is the gas dynamic viscosity [Pa s] of the pore-gas, P is the pore-gas pressure [Pa], ρ is the density of the gas [kg m^{-3}], g is the acceleration due to gravity [m s^{-2}], T is the temperature [K] and T_o is a reference temperature [K]. β is the coefficient of thermal expansion of the pore-gas, and is assumed to be equal to $\beta = \frac{1}{T_o}$ [K^{-1}] for an ideal gas (Bear, 1972). The viscosity of air is described by the temperature dependent relationship:

$$\mu = 8.38\mathrm{E}-7 + 8.36\mathrm{E}-8 * \mathrm{T}^1 - 7.69\mathrm{E}-11 * \mathrm{T}^2 + 4.64\mathrm{E}-14 * \mathrm{T}^3 - 1.06\mathrm{E}-17 * \mathrm{T}^4 \qquad 2\text{-}14$$

Equation 2-13 is applied to an out of plane thickness of 1m for 2-dimensional simulations. The minus term indicates that transport is in the direction of decreasing pressure. Simulation for advective transport considers the bulk flow of air/gas without consideration of composition. The 'Transport of Concentrated Species' interface in COMSOL considers the diffusive transport of each component of the gas through concentration gradients (Equation 2-15) and is coupled with the advective transport model to consider total transport of each component. The gas components considered for this study are O_2, CO_2 and N_2. The governing equations for diffusive transport are:

$$j_i = -\left(\rho D_i^f \nabla c_i + \rho c_i D_i^f \frac{\nabla M_n}{M_n}\right) \quad 2\text{-}15$$

$$M_n = \left(\sum_i \frac{c_i}{M_i}\right)^{-1} \quad 2\text{-}16$$

where i indicates the component of the gas (O_2, CO_2 and N_2), j_i is the diffusive flux of component i [kg m^{-2} s^{-1}], c_i is the mass percentage [1], D_i^f is the diffusion coefficient [m^2 s^{-1}], M_i is the molar mass [kg mol^{-1}] and M_n is the molar mass of the gas mixture [kg mol^{-1}].

Gas density is a function of temperature and composition (Scanlon et al., 2002). The ideal gas law is used to calculate the gas density:

$$\rho = \frac{PM_N}{RT} \quad 2\text{-}17$$

where R is the universal gas constant [J mol^{-1} K^{-1}].

The coupling of diffusive and advective transport to determine total fluxes is achieved by:

$$N_i = j_i + \rho u c_i \quad \text{2-18}$$

where N_i is total flux of species i [kg m^{-2} s^{-1}]. Equations 2-13 to 2-18 are coupled with a conservation of mass term:

$$\theta\rho\frac{\partial\omega_i}{\partial t} + \nabla . j_i + \rho(u.\nabla)c_i = Q_i \quad \text{2-19}$$

where Q_i is the production or consumption of species i [kg m^{-3} s^{-1}], which is pertinent for the consumption of O_2 and the production of CO_2 within the waste-rock. Oxygen is consumed through sulfide oxidation and the Q_{O2} term will therefore be negative, and CO_2 is produced through carbonate neutralisation and the Q_{CO2} term will be positive.

An expression for mass consumption of gaseous O_2 per volume of waste-rock as a function of concentration was used for this study (Ritchie, 2004):

$$Q_{O2} = 9.02\frac{3\gamma D_2 \varepsilon_s \omega^g \omega^s \rho_{rs}}{a^2} \quad \text{2-20}$$

where γ is a proportionality constant incorporating Henry's law and the universal gas constant [1], D_2 is the diffusion coefficient of the partially oxidised particle [m^2 s^{-1}], ε_s is the volume fraction of waste-rock material [1], ω^g is the mass concentration of O_2 in the pore-gas [1],ω^s is the mass concentration of sulfur in the waste-rock material [1], ρ_{rs} is the density of sulfur in the waste-rock material [kg m^{-3}] and a is the particle radius [m]. Sulfide oxidation has also been assumed to be occurring within the cover, according to the same expression.

The fine fraction of the waste-rock oxidises at a higher rate than the coarse fraction, and a particle radius of a = 1mm (Blowes, 2016) was assumed for this study. The Q_{O2} term in Equation 2-20, and most literature reference values, are relative to the volume of waste-rock (not including

voids). Model inputs were adjusted according to the mass percentage of this 1mm particle size fraction (5% by mass, as discussed in Cash, 2014). COMSOL inputs for consumption or production of species (Q_i) is relative to total volume and model inputs were also adjusted for porosity of the waste-rock.

The mass production of CO_2 was assumed to be proportional to the mass consumption of O_2, at a ratio that is a calibration parameter. Stoichiometrically, the maximum molar ratio of the production of CO_2 to the consumption of O_2 is 0.53 (8/15), equivalent to a mass ratio of 0.73, if each of the O_2 consuming processes of sulfide oxidation (Reactions 1-1 to 1-3) are occuring.

A more detailed shrinking core model for O_2 consumption has not been applied due to the relatively short length of the simulation time (2.5 months), however it is recognised that a shrinking core model may be more appropriate for longer term, future predictive numerical simulation studies.

2.8.3 Governing Relationships – Heat Transport

Heat transport consists of conduction and convection. The former is considered using Fourier's law of conduction;

$$q = -d_Z k_{eff} \nabla T \qquad 2\text{-}21$$

$$k_{eff} = \theta_p k_p + \left(1 - \theta_p\right) k \qquad 2\text{-}22$$

where q is heat flux due to conduction [W m^{-1}], $d_z$is the assumed out-of-plane thickness (1m for 2-dimensional models), k_{eff} is the effective thermal conductivity of the pore-gas (k) and porous media (k_p) [W m^{-1} K^{-1}], ∇T is the thermal gradient [K m^{-1}] and $\theta_p$is the porosity of the porous media.

Conduction and convection are considered using conservation of mass terms:

$$d_Z(\rho C_\rho)_{eff}\frac{\partial T}{\partial t} + d_Z \rho C_\rho u.\nabla T + \nabla.q = d_z Q \quad 2\text{-}23$$

$$(\rho C_\rho)_{eff} = \theta_p \rho_p C_{\rho,p} + (1-\theta_P)\rho C_\rho \quad 2\text{-}24$$

where ρ and ρ_p are the density of the pore-gas and porous material [kg m^{-3}], respectively, C_ρ and $C_{\rho,P}$ are the heat capacity of the pore-gas and porous material [J kg^{-1} K^{-1}], respectively, u is the Darcy velocity of the pore-gas [m s^{-1}] and Q is the production of heat due to sulfide oxidation [W m^{-3}].

The majority of the heat of reaction is produced from the initial step in the oxidation of the sulfide, to release Fe^{2+}, SO_4^{2-} and acidity (Reaction 1-1). Heat released from this reaction is ΔH=1,440kJ mol^{-1} (FeS_2), which is equivalent to 411kJ mol^{-1} (O_2) or 12,857kJ kg^{-1} (O_2). This value is multiplied by the mass consumption of O_2 that is calculated through the R_{o2} term in Equation 2-20 to determine the production of heat.

The results of the simulations can be used to quantify the relative contribution to gas transport through the action of wind, barometric pressure fluctuations and thermal gradients; however, the density and velocity multiplication term in the conservation of mass expression (Equation 2-19) indicates that the mechanisms are numerically inseparable. The relative contribution to O_2 transport through the cover from the action of wind, barometric pressure and temperature gradients were considered by comparing gas transport rates from the calibrated heat transport coupled model and predictive scenarios with the following boundary conditions:

- An assumed equal pressure distribution around the pile (considers barometric pressure only);
- Removal of the fluctuations in pressure magnitude, whilst retaining the differential pressures around the exterior of the pile (considers wind only); and
- A constant temperature distribution within the pile (removes the effect of temperature).

2.8.4 Assumptions and Limitations

Some assumptions that were applicable to the calibration models include:

- Simulation in 2-Dimensions adequately characterised the system;
- The cover has a uniform thickness of 1m;
- Input parameters are homogeneous for each material. The exception is the permeability of the waste-rock, for which a unique value was applied for each geometry layer;
- The oxidation processes were dominated by the fine fraction of the waste-rock (less than 1mm, Blowes 2016). This fraction is approximately 5% of the waste-rock by mass, and it is assumed that the entire volume of the waste-rock is heated according to the action of this fine fraction.
- Gas transport halted at the water table; and

Uncertainties in the makeup of the waste-rock pile that have not been fully captured in the models include:

- The subsurface geometry and boundary conditions beneath the batters are relatively unknown, and are a variable in the calibration process;

- The system is highly heterogeneous. Localised areas of low and high permeability are likely to have formed during construction of the pile. Preferential flow pathways may have formed through the high permeable zones;
- Localised areas of higher S content and oxidising activity may be present.

2.8.5 Geometry

The geometry of the model was determined from field survey of the exterior pressure monitoring locations (Figure 2-45). The model follows the north-south exterior pressure monitoring line, from S-3 to N-3 (Figure 2-46, the locations of BH2011-3-1 and BH2011-3-2 are shown for reference). The thickness of the cover is likely to be highly variable, however a thickness of 1m was assumed for the calibration model, based on the results of test-pitting work described in McNeill (2016). The waste-rock was separated into 14 layers to allow initial conditions to be applied at each monitoring point and to allow sufficient flexibility in the material parameters to achieve reasonable calibration. The base of the model was approximately coincident with the water table, which was measured between 16-17m below the surface at BH2011-3-1.

The geometry of the model below an elevation of 271masl, beneath the base of the batters, was relatively uncertain (Figure 2-45). The exterior pressure monitoring locations were coincident with the base of the pile at the toes, however the results of borehole drilling indicate that the waste-rock was placed below this elevation within the body of the pile.

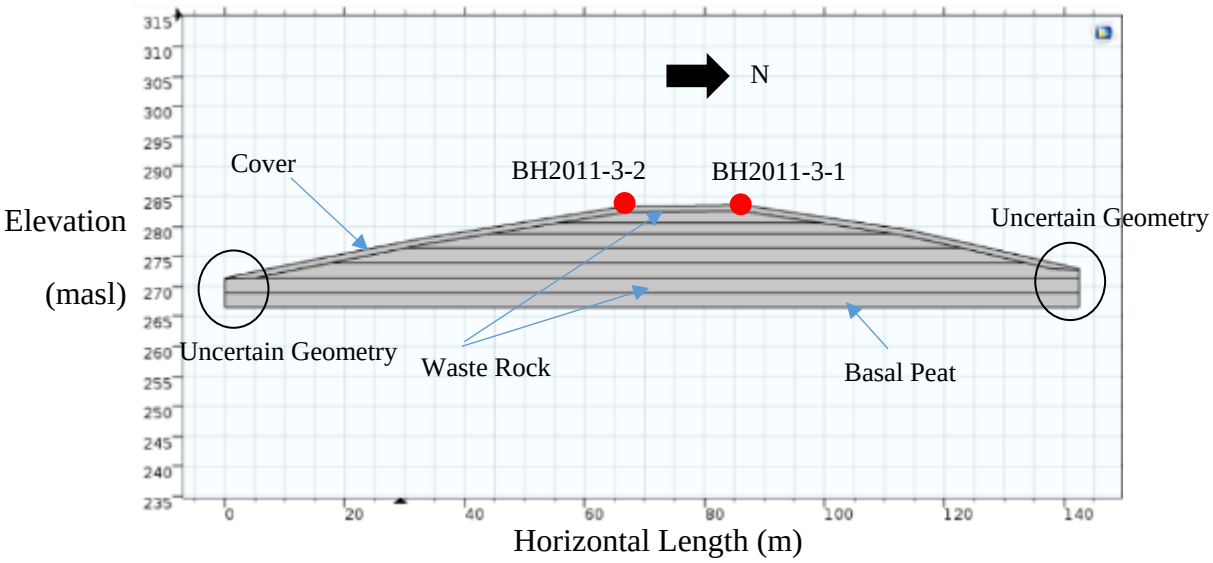

Figure 2-45 – COMSOL gas transport numerical simulation model geometry, Black circles indicate areas of uncertain geometry

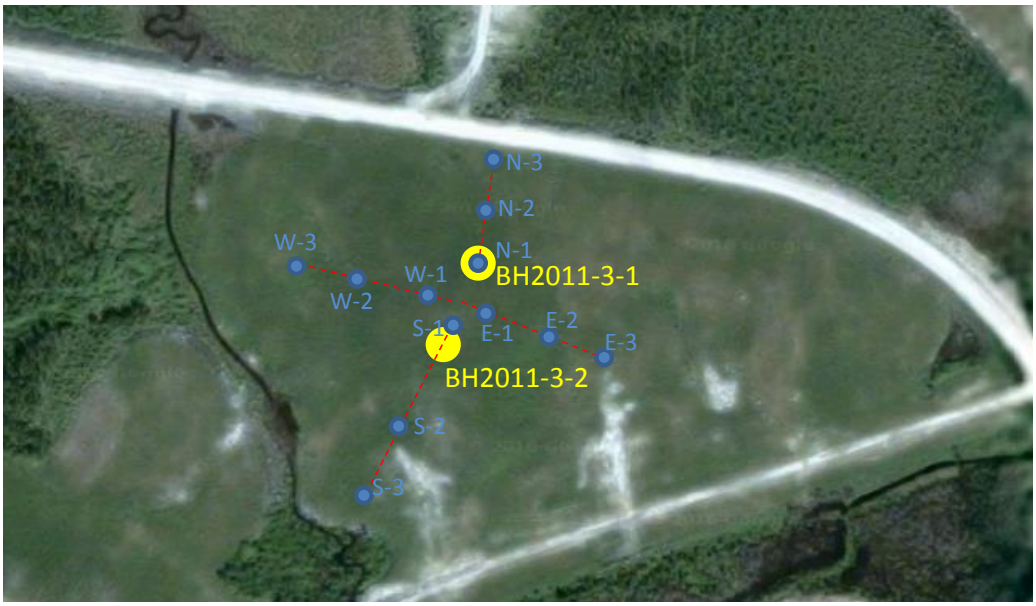

Figure 2-46 – Locations of the survey located external pressure locations

2.8.6 Boundary Conditions

Boundary conditions included atmospheric concentrations for O_2 (20.9% v/v) and CO_2 (0.055% v/v) and field measured pressures and temperatures applied on the outside of the pile. Boundary conditions for the gas-concentration calibration model are shown in Figure 2-47. The models begin at July 10, 2015 and extend for 80 days. Daily averaged data were used for the boundary

conditions, however a model that used the 10-minute averaged data for the pressure boundary conditions was considered as an alternative scenario.

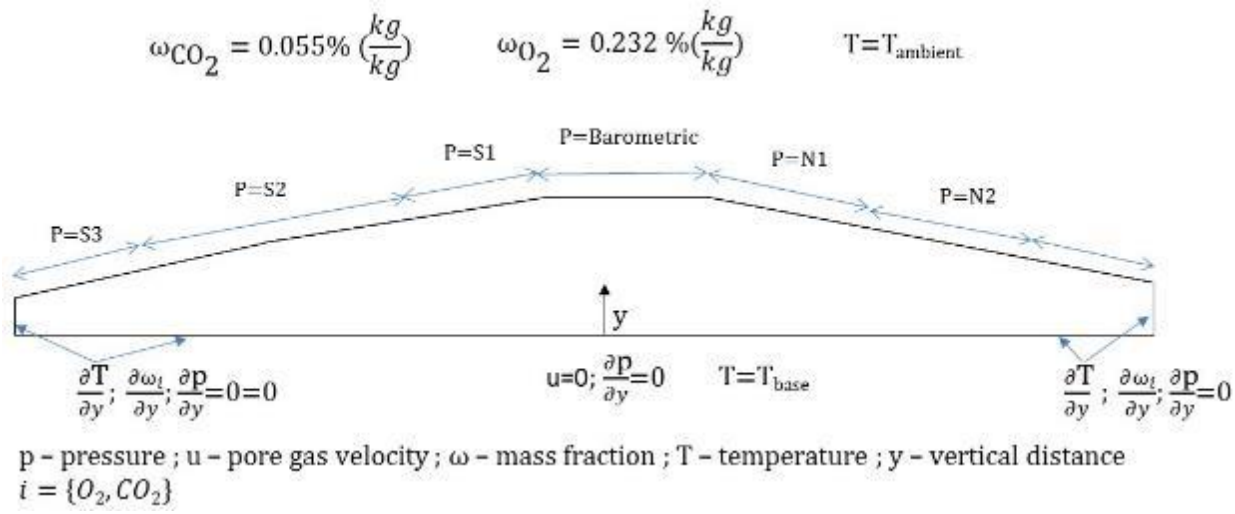

Figure 2-47 – Gas-concentration calibration model: boundary conditions

A 'no flux' gas and heat transport condition was applied to the vertical boundary beneath the batters and at the base of the geometry, which is coincident to the water table.

Initial conditions are the field measured pressure, temperature and gas-concentrations measured at the monitoring points within the waste-rock on the first day of the simulation time period (10 July, 2015).

2.8.7 Material Parameters and Calibration Process

Input material parameters for the cover and waste-rock materials were determined through *in situ* measurements, literature review and as part of the calibration process. Typical values from literature were used as constraints when calibrated parameters were assessed.

Gas permeability values and thermal properties were determined from calibration for the cover and waste-rock materials. Properties that are required to estimate oxidation rates, such as particle radii and S content of the rock, were determined from field testing (Table 2-14; Cash, 2014 and

McNeill, 2016). Typical literature values for porosity and solids density were selected from literature (Table 2-14).

The quality of the calibration was evaluated by comparing field monitored parameters on the interior of the pile with the corresponding model output, including pressures, temperatures and gas-concentrations for O_2 and CO_2. Material parameters including permeability, thermal conductivity and heat capacity were modified until reasonable agreement between model outputs and field data was achieved. The material parameters are therefore part of the results of the calibration. A review of all material parameters was conducted with respect to literature values to ensure that the values were reasonable.

The assignment of material parameters was carried out with extrapolation for future waste-rock piles in mind. Literature values are available for most input parameters; however, parameters such as oxidation rates are highly variable between field sites depending on the S content of the waste-rock. The use of a single value for oxidation rates may have allowed calibration to be achieved for this study; however, extrapolation to other piles would not have been reasonable. The model was selected to estimate oxidation rates (Equation 2-6) includes the percentage S and average particle size of the waste-rock materials, which can be determined through testing for analysis related to future piles.

2.8.8 Data Processing for Field Measured Data

The gas-concentration data collected from the 19th July to 21st August, 2015 was affected by a leak in the system. The raw data appears to have a linearly increasing component for measured O_2 or decreasing for measured CO_2 component to it, indicating that the leak increased over time. An attempt was made to remove the linear component of the data set to not lose the data

completely and include it in the data set for the calibration models. The processed data from the time period of the leak has not been included in the data analysis in Section 2.7.7 to 2.7.9.

The linear line of best fit was calculated for the period of the leak (Figure 2-48a). The line was shifted down to match the first point of the line to the measured data point at the estimated start of the leak (Figure 2-48b). The line was then subtracted from the data set to remove the linear component of the data (Figure 2-49a and b). The process was repeated for the CO_2 data set. The linear component of the data is increasing in this case (Figure 2-50a and b; Figure 2-51a and b)

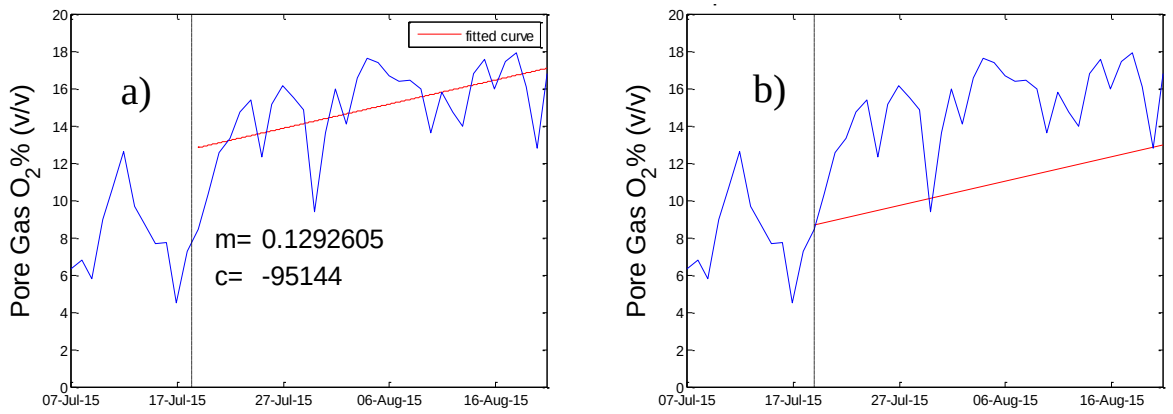

Figure 2-48 – Unprocessed O_2 data at BH2011-3-1-4.2m during the leak, with a) the linear line of best fit for the affected data and b) the downward shift of the line

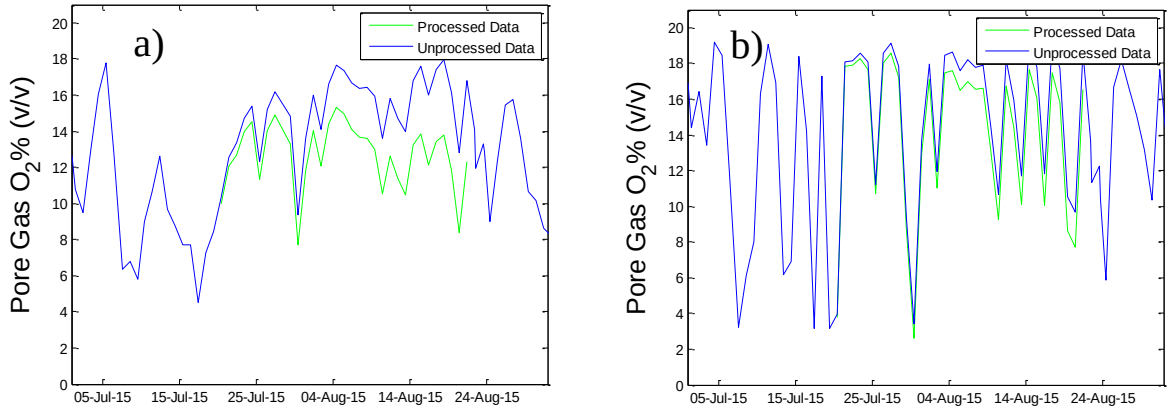

Figure 2-49 – Processed and unprocessed data O_2 time series for BH2011-3-1-4.2m and b) BH2011-3-2-5m

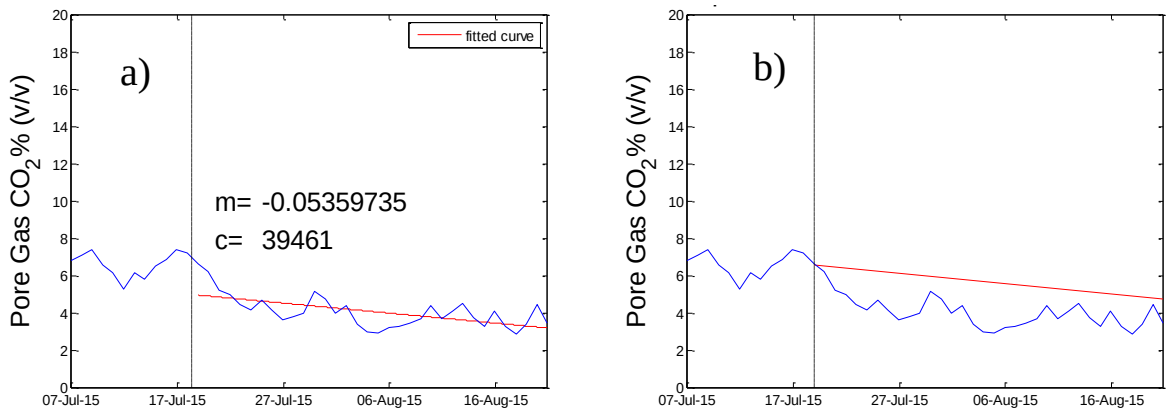

Figure 2-50 – Unprocessed CO_2 data at BH2011-3-1-4.2m during the leak, with a) the linear line of best fit for the affected data and b) the downward shift of the line

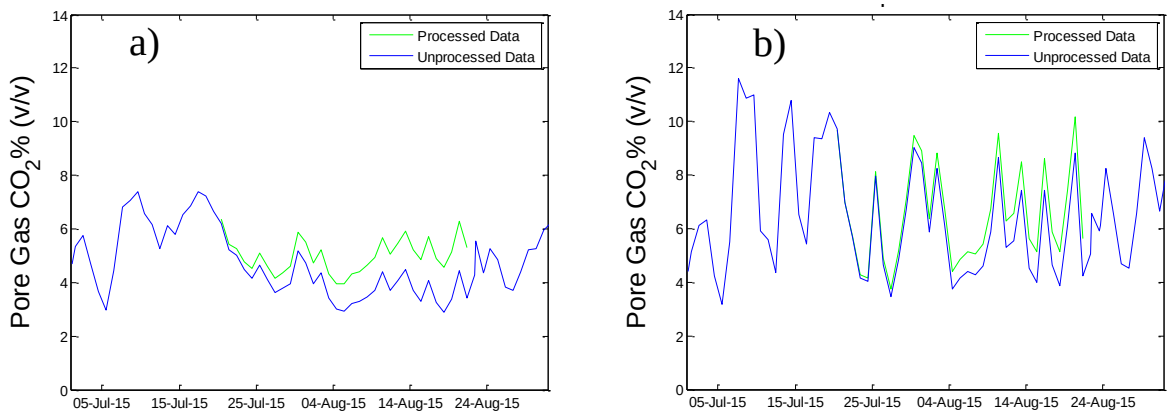

Figure 2-51 – Processed and unprocessed data CO_2 time series for BH2011-3-1-4.2m and b) BH2011-3-2-5m

2.8.9 Calibration Model Results

Full calibration would be achieved with reasonable agreement of field measured and model output internal gas pressures and concentration of O_2 and CO_2. Modelled pressures for the exterior and interior of the pile have been output relative to the pressure at the surface at BH2011-3-1 to correspond with the methodology of the field monitoring. Numerical simulation indicated that the internal gas pressures and the gas-concentrations cannot both be reasonably calibrated using the same set of input material parameters and that two calibration models are required. As such, two calibrations are performed, hereby referred to as the pressure calibration model and the gas-concentration calibration model.

The majority of the input parameters for the two calibration models are equal. The exceptions are the permeability of the waste-rock and the methodology for simulating the consumption of O_2 through oxidation. The permeability of the waste-rock is higher for the gas-concentration calibration model than the pressure calibration model (Table 2-14);

Table 2-14 – Input parameters for materials used in the numerical simulations

Cover Material	**Value for Gas Calibration Model**	**Value for Pressure Calibration Model**	**Comments**
Porosity (ϕ)	0.25	0.25	Typical value for soil materials
Permeability (k)	$1x10^{-9}$	$1x10^{-11}$ m^2	By calibration
Ratio of vertical k to horizontal k	1	1	-
Density of solids (ρ_b)	1800 kg m^{-3}	1800 kg m^{-3}	Typical value for soil materials.
Diffusion Coefficient (O_2, N_2, CO_2)	$1.5x10^{-6}$ m^2 s^{-1}	$1.5x10^{-6}$ m^2 s^{-1}	Typical value from Lahmira and Lefebvre, (2014), Pantelis and Ritchie, (1992)
Thermal Conductivity	1 W m^{-1} K^{-1}	1 W m^{-1} K^{-1}	By calibration. Within range of typical values for soils (Harries and Ritchie, 1987).
Heat Capacity	1800 J kg^{-1} K^{-1}	1800 J kg^{-1} K^{-1}	By calibration. Typical values for solids is approximately 900 J kg^{-1} K^{-1} (Lefebvre et al., (2001a), Pantelis and Ritchie (1992)), capacity increases with moisture content.

Waste-Rock			
Porosity (ϕ)	0.35	0.35	Typical value for waste-rock materials (Lefebvre et al., 2001a).
Permeability (kG)	$1x10^{-8}$ m^2	$1x10^{-12}$ to $1x10^{-11}$ m^2 (Figure 2-52)	By calibration. Reference values are typically between $2.5x10^{-9}$ m^2 and $8x10^{-12}$ m^2 (Lefebvre et al., 2001a).
Ratio of vertical k to horizontal k	20	1	By calibration.
Density of solids (ρ_b)	2600 kg m^{-3}	2600 kg m^{-3}	Typical for waste-rock materials (Lefebvre et al., 2001a).
Diffusion Coefficient (O_2, N_2, CO_2)	$1.5x10^{-5}$ m^2 s^{-1}	$1.5x10^{-5}$ m^2 s^{-1}	Typical value from Lahmira and Lefebvre (2014), Pantelis and Ritchie (1992).
Thermal Conductivity	2.5 W m^{-1} K^{-1}	2.5 W m^{-1} K^{-1}	By calibration. Within range of typical values (Lefebvre et al., (2001a), Pham et al. 2013)).
Heat Capacity	1200 J kg^{-1} K^{-1}	1200 J kg^{-1} K^{-1}	By calibration. Typical values for solids is approximately 900 J kg^{-1} K^{-1} (Lefebvre et al., (2001a), Pantelis and Ritchie (1992)), capacity increases with moisture content.
%S in the Waste-Rock	0.05% to 0.4% (Figure 2-58	Not applicable	Results from carbon sulfur testing of drill cutting samples described in McNeill (2016) used as a guide.

Particle radius for consumption of O_2 through oxidation	1mm	Not applicable	Blowes (2016).
Rate of consumption of O_2	Modelled using Equation 2-20	5 $x10^{-8}$ to 1 $x10^{-7}$ [kg m^3 s^{-1}]	By calibration. Site specific parameter.
Ratio of CO_2 production to O_2 consumption	0.4 – 0.8 Figure 2-58)	0.4 – 0.8 (Figure 2-58)	By calibration.
γ	0.03	0.03	Includes Henry's law and the Gas constant
Diffusion coefficient (D_2)	$6x10^{-9}$ m^2 s^{-1}	$6x10^{-9}$ m^2 s^{-1}	From calibration, higher than the reference value of 2.6x10-9 m^2 s^{-1} (Pantelis and Ritchie, 1992)

Note: Sulfide oxidation was assumed to be occurring within the cover, with an assumed %S = 0.05% (McNeill, 2016)

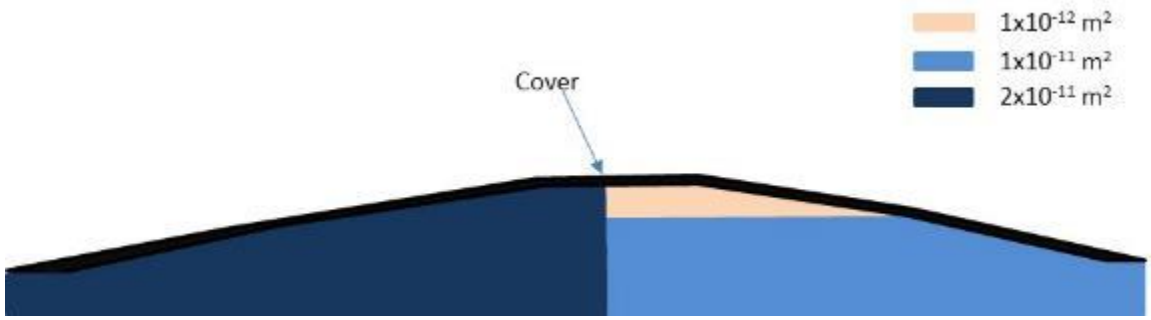

Figure 2-52 – Assigned permeability for the waste rock for the pressure calibration model

Field measured values for permeability (McNeill, 2016) within the waste-rock for WRS#3 varied from $8.5x10^{-11}m^2$ and $9x10^{-9}m^2$. Relationships for permeability (Scanlon et al., 2002) and diffusion coefficient (Molson et al., 2005) with respect to moisture content exist but have not improved calibration in this case. The permeability values of $1x10^{-12}$ to $1x10^{-11}$ m^2 that has been assigned to the waste-rock in the pressure calibration model is lower than the field measurements of $8x10^{-11}$ m^2 to $9x10^{-9}$ m^2 within WRS#3 (McNeill, 2016) but within the range of literature values (Lefebvre et al., 2001a).

It is preferred to include a model for O_2 consumption that includes the mass percentage of sulfur in the waste-rock, as this model will produce results that can be applied to other waste-rock piles. These models also include the concentration of O_2 in the pore-gas (Equation 2-19), and it has therefore not been possible to include a sulfide oxidation relationship in the pressure calibration model as the O_2 level is not calibrated to field measurements. A fixed value for oxidation rate was applied to achieve reasonable calibration for the pressure parameter, and this value is only applicable for the pile in consideration (WRS#3). The pressure calibration model can therefore not be applied to predictive simulations for other waste-rock piles. The rate of consumption of O_2 has been varied within the geometry of the waste-rock to improve calibration (Figure 2-53).

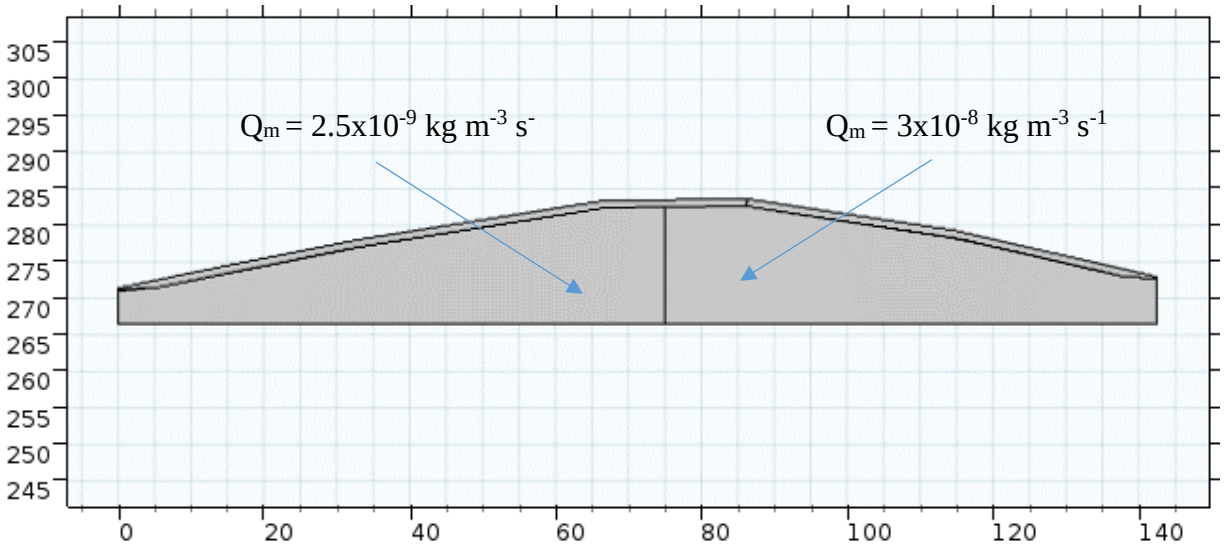

Figure 2-53 – Reaction rates for the consumption of oxygen within the waste-rock for the pressure calibration model

Time series plots for field measured internal differential pressure compared with outputs from the pressure calibration model (Figure 2-54a1 to b4) show that the average magnitude of the pressures within the timeframe of the simulations are in agreement, and the daily fluctuations (±3Pa at BH2011-3-1-4.2m to ±6Pa at BH2011-3-2-11.7m) are reasonably captured. The exceptions are at BH2011-3-1-1.7m, where the model output pressures were higher (more

positive) than the equivalent field measured values and at BH2011-3-2-15m, where the model output pressures were lower (more negative). Overall, reasonable calibration for the internal gas pressures was achieved within the context of a highly heterogeneous system and the limitations of simulating a 3-dimensional system in 2-dimensions.

Calibration for O_2 and CO_2 concentration was not achieved with the same model (Figure 2-55a and b, data that has been processed for the leak in the monitoring system is shown in red). The fixed and constant input oxidation rate was required for reasonable calibration of the pressure data, however the daily fluctuations that are evident in the field data are not observed in the simulation output.

The thermal material parameters were selected to achieve calibration with the gas calibration model, and the temperatures are under predicted when these material parameters were applied to the pressure calibration model (Figure 2-56a and b).

The simulated permeability for the cover and waste rock material in the gas calibration model are higher than the pressure calibration model, at $1x10^{-9}$ m^2 and $1x10^{-8}$ m^2 respectively. The permeability of the cover is higher than expected, indicating that gas transport into the pile is preferentially occurring through the higher permeability areas of the cover. Defects and variable thickness may cause these higher permeable areas.

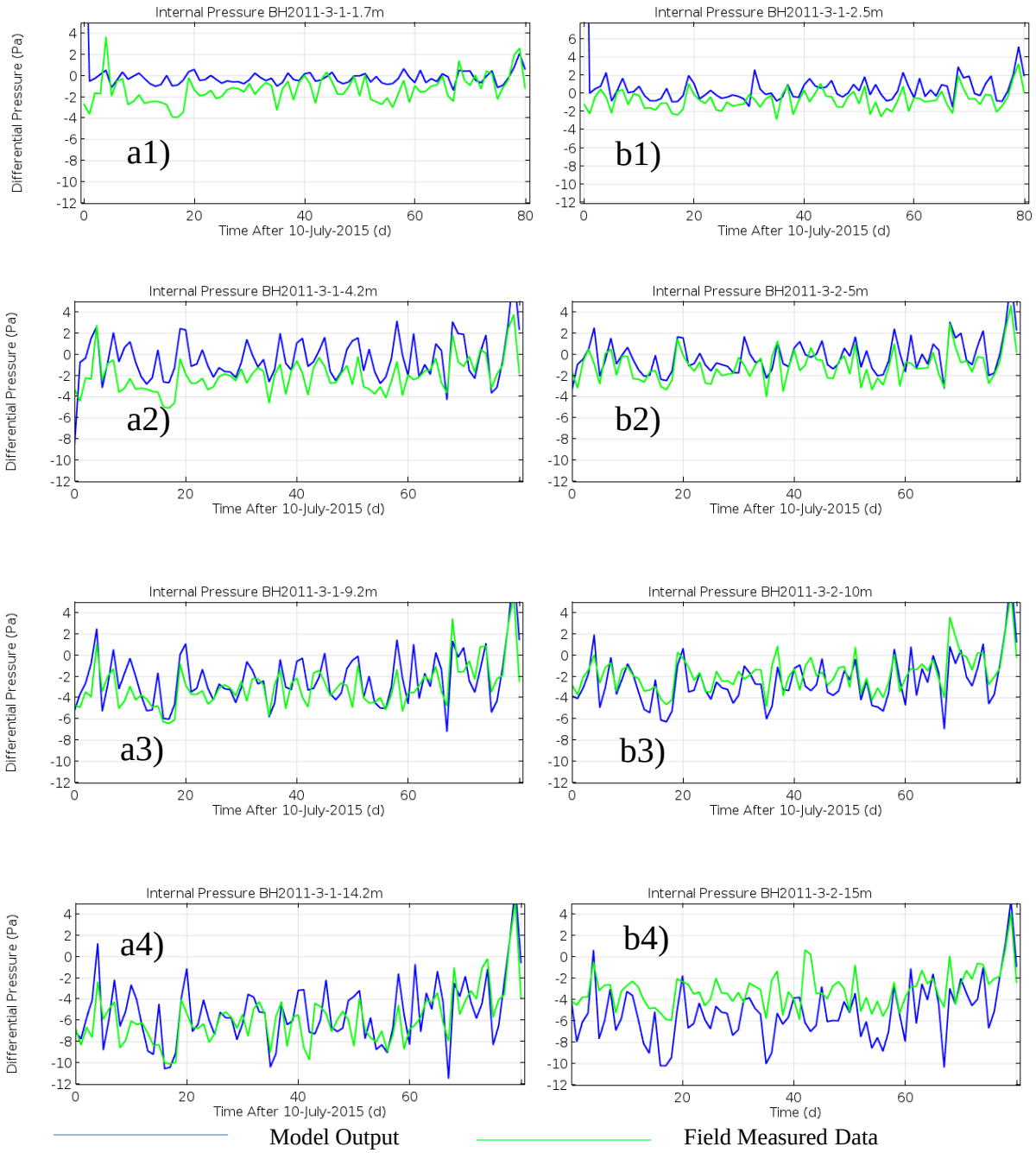

Figure 2-54 – Pressure calibration model output, internal pressures, a1) BH2011-3-1-1.7m, a2) BH2011-3-1-4.2m, a3) BH2011-3-1-9.2m, a4) BH2011-3-1-14.2m, b1) BH2011-3-2-2.5m, b2) BH2011-3-2-5m, b3) BH2011-3-2-10m, b4) BH2011-3-2-15m

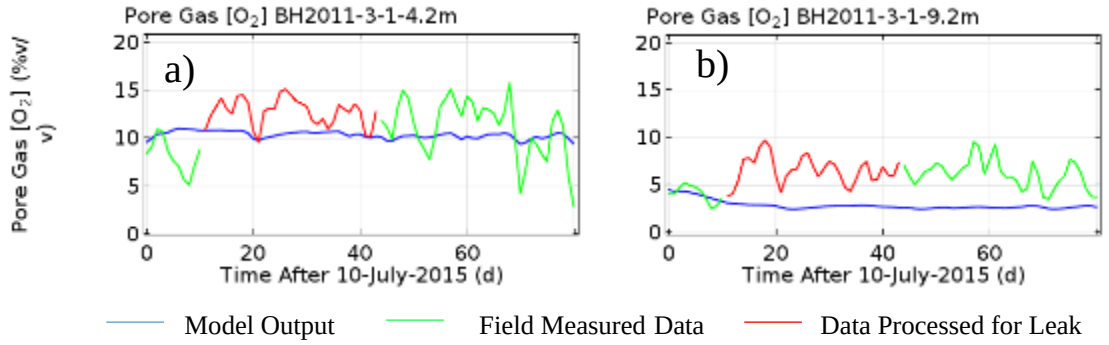

Figure 2-55 – Pressure calibration model output, pore-gas oxygen content, a) BH2011-3-1-4.2m, b) BH2011-3-1-9.2m

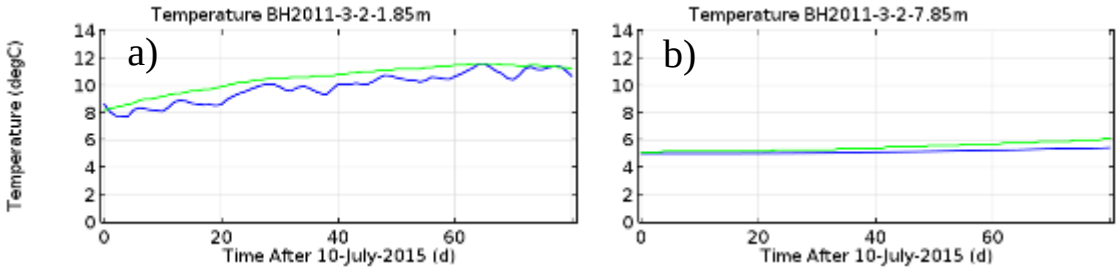

Figure 2-56 – Pressure calibration model output for temperature at a) BH2011-3-2-1.85m, b) BH2011-3-2-3.85m

Time series plots for O_2 gas content from the gas calibration model show that the agreement between model outputs and field measure values is better for the locations within BH2011-3-1 than BH2011-3-2 (Figure 2-57a1 to b4). Daily fluctuations of between 2-7% v/v are reasonably captured for BH2011-3-1-1.7m (Figure 2-57a1). The agreement is not as good for the locations BH2011-3-1-4.2m and BH2011-3-1-6.7m and the simulation O_2 gas contents are over predicted. The pore gas contours (Figure 2-60a) indicate that large differences in pore gas O_2 content occur over small distances both horizontally and vertically, complicating the process to achieve calibration agreement at specific locations. The daily fluctuations are not captured to the same extent at the locations within BH2011-3-2, however the average O_2 content over the course of the simulation time frame are in agreement. The modelled O_2 content at the lowermost locations are reasonably steady with time, as was observed in the field, and the magnitude of the concentrations is in reasonable agreement (Figure 2-57a4). Overall, reasonable calibration for

pore-gas O_2 concentration was achieved with this model within the context of a highly heterogeneous system and limitations of simulating a 3-dimensional system in 2-dimensions.

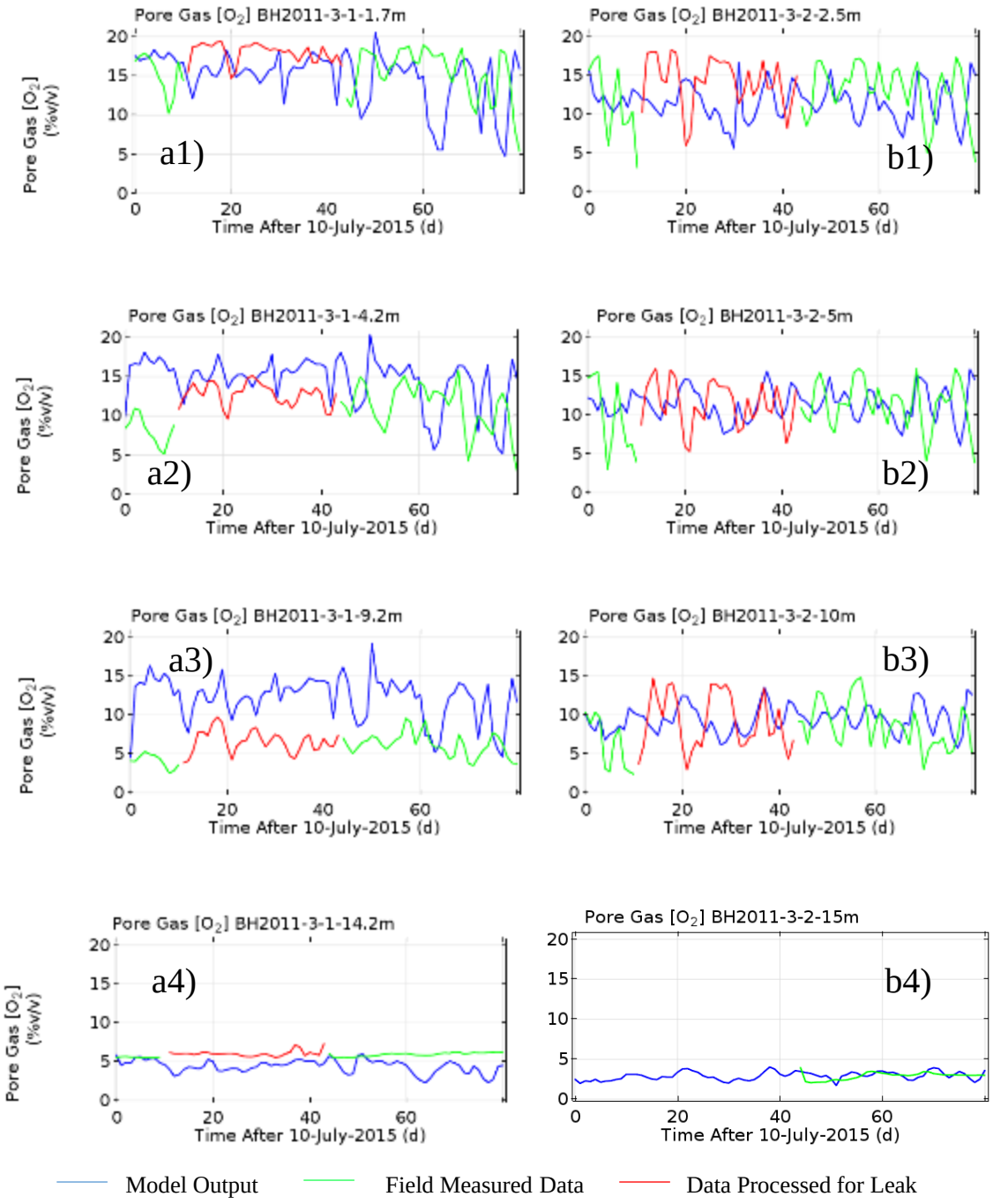

Figure 2-57 – Gas calibration model output, pore-gas oxygen content. a1) BH2011-3-1-1.7m, a2) BH2011-3-1-4.2m, a3) BH2011-3-1-9.2m, a4) BH2011-3-1-14.2m, b1) BH2011-3-2-2.5m, b2) BH2011-3-2-5m, b3) BH2011-3-2-10m, b4) BH2011-3-2-15m. Note the limited data availability for BH2011-3-2-15m.

Higher permeability values were assigned for the gas-concentration calibration model than the pressure calibration model, indicating that gas transport is dominated by high permeability zones which were sampled by the vacuum gas sampler. The gas calibration model is likely more representative of the system as a whole and the pressure calibration model is more representative of local conditions around the monitoring points. No suction was applied to measure the air pressures and it is likely that the location at which pressure was measured does not capture the location from which the gas sample was taken. It is therefore more realistic to use the material parameters for the gas-concentration calibration model as the basis for predictive scenarios.

The %S in the waste rock and the mass ratio of the production of CO_2 to the consumption of O_2 was varied over the geometry of the pile as part of the calibration process (Figure 2-58). Results from carbon sulfur testing of drill cutting samples described in McNeill (2016) were used as a guide. A higher ratio for mass production of CO_2 to the consumption of O_2 varied between 0.4 – 1 with a general increasing trend with depth. The highest stoichiometrically possible value is 0.73, which would apply if the oxidation reactions 1-1 to 1-3 are all occurring and neutralisation is taking place instantaneously at the same location as the oxidation. The higher values towards the base of the pile indicates that acid neutralisation is not occurring at the same location as the oxidation, due to heterogeneous distribution of the carbonates or rate effects.

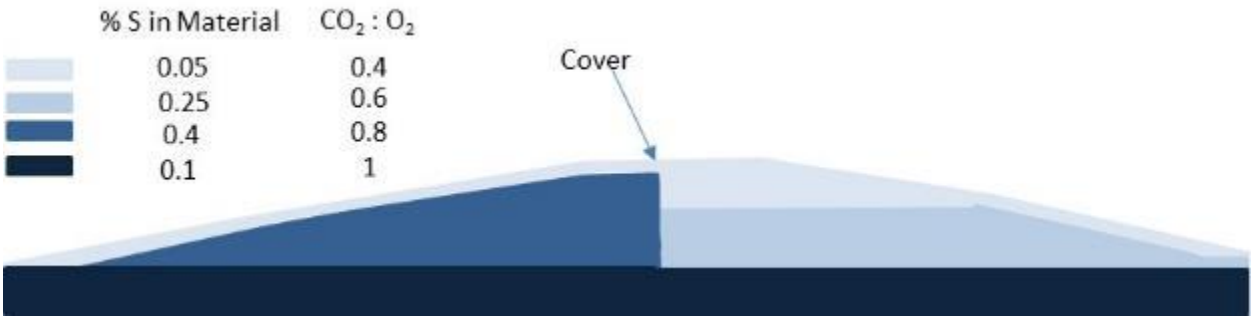

Figure 2-58 – %S in the WRS#3 materials and mass ratio of the production of carbon dioxide to the consumption of oxygen for the gas calibration model

Time series plots for CO_2 gas content from the gas calibration model show that the magnitude of the model outputs are in agreement with the field measured values (Figure 2-59a1 to b4); however, the match between model output and field measured gas CO_2 content was not as good as it was for O_2. The CO_2 content is over predicted at some locations and under predicted at others, however it is judged that the model provides sufficient accuracy on average to use as the basis for predictive scenarios.

Pore-gas O_2 content is higher and CO_2 content is lower near the batters compared with the central part of the waste rock, and the O_2 content decreases and CO_2 content increases at increasing distance into the pile (Figure 2-60a and b). At day 60, O_2 concentrations decrease from atmospheric levels at the surface to less than 10% within 10m perpendicularly from the middle of the batter, and to less than 5% within an additional 2m perpendicularly. The CO_2 concentrations increase from atmospheric levels at the surface to greater than 5% and then to greater than 10% within the same distances into the pile.

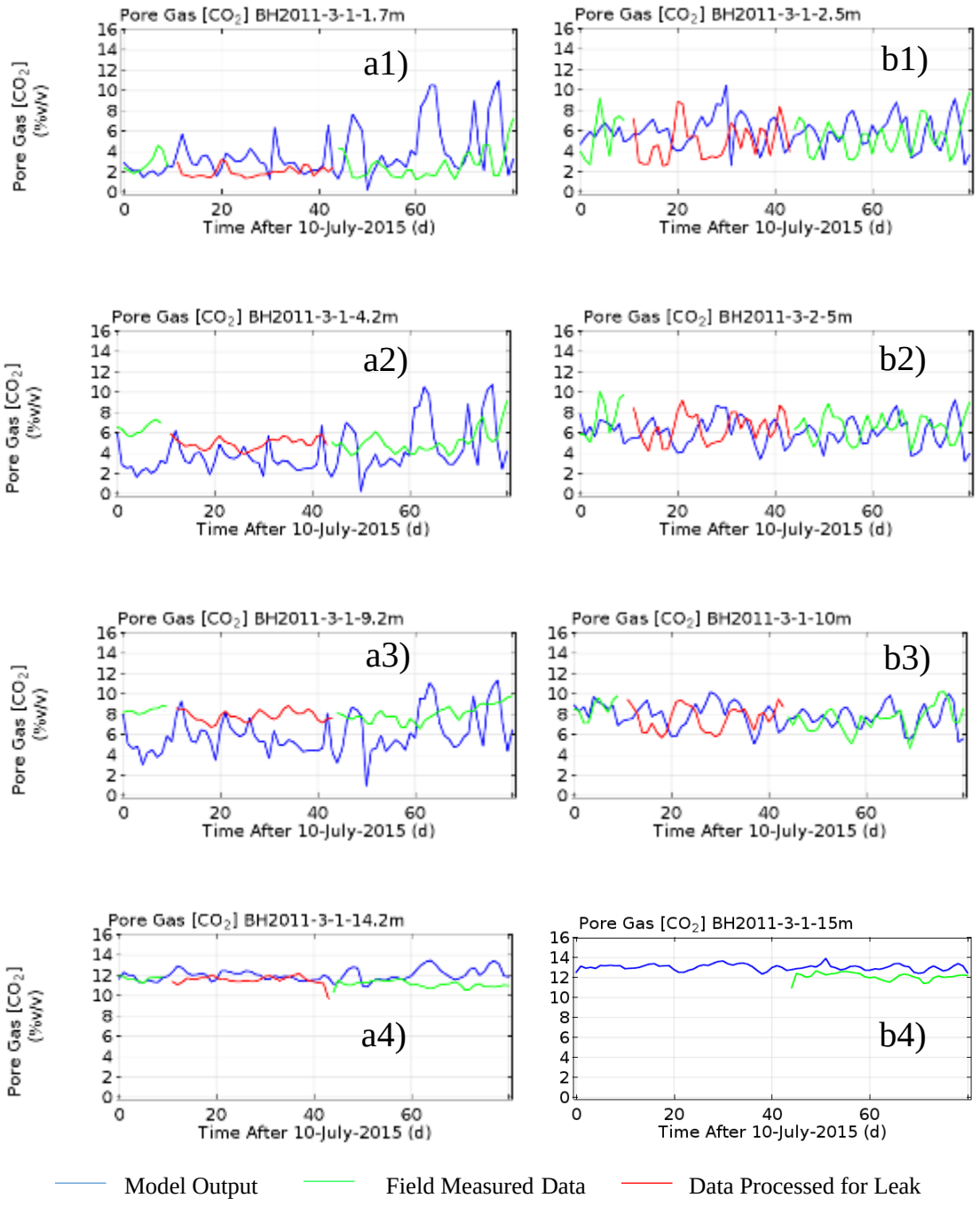

Figure 2-59 – Gas calibration model output, pore-gas carbon dioxide content. a1) BH2011-3-1-1.7m, a2) BH2011-3-1-4.2m, a3) BH2011-3-1-9.2m, a4) BH2011-3-1-14.2m, b1) BH2011-3-2-2.5m, b2) BH2011-3-2-5m, b3) BH2011-3-2-10m, b4) BH2011-3-2-15m. Note the limited data availability for BH2011-3-2-15m

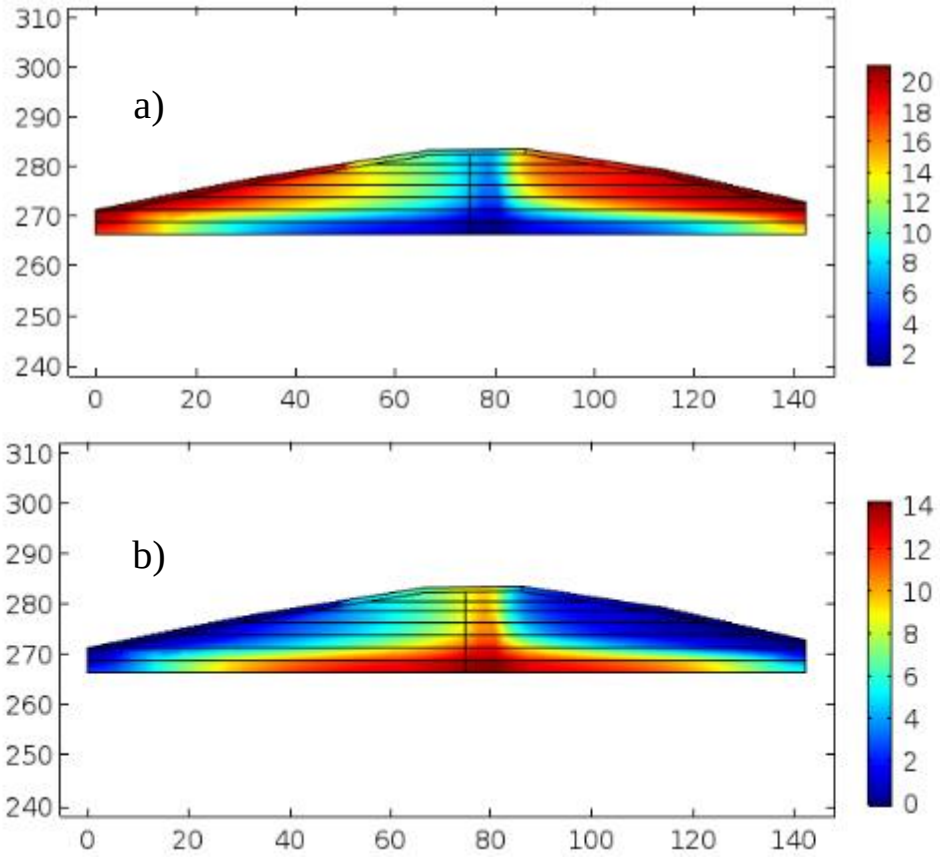

Figure 2-60 – 2D Surface from gas calibration model, a) pore-gas oxygen content, b) pore-gas carbon dioxide content on day 60 of the simulation

The time series for gas pressures were not well captured with the gas calibration model. The modelled internal gas pressures are consistently higher (more positive) than the field measured values (Figure 2-61a1 to b2). The exception is at BH2011-3-2-15m, where the model outputs and field measured data are in good agreement.

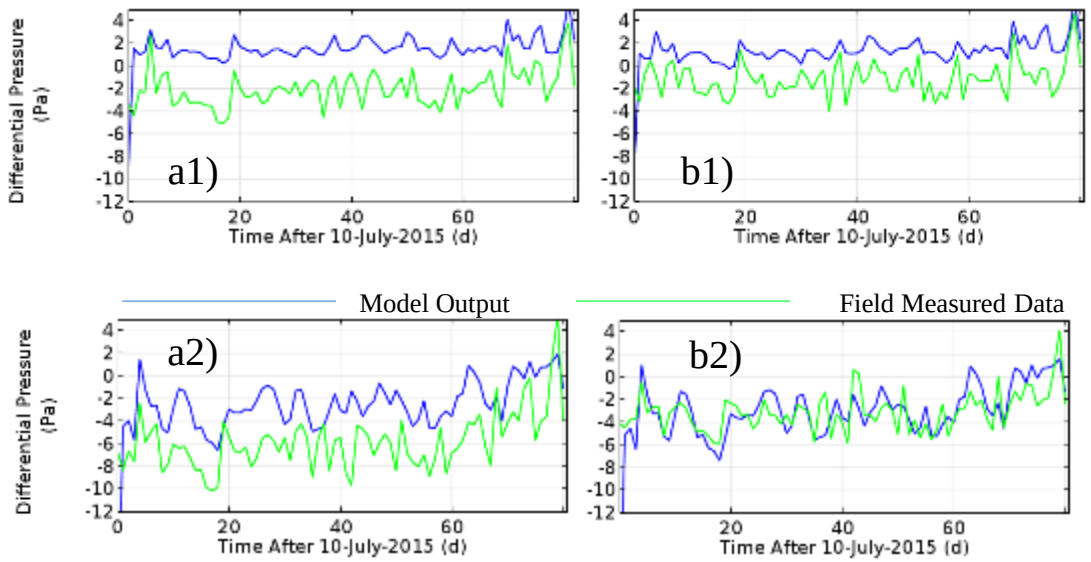

Figure 2-61 – Gas calibration model output, internal pressure. a1) BH2011-3-1-4.2m, a2) BH2011-3-1-14.2m, b1) BH2011-3-2-5m, b2) BH2011-3-2-15m

A time series plot for temperature from the calibration models shows that the general trend in increasing temperature was captured, however daily fluctuations in temperature are greater in the model than were observed in the field (Figure 2-62a and b).

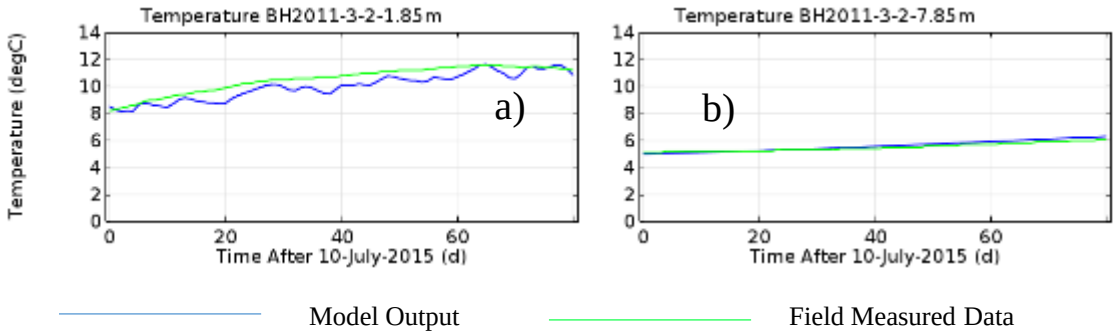

Figure 2-62 - Gas calibration model output, temperature. a1) BH2011-3-2-1.85m, b) BH2011-3-2-3.85m

The spatial distribution of temperature is reasonably consistent within the waste-rock pile (Figure 2-63). At day 60, the temperature within the waste-rock was approximately 5°C within 2 m distance into the waste-rock, and graded to an atmospheric temperature of 17°C at the surface.

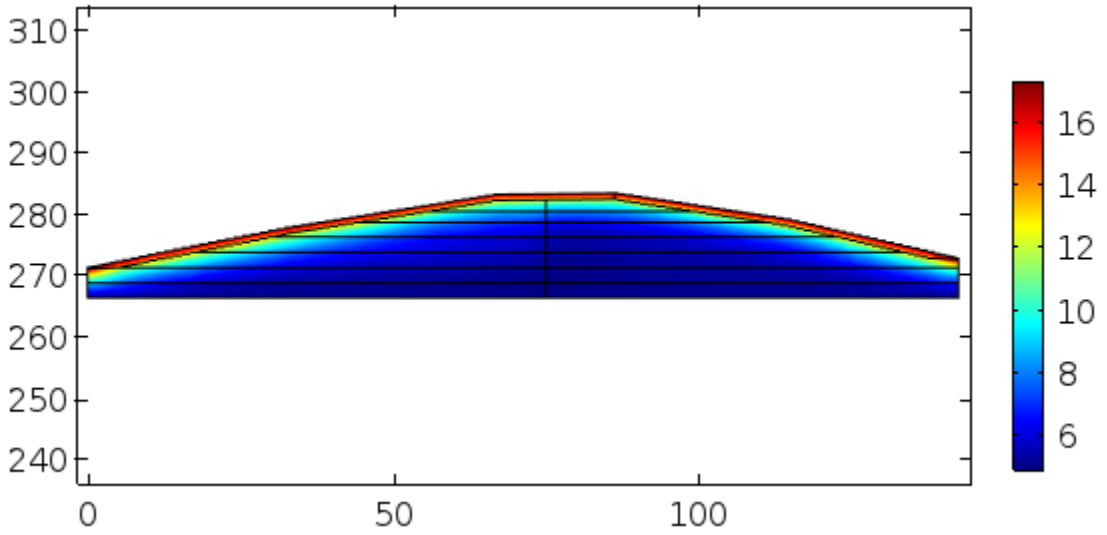

Figure 2-63 – 2D Surface from gas calibration model, temperature on day 60 of the simulation

The Darcy velocity of the pore-gas is generally less than 20 m d^{-1} within the waste-rock, except near the toe of the batters, where velocities in excess of 160 m d^{-1} in the inward direction are indicated on day 60 (Figure 2-64) at the toe of the pile.

Flow arrows indicate that the bulk of the gas transport into the pile occurs at the toe and outflow of the gas occurs through the crest (Figure 2-65). This flow direction occurs because the differential pressures are higher at the toe than the crest due to the action of wind, and temperatures within the pile at higher at the crest of the pile than towards the base due to buoyancy. Comparatively less flow occurs within the waste rock beneath the toe. Oxygen depleted gas in this area is less readily recharged from atmospheric air than the areas above the toe.

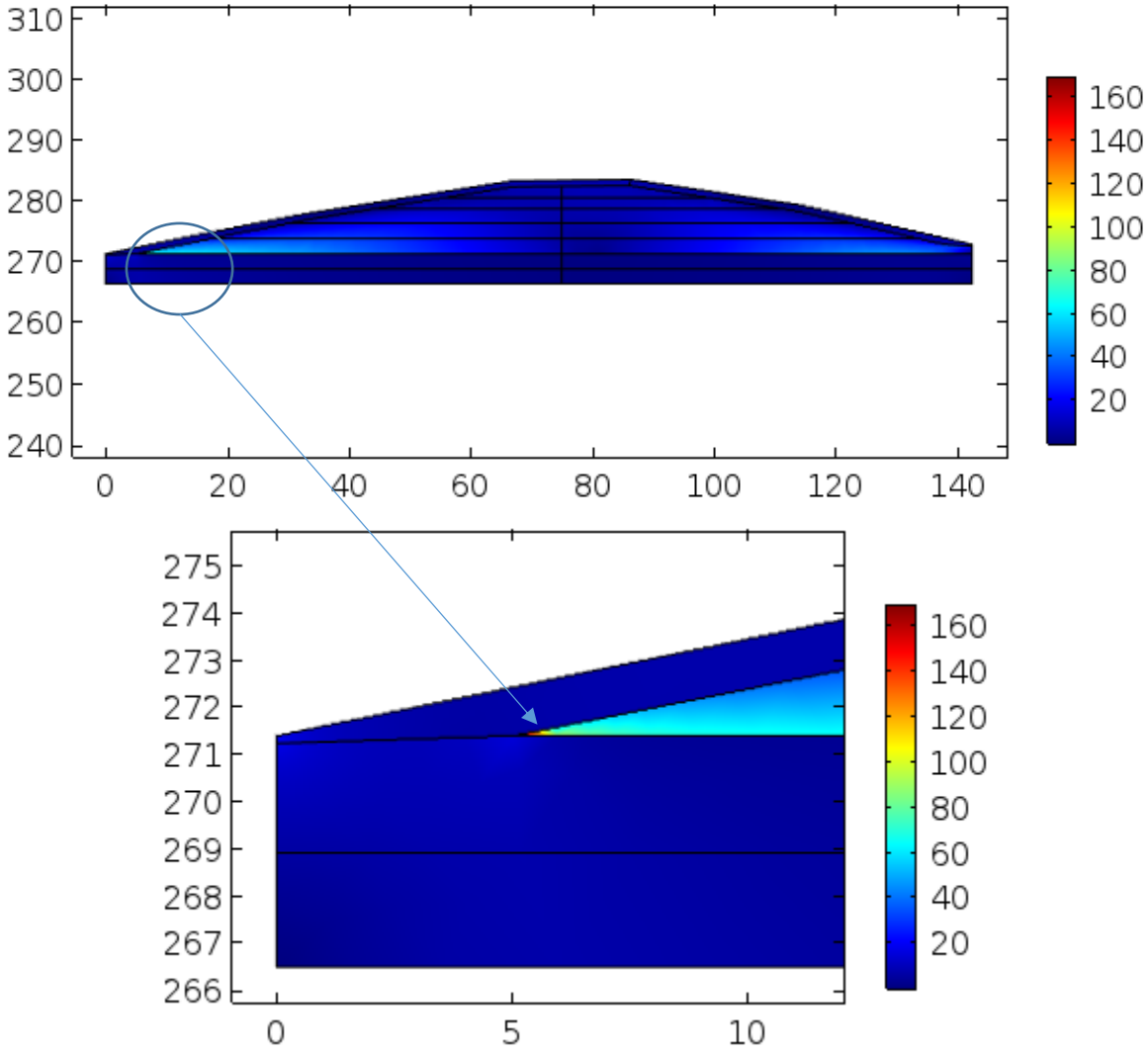

Figure 2-64 – 2D Surface from gas calibration model, Darcy gas velocity on day 60 of the simulation

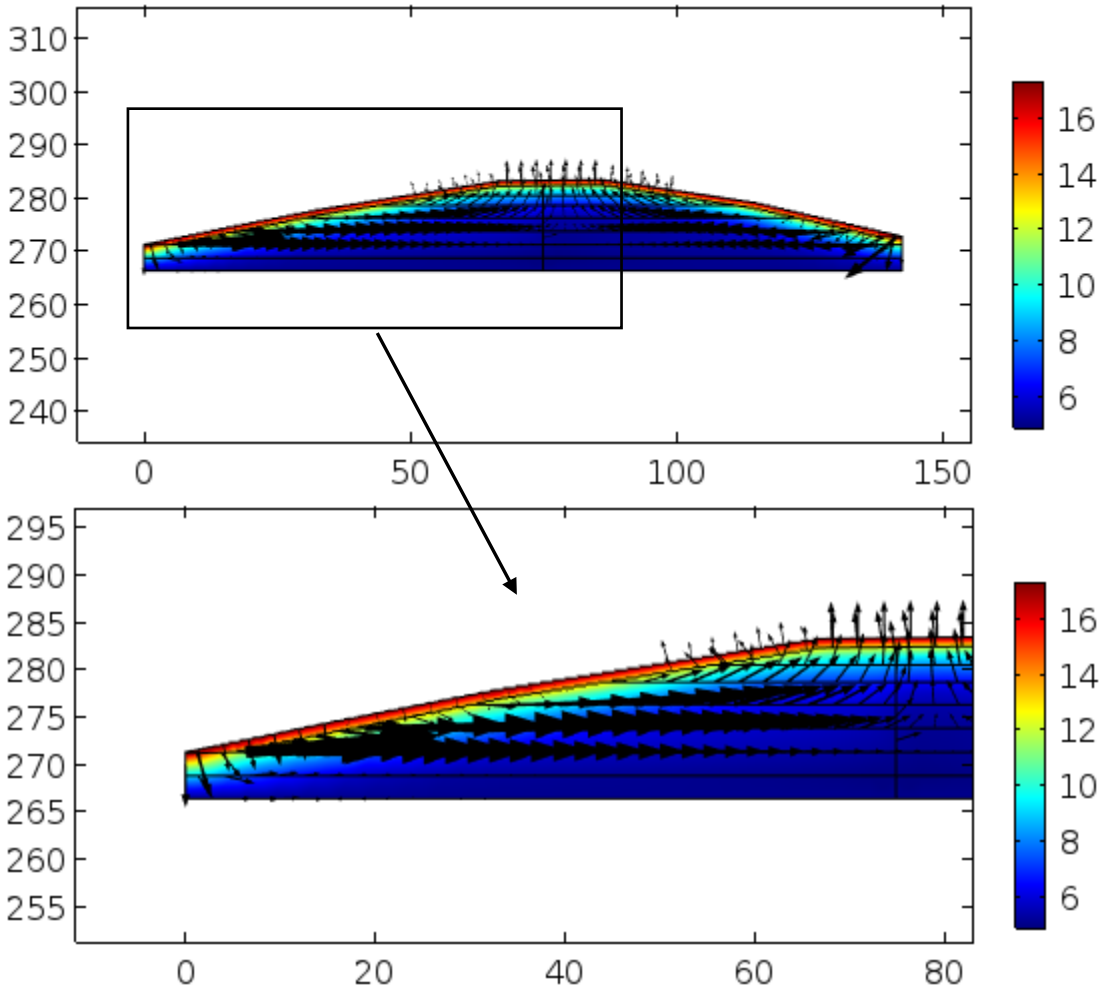

Figure 2-65 – Flow arrow diagram for gas calibration model, overlaid with the temperature surface on day 60 of the simulation

The rate of consumption of O_2 within the centre of the waste-rock is approximately $3x10^{-8}$ to $3.3x10^{-7}$ kg(O_2) m^{-3} s^{-1} (Figure 2-66a) and heat production is between 0.03 to 0.2 W m^3 (Figure 2-66b). The oxidation rates are higher and the heat production is lower than that observed by Harries and Ritchie (1981) at Rum Jungle, Northern Territory, Australia ($8x10^{-8}$ kg(O_2) m^{-3} s^{-1} and a maximum of 5.0 W m^{-3} at one location). Calculations for heat production were carried out from trends in field data for that study, and the oxidation rate was estimated according to a simple calculation relating the heat produced and the stoichiometry of the oxidation reactions.

Gas transport in and out of the pile will affect the temperature distribution within the pile, and this cannot be captured with integral analysis from field data.

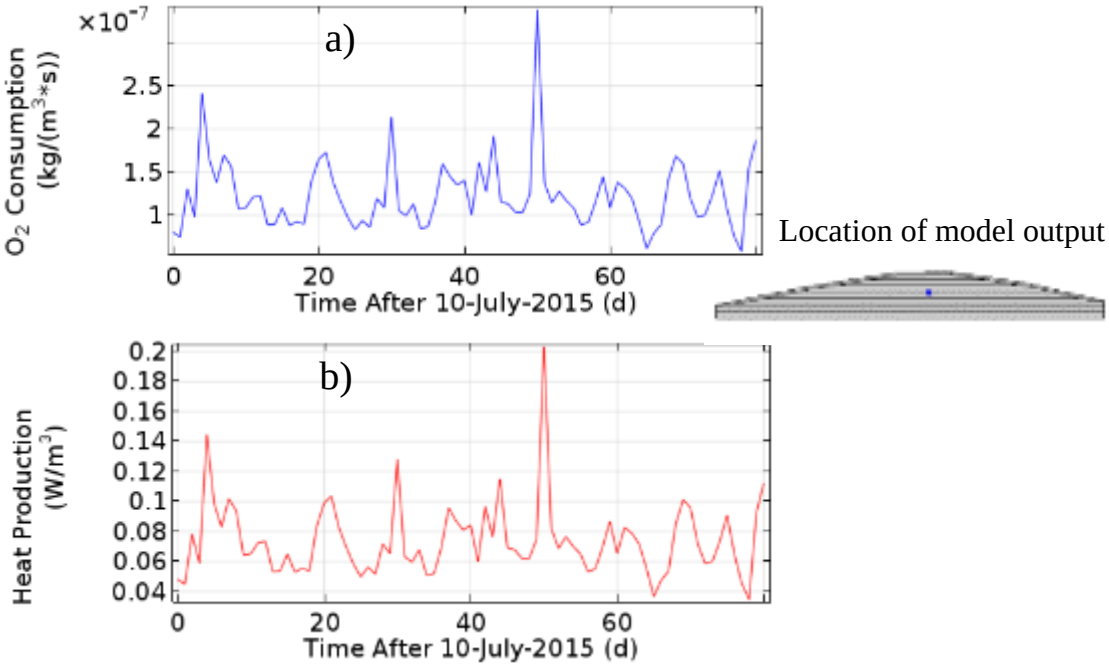

Figure 2-66 - Gas calibration model output, a) oxygen consumption rate and, b) heat production in the centre of the waste-rock

The flux of O_2 through the cover and into the body of the pile is predominately through advective means (Figure 2-67, the plot is the integrated flux over the entire surface area of the pile). The advective transport is approximately 100 times that of the diffusive transport. The permeability of the cover is above the threshold of $1x10^{-10}m^2$ that is generally considered applicable for diffusion dominated transport (Lefebvre et al., 2001a).

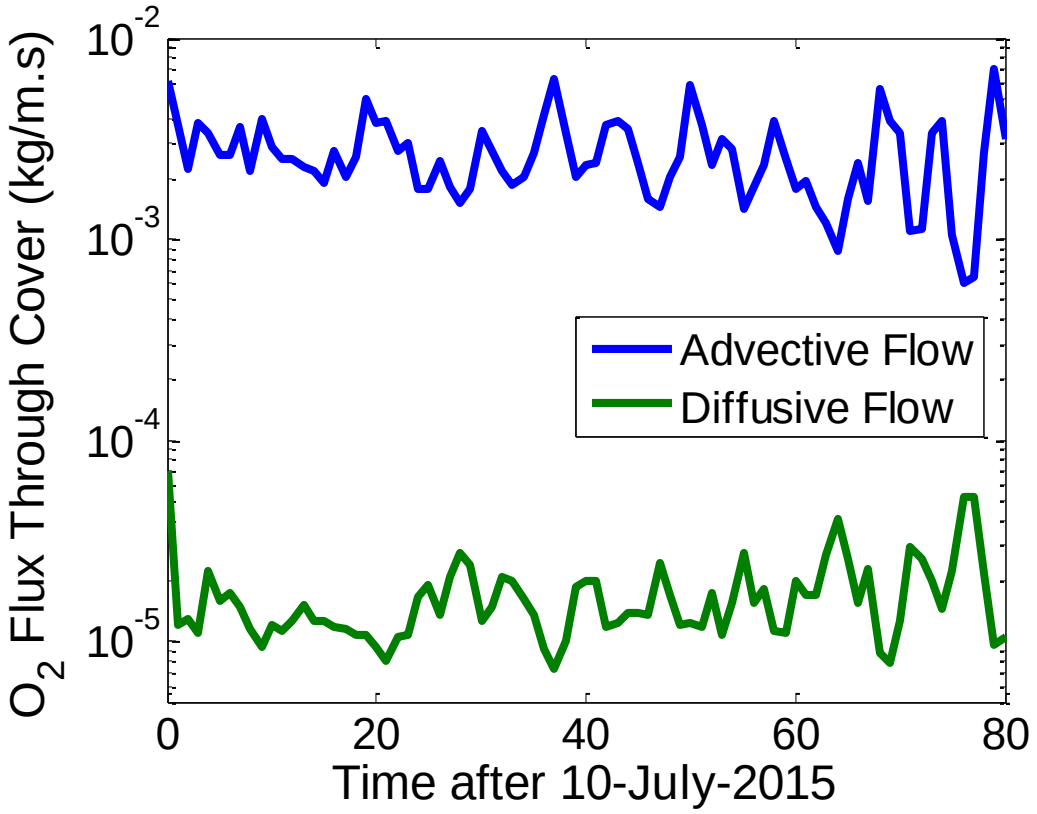

Figure 2-67 - Gas calibration model output, advective and diffusive flux through the cover

2.9 Predictive Scenarios

Theoretical predictive scenarios were considered using the material parameters resulting from the gas concentration calibration process. The aim of the simulations was to determine possible techniques that could be applied to the current WRS#3 to reduce O_2 gas ingress into the pile and promote suboxic conditions. Some simulations were also carried out to provide additional insight into the role that the cover material might be playing in gas transport through the system. Model outputs for the theoretical scenarios were compared to the original field data to assess the effect of the imposed system modifications.

2.9.1 Contributions from each advective transport mechanism

Simulations have been prepared to quantify the effect of wind, barometric pressure and temperature gradients to advective gas transport through WRS#3. The boundary condition has been altered to isolate the mechanism that has been considered according to the following methodology:

- Wind only model: constant temperature distribution within the pile, removal of the magnitude fluctuations of the barometric pressure whilst retaining the differential pressures around the pile;
- Barometric pressure only model: constant temperature distribution within the pile, barometric pressure measured at the crest applied around the exterior of the pile; and
- Temperature gradient only model: constant pressure of 1 atmosphere around the exterior of the pile.

The constant and equally distributed temperature that has been applied for the wind and barometric pressure only models is 5°C, which is the approximate average field measured temperature for the waste-rock within the period of the simulation.

The average flux of O_2 through the cover has been compared for each of these models to determine the relative contribution of gas transport through the system (Figure 2-68). Over the course of the simulation, wind contributes approximately 58% of the flux of O_2 through the cover and temperature gradients contribute the remaining 42%. Barometric pressure fluctuations contribute less than 1% of the O_2 supply into the waste rock. The action of wind can result in a surge in O_2 supply into the pile, as indicated by the peaks in flux at Day 50 and 78.

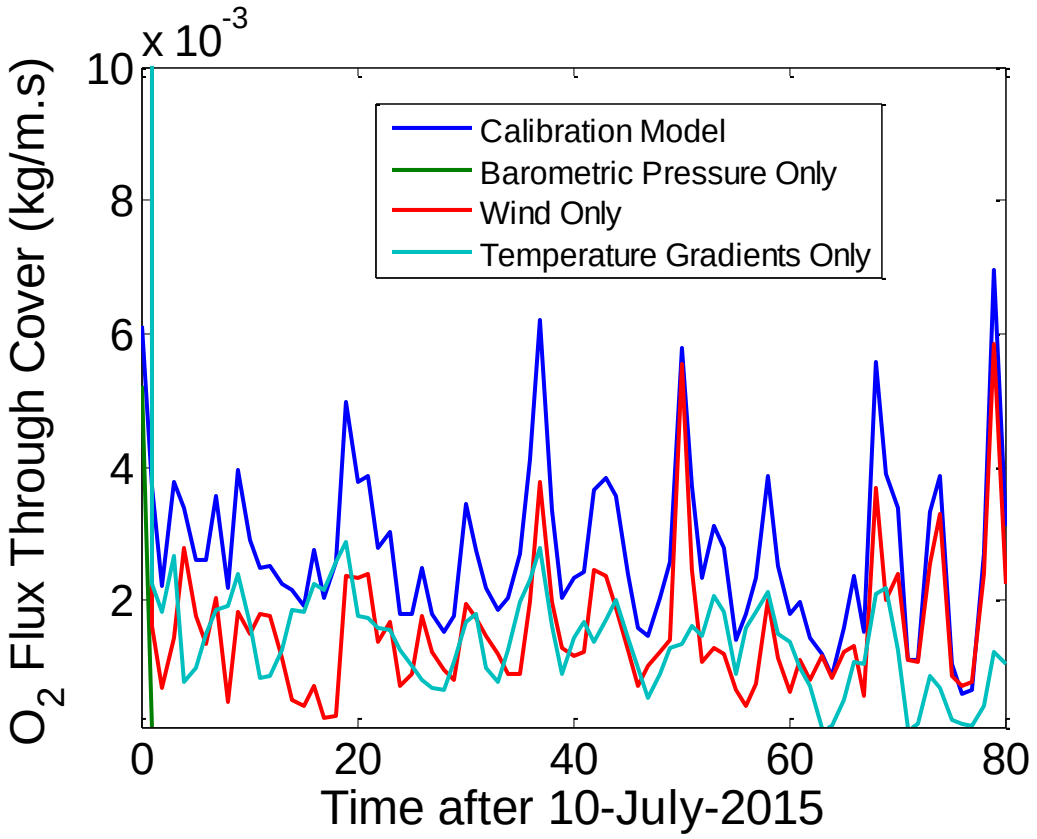

Figure 2-68 – Flux of O_2 through the cover from the individual advective transport mechanism models compared with the flux from the gas calibration model

The dominance of wind and thermally driven flow within a waste rock stockpile was previously observed by Anne and Pantelis (1997). Barometric pumping was identified as an important mechanism in gas transport in other studies (Elberling et al., 1998 and Auer et al., 1996) that were not in the waste rock scenario and wind was not included in analysis. This mechanism is not considered to contribute significantly to oxygen influx into WRS#3 in comparison to wind and thermal gradients, however a plot of the data in isolation indicates that the mechanism does drive some gas transport.

The summation of the flux of O_2 through the cover from the individual advective mechanism models has been compared to the output from the gas calibration simulation to consider the applicability of this analysis (Figure 2-69). The summation is consistently around 10% higher

than the output from the gas calibration model, and the same trends in the time series are indicated. Each transport mechanisms works together to form the gas transport regime within the pile, so exact agreement of the plots would not be expected, however the difference is sufficiently small to indicate that the mechanisms have been sufficiently separated within the individual mechanism models.

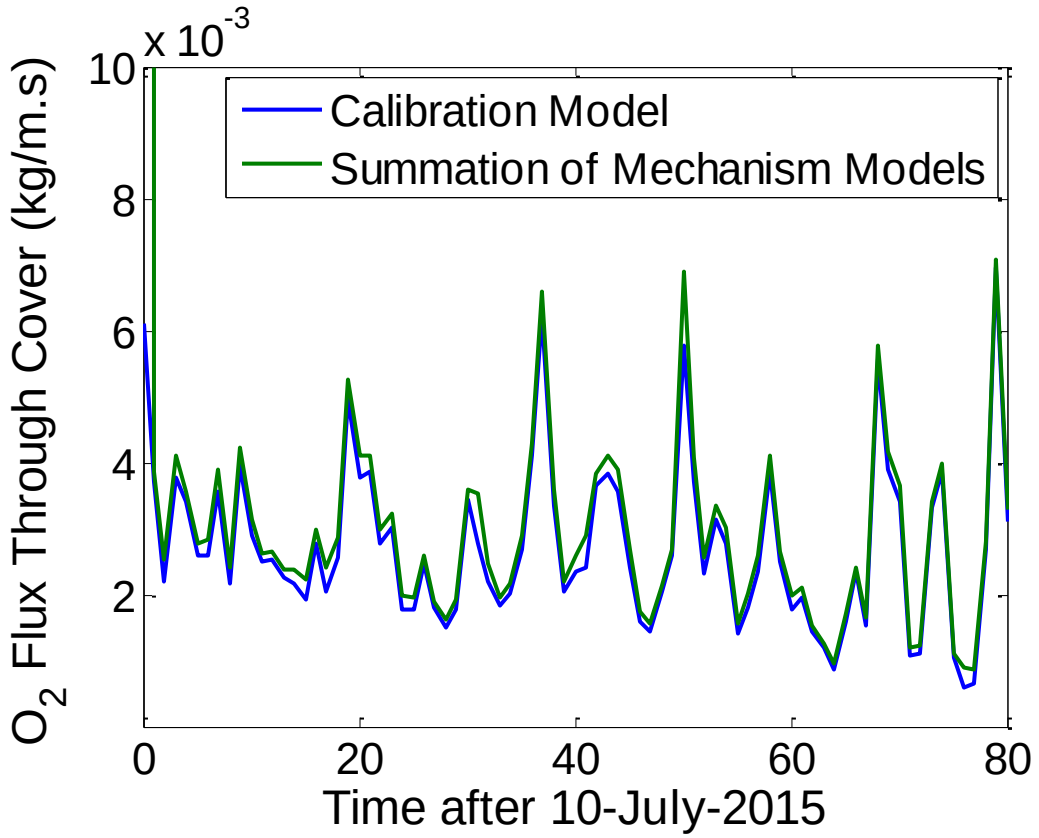

Figure 2-69 – Calculation check on the individual advection mechanism model. A comparison of the summation of the O_2 flux from each model to the gas calibration model

2.9.2 10-minute Averaged Data

A model has been run with the 10 minute averaged data for external pressure applied as boundary conditions. The model length has been reduced to 10 days from 10-July-2015 to reduce calculation time.

A diurnal component to pore-gas O_2 content is evident in the output for the model (Figure 2-70a and b). This component cannot be distinguished with the daily monitoring of pore-gas concentrations at Detour. Changes in pore-gas O_2 content of up to 10% v/v are indicated in the simulation outputs over the course of approximately half a day.

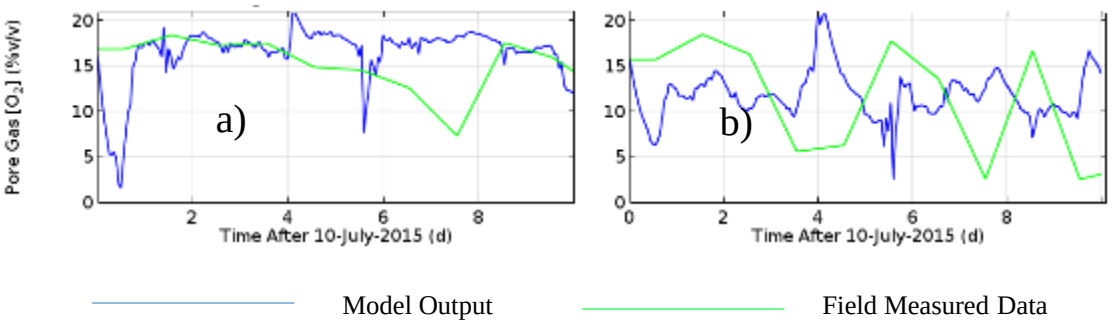

Figure 2-70 - 10 minute averaged data model, pore-gas oxygen content. a) BH2011-3-1-1.7m, b) BH2011-3-2-2.5m

2.9.3 Variable Cover Thickness

The cover thickness for the calibration models has been assumed to be approximately 1 m. The effects of removing the cover, and alternatively increasing the thickness to 2 m, have been considered.

The geometry and boundary conditions remained the same as the gas transport calibration model, to maintain the applicability of the external measured pressures. For the no-cover scenario, the permeability and thermal properties for the upper most waste-rock layers were assigned to the domain that was previously used for the cover. Oxygen consumption and heat production from sulfide oxidation was included in this layer. The thickness of the cover was extended 2m from the surveyed surface for the thicker cover model.

Time series plots for pore-gas O_2 content (Figure 2-71a and b) from the no-cover scenario, and an example 2-dimensional surface for O_2 content at day 60 (Figure 2-72), indicate that the pore-gas O_2 content is consistently higher throughout the pile. The simulated O_2 content at BH2011-3-

1-1.7m is generally around 20% and BH2011-3-2-2.5m is generally between 15-20% v/v. The O_2 depletion towards the base of the pile is still indicated (Figure 2-72). Oxygen concentrations remain above 10% for the majority of the waste-rock geometry (Figure 2-72), as opposed to becoming less than 10% within 10m perpendicularly from the middle of the batter which was observed for the gas calibration model (Figure 2-60).

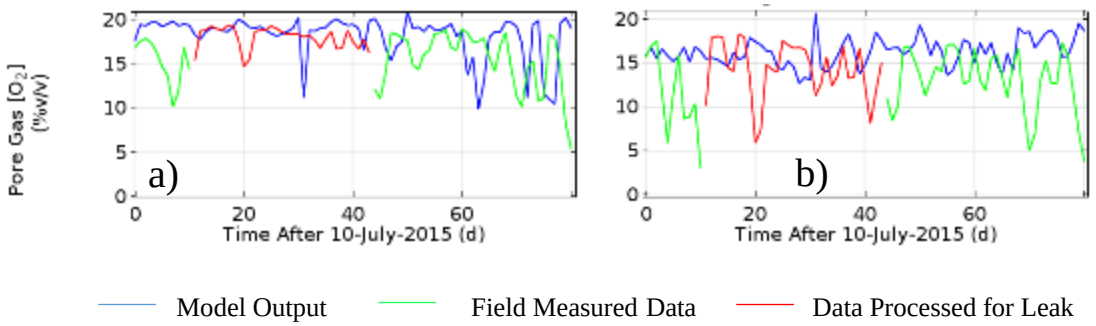

Figure 2-71 – No cover model, pore-gas oxygen content compared with field data. a) BH2011-3-1-1.7m, b) BH2011-3-2-2.5m

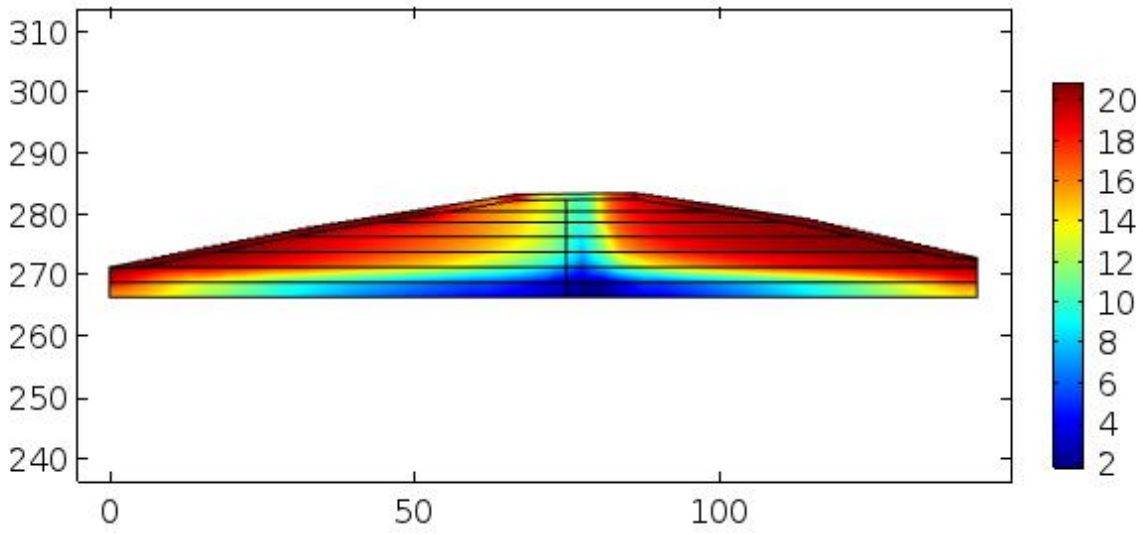

Figure 2-72 – 2D Surface from no cover model, pore-gas oxygen content on day 60 of the simulation

The simulated temperature close to the surface of the pile at BH2011-3-2-1.85m is approximately 0.6°C lower to the output from the calibration model at the end of the simulation time (Figure 2-73a and b), however the simulated temperature at the deeper location of BH2011-

3-2-7.85m is approximately 0.5°C higher than the output from the calibration model. This indicates that the temperature distribution is unevenly altered with the use of low permeability soil covers.

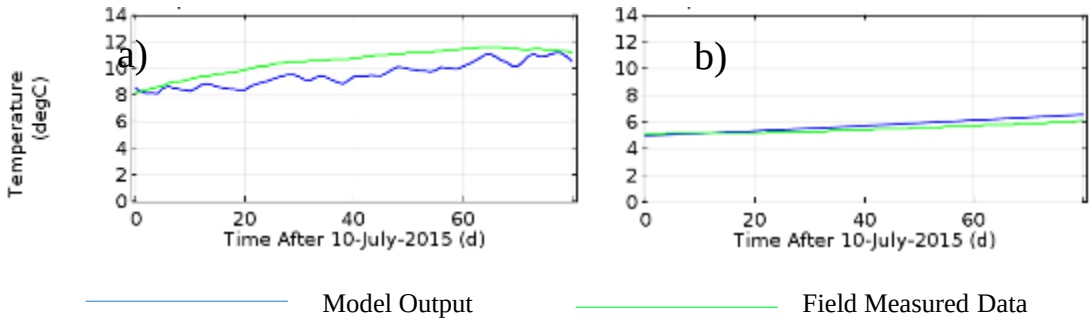

Figure 2-73 – No cover model output, temperature compared with field data at a) BH2011-3-2-1.85m and b) BH2011-3-2-7.85m

Time series plots for pore-gas O_2 content (Figure 2-74a and b) from the thicker (2m) cover model indicate that the pore-gas O_2 content is lower when compared with the calibration model; however, the decrease is only 2-5% v/v at BH2011-3-1-4.2m and BH2011-3-2-2.5m. This same decrease is indicated throughout the entire waste rock pile at day 60 of the simulation (Figure 2-75).

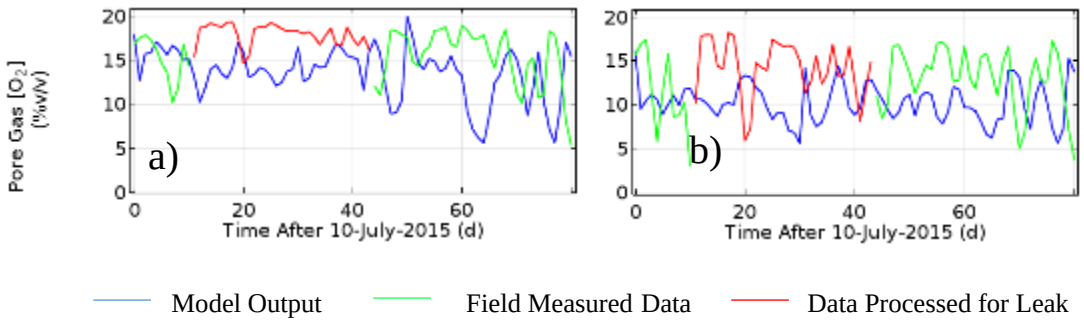

Figure 2-74 – 2m thick cover model, pore-gas oxygen content compared with field data. a) BH2011-3-1-1.7m and b) BH2011-3-2-2.5m

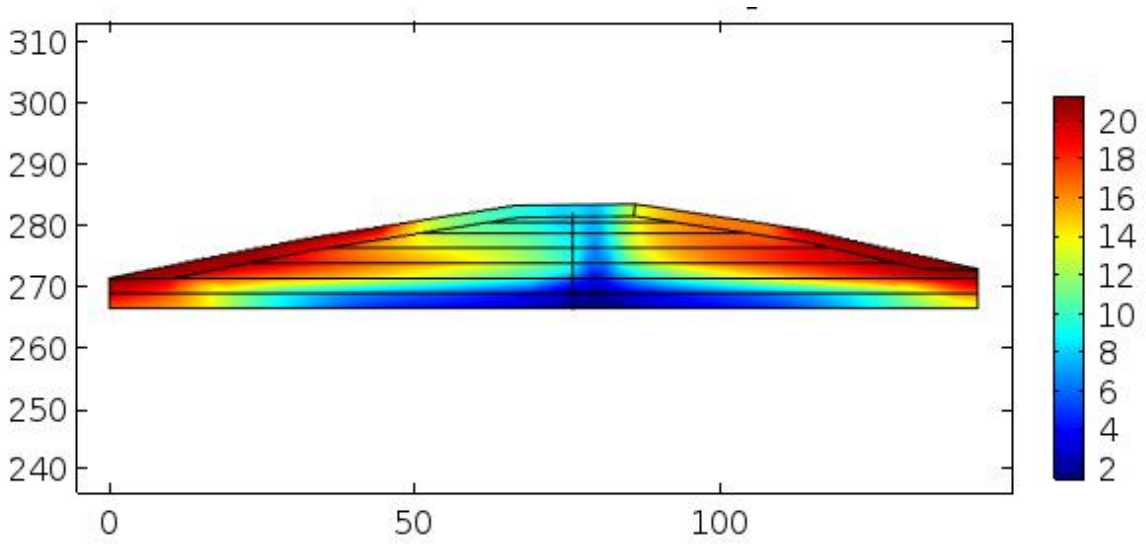

Figure 2-75 – 2D Surface from 2m thick cover model, pore-gas oxygen content on day 60 of the simulation

Oxidation rates in the middle of the pile are approximately 40% lower on average for the 1 m thick cover compared with no cover (Figure 2-76). The oxidation rates at the reference point are indicated to be approximately 10% higher for the 2m thick cover model compared with the 1m thick cover, however the distribution of O_2 within the pile changed for this simulation and the reference point was in a more oxygenated region (Figure 2-77a and b). The benefit of increasing the thickness of the cover is indicated in the reduced O_2 content in the time series plots (Figure 2-74a and b).

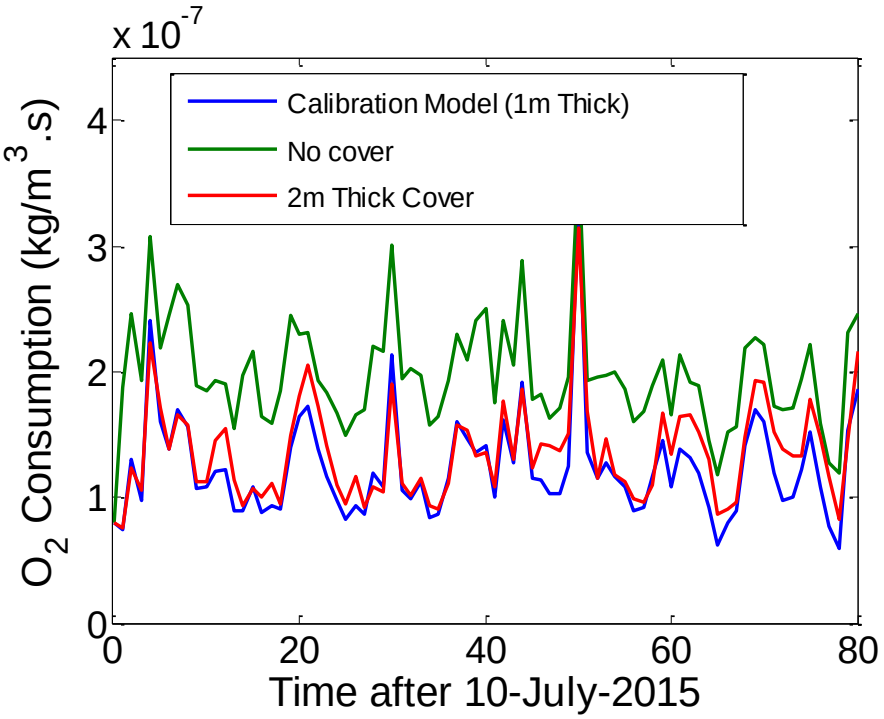

Figure 2-76 – Oxygen consumption rate for no cover, calibration and 2m thick cover models compared

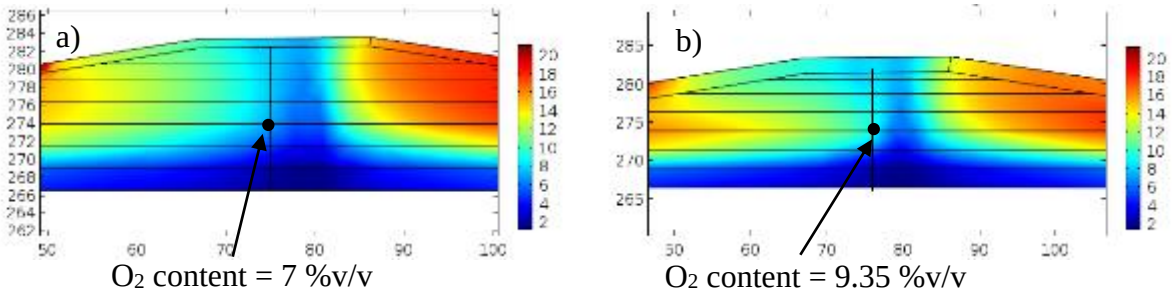

Figure 2-77 – 2D Surface for pore-gas oxygen content on day 60 of the simulation from a) gas calibration model (1m thick cover), b) 2m thick cover model

2.9.4 Varying Cover Permeability

Models have been run to consider the effect that lower values for the cover permeability may have on gas transport and oxidation rates. Permeability values of $1x10^{-10}$ m^2 and $1x10^{-11}$ m^2 (compared to the calibrated value of $1x10^{-9}$ m^2) have been considered for the cover, and the

permeability of the waste-rock has not been altered from the calibration model. The thickness of the cover has been assumed to be 1 m, as was assumed for the calibration model

The pore-gas O_2 content is consistently lower within the pile when the permeability of the cover is reduced from 1 $x10^{-9}$ m^2 (calibration model) to $1x10^{-10}$ m^2 (Figure 2-78a1 to b2). The difference in O_2 content at BH2011-3-1-1.7m between the two models is between 10-15% v/v.

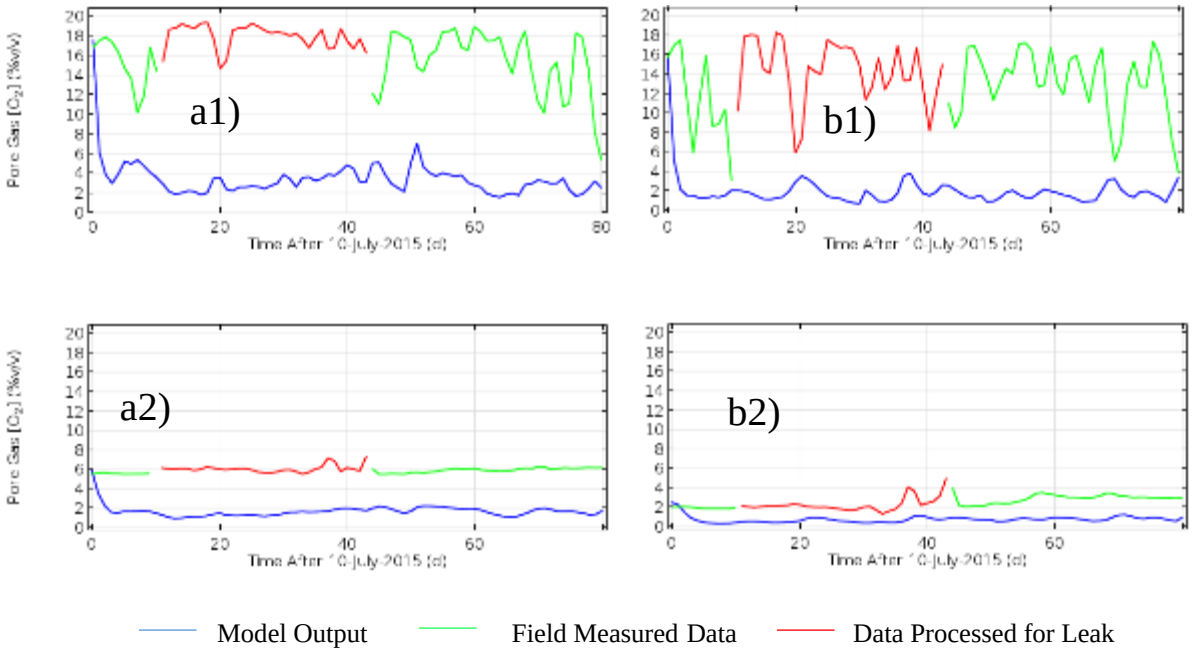

Figure 2-78 – kcover=1x10^{-10}m^2 model, pore-gas oxygen content compared with field data. a1) BH2011-3-1-4.2m, a2) BH2011-3-1-14.2m, b1) BH2011-3-2-2.5m, b2) BH2011-3-2-15m

As expected, the pore-gas O_2 content is reduced further when the permeability of the cover is reduced from $1x10^{-10}$ m^2 to $1x10^{-11}$ m^2 , and the O_2 content is less than 2% v/v at the calibration locations (Figure 2-79a1 to b2). On day 60, the O_2 content reduces from atmospheric temperature to below 5% within 4m perpendicularly around the middle of the batters.

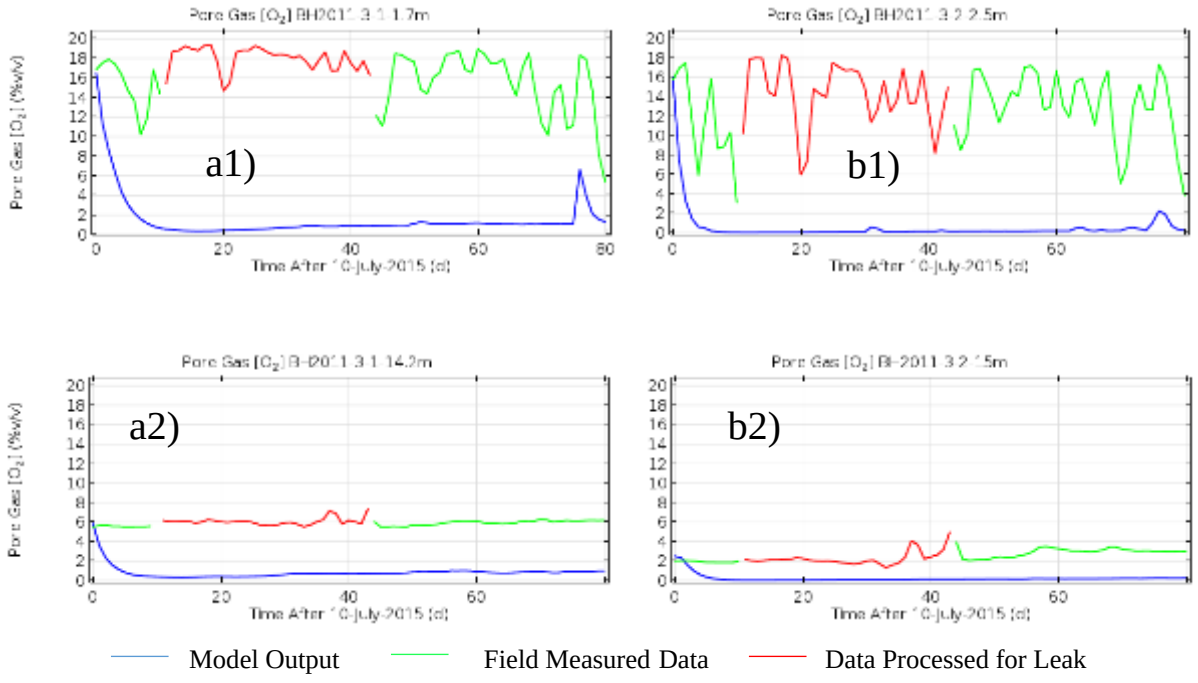

Figure 2-79 – kcover=1x10^{-11} m2 model, pore-gas oxygen content compared with field data. a1) BH2011-3-1-4.2m, a2) BH2011-3-1-14.2m, b1) BH2011-3-2-2.5m, b2) BH2011-3-2-15m

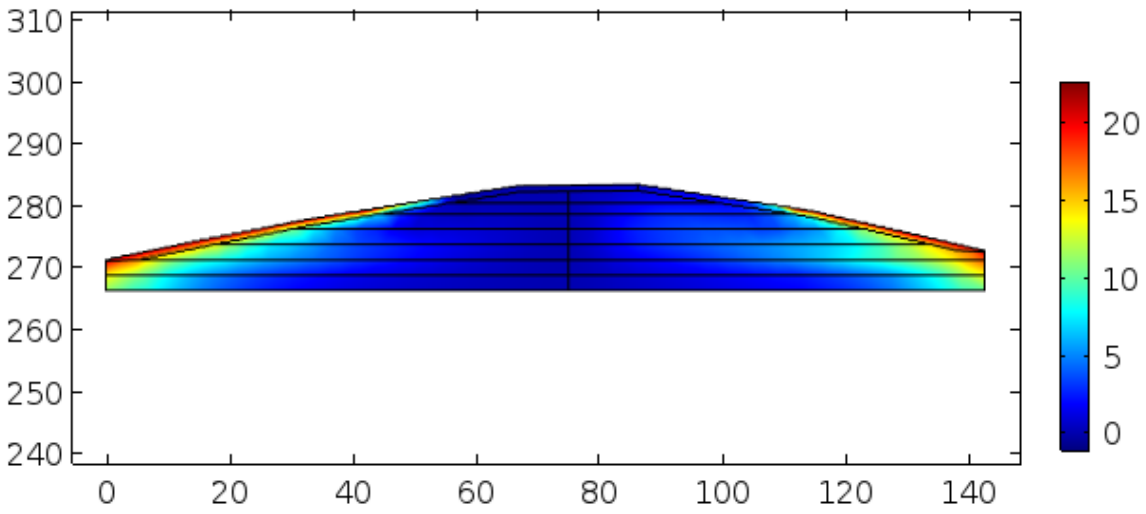

Figure 2-80 – 2D Surface from kcover = 1x10^{-11} m^2 model, pore-gas oxygen content on day 60 of the simulation

Oxidation rates for the varying cover permeability models are approximately 80% lower on average for the 1x10^{-10} m^2 model, and an additional 81% reduction is indicated if the cover thickness is further reduced to 1x10^{-11} m^2 (Figure 2-81). The results of this simulation indicate

that using a cover material with a lower permeability, i.e. a more clay-rich material, will reduce the oxidation rates within the waste-rock.

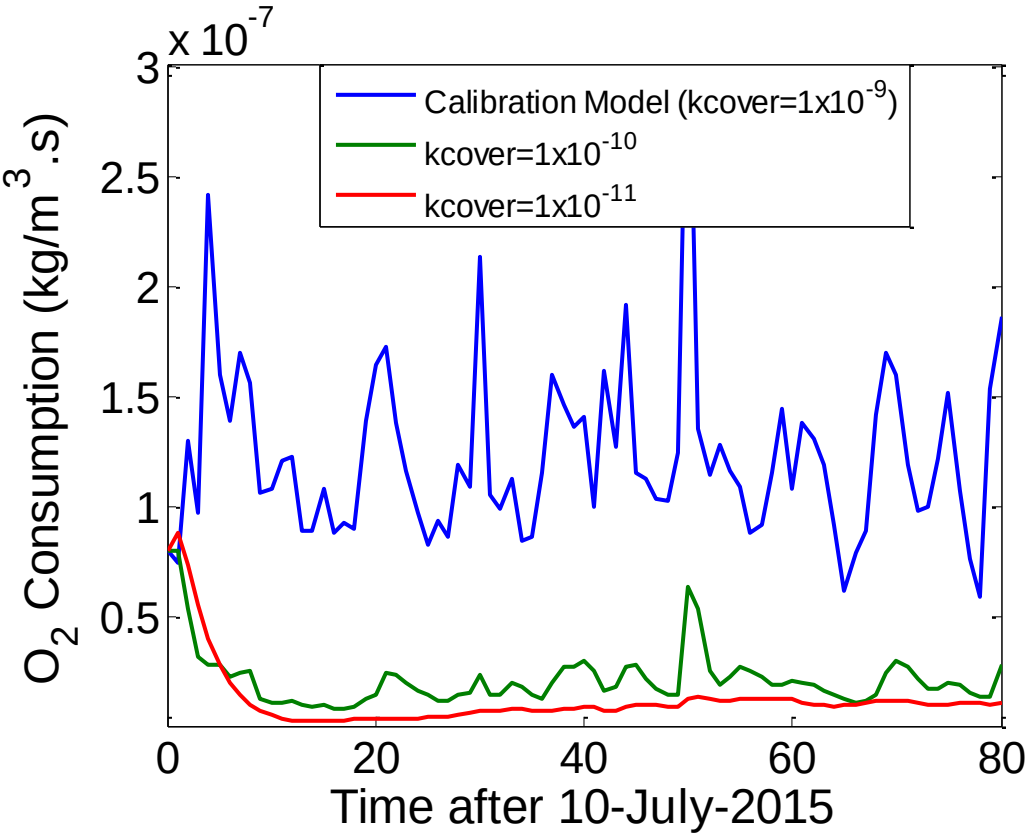

Figure 2-81 – Oxygen consumption rate for calibration model (kcover=1 x10^{-9}m^2), kcover=1x10^{-10}m^2 and kcover=1x10^{-11}m^2 models compared

The flow arrows indicate that flow is in a circular direction within the pile (Figure 2-82). Temperature and pressure gradients are present within the pile, however the low permeability cover has sufficiently impeded inflow of atmospheric air and outflow of pore gas to the atmosphere that the majority of the gas flow remains within the pile.

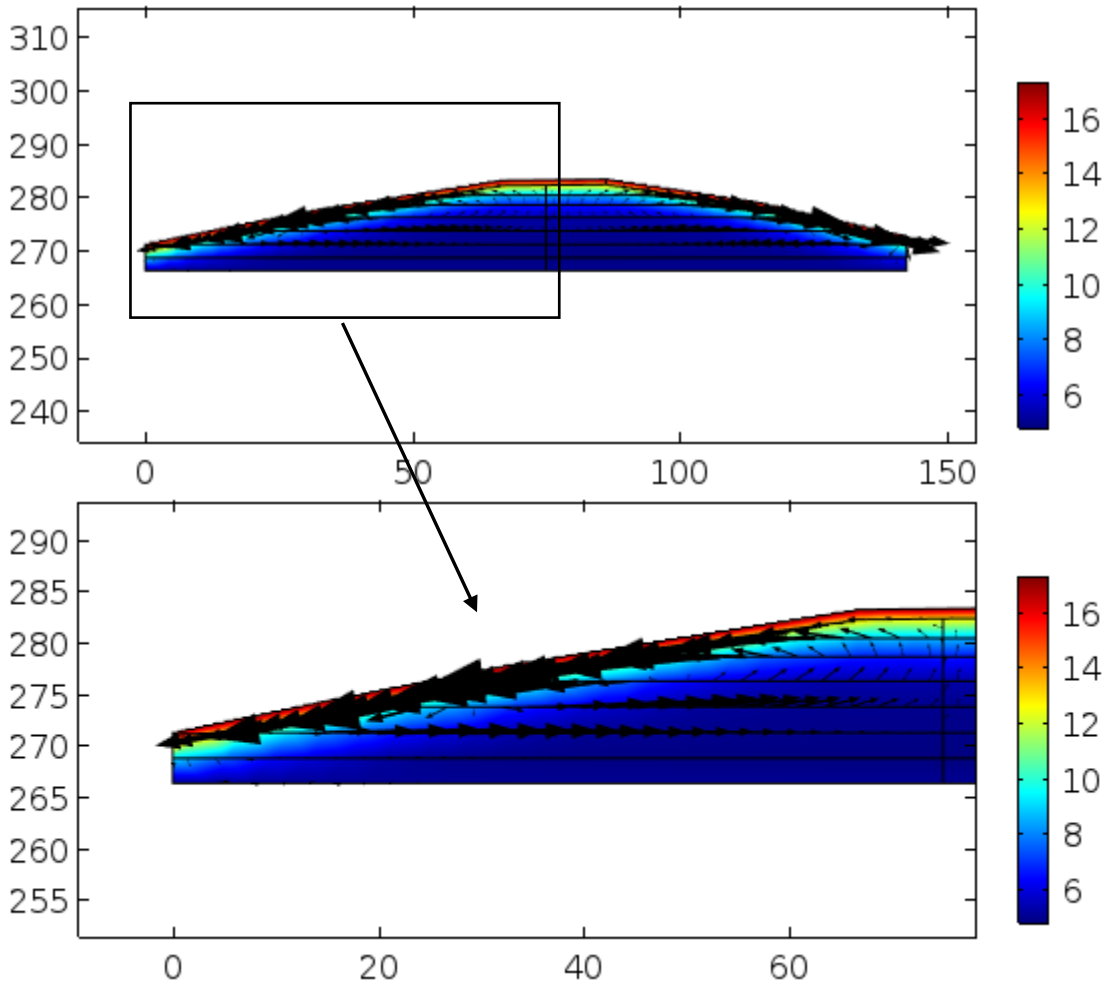

Figure 2-82 – Flow arrow diagram for 2m thick cover model, overlaid with the temperature surface on day 60 of the simulation

2.10 Conclusions

The results of the field monitoring and numerical simulations for gas transport at WRS#3 at Detour Gold mine have confirmed that wind and barometric pressure affect the pressure regime on the exterior and interior of the waste-rock pile. Advective transport through the action of wind and temperature gradients are the dominant mechanisms during the summer, despite the placement of a relatively low permeable soil cover in the late 1990s. The simulations indicate that the supply of O_2 into the waste rock is affected by barometric pressure fluctuations

(barometric pumping), however the effect of this mechanism is minimal compared with wind and temperature gradients.

The calibrated input for the permeability of the waste rock was higher than expected, indicating that regions of high permeability are present within the pile. Design of future piles will likely have to account for the possibility of these zones by applying permeability values in the range of $10^{-8}m^2$ to the waste-rock in gas transport analyses.

The calibrated material input for the cover was also higher than expected ($1x10^{-9}$ m^2), indicating that defects or variable thickness is increasing the overall permeability of the cover. The cover that has been placed has provided some benefit in encouraging subatmospheric O_2 content of the pore-gas within the pile; however, the permeability of the cover has not been sufficient to completely retard advective gas transport. Numerical simulations indicated that oxidation rates can be reduced within the waste rock through the use of lower permeability covers, i.e. a more clay-rich material.

Chapter 3 – Synchrotron Analysis of the Speciation of the Sulfur Species Produced By Acid Rock Drainage

3.1 Introduction

Iron-sulfide minerals are typically present in mine waste materials, including tailings and waste-rock. The minerals may oxidise on exposure to the atmosphere, releasing metals, sulfate and acidity to the hydrosphere (Belzile et al., 2004; Nordstrom and Southam, 1997; Blowes et al., 2003).

The oxidation of the sulfide mineral pyrite (FeS_2) is described by the following reaction, hereby referred to as the 'sulfide oxidation reaction':

$$FeS_{2(s)} + \frac{15}{4}O_2 + \frac{7}{2}H_2O \rightarrow 2SO_4^{2-} + Fe(OH)_{3(s)} + H^+ \qquad 3\text{-}1$$

Other typical sulfide minerals present in mine wastes at other sites include troilite (FeS) and the iron deficient pyrrhotite ($Fe_{1-x}S_x$, sphalerite (Zn,Fe)S, chalcopyrite ($CuFeS_2$), pentlandite $(Fe,Ni)_9S_8$, covellite (CuS) and arsenopyrite (FeAsS), as described in Jambor et al. (2000). Oxidation of all iron sulfides releases Fe and SO_4^{2-}, and Cu, Ni, Zn and As are also released when they are present within the mineral structure.

The ARD reaction represents the complete oxidation of S^{2-} to S^{6+}, however it does not describe the intermediate species that are produced as the reaction progresses. The mobility of the intermediate species and the role that they play in the liberation of metals is not well understood. These processes have implications in reactive transport modelling and other predictive simulation for the production of acid rock drainage.

Typical sulfidic species that are produced through oxidation include sulfides, polysulfides, elemental S, sulfoxyanions and sulfate (Suzuki, 1999). The initial response to oxidation is for solid state diffusion of Fe to the grain edges (Pratt and Nesbitt, 1997), where the Fe is oxidised. The remaining sulfide mineral becomes more S rich and is replaced with marcasite. The sulfide core is then oxidised by dissolved O_2 or Fe(III) , which must diffuse through the precipitated Fe species at the edge of the grain. The stability of the subsequent oxidised S species in the solid form will depend on the pH conditions, which are circumneutral to slightly acidic at Detour due to acid neutralisation by carbonate minerals (McNeill, 2016). Thiosulfate ($S_2O_3^{2-}$) is more stable in the solid phase at pH<7 (Druschel et al., 2003) and chain lengthening by additional oxidation to tetrathionate ($S_4O_6^{2-}$) and other polythionates may also occur in these pH conditions (Moses et al., 1984). Sulfate is more readily released to the hydrosphere than the less oxidised species (Langman et al., 2015).

Langman et al. (2015) identified oxidation states for S of -2, -1, 0, +4 and +6 in a synchrotron based study of oxidising pyrrhotite and pentlandite. The corresponding S-containing species were sulfide ($Fe_{(1-x)}S$), marcasite (FeS_2), elemental S (S^0), thiosulfate ($S_2O_3^{2-}$), sulfite (SO_3^{2-}) and sulfate (SO_4^{2-}). This study builds on the work of Langman et al. (2015) to confirm the identity of the intermediate species within pyrrhotite and chalcopyrite grains from Detour.

Neutralisation reactions may occur in the presence of carbonate minerals, the most common of which in waste-rock are calcite ($CaCO_3$), dolomite ($CaMg(CO_3)_2$), ankerite ($CaFe(CO_3)_2$) and siderite ($FeCO_3$) (Blowes et al., 2003). The neutralisation reaction from calcite is as follows:

$$CaCO_3 + H^+ \rightarrow Ca^{2+} + HCO_3^- \quad 3\text{-}2$$

$$HCO_3^- + H^+ \rightarrow CO_2 + H_2O \quad 3\text{-}3$$

The pH of waste-rock pore water remains near neutral where carbonates are present, and Fe (oxyhydr)oxides including hematite (Fe_2O_3), magnetite (Fe_3O_4), goethite (α-FeO(OH)), lepidocrocite (γ-FeO(OH)) and ferrihydrite ($Fe_2O_3.0.5H_2O$) are likely to precipitate under these conditions (Blowes et al., 2003).

3.2 Methods

Select sulfide grains from Detour were used to examine variations in S and Fe speciation resulting from sulfide oxidation. The grains were selected from glass slides that had been prepared from samples collected during test pitting work at WRS#1 for X-Ray Diffraction analysis by McNeill, (2016). Grab samples were sieved and a subsample was taken from the 63µm sieve and washed to concentrate the sulfide grains. Suitable sulfide grains were identified for further study through visual inspection under an optical microscope and grains that exhibited differential weathering from the edge to the centre were considered for analysis. The S and Fe content of these grains was assessed by scanning electron microscopy with energy dispersive spectroscopy (SEM-EDX) using a Hitachi TM3000 scanning electron microscope (SEM) with a Bruker QUANTAX 70 energy dispersive spectroscope (EDS) at the University of Waterloo. Two grains were selected for further testing at beamline 13 ID-E at the Advanced Photon Source (APS) at Argonne National Laboratory in Lemont, Illinois, USA.

Sulfur and iron speciation was evaluated using X-ray absorption near edge spectroscopy (XANES). SEM-EDX spectra from the unweathered part of the grains was used to identify the mineral. Suitable locations for XAS testing were identified through the collection of µ-XRF maps. XANES was carried out on the weathered and unweathered parts of the grain to evaluate variations in the speciation of S and Fe. The sulfur speciation was studied during a visit in November, 2014 and one of the grains was examined to assess iron speciation in March, 2016.

The beamline has a Si(III) monochromator and can deliver an incident beam with approximate dimensions of 2 x 2 µm and an energy of between 2.4 to 28keV. An energy range of 2450-2600eV was used for collection of S and Fe spectra over the energy range from 7000-7300eV. Absorption data was collected using a four element Hitachi Vortex, silicon drift detector.

The XANES spectra were interpreted using linear combination analysis of normalised spectra and the derivative of the spectra with the XANES software ATHENA (Ravel and Newville, 2005). The normalisation process assigns a regression to the pre-edge part of the spectra to effect a shift to an absorption of 0, and to the post-edge part of the spectra to effect a shift to an absorption of 1 (Figure 3-1a and b).

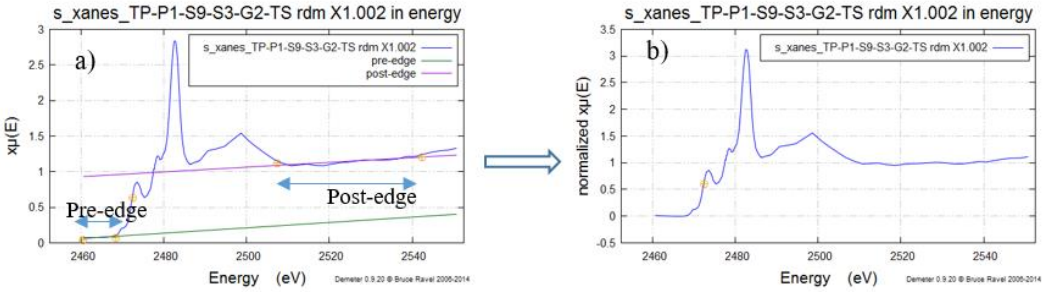

Figure 3-1 – Normalisation procedure for XANES; a) collected spectra and the pre and post-edge lines, b) normalised spectra

Reference spectra for S and Fe species were collected during the visits to the APS and were also collected from established databases that were made available to the public (ID21 Sulfur XANES Spectra Database of European Synchrotron Radiation Facility (2014), International X-ray Absorption Society (2016), Center for Advanced Radiation Sources (2016)) and from previous visits to the APS (Lindsay, 2016).

The energy positions for the standard spectra were calibrated to reference energy values (Table 3-1). The energy point that is typically used is the inflection on the first peak in the spectra (Prietzel et al., 2007) known as the absorption edge (e0; Figure 3-2).

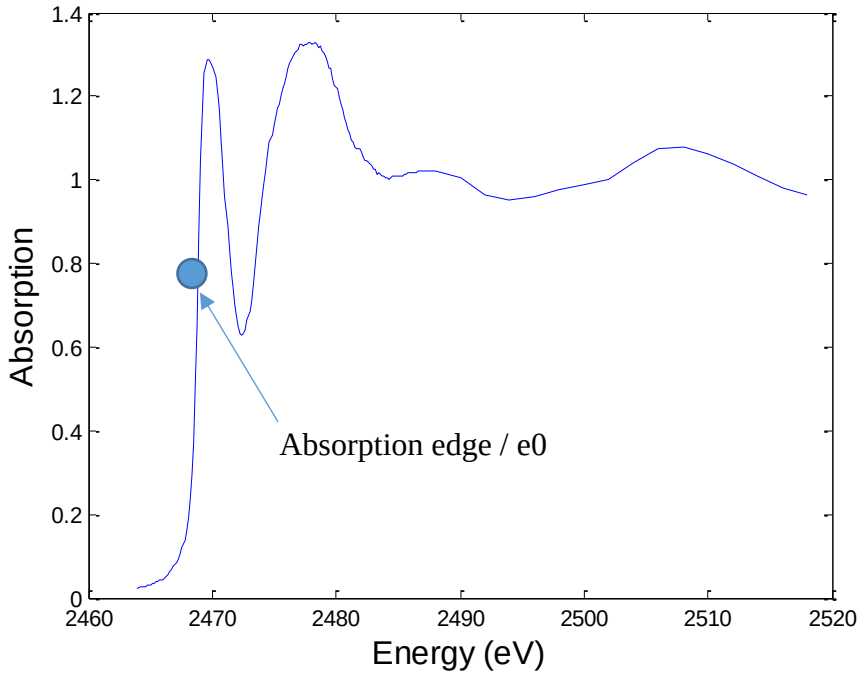

Figure 3-2 – Standard normalised XANES for pyrrhotite in the sulfur absorption range; location of the absorption edge, or e0, that is typically used to calibrate collected spectra to references

The S spectra for troilite and pyrrhotite have an equal reference e0 and are very similar in shape (Fleet, 2005). Distinguishing between these two species was not possible using XANES analysis. The Fe spectra for the Fe (oxyhydr)oxides noted in Table 3-1 are also very similar and distinguishing different species was also not achievable (Prietzel et al., 2007). The Fe spectra for goethite was collected during the March 2016 visit to the APS, and represents all typical Fe (oxyhydr)oxides that are produced by the ARD reaction for the purpose of this study.

Table 3-1 – Standard Spectra Reference e0 values

S Species	**e0 value (eV)**	**Sulfur Oxidation State**	**Reference**
Chalcopyrite $CuFeS_2$	2469.5	-2	Fleet (2005)
Pyrrhotite $Fe_{1-x}\,S_x$	2469.5	-2	Fleet (2005)
Sphalerite $(Zn, Fe)S$	2473.3	-2	Fleet (2005)
Marcasite FeS_2	2471.5	-1	Li et al. (1994)
Elemental (S^0)	2472	0	Fleet (2005)
Thiosulfate ($S_2O_3^{2-}$)	2471.4	-1, +5	Fleet (2005)
Tetrathionate ($S_4O_6^{2-}$)	2472.3	0, +5	Morra et al. (1997)
Sulfite (SO_3^{2-})	2477.7	+4	Fleet (2005)
Sulfate (SO_4^{2-})	2482	+6	Fleet (2005)
Fe Species	**e0 value**	**Iron Oxidation State**	**Reference**
Troilite	7116.6	+2	Prietzel et al. (2007)
Chalcopyrite $CuFeS_2$	7118.9	+2	-
Pyrrhotite $Fe_{1-x}\,S_x$	7123.5	+2	O'Day et al. (2004)
Ferrihydrite ($Fe_2O_3.0.5H_2O$)	7123.2	+3	Prietzel et al. (2007)
Goethite ($\alpha - FeO(OH)$)	7123.5	+3	Prietzel et al. (2007)
Lepidocrocite ($\gamma - FeO(OH)$)	7123.5	+3	Prietzel et al. (2007)
Hematite (Fe_2O_3)	7123.1	+3	Prietzel et al. (2007)

No reference value for e0 for the Fe spectra for chalcopyrite could be located in the literature. This spectra was collected during the March 2016 visit to APS, and other spectra including pyrrhotite was obtained at the same trip. A shift in the energy axis was applied to the pyrrhotite spectra to obtain calibration to the reference value, and the same shift was applied to the chalcopyrite spectra.

3.3 Results and Discussion

Two grains were selected from slide TP-P1-S9-S3 (McNeill, 2016) that contained crushed rock from waste-rock stockpile #1 (Figure 3-3). This pile is open on the batters and is therefore likely to have been more oxygenated than WRS#3 since the cover was placed on that pile in 1998.

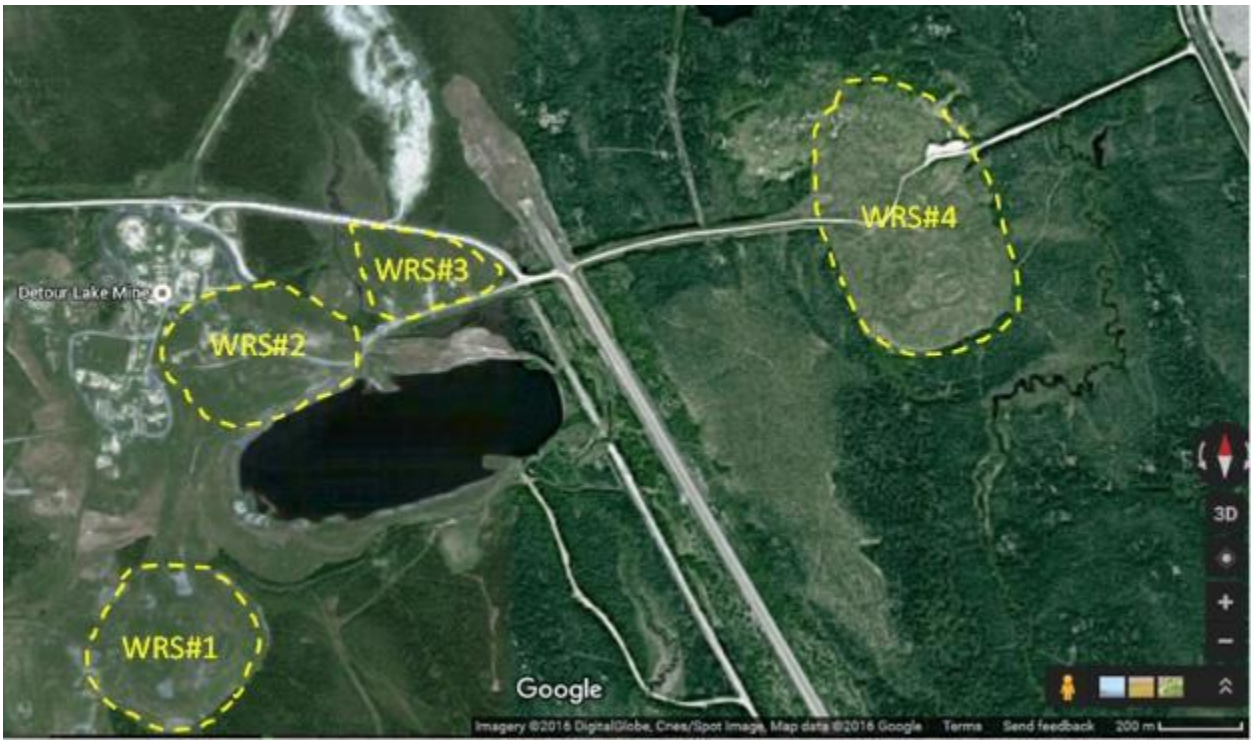

Figure 3-3 – Location of waste-rock stockpile #1 at Detour Gold Mine

The sulfide grains are hereby named Grain 1 and 2 (Figure 3-4a and b). SEM-EDX analysis previously was carried out on the grains and the results were provided (Smith, 2016).

XANES spectra for sulfur were collected for both grains, and Fe spectra were collected on grain 2.

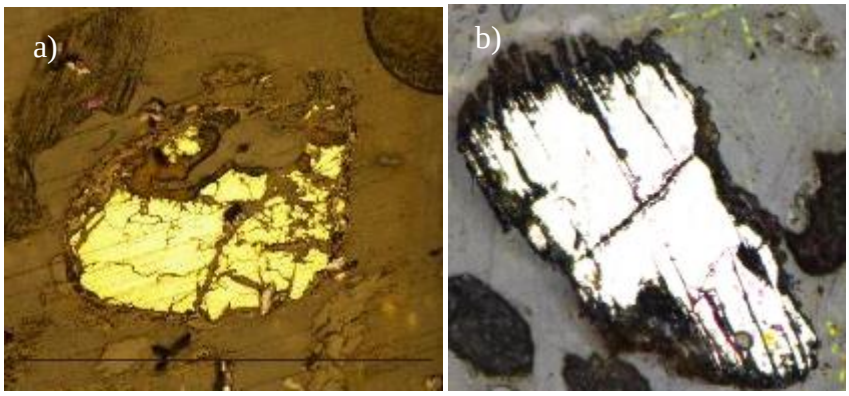

Figure 3-4 – Optical microscope photographs for a) grain 1 and b) grain 2

3.3.1 Sulfur Speciation Analysis

The SEM-EDX spectra for Grain 1 were collected at the unweathered part of the grain (Figure 3-5) and are all similar (Figure 3-6a to c). Peaks in the EDX spectra are present at approximately 2,300keV, 6,400keV and 8,000keV that are attributed to S, Fe and Cu respectively. The magnitude of the Fe and Cu peaks are approximately 25 mass % and 15 mass % of the S peak respectively for all locations. These features are also present in the standard spectra for chalcopyrite (Figure 3-5d, modified from Severin (2004)) and the unaltered grain can therefore be identified as this mineral.

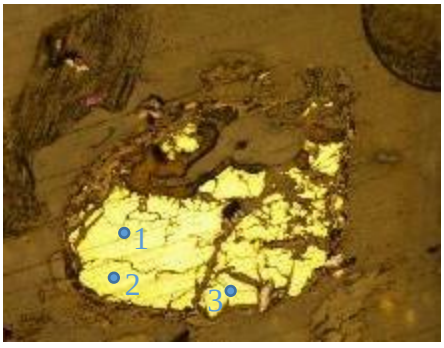

Figure 3-5 – Location of SEM-EDX spectra collection on grain 1

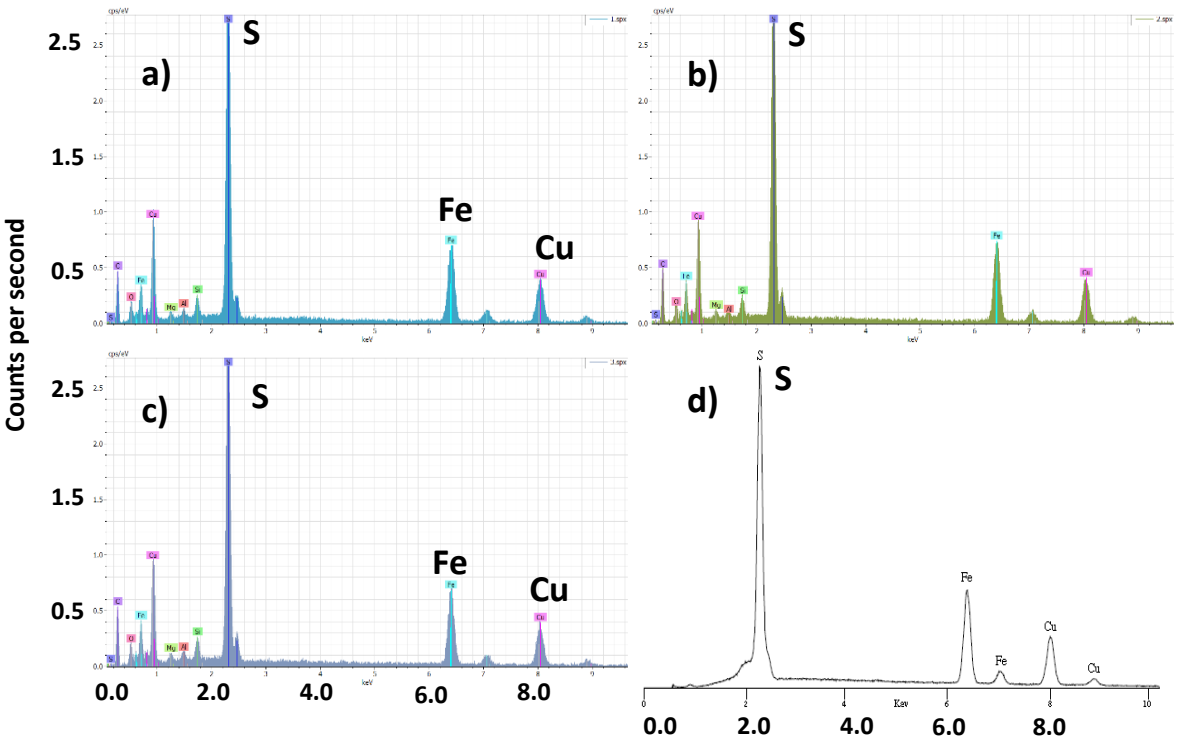

Figure 3-6 – SEM-EDX Spectra for the unweathered part of grain 1, a) location 1, b) location 2 c) location 3, and d) reference spectra for chalcopyrite (modified from Severin, 2004)

µ-XRF maps of Grain 1 show the spatial distribution of Fe, S, Cu and Zn; a brighter colour indicates a higher absorbance and therefore greater abundance of the element. Variable weathering is indicated by the inconsistent absorbance of Fe (Figure 3-7a) and S (Figure 3-7b). A weathered area (circled in Figure 3-7a) shows almost complete loss of S and Zn but some Fe and Cu remain. A relatively unweathered area (circled in Figure 3-7b) shows higher absorbance of Fe and S.

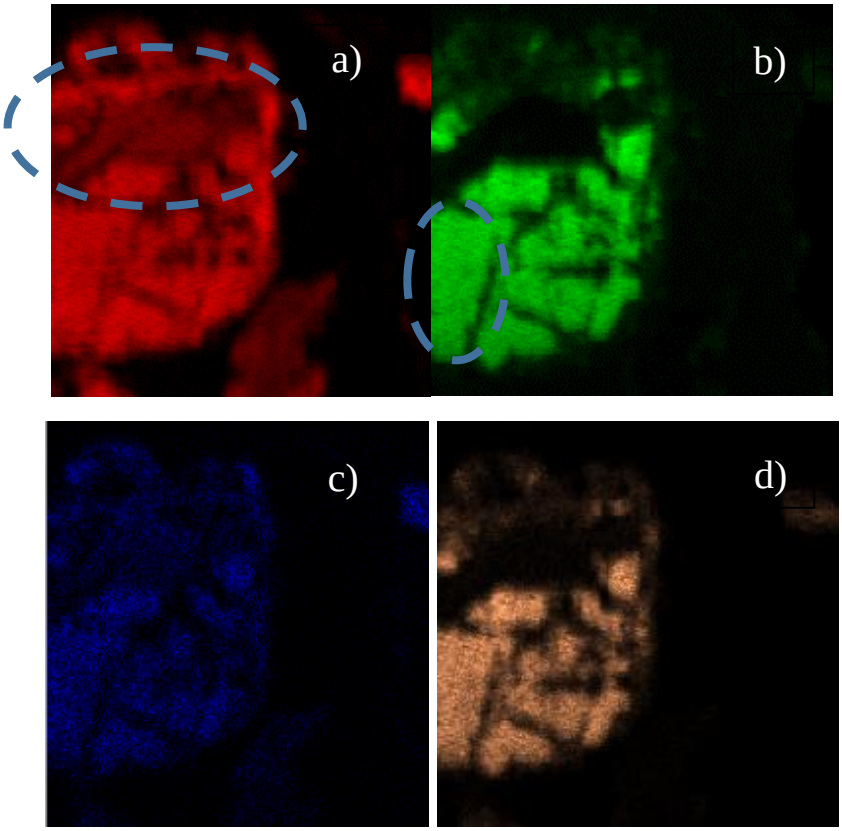

Figure 3-7 – Grain 1 µ-XRF maps showing the relative distribution of a) Fe b) S c) Zn and d) Cu over the grain. Encircled area in a) is a relatively weathered area and in b) is a relatively unweathered section

A total of 11 locations were selected for XANES collection (Figure 3-8) in the S absorption range based on distribution of S on the map images. One location was selected in the unweathered section (location 1), and the remainder were distributed over the grain.

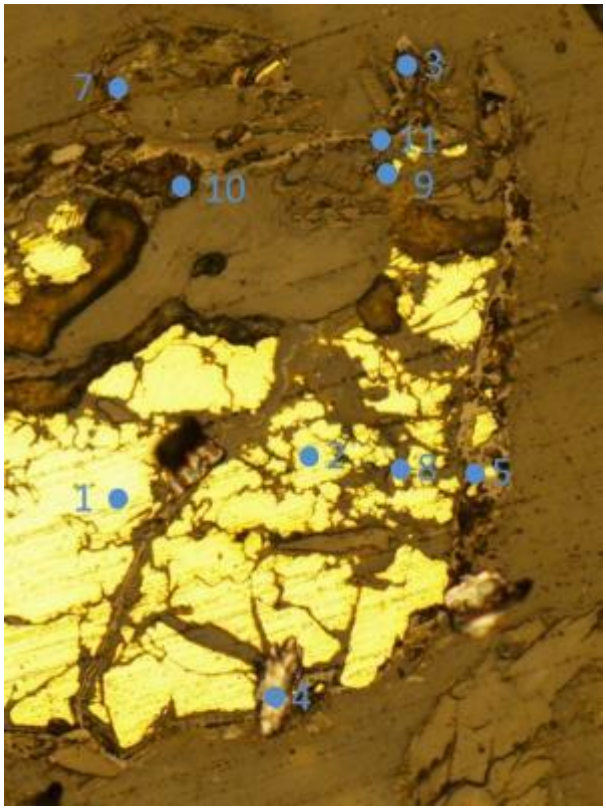

Figure 3-8 – Locations of S XANES collection, grain 1

The results of linear combination analysis of the S spectra indicate that the spectra exhibits variable contributions from $CuFeS_2$, Fe_xS_{1-x}/FeS, FeS_2 (marcasite), S^0, $S_2O_3^{2-}$, $S_4O_6^{2-}$, SO_3^{2-} and SO_4^{2-} (Table 3-2). Except for $CuFeS_2$, which would only be expected in a chalcopyrite grain, these same species were identified in the pyrrhotite/pentlandite grains by Langman et al. (2015).

Locations 1, 2, 6, 8 and 9 were on an unweathered mineral and the analysis indicated that chalcopyrite dominates the spectra. Locations 3, 7, 10 and 11 were on a heavily weathered area and elemental S dominates the signal. Prange et al. (2002) suggested that the initial peak in the tetrathionate spectra (at approximately 2473 eV) is due to the presence of elemental S^0 within the chain structure. It is therefore possible that the dominance of S^0 in the spectra is representative of the presence of $S_4O_6^{2-}$ (or other polythionates). Langman et al. (2015) identified $S_2O_3^{2-}$ more

frequently than S^0. The other S species are variable over the grain. Example XANES for the mineral are presented with the standard spectra of the identified species superimposed (Figure 3-9a and b).

The results of the linear combination analysis for the normalised and derivative spectra generally agree within 15% (Table 3-2), which is a good correlation for reasonable assurance of the results. Marcasite was only identified in the derivative spectra at location 7, and sulfate was only identified in the derivative spectra at location 9. The results of the analysis of the normalised spectra for location 7 were similar to the results from location 10 and 11 and it is likely that this spectra is more representative of the pattern of oxidation. The normalised spectra is also likely more representative for location 9, as the results are similar to other locations in the less weathered parts of the grain. Both pyrrhotite/troilite and thiosulfate were identified at four locations in relatively low quantities (less than 10%) within either the normalised spectra or the derivative spectra but not both. It is not certain if the analysis method is sufficiently sensitive to differentiate between these species within both spectra.

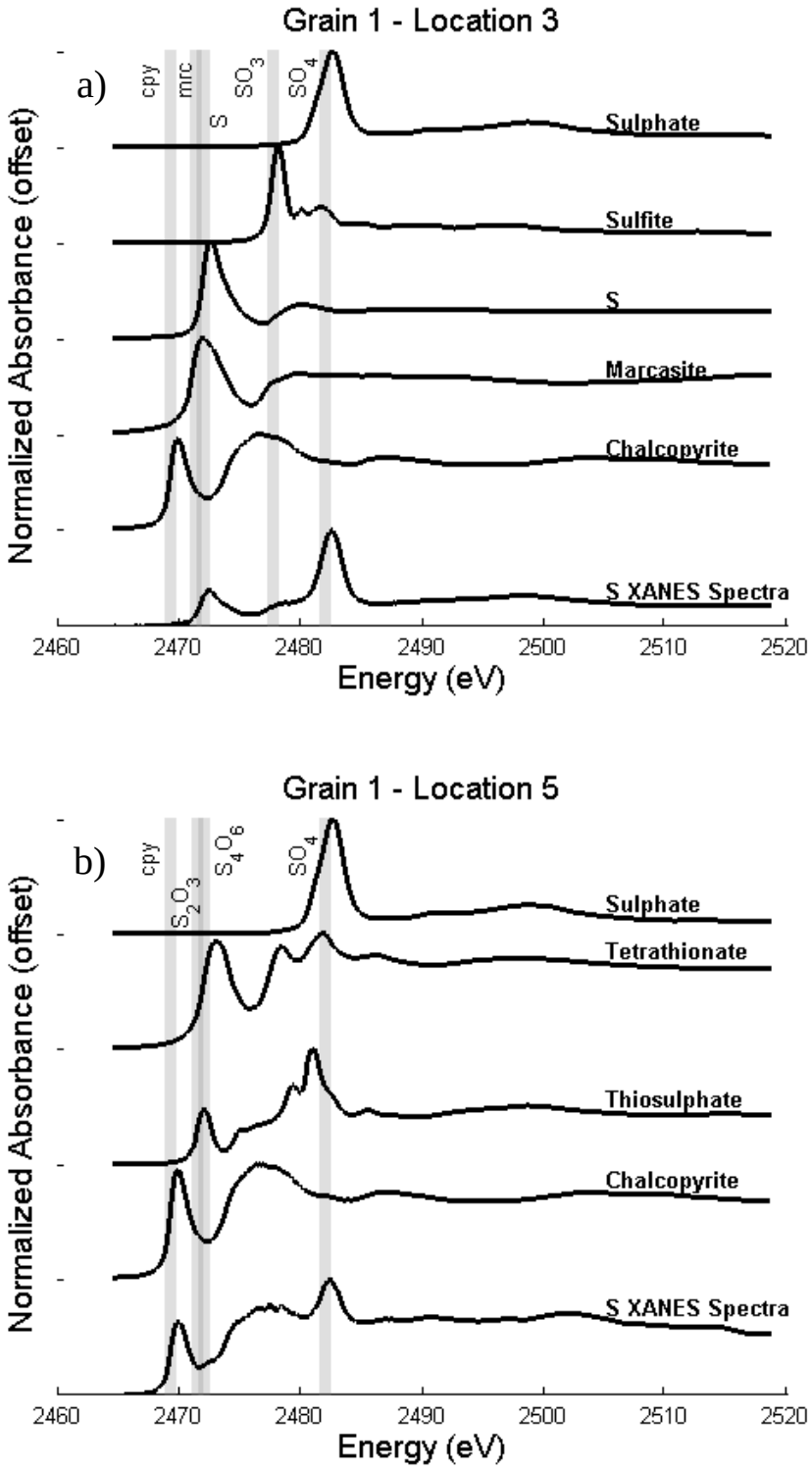

Figure 3-9 – Example S XANES for Grain 1 at a) location 3 and b) location 5. The XANES for the standards of the species that were identified through linear combination analysis are superimposed. The grey bar lines indicate the reference e0 values for the standards

Table 3-2 – Results of linear combination analysis for the sulfur speciation of grain 1. Plain text indicates the results for the normalised spectra, and bold text is for the derivative spectra

Location	Chalcopyrite	Pyrrhotite Troilite	Marcasite	Elemental S	Thiosulfate	Tetrathionate	Sulfite	Sulfate
S-1	1 / **1**	- / -	- / -	- / -	- / -	- / -	- / -	- / -
S-2	1 / **0.99**	- / -	- / -	- / -	- / -	- / -	- / -	- / -
S-3	0.1 / **0.04**	- / -	0.17 / **0.22**	0.38 / **0.36**	- / -	- / -	0.04 / **0.02**	0.31 / **0.35**
S-4	0.62 / **0.71**	- / -	- / -	- / **0.03**	0.1 / -	0.22 / **0.14**	- / -	0.07 / **0.1**
S-5	0.77 / **0.79**	- / **0.04**	- / -	- / **0.02**	0.06 / -	0.13 / **0.09**	- / -	0.04 / **0.06**
S-6	1 / **0.97**	- / **0.03**	- / -	- / -	- / -	- / -	- / -	- / -
S-7	- / -	- / -	- / **0.22**	0.61 / **0.49**	- / -	- / -	0.12 / **0.03**	0.27 / **0.26**
S-8	0.97 / **0.94**	- / **0.06**	- / -	- / -	- / -	0.03 / -	- / -	- / -
S-9	0.97 / **0.64**	- / **0.05**	- / -	- / **0.06**	- / -	0.03 / -	- / -	- / **0.25**
S-10	- / -	- / -	0.24 / **0.27**	0.69 / **0.6**	- / **0.09**	- / -	0.03 / -	0.03 / **0.03**
S-11	- / -	0.02 / -	0.16 / **0.27**	0.75 / **0.63**	- / **0.06**	- / -	0.03 / -	0.04 / **0.04**

plain text indicates the results for the normalised spectra, and bold text is for the derivative spectra

3.3.2 Sulfur and Iron Speciation of Grain 2

The SEM-EDX spectra for Grain 2 are very similar for the locations collected (Figure 3-10a to c). Peaks were identified at approximately 2,300keV and 6,400keV that are ascribed to S and Fe respectively (Figure 3-11a to c), and the magnitude of the Fe peak is approximately 55% of the S peak. These features are similar to the standard spectra for pyrrhotite (Figure 3-11d).

Figure 3-10 – Location of SEM-EDX spectra collection on grain 2

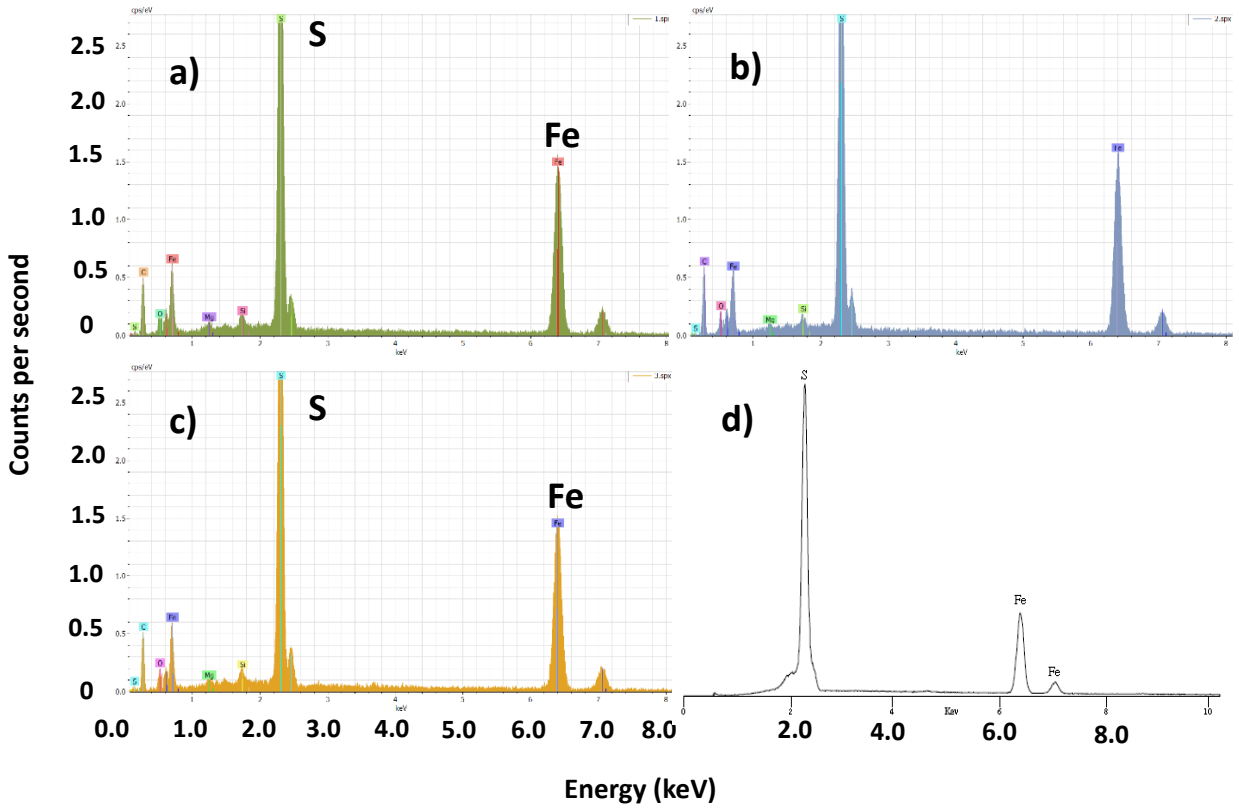

Figure 3-11 – SEM-EDX spectra for the unweathered part of grain 2, a) location 1, b) location 2 c) location 3, and d) reference spectra for chalcopyrite (modified from Severin, 2004)

Variable weathering is shown on the µ-XRF maps of Grain 2 (Figure 3-12a to c). Weathering is pronounced around the perimeter of the grain and the transition to fresh sulfide is quite sharp (circled area in Figure 3-12a). Some Fe and S was retained within the weathered rims, however more extensive loss of Cu and Zn is indicated. Some local enrichment of Cu is evident on the left hand edge.

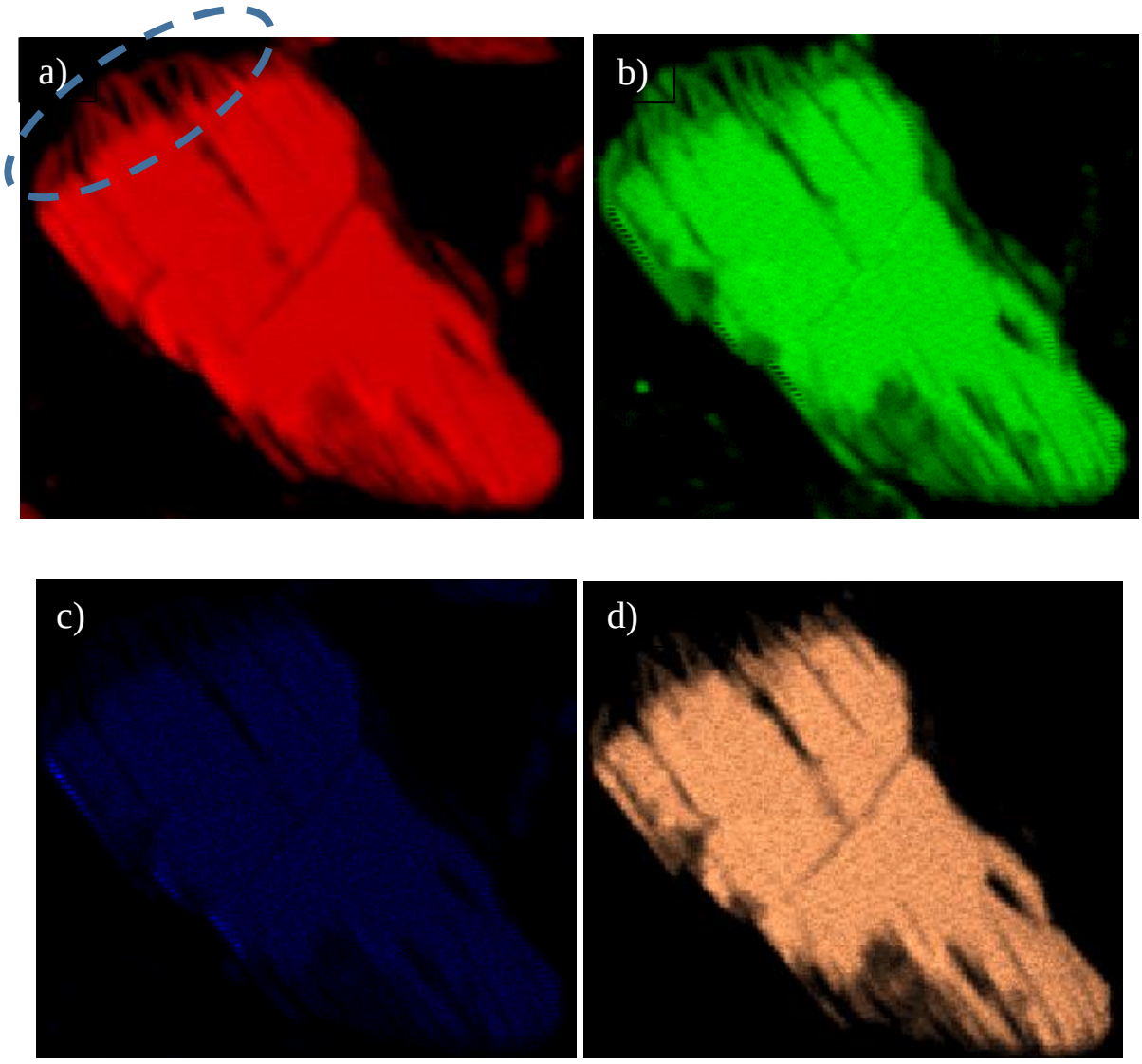

Figure 3-12 – Grain 2 µ-XRF maps showing the relative distribution of a) Fe b) S c) Zn and d) Cu over the grain. Encircled area in a) is a relatively weathered area that transitions quickly to a relatively unweathered area

A total of 18 locations were selected for XANES collection in the S absorbance range based on the map images, spread between the relatively fresh centre and around the weathered perimeter. (Figure 3-13).

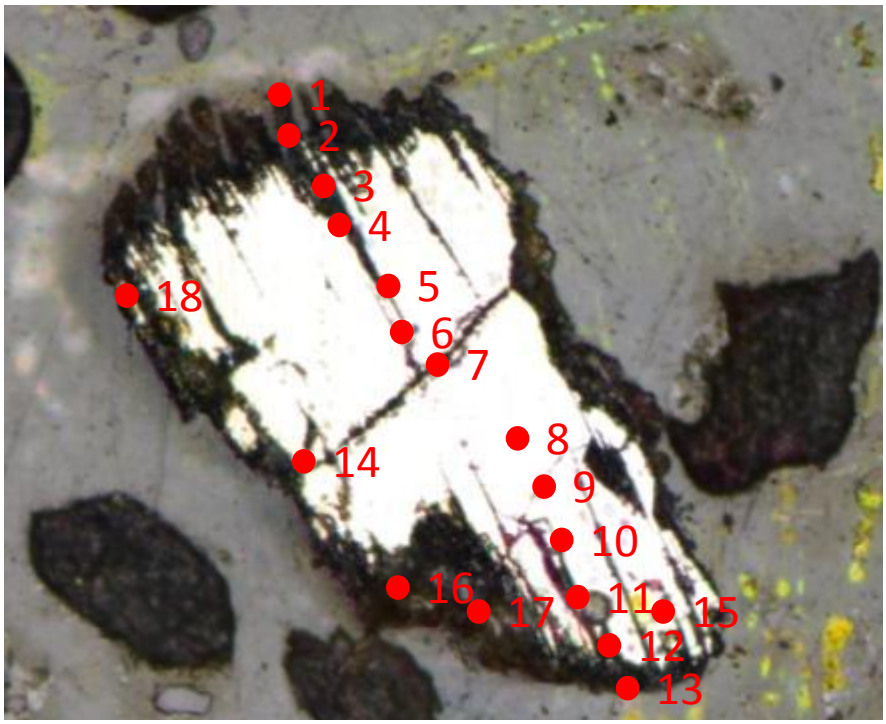

Figure 3-13 – Sulfur XANES testing locations

The spectra exhibited variable contributions of $CuFeS_2$, Fe_xS_{1-x}/FeS, FeS_2 (marcasite), $S_2O_3^{2-}$, $S_4O_6^{2-}$, SO_3^{2-} and SO_4^{2-} (Table 3-3). SEM results indicated that the grain is pyrrhotite, and the presence of chalcopyrite within the signal is likely due to penetration of the beam into the grain, which may be as far as 30µm (Prietzel et al., 2011). Locations 3 – 12 and 15 were on a relatively unweathered section of the grain and the signal was dominated by $CuFeS_2$ and $Fe_{1-x}S_x$. Locations 1, 2, 16 and 17 were near the weathered edge of the grain and $S_4O_6^{2-}$ was the principal component, accounting for more than 50% of the signal. The dominant species in the weathered areas of Grain 1 was S^0, although it is likely that its presence is representative of both S^0 and $S_4O_6^{2-}$. Locations 13 and 14 showed a high marcasite component to the signal, which was not observed at any other locations. The other S species were variable throughout the grain in minor quantities, less than 20%. Example XANES for the mineral are presented with the standard spectra of the identified species superimposed (Figure 3-14a and b).

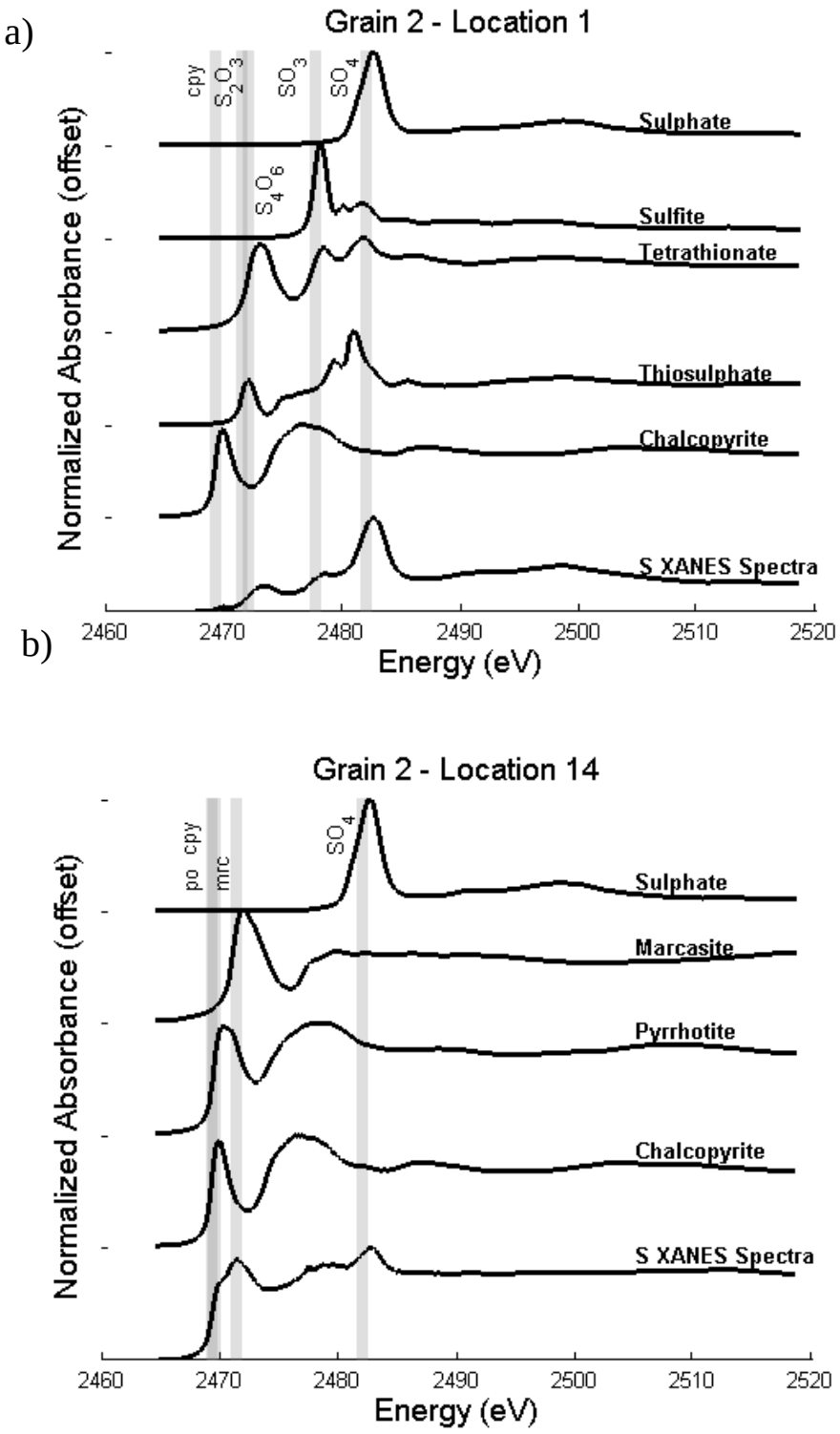

Figure 3-14 – Example sulfur XANES for grain 2 at a) location S-1 and b) location S-14. The XANES for the standards of the species that were identified through linear combination analysis are superimposed. The grey bar lines indicate the reference e0 values for the standards

The results of the linear combination analysis for the normalised and derivative spectra are generally within 15% for $CuFeS_2$, $Fe_{1-x}S_x$ /FeS, FeS_2 (marcasite), $S_4O_6^{2-}$, SO_3^{2-} and SO_4^{2-}, however $S_2O_3^{2-}$ was observed at six locations in the normalised spectra but not in the derivative spectra. It is not certain if the analysis method sufficiently differentiated this species from other species identified within both spectra.

Table 3-3 – Results of linear combination analysis for the sulfur speciation of grain 2. Plain text indicates the results for the normalised spectra, and bold text is for the derivative spectra

Location	Chalcopyrite	Pyrrhotite Troilite	Marcasite	Thiosulfate	Tetrathionate	Sulfite	Sulfate
S-1	0.17 / **0.18**	- / -	- / **0.09**	0.04 / -	0.56 / **0.54**	0.03 / **0.18**	0.2 / -
S-2	0.17 / **0.19**	- / -	- / **0.09**	0.07 / -	0.54 / **0.53**	0.04 / -	0.19 / **0.18**
S-3	0.42 / **0.35**	0.27 / **0.37**	0.21 / **0.18**	- / -	0.05 / **0.03**	0.06 / -	- / 0.07
S-4	0.37 / **0.36**	0.52 / **0.55**	0.12 / **0.09**	- / -	- / -	- / -	- / -
S-5	0.38 / **0.37**	0.54 / **0.58**	0.08 / **0.06**	- / -	- / -	- / -	- / -
S-6	0.37 / **0.37**	0.55 / **0.59**	0.08 / **0.05**	- / -	- / -	- / -	- / -
S-7	0.37 / **0.35**	0.49 / **0.54**	0.13 / **0.1**	- / -	- / -	- / -	- / -
S-8	0.39 / **0.35**	0.53 / **0.59**	0.08 / **0.06**	- / -	- / -	- / -	- / -
S-9	0.39 / **0.35**	0.52 / **0.6**	0.09 / **0.06**	- / -	- / -	- / -	- / -
S-10	0.39 / **0.35**	0.53 / **0.59**	0.09 / **0.06**	- / -	- / -	- / -	- / -
S-11	0.47 / **0.34**	0.32 / **0.53**	0.13 / **0.1**	0.06 / -	- / -	- / -	0.02 / **0.03**
S-12	0.4 / **0.35**	0.5 / **0.58**	0.1 / **0.07**	- / -	- / -	- / -	- / -
S-13	0.39 / **0.19**	- / **0.29**	0.28 / **0.27**	0.1 / -	0.16 / **0.17**	- / -	0.07 / **0.08**
S-14	0.14 / **0.14**	0.42 / **0.48**	0.42 / **0.34**	- / -	- / -	- / -	0.02 / **0.03**
S-15	0.41 / **0.35**	0.47 / **0.57**	0.11 / **0.08**	- / -	- / -	- / -	- / -
S-16	0.15 / **0.29**	- / -	- / **0.08**	0.21 / -	0.46 / **0.44**	0.02 / **0.02**	0.16 / **0.17**
S-17	0.14 / **0.3**	- / -	- / **0.09**	0.23 / -	0.47 / **0.43**	- / **0.02**	0.15 / **0.16**
S-18	0.43 / **0.34**	0.26 / **0.42**	0.14 / **0.13**	- / -	0.12 / **0.06**	- / -	0.05 / **0.06**

plain text indicates the results for the normalised spectra, and bold text is for the derivative spectra

A total of 13 locations were selected for collected of spectra in the Fe absorption range, mostly around the perimeter of the grain (Figure 3-15).

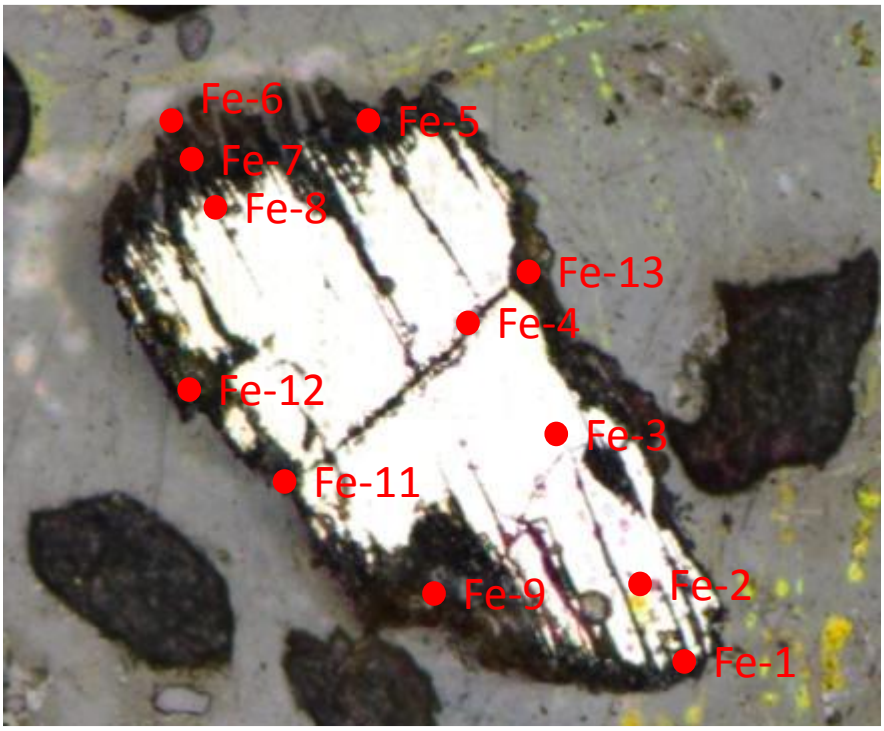

Figure 3-15 – Iron XANES testing locations

Analysis of the spectra for S could not differentiate pyrrhotite from troilite. However, the results of linear combination analysis for the Fe spectra indicate that the unweathered grain is troilite. The presence of Fe (oxyhydr)oxides around the perimeter of the grain would have been expected, however they were only identified at locations 6 and 7. Example XANES for the mineral are presented with the standard spectra of the identified species superimposed (Figure 3-16a and b).

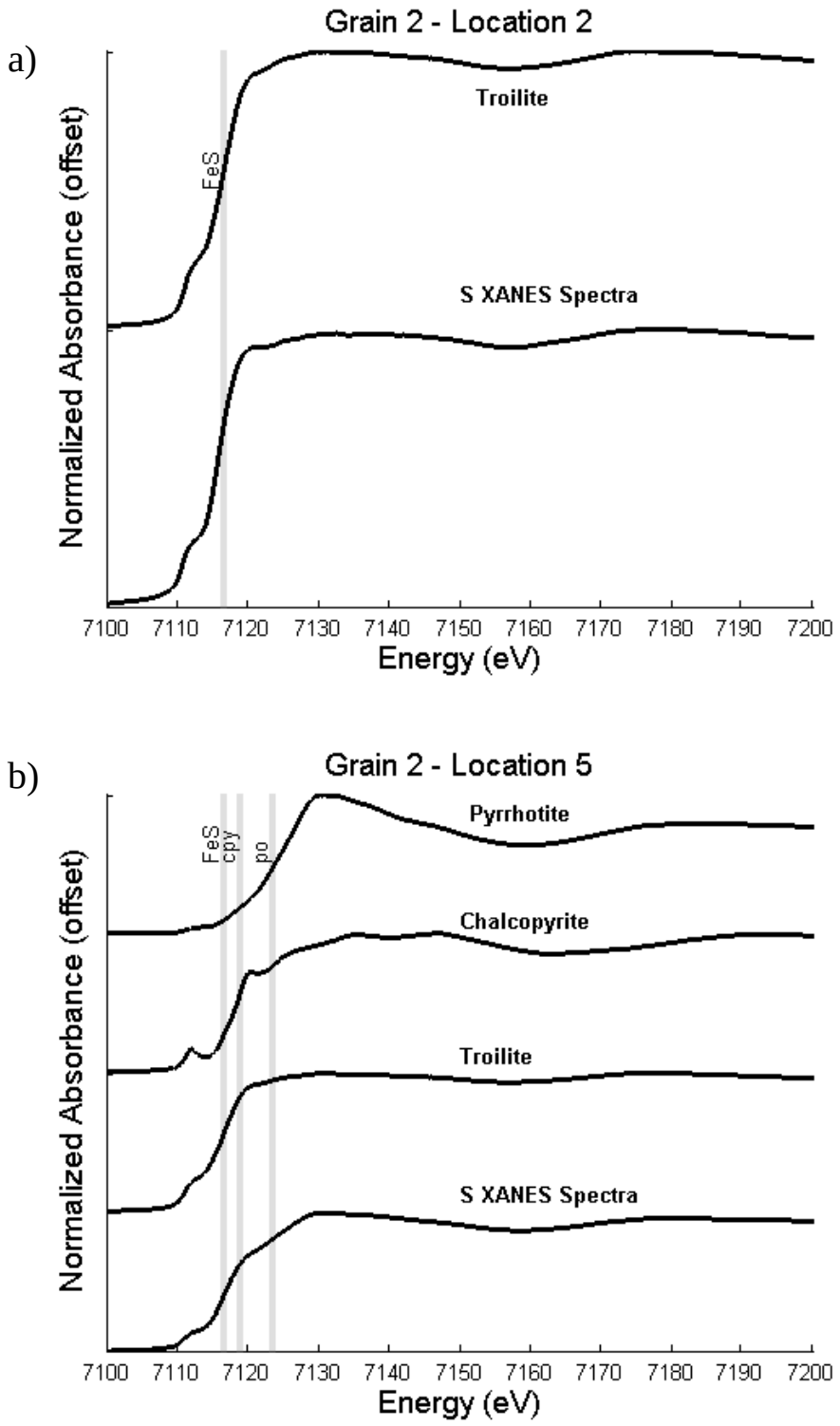

Figure 3-16 – Example sulfur XANES for grain 2 at a) location Fe-2 and b) location Fe-5. The XANES for the standards of the species that were identified through linear combination analysis are superimposed. The grey bar lines indicate the reference e0 values for the standards

The results of the linear combination analysis for the normalised and derivative spectra are generally within 15%, except for locations 7 and 9, where the ratio of the speciation differed significantly. The analysis results for the derivative spectra are more representative for location 7, as they are similar to that for the adjacent location 6. The analysis results for the normalised and derivative spectra for location 9 were not observed at any other location and it is not known which is representative.

Table 3-4 – Results of linear combination analysis for the iron speciation of grain 2

Location	**Troilite**	**Chalcopyrite**	**Pyrrhotite**	**Fe (oxyhydr)oxides**
Fe-1	0.87 / **1**	0.09 / -	0.04 / -	- / -
Fe-2	1 / **1**	- / -	- / -	- / -
Fe-3	1 / **1**	- / -	- / -	- / -
Fe-4	1 / **1**	- / -	- / -	- / -
Fe-5	0.57 / **0.71**	0.24 / **0.06**	0.19 / **0.23**	- / -
Fe-6	0.64 / **0.56**	- / -	- / -	0.36 / **0.44**
Fe-7	0.91 / **0.64**	- / -	- / -	0.09 / **0.36**
Fe-8	1 / **1**	- / -	- / -	- / -
Fe-9	0.05 / **0.18**	0.47 / **0.08**	0.46 / **0.73**	- / -
Fe-11	0.65 / **0.73**	0.13 / **0.03**	0.22 / **0.24**	- / -
Fe-12	0.98 / **1**	- / -	- / -	0.02 / -
Fe-13	0.92 / **0.98**	0.03 / -	0.05 / **0.02**	- / -

3.4 Summary

The synchrotron study illustrates the process of sulfide oxidation within the waste-rock piles at the Detour mine-site and illustrates similarities and differences between oxidation products observed by Langman et al. (2015). The Detour waste-rock contains a suite of sulfide minerals containing pyrrhotite, pyrite, chalcopyrite and covellite (McNeill, 2016) and the results of linear

combination analysis of S spectra indicate that variable $CuFeS_2$ (grain 1), Fe_xS_{1-x}/FeS, FeS_2 (marcasite), S^0, $S_2O_3^{2-}$, $S_4O_6^{2-}$, SO_3^{2-} and SO_4^{2-} are present in the solid form within the grains. Pyrrhotite is the principal sulfide mineral present within samples from Langman et al. (2015) and the same S species were identified, however $S_2O_3^{2-}$ was more frequently detected in that study than S^0 and $S_4O_6^{2-}$, which were more frequently detected at Detour.

The analysis of the S spectra was not able to differential pyrrhotite from troilite, however the analysis of the Fe spectra indicated that Grain 2 is predominately troilite, demonstrating the benefit of integrating S and Fe synchrotron analyses in accurate determination of sulfide mineralogy. Fe (oxyhydr)oxides were only identified at two select locations around the perimeter of the grain. The persistence of unoxidised Fe in visibly weathered areas with oxidised S species was unexpected.

The observation of variations in sulfide oxidation products can be used to inform numerical models developed to predict the rate of sulfide oxidation and release of ARD reaction products.

Chapter 4 – Conclusions and Recommendations

4.1 Summary

This study had two distinctive components, a field based study of gas transport mechanisms and rates through a covered waste-rock pile and a synchrotron-based study of the speciation of S and Fe as the ARD reaction goes to completion. The aim of both components was to improve the understanding of physical and chemical processes that affect the production of acid rock drainage, and will provide a foundation for improved predictive techniques. The two components were considered at different size scales, the field scale (hundreds of metres) for the gas transport studies and the single grain scale (micrometres) for the synchrotron studies.

The gas transport study involved field monitoring of air pressure and temperature on the exterior and interior of waste-rock pile WRS#3 and pore-gas O_2 and CO_2 concentration on the interior. Field monitoring indicated that subatmospheric O_2 levels are present within the pore space of the waste-rock pile and that O_2 levels are higher during the summer than the winter. Oxygen deficient conditions are desirable within waste-rock to inhibit the ARD reaction, and summertime conditions would therefore be the criteria for future design at Detour. Recorded data was used to prepare a calibrated gas transport model using the COMSOL, version 5.1, software package. Field measured pressures and temperatures on the outside of the pile were the boundary conditions and calibration of the model was conducted through a comparison of the field measured and model output pressures, temperatures and gas O_2/CO_2 concentrations on the interior of the pile. Numerical simulations indicated that the transport of O_2 through the system is primarily advective through the summer. The action of wind and temperature gradients provide the main supply of O_2 into the waste rock, and the effect barometric pressure fluctuations

comparatively minimal. The cover that is in place is helping to reduce O_2 ingress, and reducing the permeability of the cover will further reduce the O_2 content within the pore space.

The synchrotron studies identified chalcopyrite, pyrrhotite/troilite, marcasite, elemental S^0, thiosulfate, tetrathionate, sulfite and sulfate as the species of S within oxidising sulfide grains from Detour. Further study is required in this area of research to determine the role that the intermediate sulfur species play in the release of metals to the hydrosphere and to determine if they should be included them in reactive transport modelling for improved predictive accuracy.

4.2 Recommendations for Future Work

An improved understanding of gas transport and the pathway of the oxidation of S within the ARD reaction will lead to improvements in predictive simulations for the production of acid rock drainage in the waste-rock situation.

WRS#3 at the Detour mine-site is highly heterogeneous with respect to cover thickness and material properties for both the waste-rock and cover. Numerical simulations assumed a uniform thickness of 1m, however the actual thickness is more variable (McNeill, 2016). The role that the flaws and variations in the cover are playing in gas transport rates is not known, and additional insight may be attained with a more controlled system.

This field of research could be continued at other mine sites with the construction of suitably designed and constructed test piles, such as those constructed by Smith et al. (2013). Instrumentation was installed within those test piles as construction progressed, and this approach is recommended for future test piles to reduce the effect that the installation process (drilling) would have on the system for instrumentation installed in completed piles. Gas

transport simulations, similar to that carried out for this thesis, are recommended to quantify gas transport rates.

Synchrotron based research is recommended to map the locations of S species over the entirety of iron-sulfide grains. µ-XRF maps collected at specific energies that correspond with significant features of the XANES can be used to generate simplified ‘spectra’ for each map pixel using the absorbance for each pixel at each map energy. The speciation could then be calculated for each map pixel through linear combination theory and a speciation distribution map should be prepared. It will be of interest to produce these maps for oxidising sulfide grains over time, possibly years, and compare them with maps of the metals to understand the role that each species plays in the containment or release of metals to the hydrosphere. Ultimately, this information can be applied to reactive transport modelling to improve the accuracy of predictive simulations for the production of ARD and the release of metals to the hydrosphere.

References

Amos, R., Smith, L., Neuner, M., Gupton, M., Blowes, D., Smith, L. & Sego, D., 2009. Diavik waste rock project: oxygen transport in covered and uncovered piles. In: Proceedings International Conference on Acid Rock Drainage (ICARD) Skellefteå, 8th, Sweden, 22-26 June, 2009.

Amos, R. T., Blowes, D. W., Bailey, B. L., Sego, D. C., Smith, L. & Ritchie, A. I. M., 2015. Waste-rock hydrogeology and geochemistry. Applied Geochemistry 57, 140-156.

Amos, R. T., Blowes, D. W., Smith, L. & Sego, D. C., 2009. Measurement of wind-induced pressure gradients in a waste rock pile. Vadose Zone Journal 8(4), 953-962.

Anne, R. & Pantelis, G., 1997. Coupled natural convection and atmospheric wind forced advection in above ground reacting heaps. In: International Conference on Computational Fluid Dynamics in Mineral and Metal Processing and Power Generation. Melbourne, Australia, 3–4 July, 1997. CSIRO, Australia, pp. 453–458.

Auer, L., Rosenberg, N., Birdsell, K. & Whitney, E., 1996. The effects of barometric pumping on contaminant transport. Journal of Contaminant Hydrology 24(2), 145-166.

Bear, J., 1972. Dynamics of fluids in porous media. Dover Publications, Inc.

Belzile, N., Chen, Y.-W., Cai, M.-F. & Li, Y., 2004. A review on pyrrhotite oxidation. Journal of Geochemical Exploration 84(2), 65-76.

Binning, P. J., Postma, D., Russell, T., Wesselingh, J. & Boulin, P., 2007. Advective and diffusive contributions to reactive gas transport during pyrite oxidation in the unsaturated zone. Water Resources Research 43(2).

Bird, R. B., Stewart, W. E. & Lightfoot, E. N., 1960. Transport Phenomena. John Wiley & Sons.

Birkham, T. K., Hendry, M. J., Wassenaar, L., Mendoza, C. A. & Lee, E. S., 2003. Characterizing geochemical reactions in unsaturated mine waste-rock piles using gaseous O2, CO2, 12CO2, and 13CO2. Environmental Science & Technology 37(3), 496-501.

Blowes, D.W., 2016. Personal communication.

Blowes, D.W., Ptacek, C.J., Jambor, J.L.,Weisener, C.G., 2003. The geochemistry of acidmine drainage. In: Lollar, B.S. (Ed.), Environmental Geochemistry. Treatise on Geochemistry 9. Elsevier-Pergamon, pp. 149–204.

Cash, A., 2014. Structural and Hydrologic Characterization of Two Historic Waste Rock Piles (Master's thesis, University of Alberta). Unpublished.

Center for Advanced Radiation Sources. http://cars.uchicago.edu/xaslib/search (accessed March, 2016).

Chi, X., Amos, R. T., Stastna, M., Blowes, D. W., Sego, D. C. & Smith, L., 2013. The Diavik Waste Rock Project: implications of wind-induced gas transport. Applied geochemistry 36, 246-255.

COMSOL Multiphysics® v. 5.1. Stockholm, Sweden: COMSOL AB, 2015.

Detour Gold Corporation, 2010. Technical Report: Feasibility Study of the Detour Lake Project, Ontario for Detour Gold Corporation. Retrieved from http://www.detourgold.com/files/doc_downloads/Detour_Gold_Corporation_Technical_Report_2010.pdf .

Detour Gold Corporation, 2012. Projects – At a Glance. Retrieved July 2016, from Detour Gold: http://www.detourgold.com/projects/at-a-glance/default.aspx

Druschel, G. K., Hamers, R. J. & Banfield, J. F., 2003. Kinetics and mechanism of polythionate oxidation to sulfate at low pH by O 2 and Fe 3+. Geochimica et Cosmochimica Acta 67(23), 4457-4469.

Elberling, B., Larsen, F., Christensen, S. & Postma, D., 1998. Gas transport in a confined unsaturated zone during atmospheric pressure cycles. Water Resources Research 34(11), 2855-2862.

Elliott, D. F. & Rao, K. R., 1983. Fast transforms algorithms, analyses, applications. Elsevier.

Fleet, M. E., 2005. XANES spectroscopy of sulfur in earth materials. The Canadian Mineralogist 43(6), 1811-1838.

Garvie, A., Bennett, J. & Ritchie, A. I. M., 1997. Quantifying the spatial dependence of the sulfide oxidation rate in a waste rock dump at Mt Lyell, Tasmania. In: Proc. of the Fourth Int. Conf. on Acid Rock Drainage, Vancouver, BC, Canada, Vol. 30.

Google Maps., 2016. Retrieved July 17, 2106, from https://www.google.ca/maps/@50.0246795,-79.6869435,4660m/data=!3m1!1e3

Harries, J. & Ritchie, A. I. M., 1981. The use of temperature profiles to estimate the pyritic oxidation rate in a waste rock dump from an opencut mine. Water, Air, and Soil Pollution 15(4), 405-423.

Harries, J. & Ritchie, A. I. M., 1987. The effect of rehabilitation on the rate of oxidation of pyrite in a mine waste rock dump. Environmental Geochemistry and Health 9(2), 27-36.

ID21 Sulfur XANES Spectra Database of European Synchrotron Radiation Facility, 2014. http://www.esrf.eu/UsersAndScience/Experiments/Imaging/ID21/php (accessed November, 2014).

Internation X-ray Absorption Society, 2008. http://ixs.iit.edu/database/ (accessed March 2016).

Janzen, M. P., Nicholson, R. V. & Scharer, J. M., 2000. Pyrrhotite reaction kinetics: reaction rates for oxidation by oxygen, ferric iron, and for nonoxidative dissolution. Geochimica et Cosmochimica Acta 64(9), 1511-1522.

Jambor, J. L., Nordstrom, D. K. & Alpers, C. N., 2000. Metal-sulfate salts from sulfide mineral oxidation. Reviews in Mineralogy and Geochemistry 40(1), 303-350.

Jambor J. L., 2003 Mine-waste mineralogy and mineralogical perspectives of acid—base accounting. In Environmental Aspects of Mine Wastes (eds. J. L. Jambor, D. W. Blowes, and A. I. M. Ritchie). Mineralogical Association of Canada 31, 117–145.

Johnson, R., Blowes, D., Robertson, W. & Jambor, J., 2000. The hydrogeochemistry of the Nickel Rim mine tailings impoundment, Sudbury, Ontario. Journal of Contaminant Hydrology 41(1), 49-80.

Kim, H. & Benson, C. H., 2004. Contributions of advective and diffusive oxygen transport through multilayer composite caps over mine waste. Journal of Contaminant Hydrology 71(1), 193-218.

Lahmira, B., Lefebvre, R., Hockley, D. & Phillip, M., 2014. Atmospheric Controls on Gas Flow Directions in a Waste Rock Dump. Vadose Zone Journal 13(10).

Langman, J.B., Blowes, D.W., Veeramani, H., Wilson, D., Smith, L., Sego, D.C., Paktunc, D., 2015. The mineral and aqueous phase evolution of sulfur and nickel with weathering of pyrrhotite in a low sulfide, granitic waste rock. Chemical Geology 401, 169–179.

Leaver, J. D. & Unsworth, C. P., 2007. Fourier analysis of short-period water level variations in the Rotorua geothermal field, New Zealand. Geothermics 36(6), 539-557.

Lee, E.S., Hendry, M.J., Hollings,P., 2003. Use of O2 consumption and CO2 production in kinetic cells to delineate pyrite oxidation– carbonate buffering and microbial respiration in unsaturated media. Journal of Contaminant Hydrology 65, 203– 217.

Lefebvre, R., Hockley, D., Smolensky, J. & Gélinas, P., 2001a. Multiphase transfer processes in waste rock piles producing acid mine drainage: 1: Conceptual model and system characterization. Journal of Contaminant Hydrology 52(1), 137-164.

Lefebvre, R., Hockley, D., Smolensky, J. & Lamontagne, A., 2001b. Multiphase transfer processes in waste rock piles producing acid mine drainage: 2. Applications of numerical simulation. Journal of Contaminant Hydrology 52(1), 165-186.

Levenspiel, O., 1972. Non-ideal flow. Chemical Reaction Engineering 2, 254-325.

Li, D., Bancroft, G., Kasrai, M., Fleet, M., Yang, B., Feng, X., Tan, K. & Peng, M., 1994. Sulfur K-and L-edge X-ray absorption spectroscopy of sphalerite, chalcopyrite and stannite. Physics and Chemistry of Minerals 20(7), 489-499.

Lindsay, M.B.J., 2016. Personal communication.

Linklater, C. M., Sinclair, D. J. & Brown, P. L., 2005. Coupled chemistry and transport modelling of sulphidic waste rock dumps at the Aitik mine site, Sweden. Applied Geochemistry 20(2), 275-293.

Lowson, R. T., 1982. Aqueous oxidation of pyrite by molecular oxygen. Chemical Reviews 82(5), 461-497.

Lundgren, T., 2001. The dynamics of oxygen transport into soil covered mining waste deposits in Sweden. Journal of Geochemical Exploration 74(1), 163-173.

Massmann, J. & Farrier, D. F., 1992. Effects of atmospheric pressures on gas transport in the vadose zone. Water Resources Research 28(3), 777-791.

MathWorks, 2016. Fast Fourier Transform. Retrieved January, 2016, from Mathworks: http://www.mathworks.com/help/matlab/ref/fft.html

McNeill, B., 2016. Geochemical and microbiological characterization of the historic waste rock piles at the Detour Lake gold mine (Master's thesis, University of Waterloo). Unpublished.

Molson, J., Fala, O., Aubertin, M. & Bussière, B., 2005. Numerical simulations of pyrite oxidation and acid mine drainage in unsaturated waste rock piles. Journal of Contaminant Hydrology 78(4), 343-371.

Morra, M. J., Fendorf, S. E. & Brown, P. D., 1997. Speciation of sulfur in humic and fulvic acids using X-ray absorption near-edge structure (XANES) spectroscopy. Geochimica et Cosmochimica Acta 61(3), 683-688.

Moses, C. O., Nordstrom, D. K. & Mills, A. L., 1984. Sampling and analysing mixtures of sulphate, sulphite, thiosulphate and polythionate. Talanta 31(5), 331-339.

Nield, D. A. & Bejan, A., 2013. Convection in porous media. Springer Science & Business Media.

Nordstrom D.K. and Munoz J. L., 1994. Geochemical Thermodynamics, 2nd ed. Blackwell.

Nordstrom, D. K. & Southam, G., 1997. Geomicrobiology of sulfide mineral oxidation. Reviews in Mineralogy 35, 361-390.

O'day, P. A., Rivera, N., Root, R. & Carroll, S. A., 2004. X-ray absorption spectroscopic study of Fe reference compounds for the analysis of natural sediments. American Mineralogist 89(4), 572-585.

O'kane, M., Wilson, G. & Barbour, S., 1998. Instrumentation and monitoring of an engineered soil cover system for mine waste rock. Canadian Geotechnical Journal 35(5), 828-846.

Pantelis, G. & Ritchie, A. I. M., 1992. Rate-limiting factors in dump leaching of pyritic ores. Applied Mathematical Modelling 16(10), 553-560.

Pantelis, G., Ritchie, A. I. M. & Stepanyants, Y., 2002. A conceptual model for the description of oxidation and transport processes in sulphidic waste rock dumps. Applied Mathematical Modelling 26(7), 751-770.

Pham, N. H., 2013. Heat Transfer in Waste-Rock Piles Constructed in a Continuous Permafrost Region (PhD thesis, University of Alberta). Unpublished.

Prange, A., Chauvistrй, R., Modrow, H., Hormes, J., Trüper, H. G. & Dahl, C., 2002. Quantitative speciation of sulfur in bacterial sulfur globules: X-ray absorption spectroscopy reveals at least three different species of sulfur. Microbiology 148(1), 267-276.

Pratt, A. R. & Nesbitt, H. W., 1997. Pyrrhotite leaching in acid mixtures of HCl and H2SO4. American Journal of Science 297(8), 807-828.

Prietzel, J., Thieme, J., Eusterhues, K. & Eichert, D., 2007. Iron speciation in soils and soil aggregates by synchrotron-based X-ray microspectroscopy (XANES, μ-XANES). European Journal of Soil Science 58(5), 1027-1041.

Prietzel, J., Botzaki, A., Tyufekchieva., N., Brettholle, M., Thieme, J. & Wantana, K., 2011. Speciation in Soil by S K-Edge XANES Spectroscopy: Comparison of Spectral Deconvolution and Linear Combination Fitting. Environmental Science & Technology 45, 2878–2886.

Ravel, B. & Newville, M., 2005. ATHENA, ARTEMIS, HEPHAESTUS: Data analysis for X-ray absorption spectroscopy using IFEFFIT, J. Synchrotron Radiat. 12, 537–541.

Ritchie, A. I. M., 1994. Sulfide oxidation mechanisms: controls and rates of oxygen transport. The Environmental Geochemistry of Sulfide Mine Wastes 201-245.

Ritchie, A. I. M., 2003. Oxidation and gas transport in piles of sulfidic material. Environmental Aspects of Mine Wastes, Short Course 31, 73-94.

Ritchie, A. I. M. & Miskelly, P. (2000). Geometric and physico-chemical properties determining sulfide oxidation rates in waste rock dumps. In Proceedings of the 5th International Conference on Acid Rock Drainage, ICARD-2000, Denver, CO. May 21–24, 2000. Society for Mining, Metallurgy, and Exploration Inc., Littleton, Colorado, USA, pp. 277–287.

Scanlon, B. R., Nicot, J. P. & Massmann, J. W., 2002. Soil gas movement in unsaturated systems. Soil Physics Companion, CRC Press, 297-341.

Severin, K. P., 2004. Energy dispersive spectrometry of common rock forming minerals. Springer.

Singurindy, O., Lorca, M., Peterson, H., Hirsche, T., Javadi, M., Blackmore, S., Aranda, C., Mayer, K., Beckie, R. & Smith, L., 2012. Spatial and temporal variations of O2 and CO2 pore gas concentrations in an experimental waste rock pile at the Antamina mine, Peru. In: Proceedings International Conference on Acid Rock Drainage (ICARD) Ottawa, 9th, Canada, 20-24 May, 2012.

Smith, L., 2016. Personal communication.

Smith, L. J., Moncur, M. C., Neuner, M., Gupton, M., Blowes, D. W., Smith, L. & Sego, D. C., 2013. The Diavik Waste Rock Project: Design, construction, and instrumentation of field-scale experimental waste-rock piles. Applied Geochemistry 36, 187-199.

Smolensky, J., Hockley, D., Lefebvre, R. & Paul, M., 1999. Oxygen transport processes in the Nordhalde of the Ronnenburg mining district, Germany. Proceedings Mining and the Environment II 1999, 271-280.

Stade, E., 2011. Fourier analysis, Vol. 109. John Wiley & Sons.

Suzuki, I., 1999. Oxidation of inorganic sulfur compounds: chemical and enzymatic reactions. Canadian Journal of Microbiology 45(2), 97-105.

NOAA., NASA., & USAF., 1976. US standard atmosphere.

Wunderly, M,D., Blowes, D.W., Frind, E.O., Ptacek, C.J., 1996. Sulfide mineral oxidation and subsequent reactive transport of oxidation products in mine tailings impoundments: A numerical model. Water Resources Research 32(10), 3173-3187.

Appendix A

Data Plots for Field Monitoring of Gas Transport at WRS#3

Appendix A contains the analysis plots of the field monitoring data at WRS#3, discussed in Chapter 2. Example plots were generally included in the main text. The following plots are included:

- Figure A2 : Time series for wind speed;
- Figure A3 : Time series for barometric pressure;
- Figure A4 – A5 : Time series for external differential pressure;
- Figure A6 – A7 : Time series for internal differential pressure;
- Figure A8 – A9 : Time series for internal temperature;
- Figure A10 – A11 : Time series for pore gas O_2 content;
- Figure A12 – A13 : Time series for pore gas CO_2 content;
- Figure A14 – A17 : Discrete Fourier transform for external pressure;
- Figure A18 – A21 : Discrete Fourier transform for internal pressure;
- Figure A22 – A25 : Discrete Fourier transform for internal temperature;
- Figure A26 – A27 : Discrete Fourier transform for pore gas O_2 content;
- Figure A28 – A29 : Discrete Fourier transform for pore gas CO_2 content;
- Figure A30 – A33 : Correlation plot for wind speed versus external pressure;
- Figure A34 – A37 : Correlation plot for wind speed versus internal pressure;
- Figure A38 – A57: Correlation plot for external pressure versus internal pressure;
- Figure A58 – A59: Correlation plot for internal pressure versus the location immediately below;
- Figure A60 : Correlation plot for internal pressure versus the location horizontally adjacent;
- Figure A61 : Correlation plot for ambient temperature versus internal temperature;

- Figure A62 – A63 : Correlation plot for pore gas O_2 content versus the location immediately below;
- Figure A64 : Correlation plot for pore gas O_2 content versus the location horizontally adjacent; and
- Figure A65 – A66 : Correlation plot for pore gas O_2 content versus CO_2 content.

For reference, the location of the external and internal monitoring locations are shown on Figure A-1a and b.

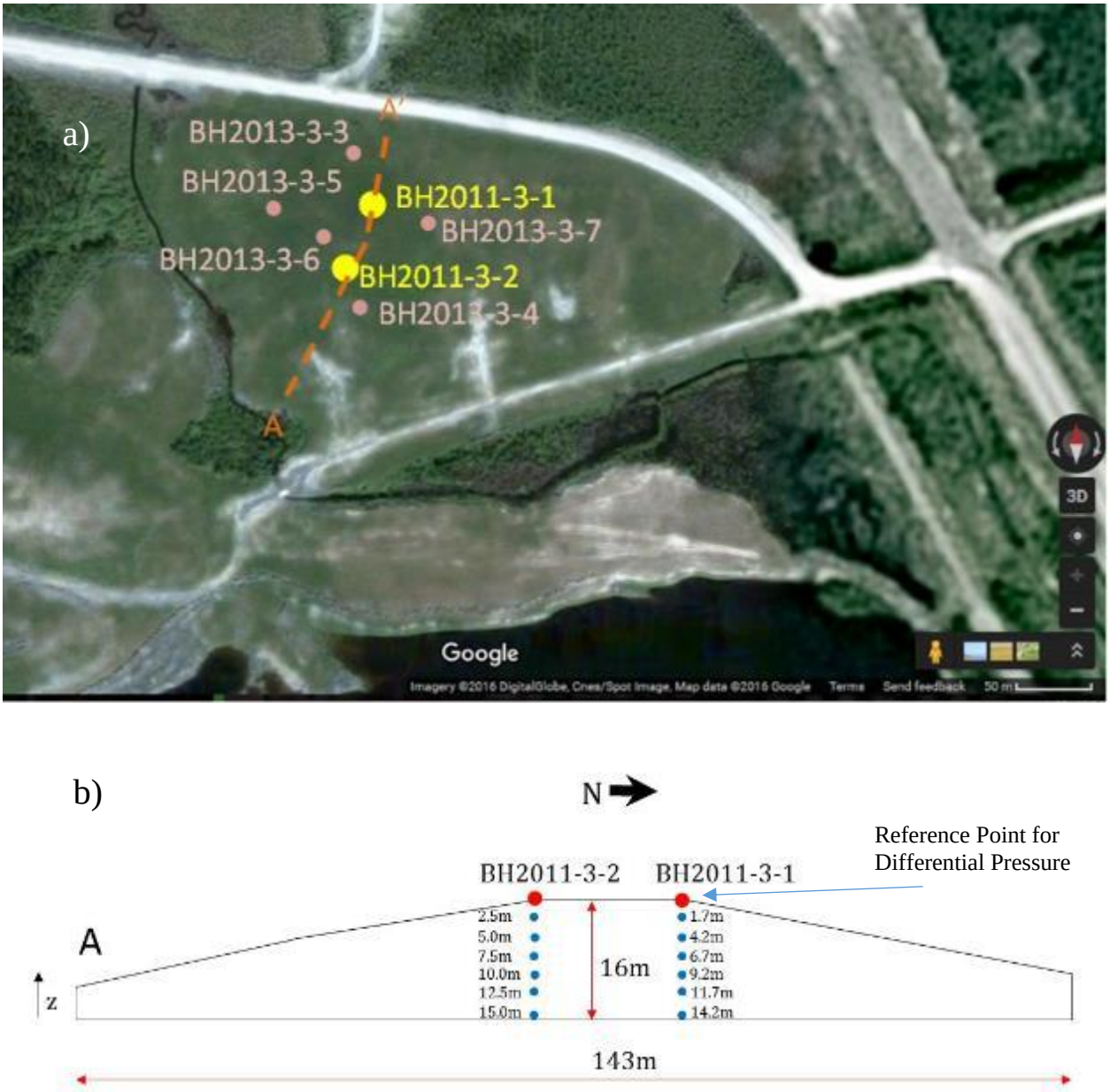

Figure A-1 – a) Location of boreholes BH2011-3-1 and BH2011-3-2 and test-pits BH2013-3-3 to BH2011-3-7 on WRS#3 (Modified From Google Maps, 2016) b) cross section along A-A'

Time series for wind speed

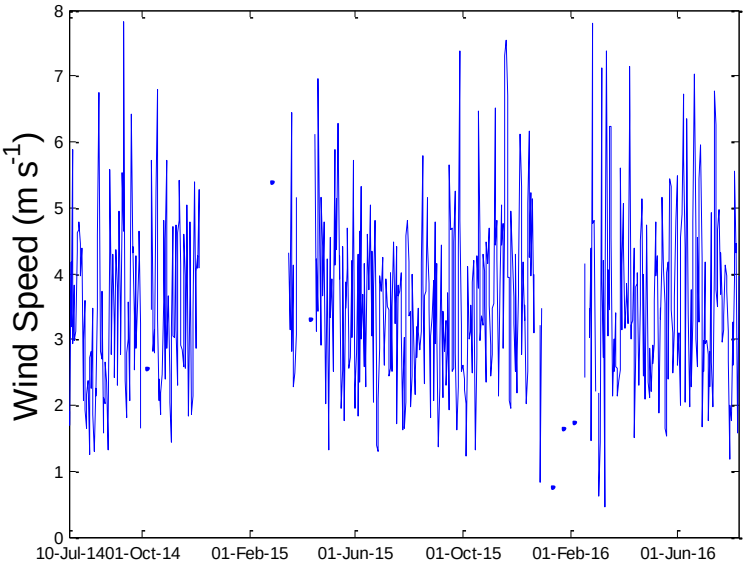

Figure A-2 – Time series for wind speed, measured at the crest of WRS#3. Daily averaged data

Time series for barometric pressure

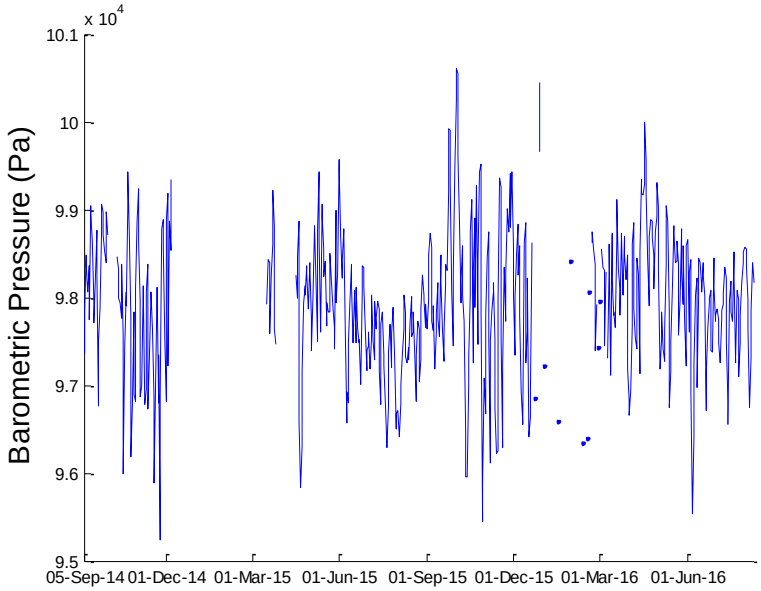

Figure A-3 – Time series for barometric pressure, measured at the crest of WRS#3. Daily averaged data

Time series for external pressure

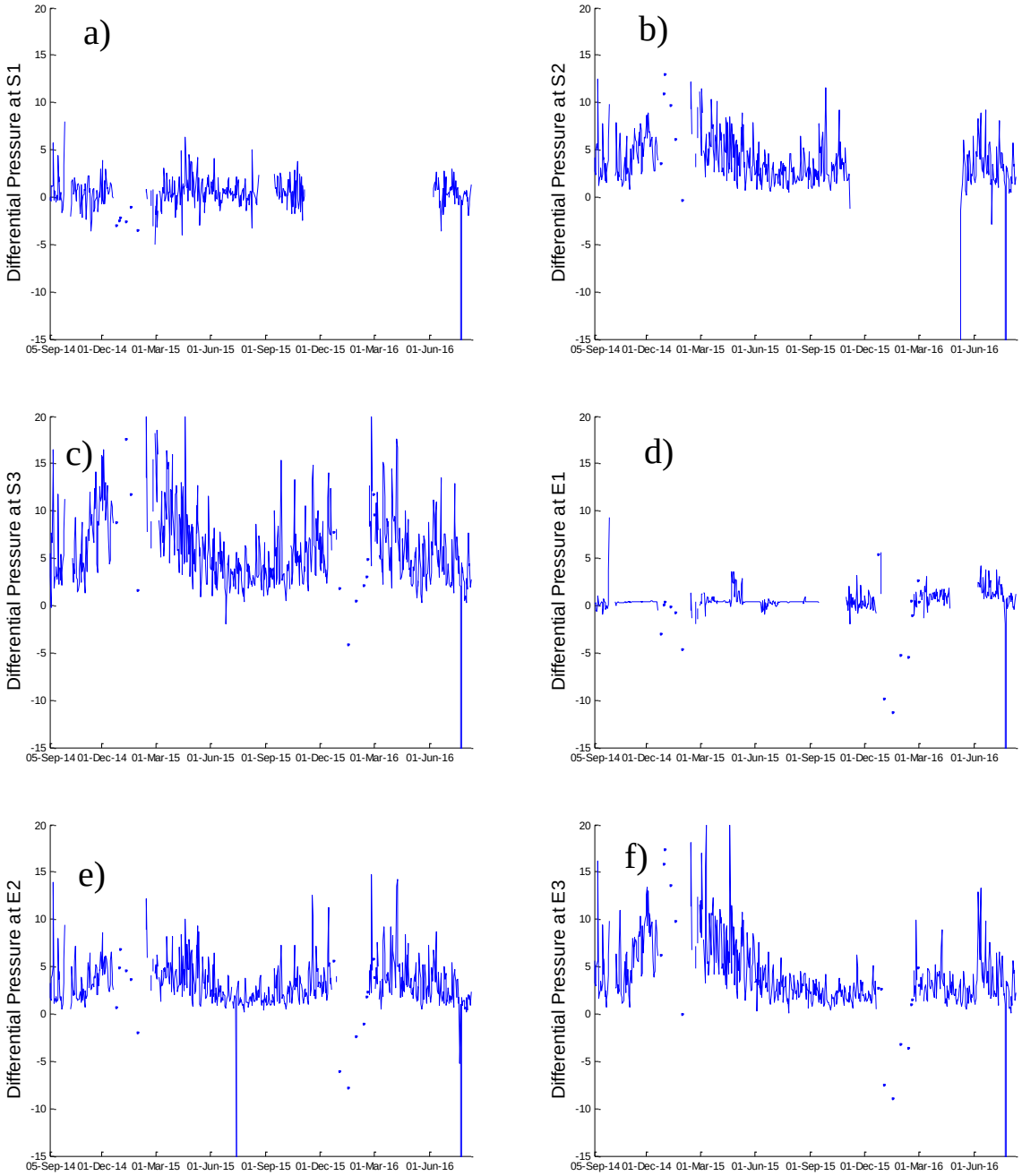

Figure A-4 – Time series for external differential pressure. Daily averaged data at a) S1 b) S2 c) S3 d) E1 e)E2 and f) E3

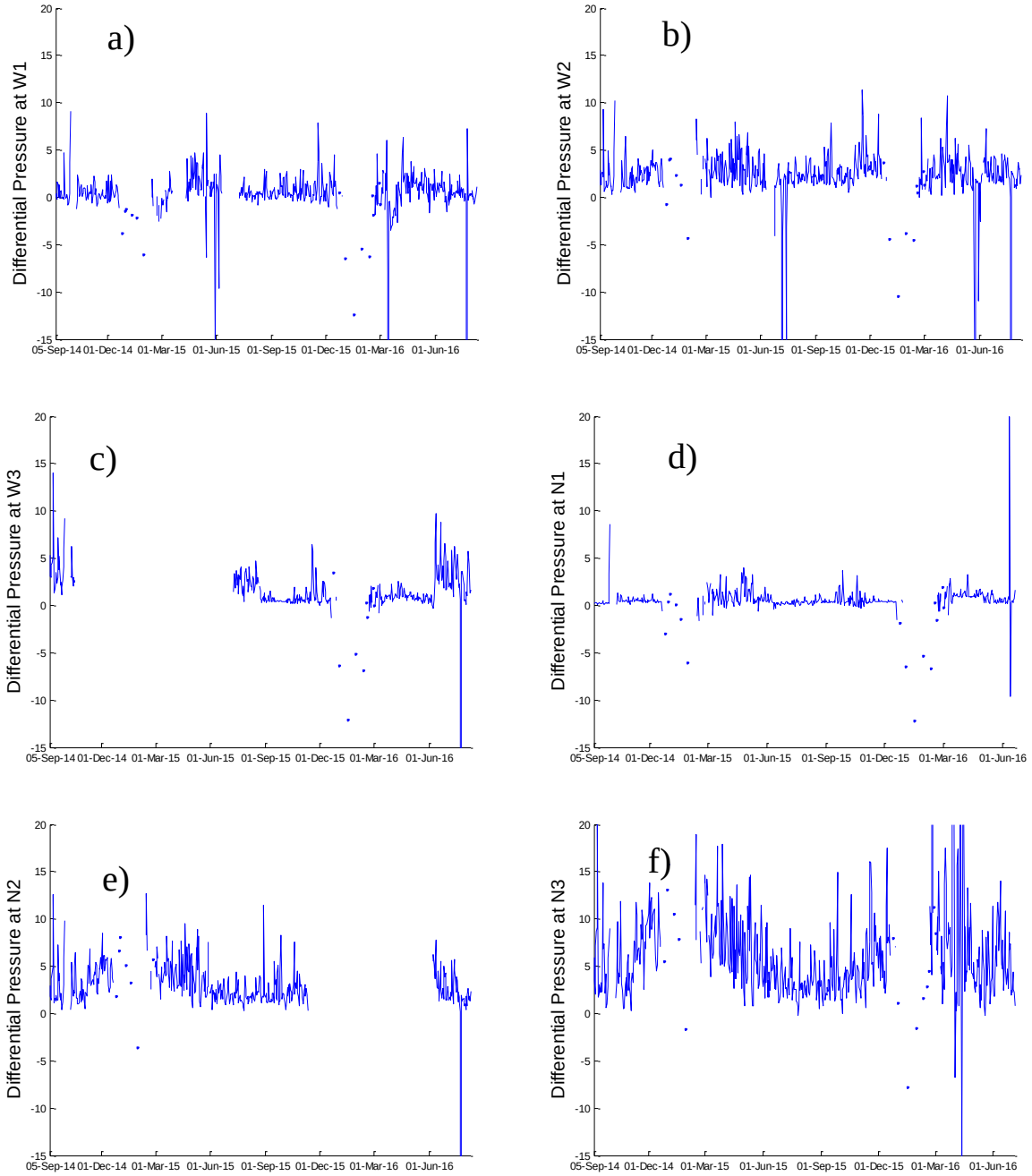

Figure A-5 – Time series for external differential pressure. Daily averaged data at a) W1 b) W2 c) W3 d) N1 e) N2 f) N3

Time series for internal pressure

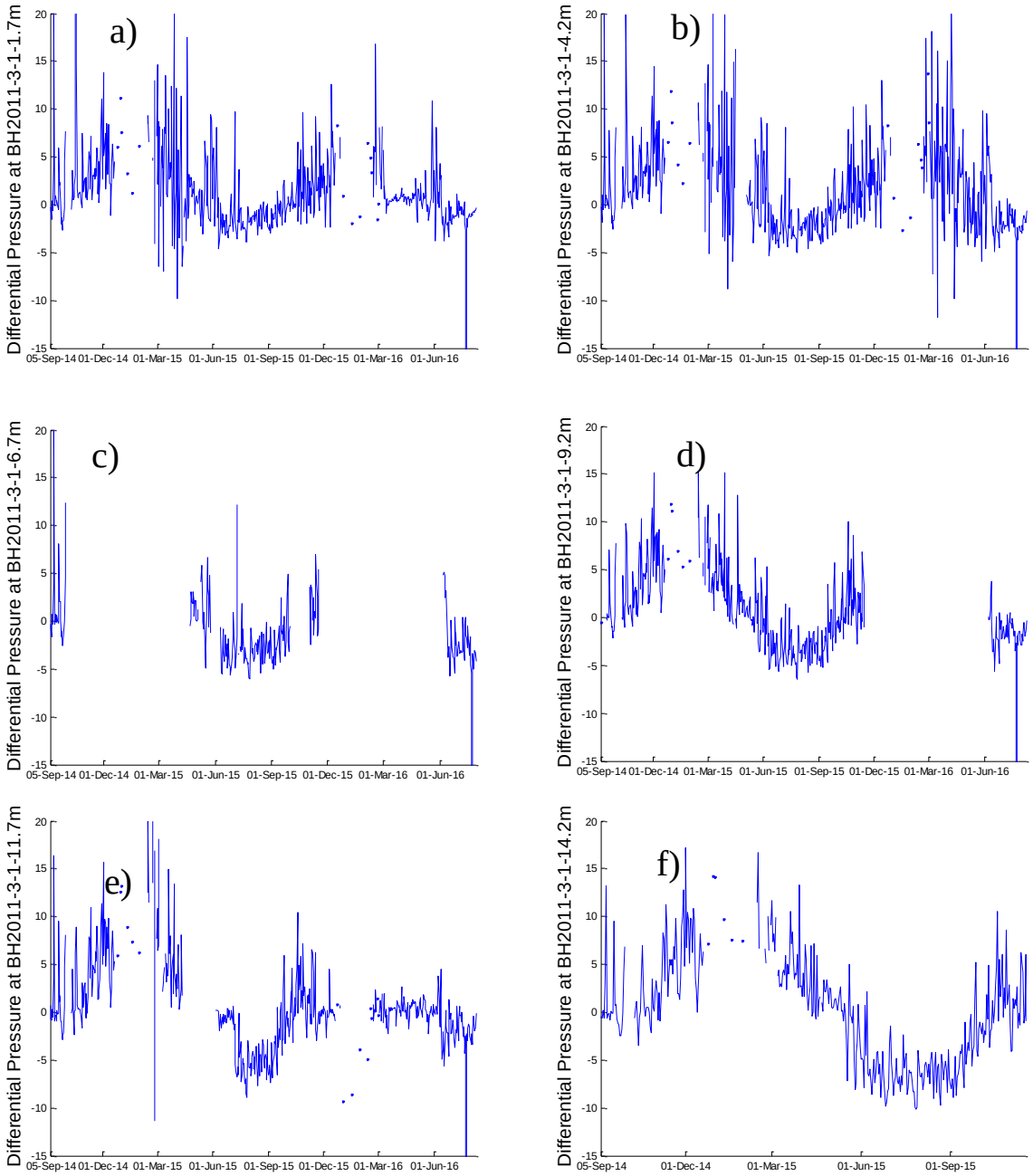

Figure A-6 – Time series for internal differential pressure. Daily averaged data at a) BH2011-3-1-1.7m b) BH2011-3-1-4.2m c) BH2011-3-1-6.7m d) BH2011-3-1-9.2m e) BH2011-3-1-11.7m f) BH2011-3-1-14.2m

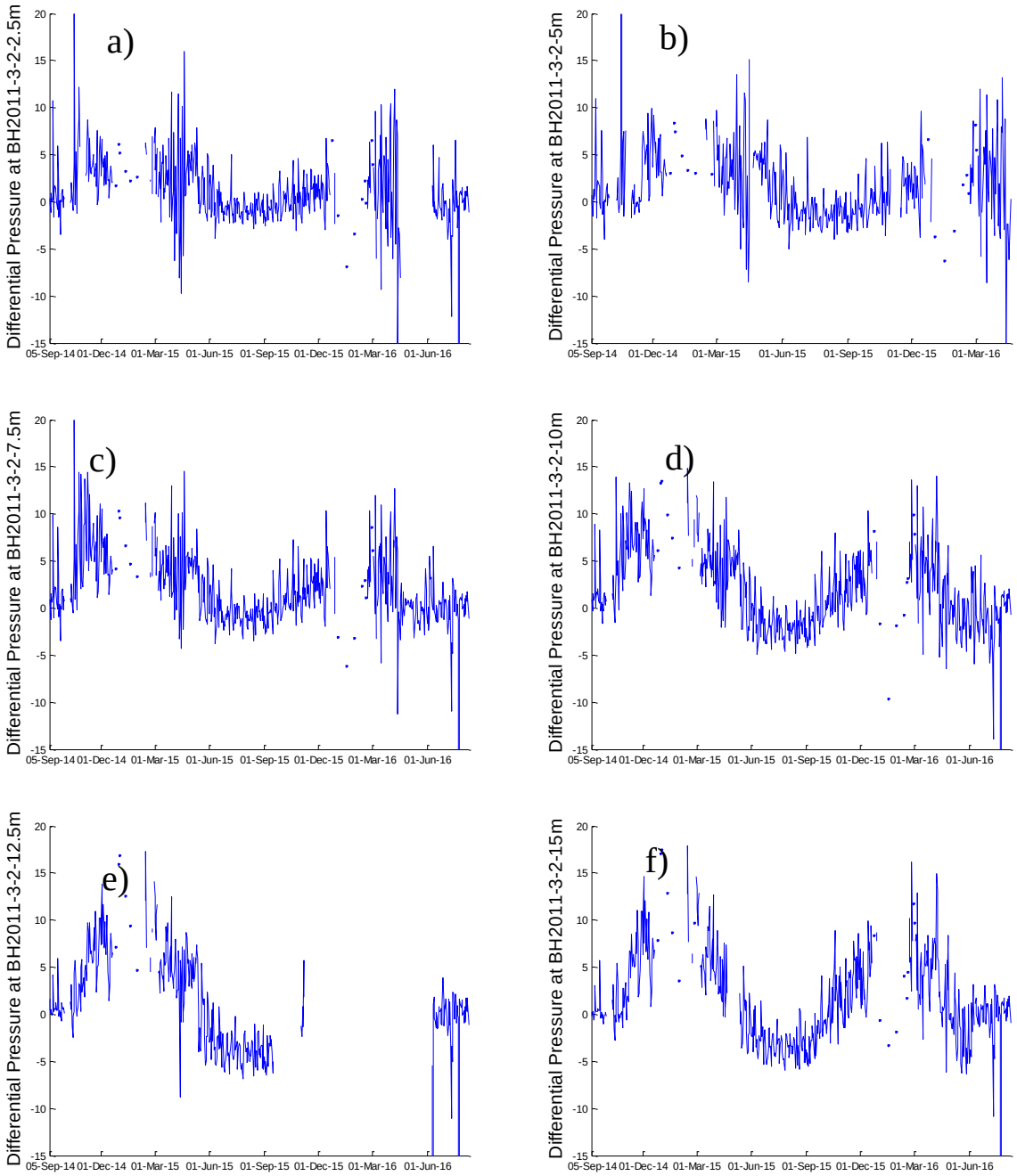

Figure A-7 – Time series for internal differential pressure. Daily averaged data at a) BH2011-3-2-2.5m b) BH2011-3-2-5m c) BH2011-3-2-7.5m d) BH2011-3-2-10m e) BH2011-3-2-12.5m f) BH2011-3-2-15m

Time series for internal temperature

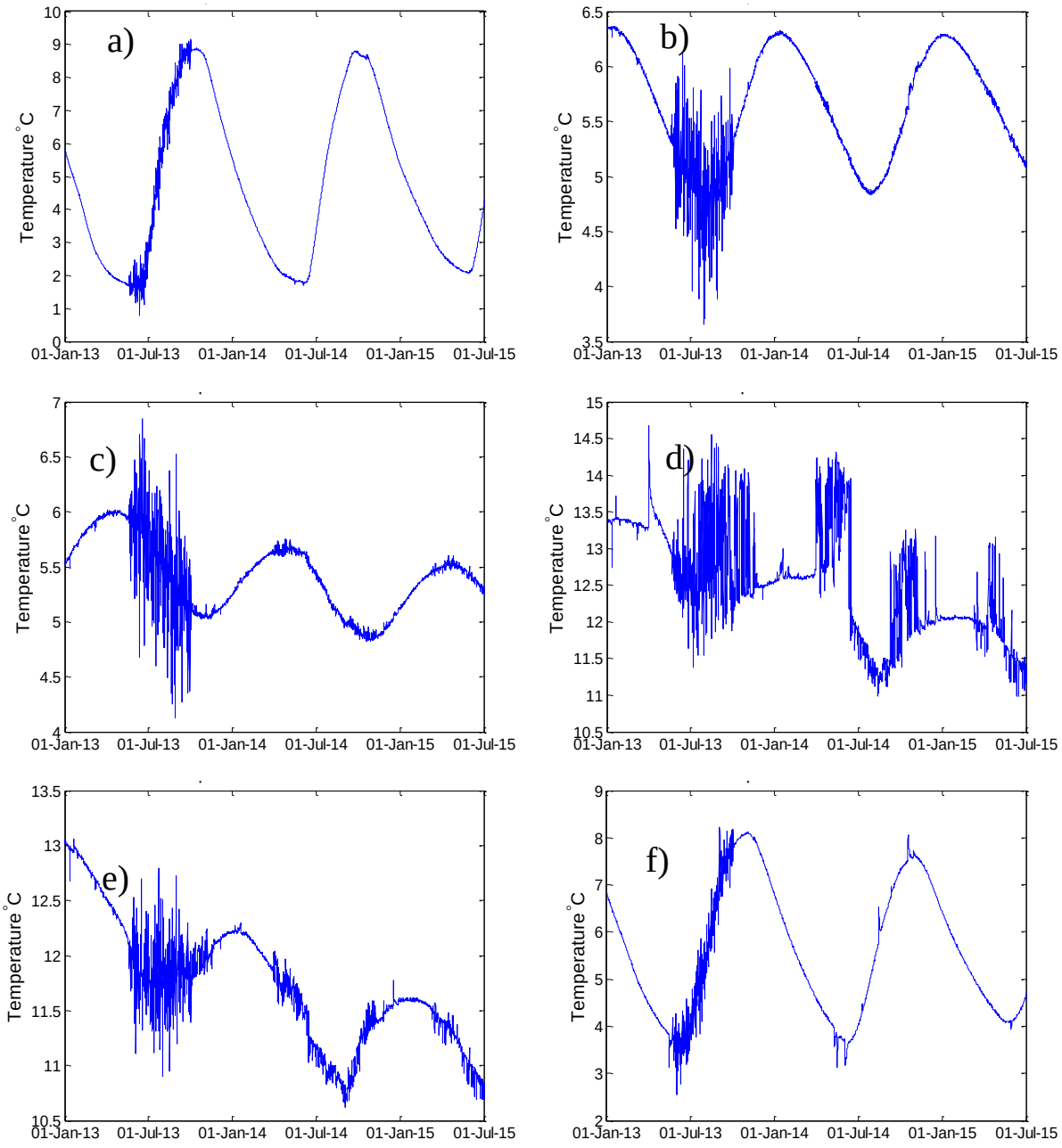

Figure A-8 – Time series for internal temperature. Daily averaged data at a) BH2011-3-!-4.18m b) BH2011-3-!-9.18m c) BH2011-3-!-14.18m d) BH2011-3-!-18.78m e) BH2011-3-!-19.18m f) BH2011-3-2-4.85m

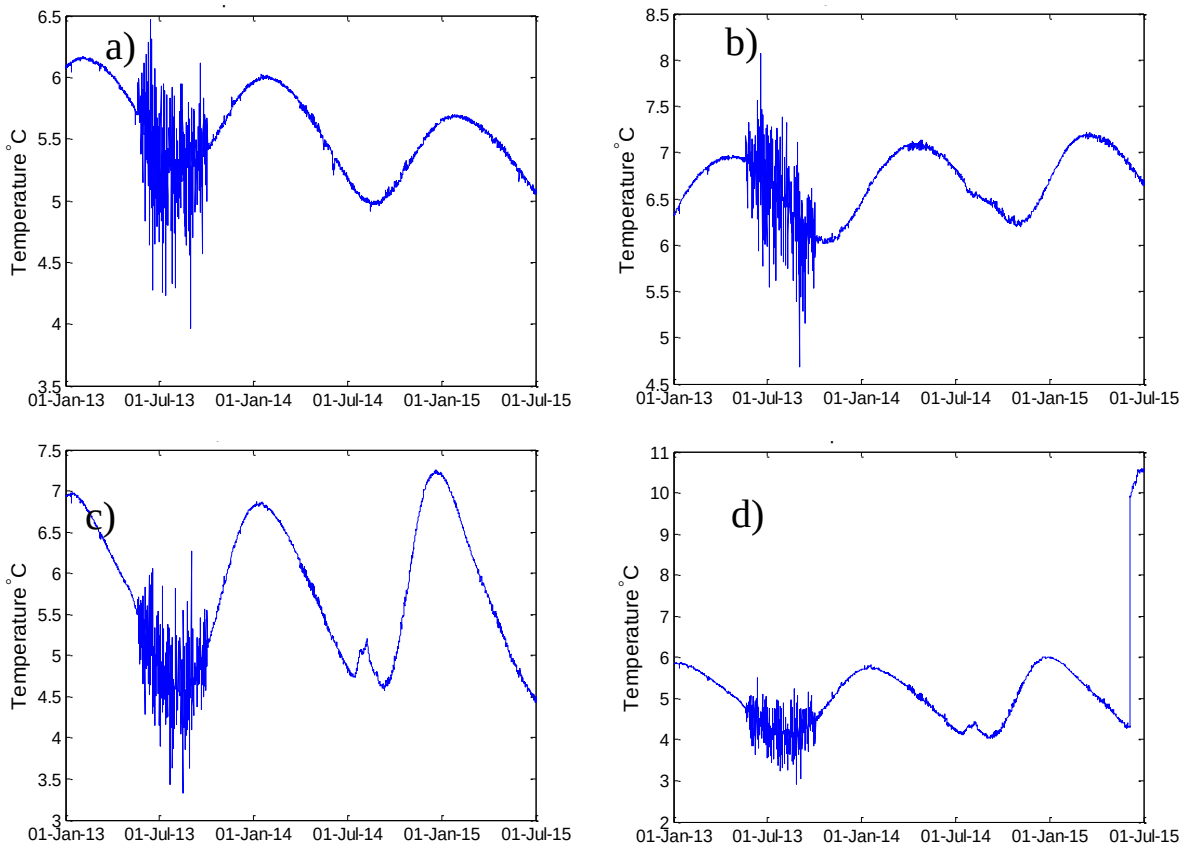

Figure A-9 – Time series for internal temperature. Daily averaged data at a) BH2011-3-2-9.85m b) BH2011-3-2-14.85m c) BH2011-3-2-19.85m d) BH2011-3-2-22.1m

Time series for pore gas O_2 content

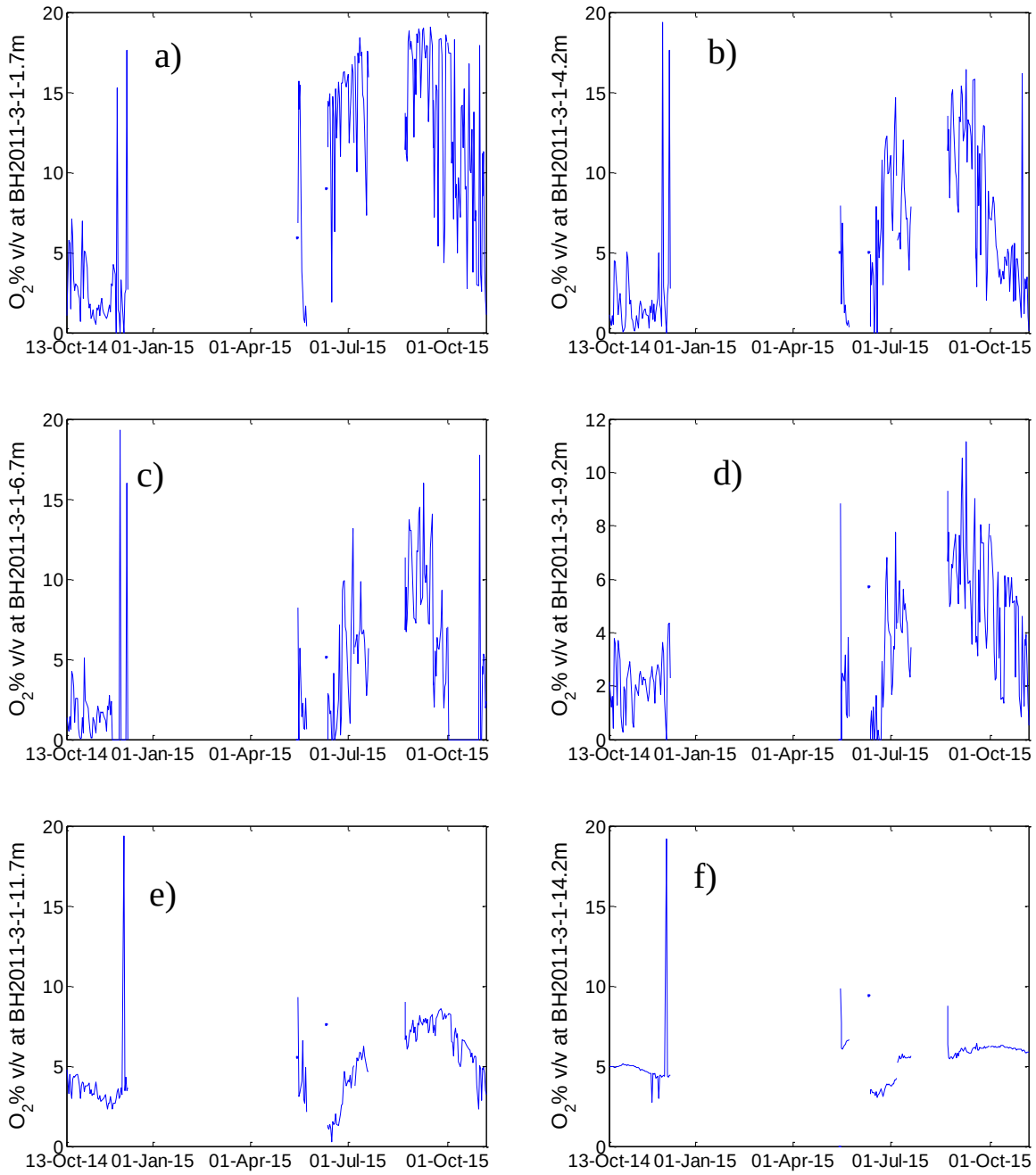

Figure A-10 – Time series for pore gas O_2 content. Daily averaged data at a) BH2011-3-1-1.7m b) BH2011-3-1-4.2m c) BH2011-3-1-6.7m d) BH2011-3-1-9.2m e) BH2011-3-1-11.7m f) BH2011-3-1-14.2m

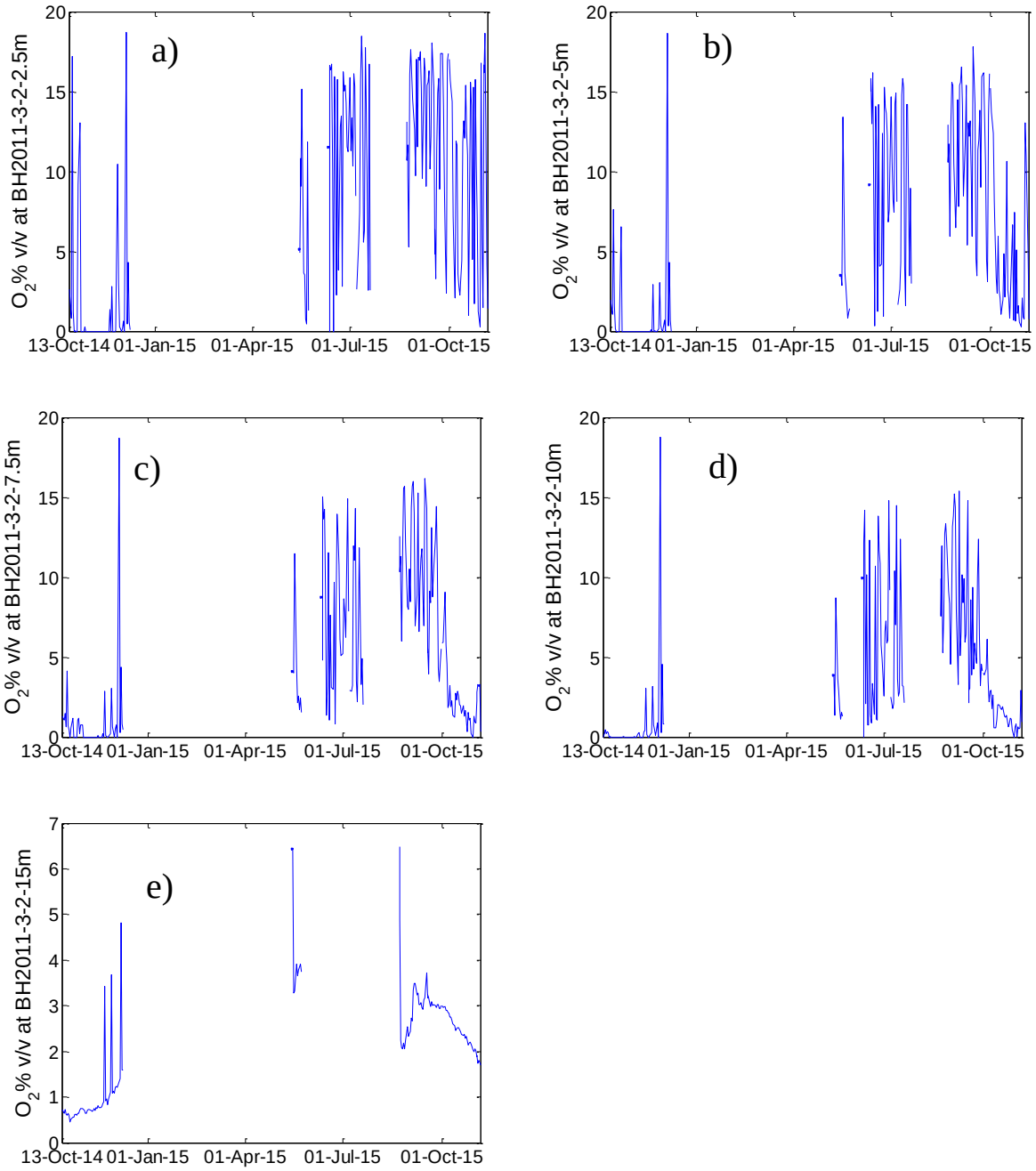

Figure A-11 – Time series for pore gas O_2 content. Daily averaged data at a) BH2011-3-2-2.5m b) BH2011-3-2-5m c) BH2011-3-2-7.5m d) BH2011-3-2-10m e) BH2011-3-2-15m. Location BH2011-3-12.5m has limited reliable data availability

Time series for pore gas CO_2 content

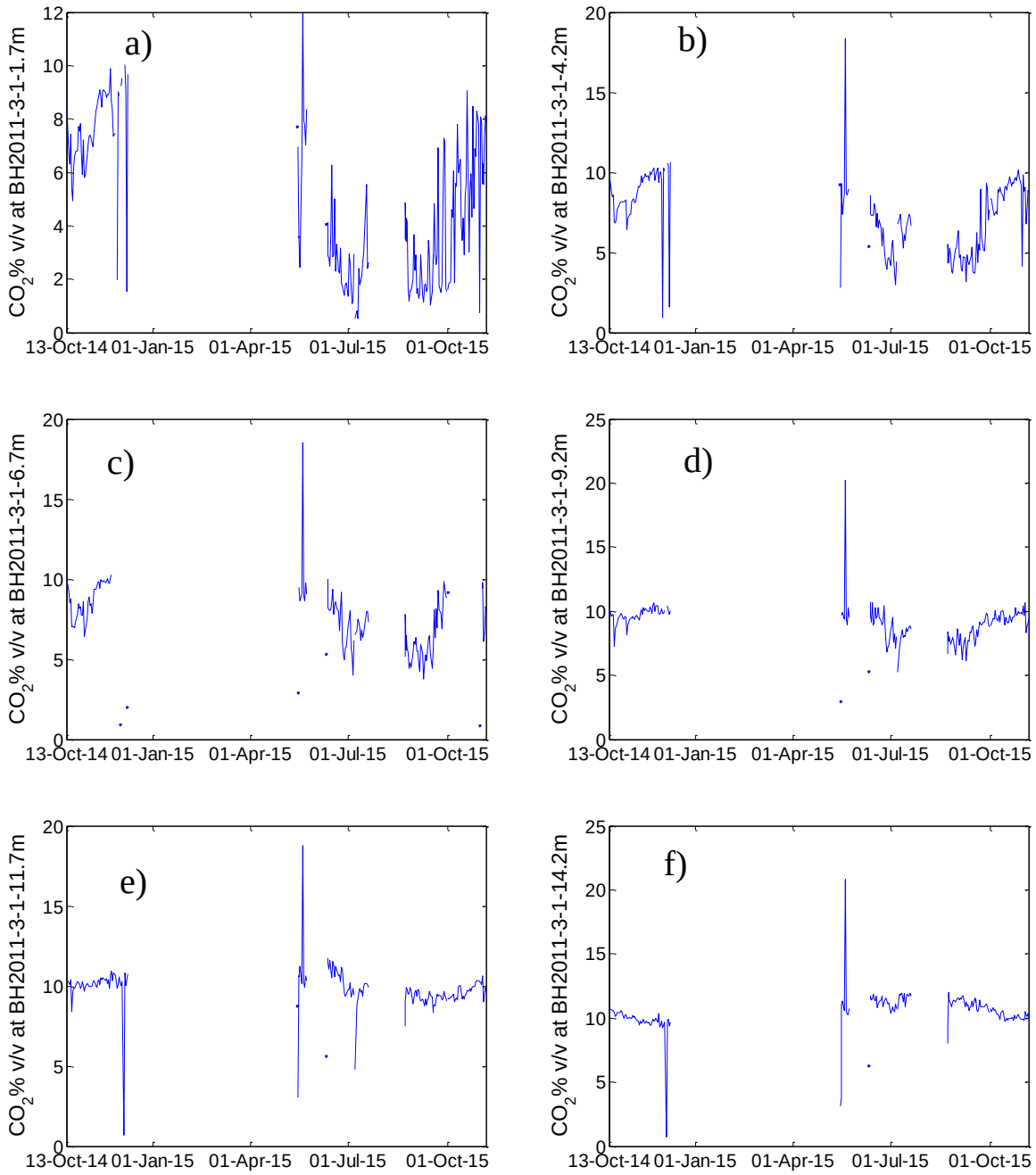

Figure A-12 – Time series for pore gas CO_2 content. Daily averaged data at a) BH2011-3-1-2.5m b) BH2011-3-1-5m c) BH2011-3-1-7.5m d) BH2011-3-1-10m e) BH2011-3-1-15m

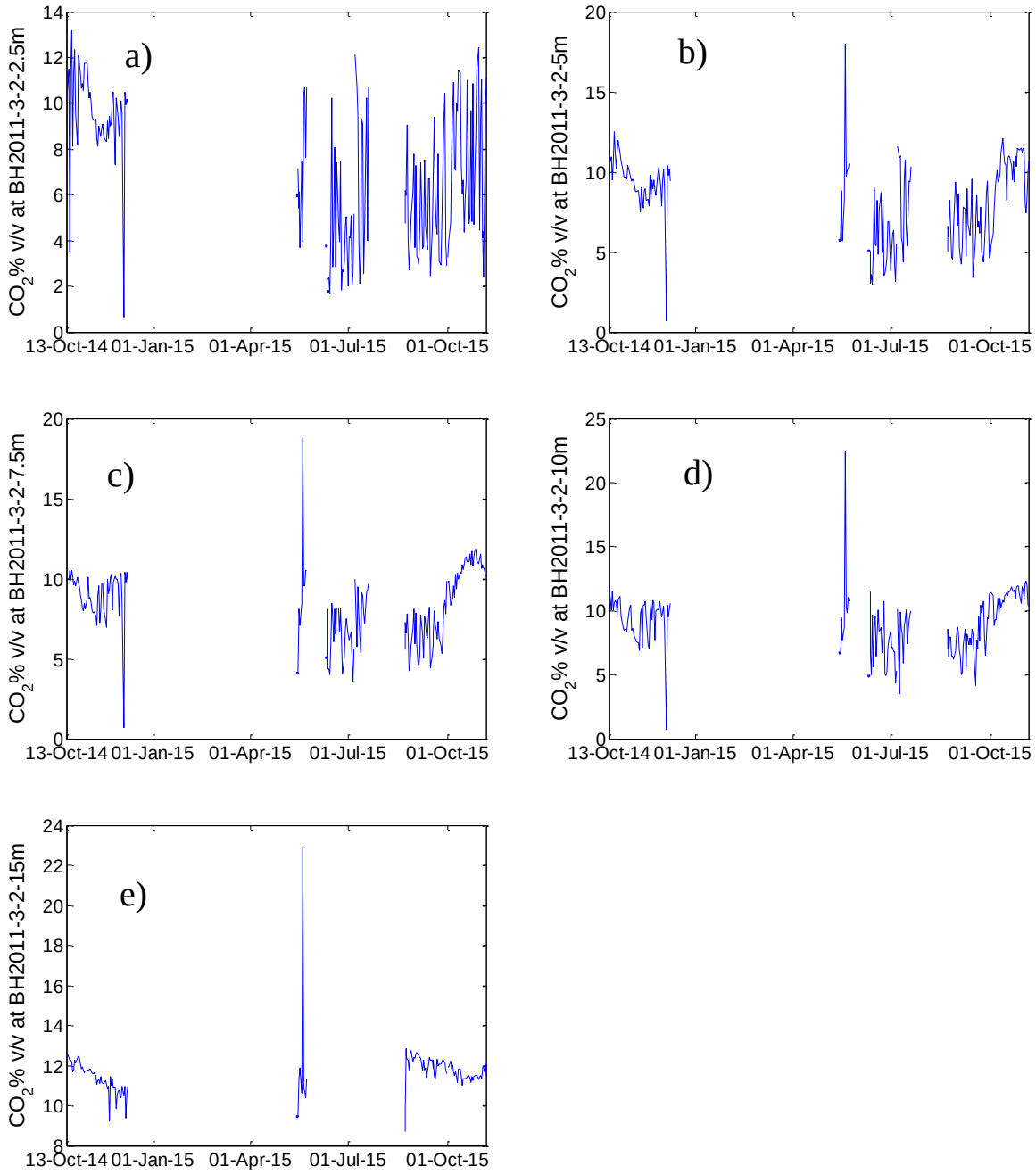

Figure A-13 – Time series for pore gas CO_2 content. Daily averaged data at a) BH2011-3-2-2.5m b) BH2011-3-2-5m c) BH2011-3-2-7.5m d) BH2011-3-2-10m e) BH2011-3-2-15m. Location BH2011-3-12.5m has limited reliable data availability

Discrete Fourier Transform amplitude – period plots for external pressure

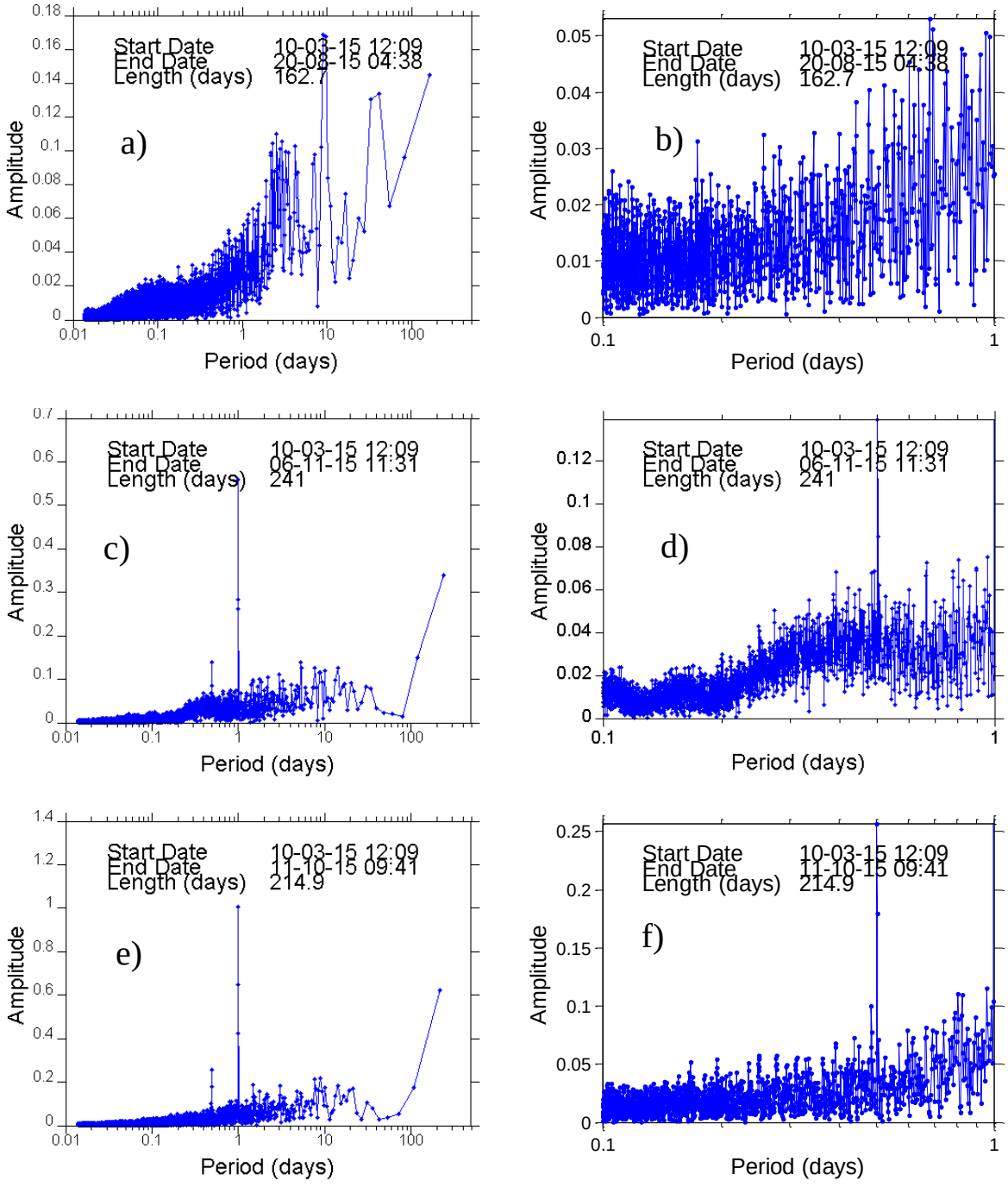

Figure A-14 – Discrete Fourier transform for external differential pressure. 10 minute data at a) S1 b) periods less than 1 day c) S2 d) periods less than 1 day e) S3 f) periods less than 1 day

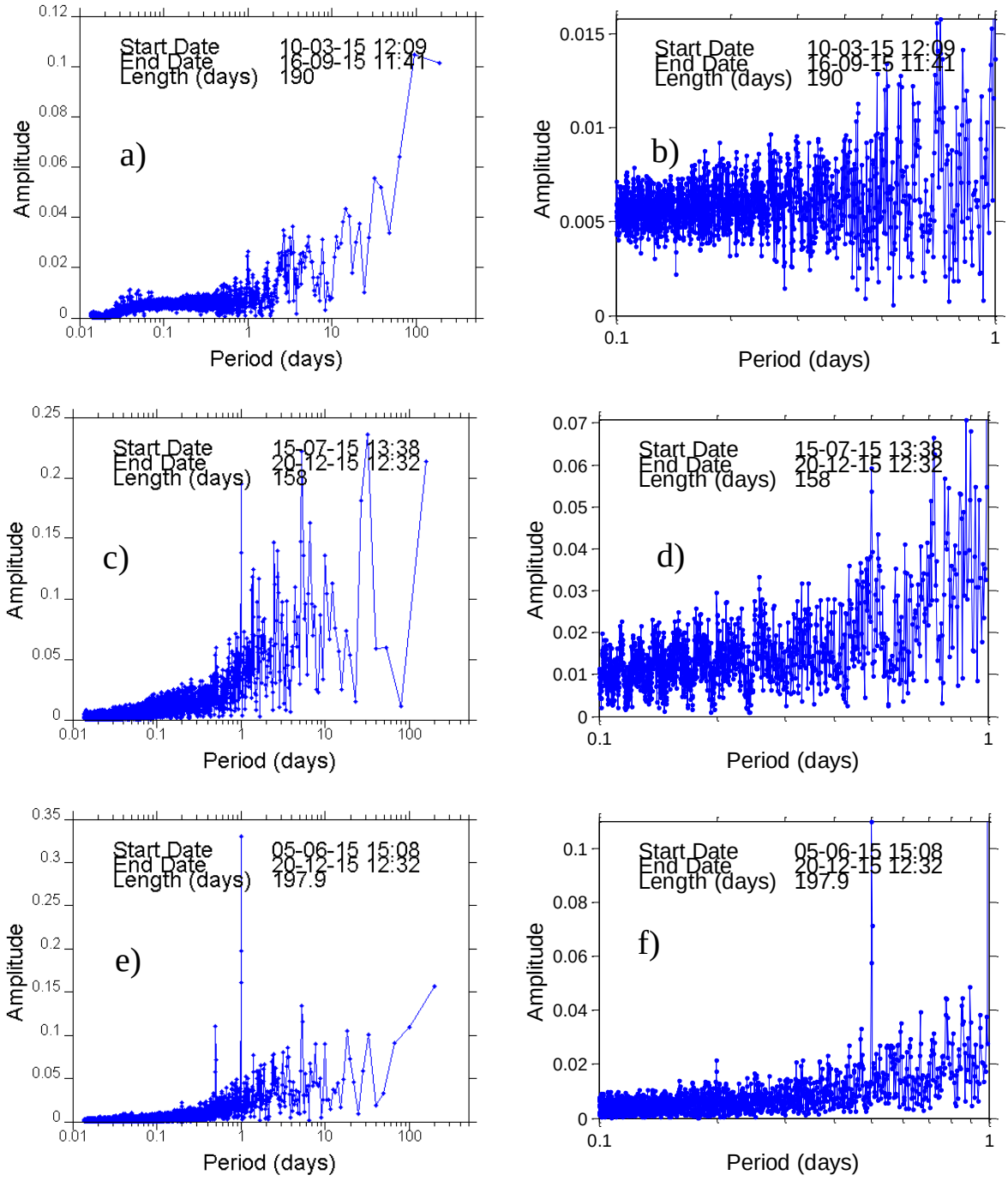

Figure A-15 – Discrete Fourier transform for external differential pressure. 10 minute data at a) W1 b) periods less than 1 day c) W2 d) periods less than 1 day e) W3 f) periods less than 1 day

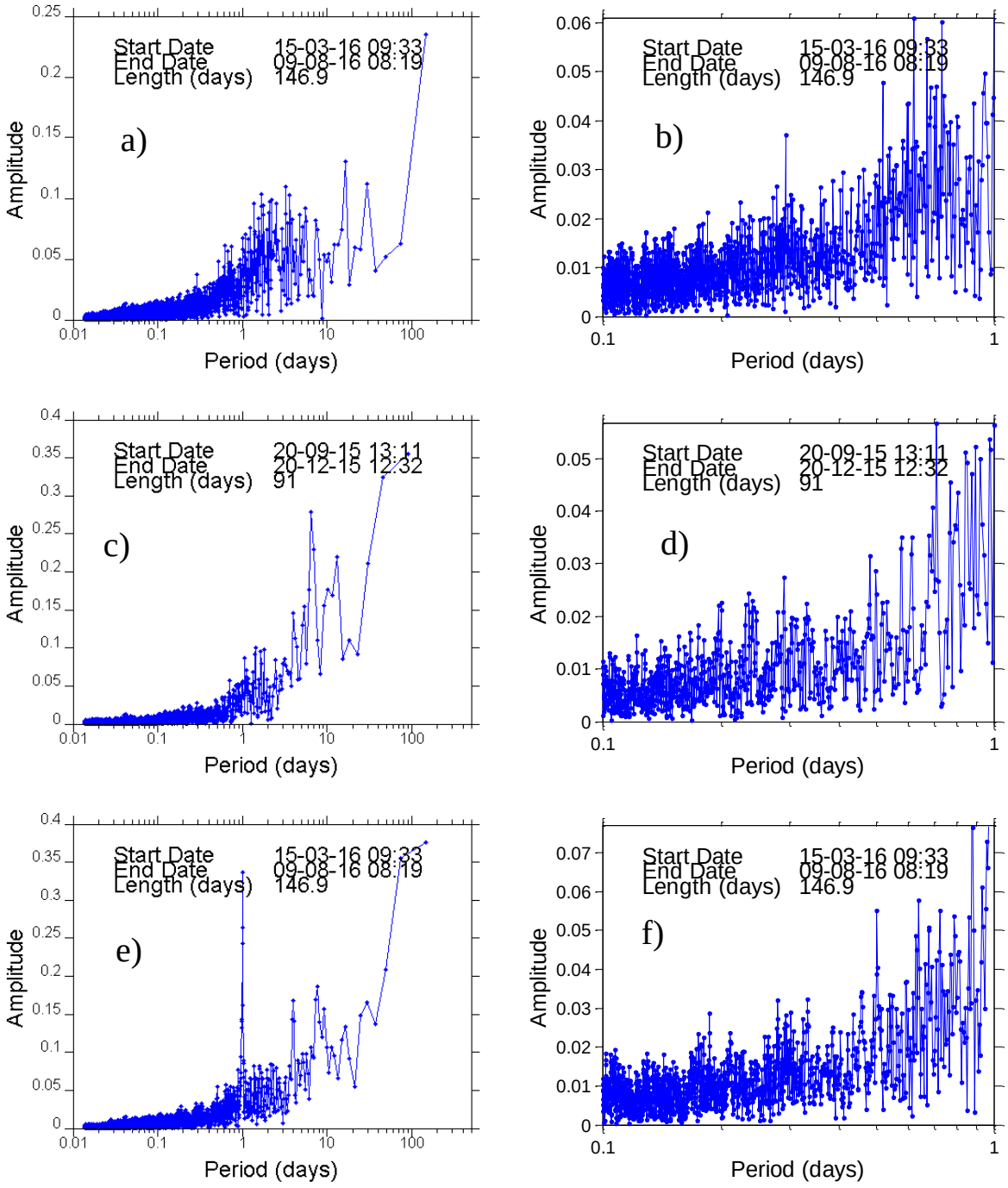

Figure A-16 – Discrete Fourier transform for external differential pressure. 10 minute data at a) E1 b) periods less than 1 day c) E2 d) periods less than 1 day e) E3 f) periods less than 1 day

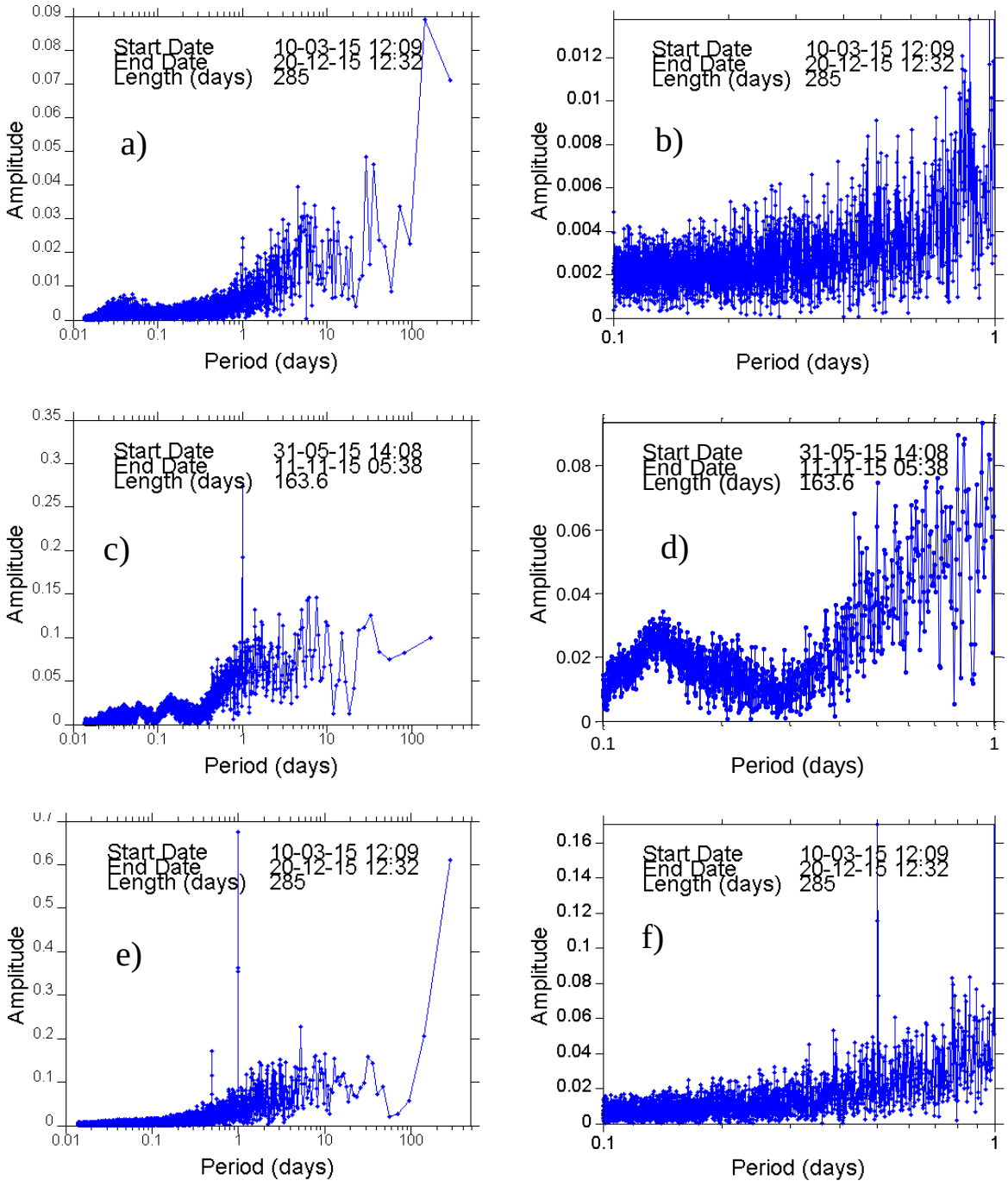

Figure A-17 – Discrete Fourier transform for external differential pressure. 10 minute data at a) N1 b) periods less than 1 day c) N2 d) periods less than 1 day e) N3 f) periods less than 1 day

Discrete Fourier Transform amplitude – period plots for internal pressure

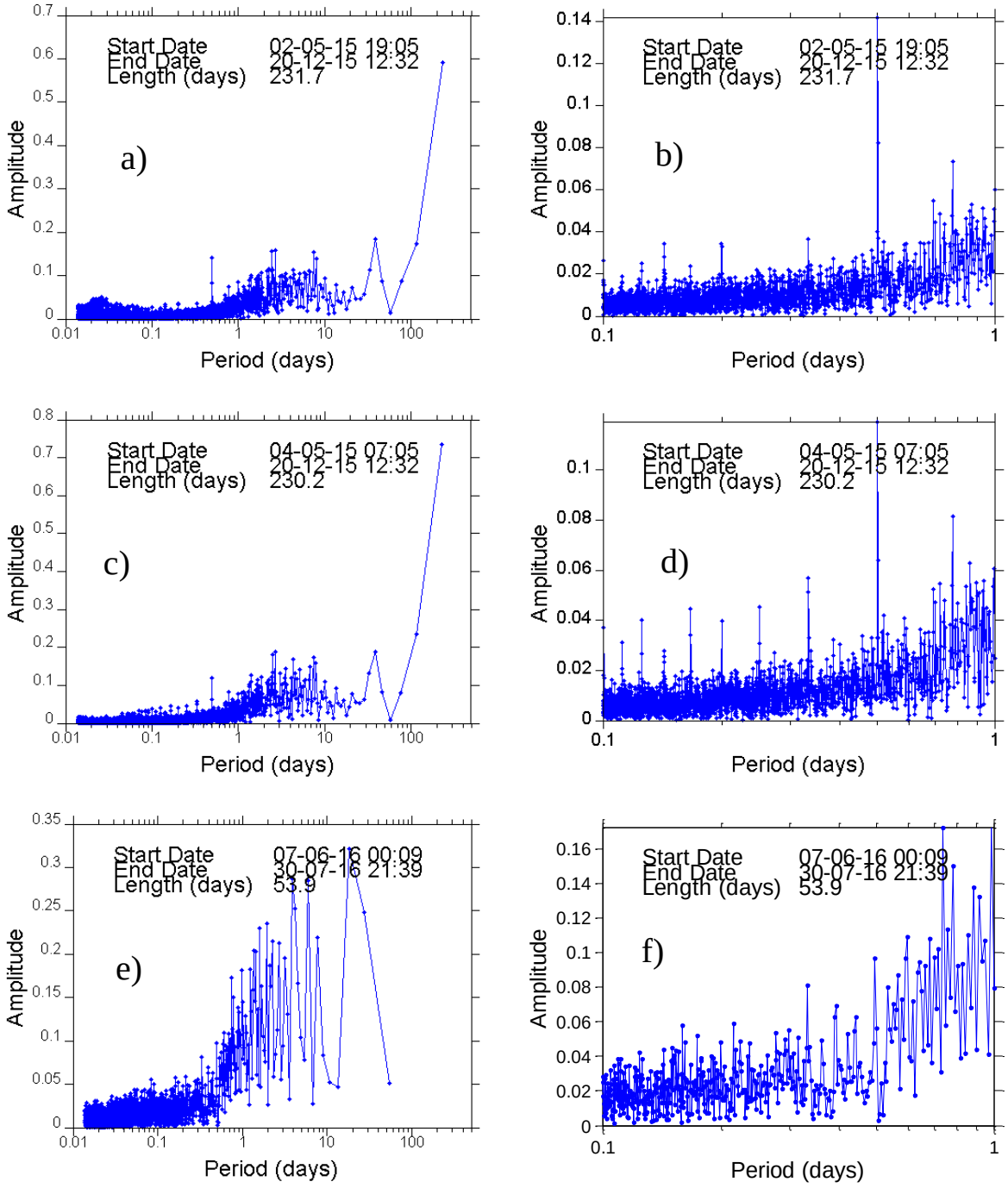

Figure A-18 – Discrete Fourier transform for internal differential pressure. 10 minute data at a) BH2011-3-1-1.7m b) periods less than 1 day c) BH2011-3-1-4.2m d) periods less than 1 day e) BH2011-3-1-6.7m f) periods less than 1 day

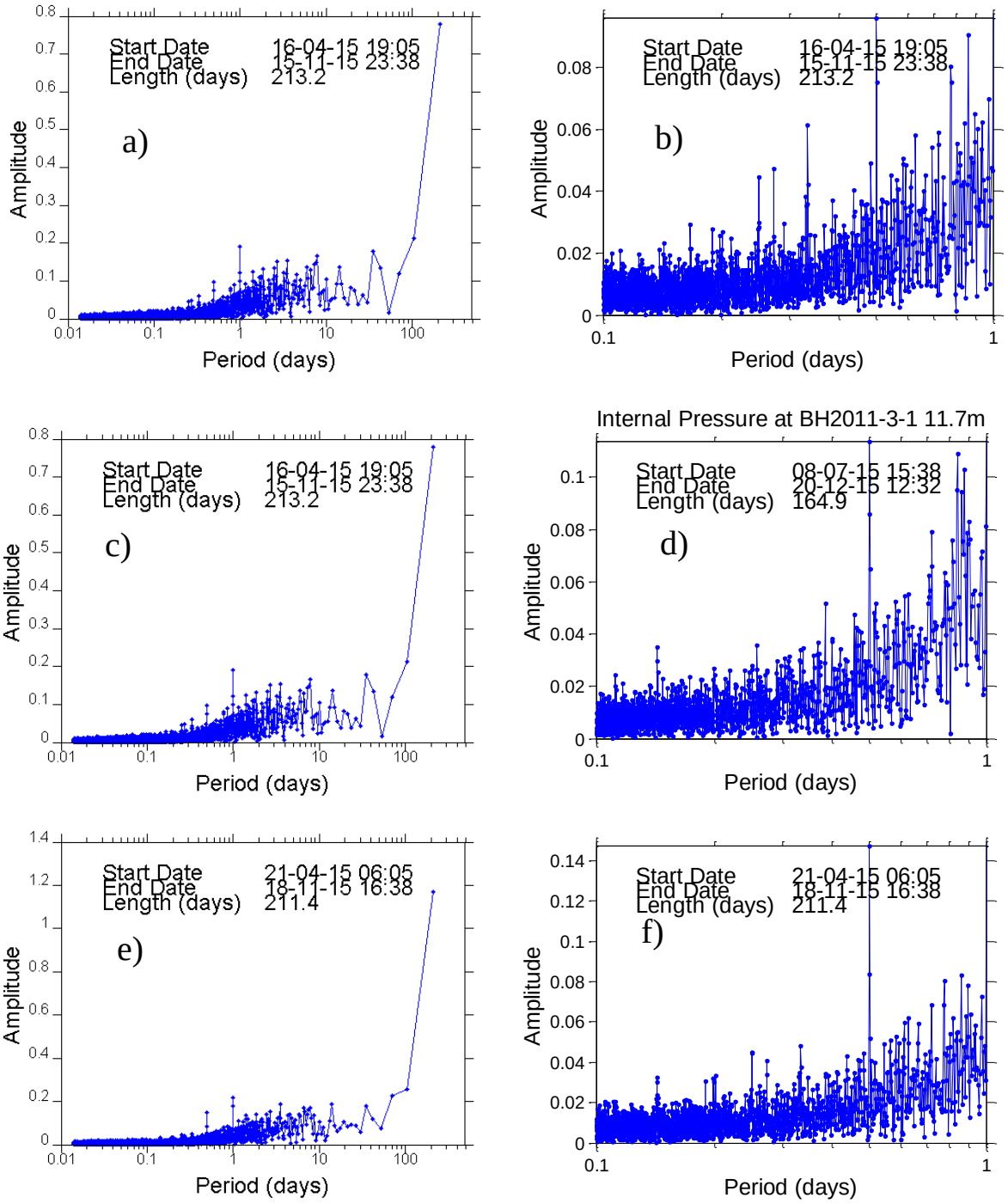

Figure A-19 – Discrete Fourier transform for internal differential pressure. 10 minute data at a) BH2011-3-1-9.2m b) periods less than 1 day c) BH2011-3-1-11.7m d) periods less than 1 day e) BH2011-3-1-14.2m f) periods less than 1 day

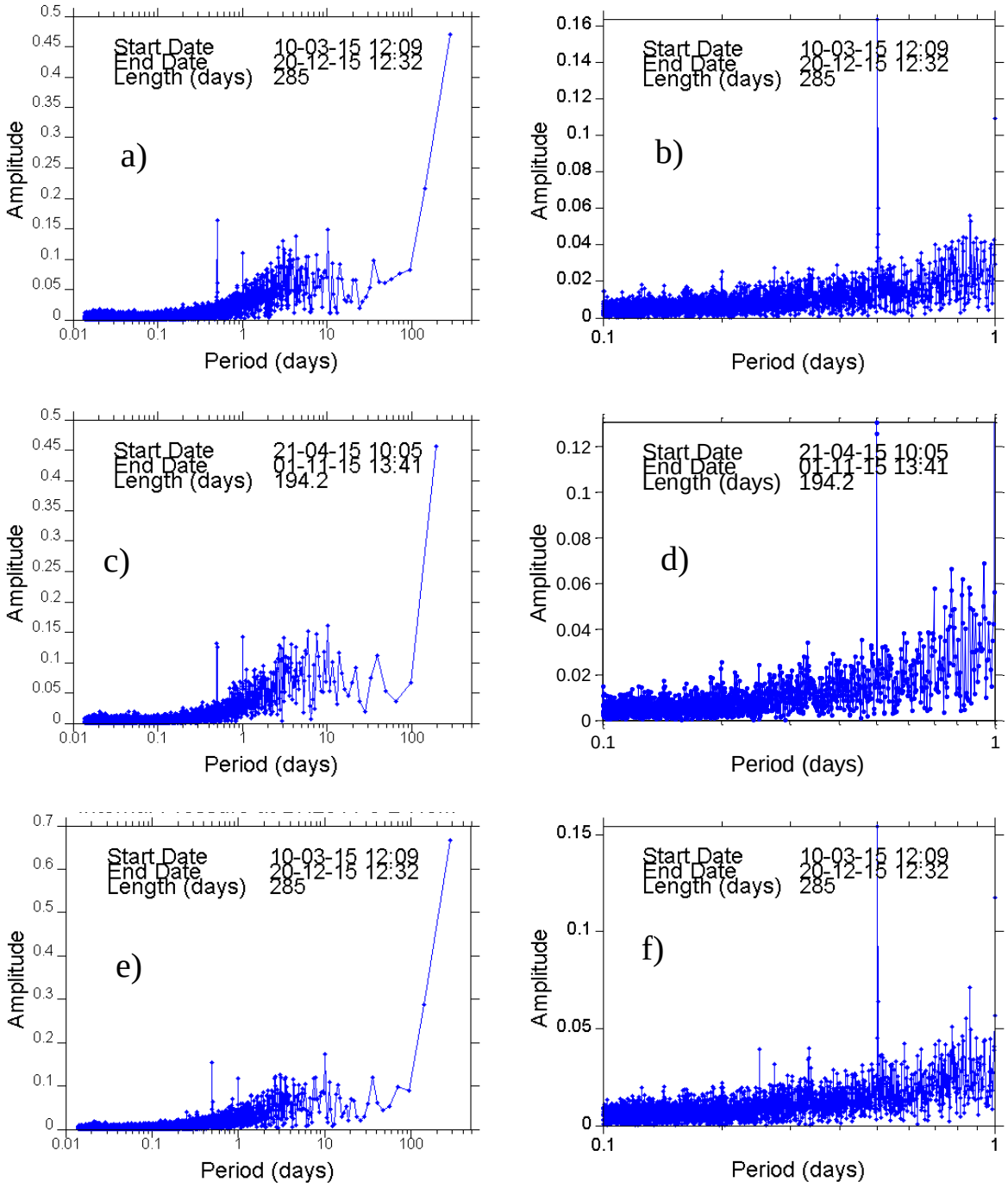

Figure A-20 – Discrete Fourier transform for internal differential pressure. 10 minute data at a) BH2011-3-2-2.5m b) periods less than 1 day c) BH2011-3-2-5m d) periods less than 1 day e) BH2011-3-2-7.5m f) periods less than 1 day

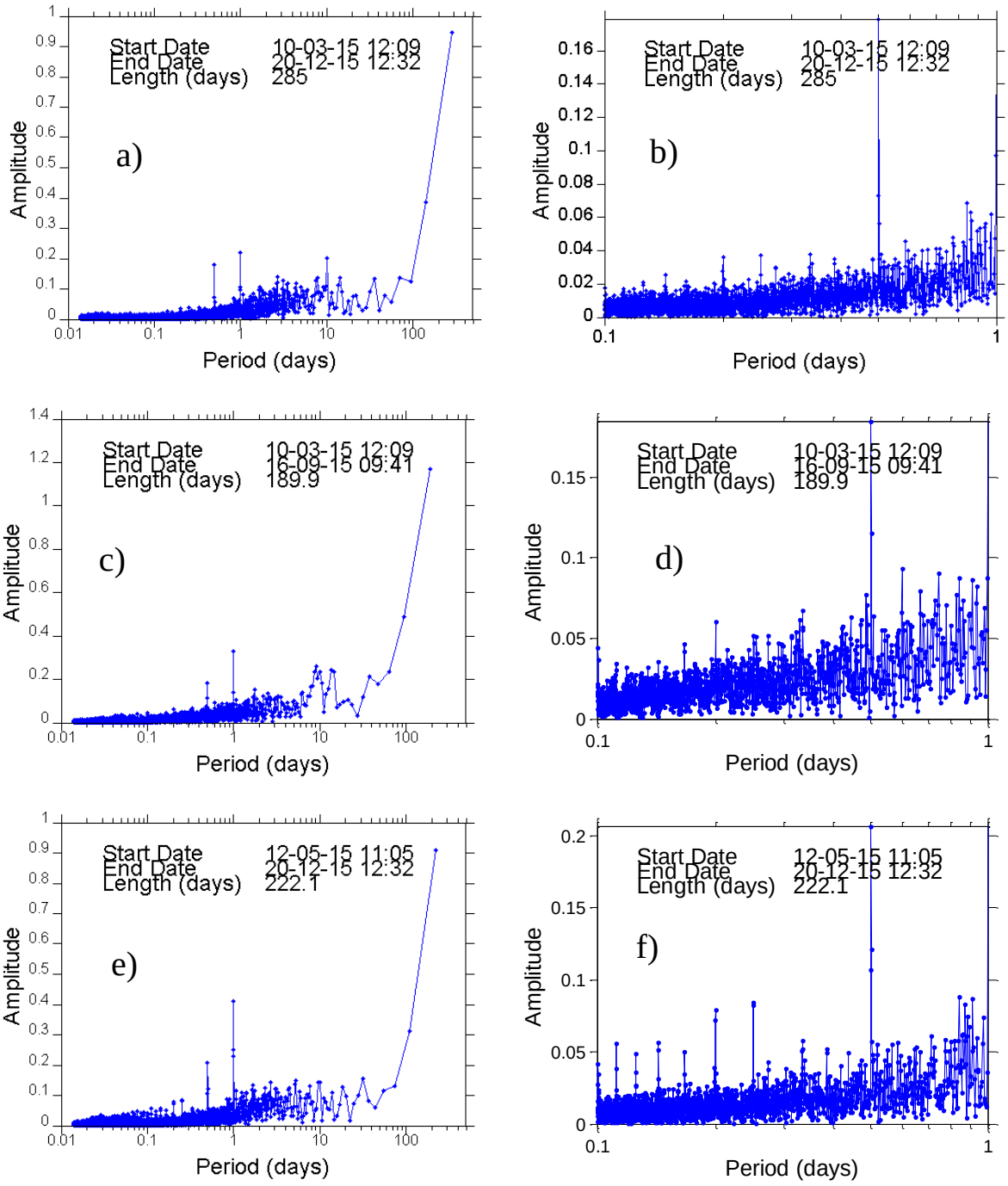

Figure A-21 – Discrete Fourier transform for internal differential pressure. 10 minute data at a) BH2011-3-2-10m b) periods less than 1 day c) BH2011-3-2-12.5m d) periods less than 1 day e) BH2011-3-2-15m f) periods less than 1 day

Discrete Fourier Transform amplitude – period plots for internal temperature

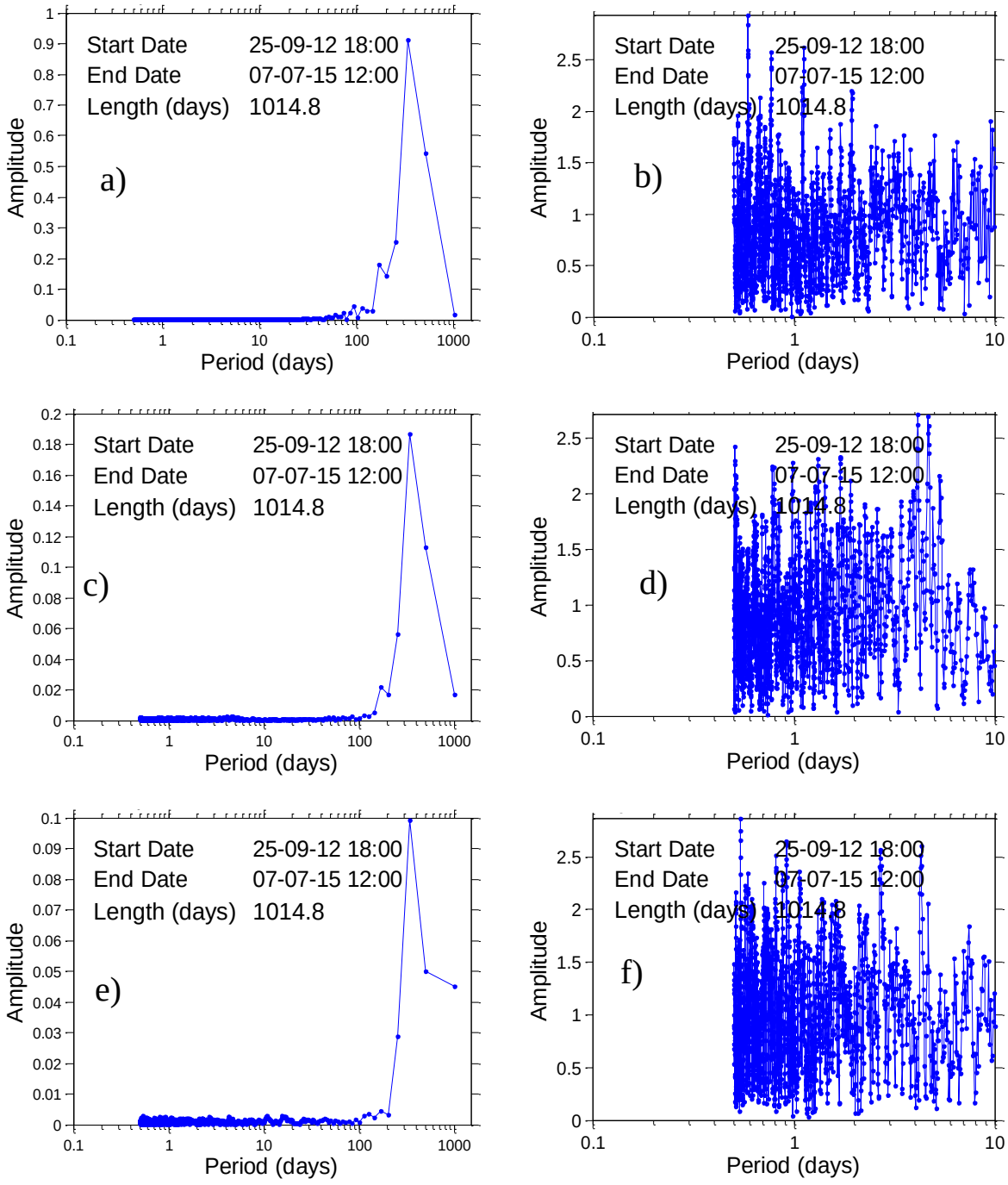

Figure A-22 – Discrete Fourier transform for internal temperature. 6 hourly data at a) BH2011-3-1-4.18m b) periods less than 1 day (amplitude x10^{-3}) c) BH2011-3-1-9.18m d) periods less than 1 day (amplitude x10^{-3}) e) BH2011-3-1-14.18m f) periods less than 1 day (amplitude x10^{-3})

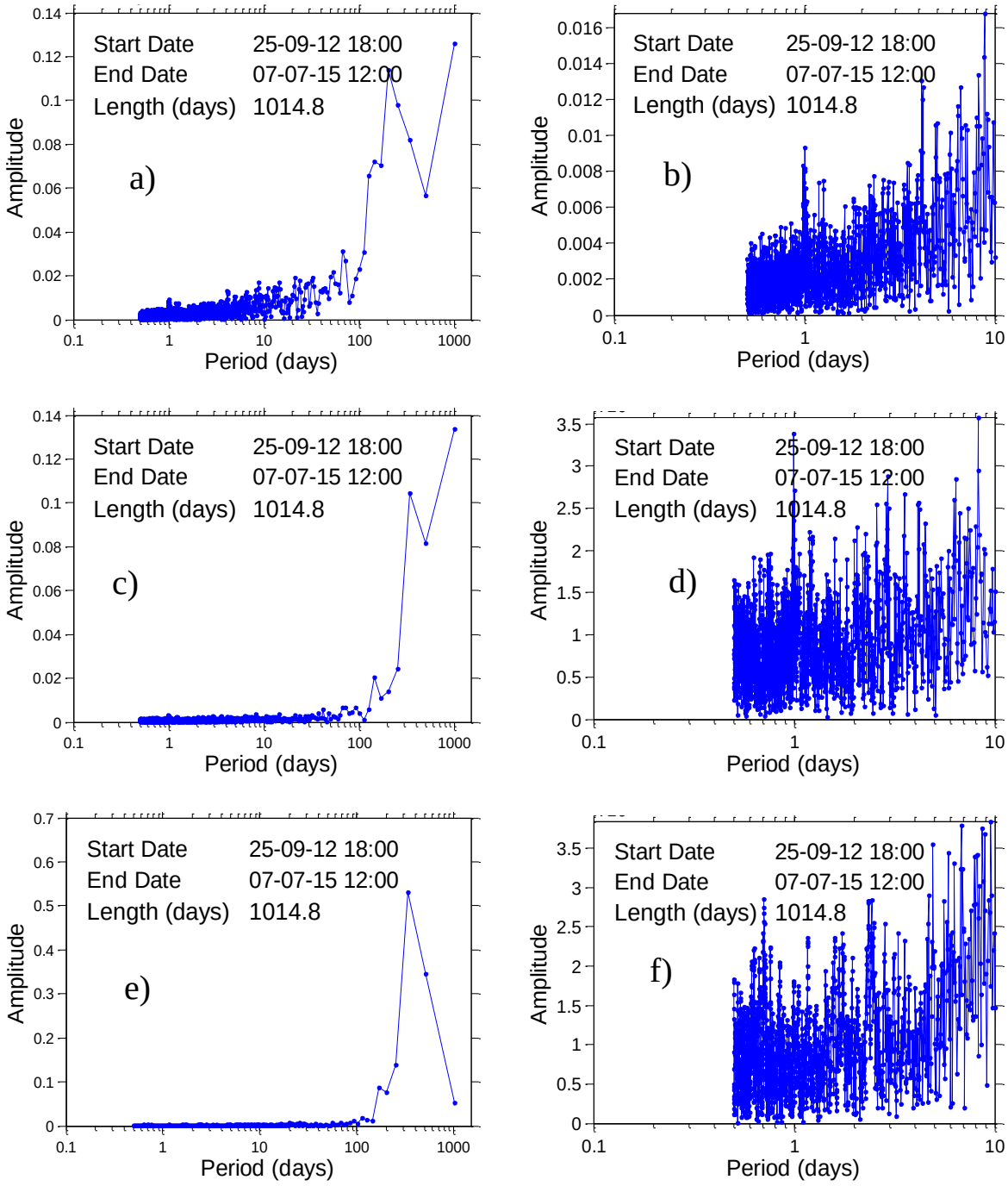

Figure A-23 – Discrete Fourier transform for internal temperature. 6 hourly data at a) BH2011-3-1-18.78m b) periods less than 1 day (amplitude x10^{-3}) c) BH2011-3-1-19.18m d) periods less than 1 day (amplitude x10^{-3}) e) BH2011-3-2-4.85m f) periods less than 1 day (amplitude x10^{-3})

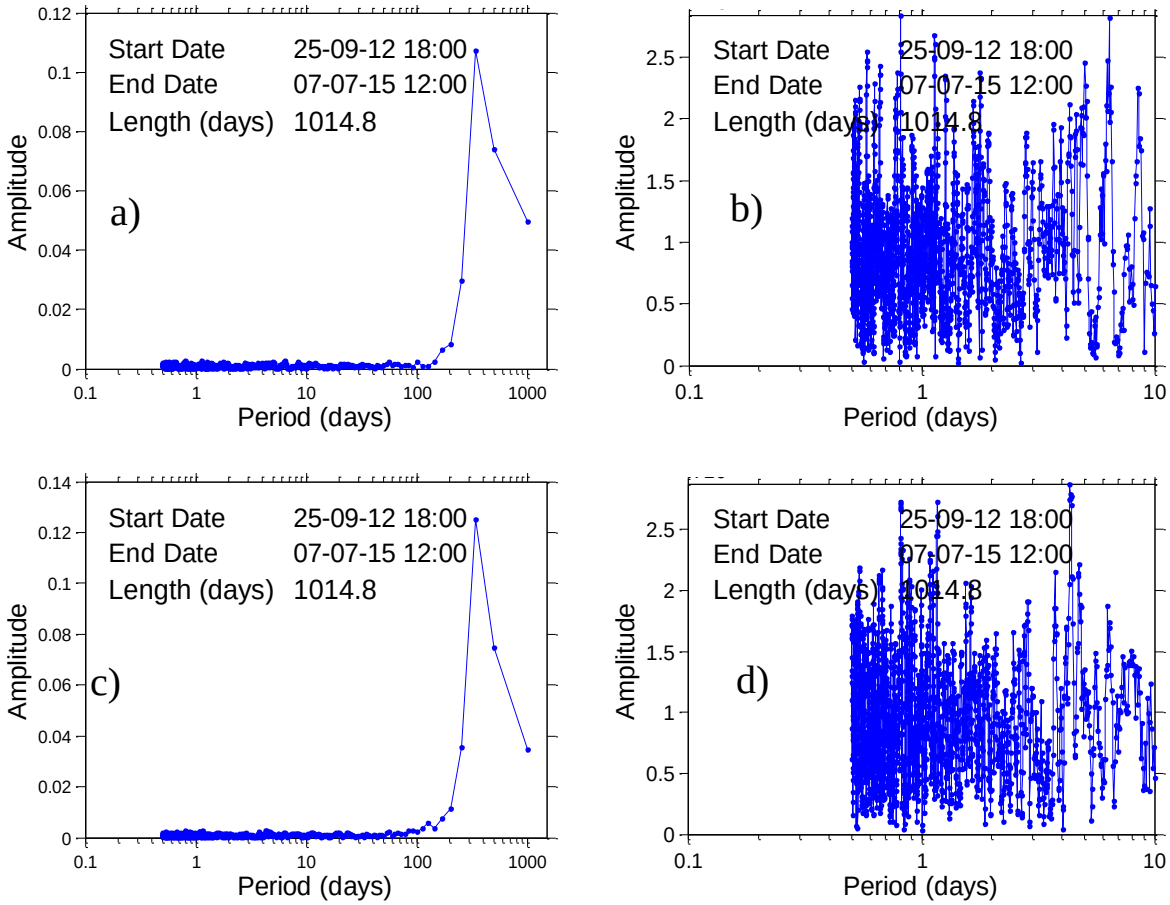

Figure A-24 – Discrete Fourier transform for internal temperature. 6 hourly data at a) BH2011-3-2-9.85m b) periods less than 1 day (amplitude x10^{-3}) c) BH2011-3-2-14.85m d) periods less than 1 day (amplitude x10^{-3})

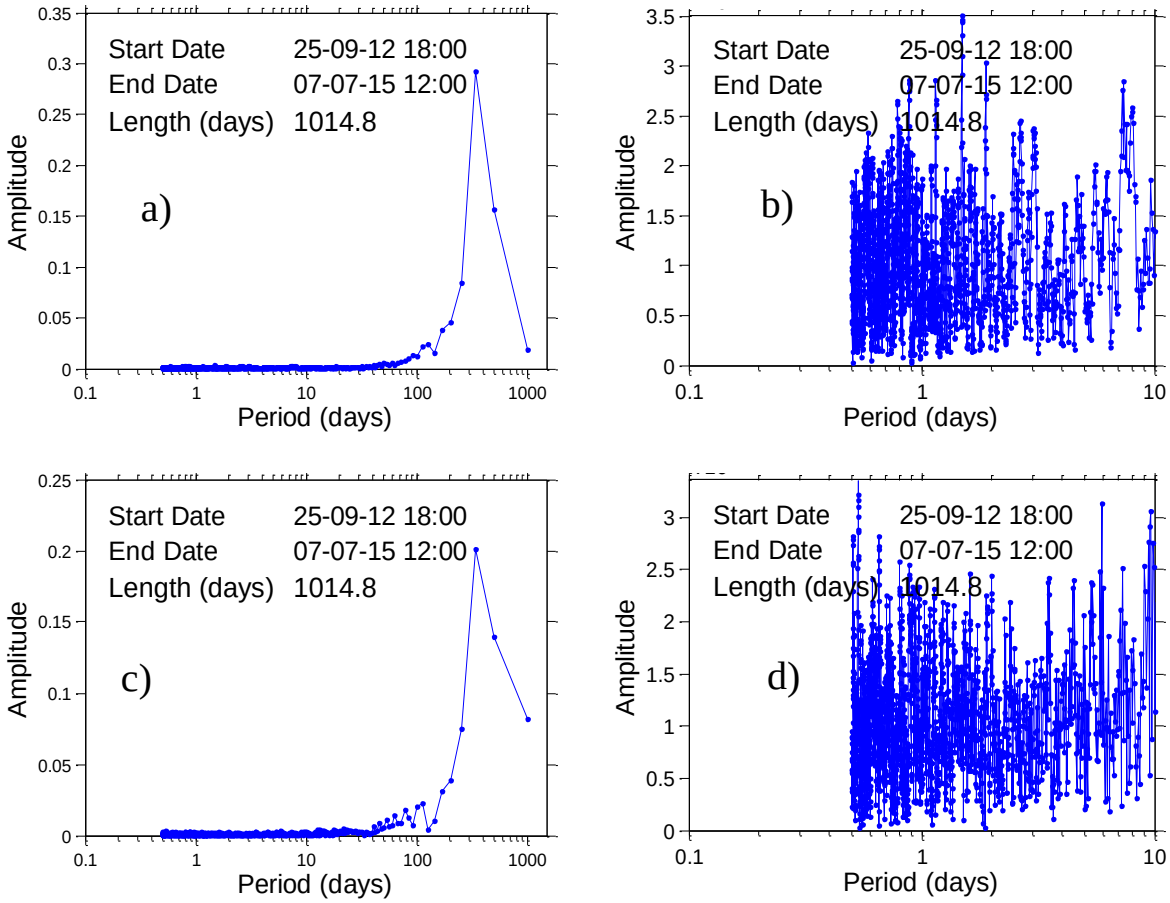

Figure A-25 – Discrete Fourier transform for internal temperature. 6 hourly data at a) BH2011-3-1-19.85m b) periods less than 1 day (amplitude x10^{-3}) c) BH2011-3-1-22.1m d) periods less than 1 day (amplitude x10^{-3})

Discrete Fourier Transform amplitude – period plots for pore gas O_2 content

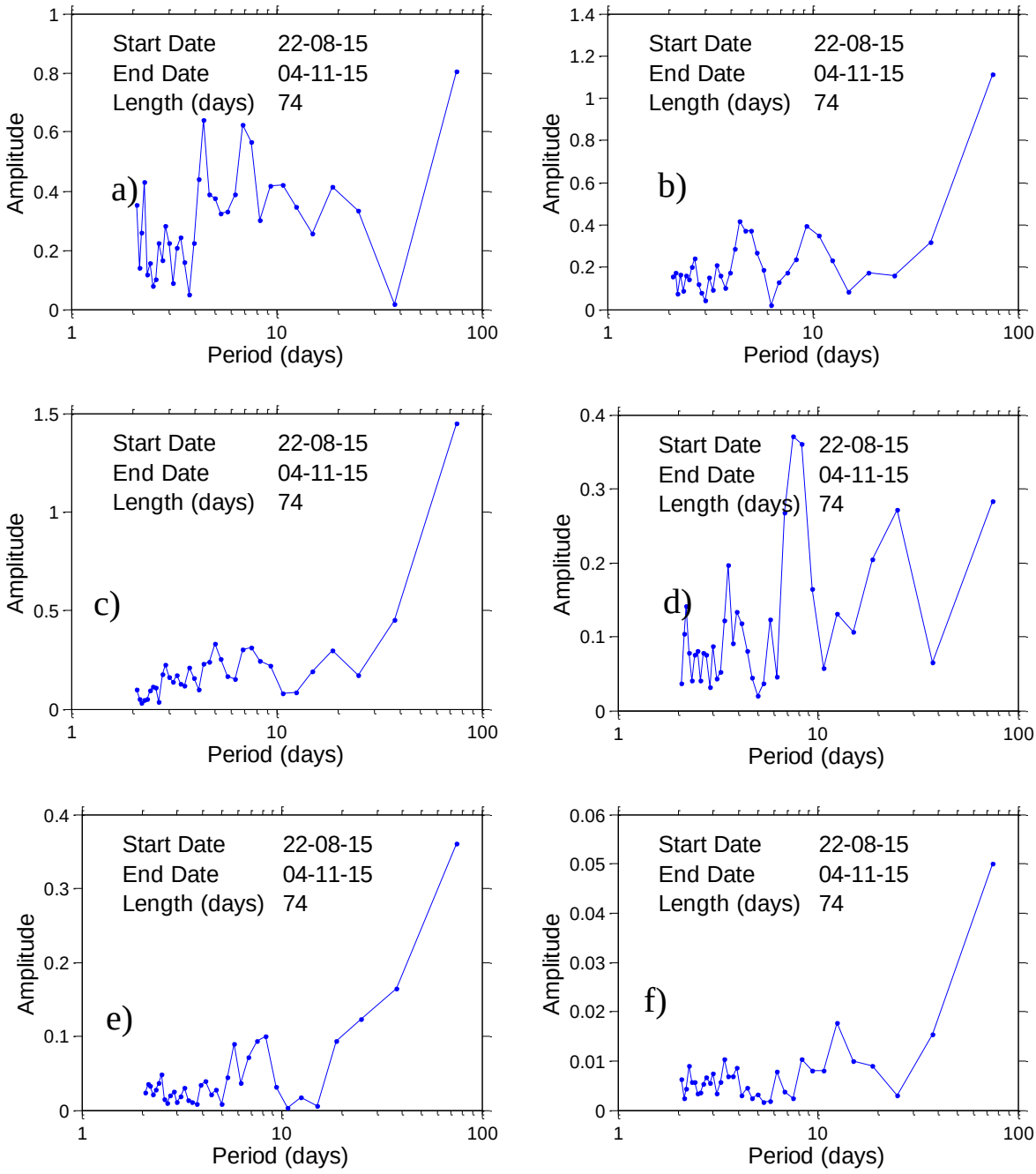

Figure A-26 – Discrete Fourier transform for pore gas O_2 content. Daily data at a) BH2011-3-1-1.7m b BH2011-3-1-4.2m c) BH2011-3-1-6.7m d) BH2011-3-1-9.2m e) BH2011-3-2-11.7m f) BH2011-3-1-14.2m

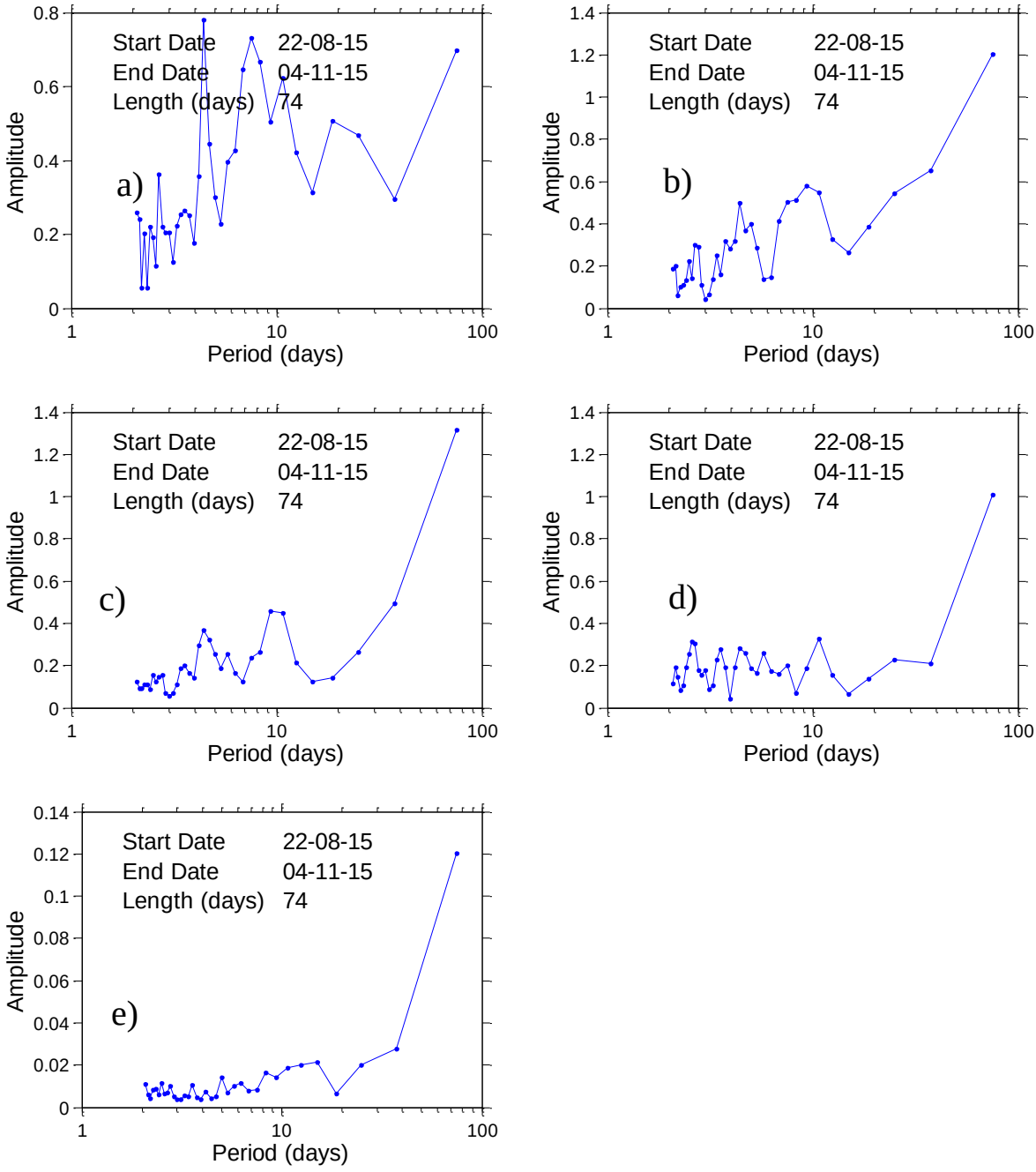

Figure A-27 – Discrete Fourier transform for pore gas O_2 content. Daily data at a) BH2011-3-2-2.5m b BH2011-3-2-5m c) BH2011-3-2-7.5m d) BH2011-3-2-10m e) BH2011-3-2-15m

Discrete Fourier Transform amplitude – period plots for pore gas CO_2 content

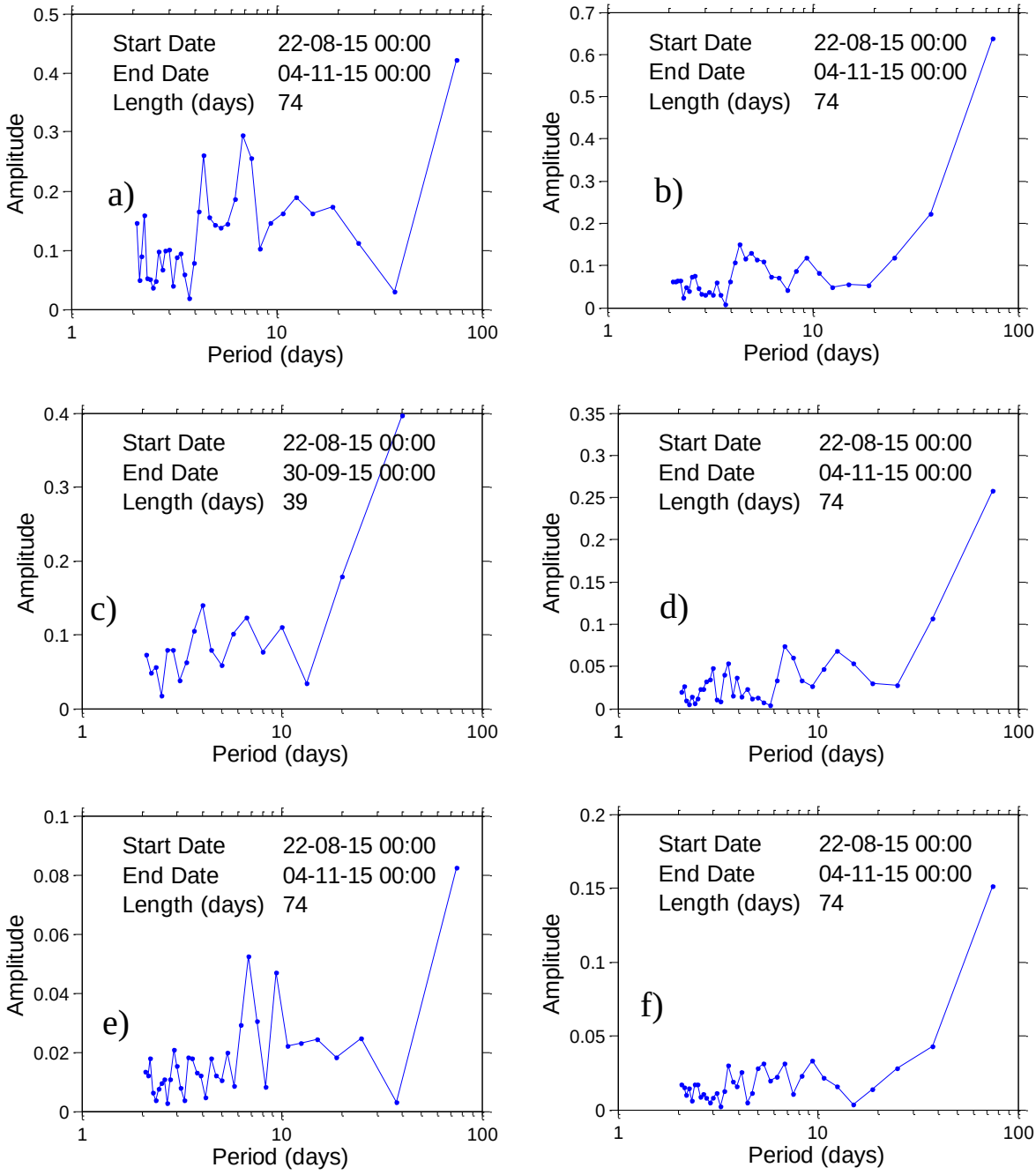

Figure A-28 – Discrete Fourier transform for pore gas CO_2 content. Daily data at a) BH2011-3-1-1.7m b BH2011-3-1-4.2m c) BH2011-3-1-6.7m d) BH2011-3-1-9.2m e) BH2011-3-2-11.7m f) BH2011-3-1-14.2m

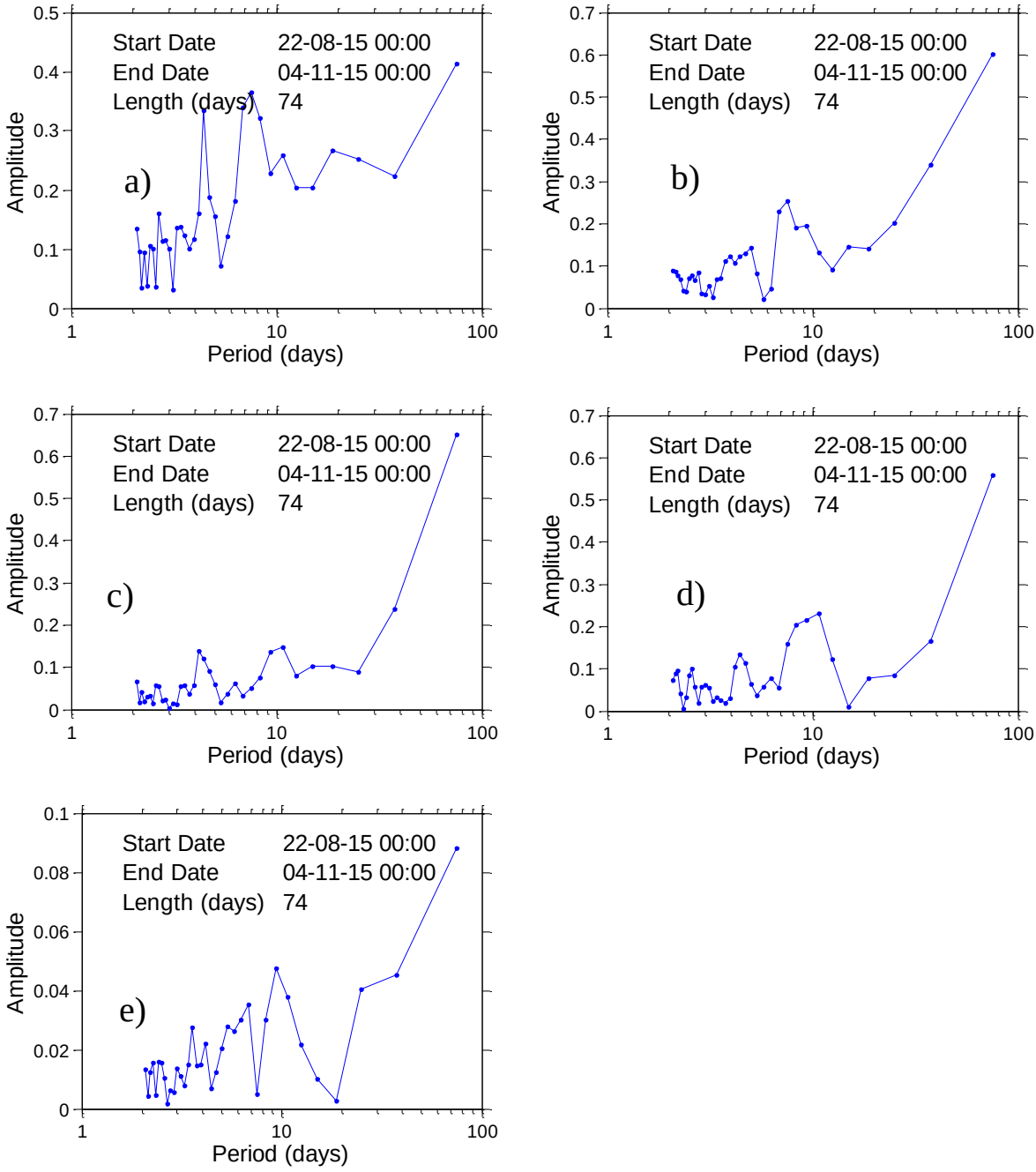

Figure A-29 – Discrete Fourier transform for pore gas CO2 content. Daily data at a) BH2011-3-2-2.5m b BH2011-3-2-5m c) BH2011-3-2-7.5m d) BH2011-3-2-10m e) BH2011-3-2-15m

Correlation plots for wind speed – external differential pressure

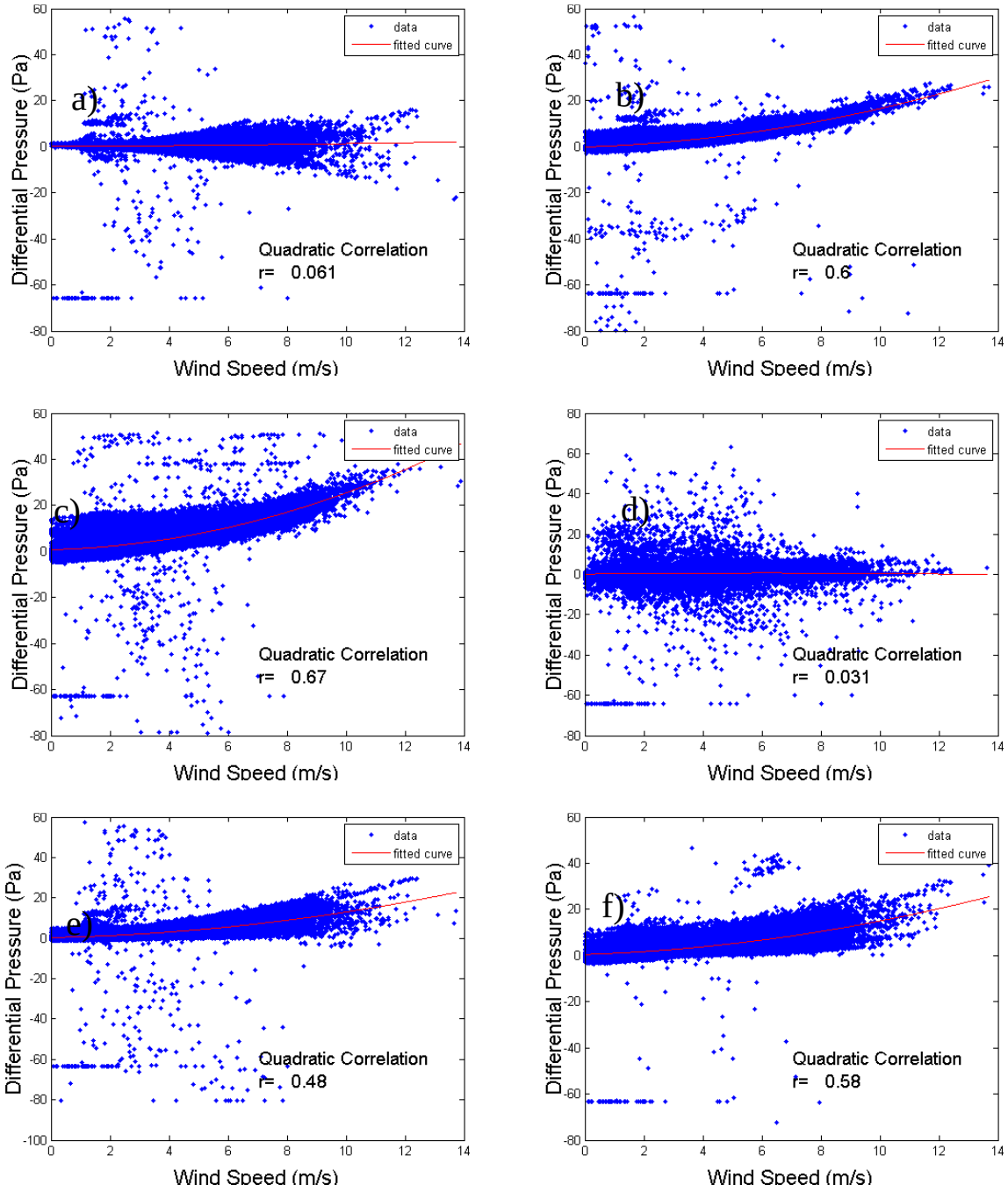

Figure A-30 – Correlation plot for wind speed versus differential external pressure. 10 minute data at a) S1 b) S2 c) S3 d) E1 e) E2 f) E4

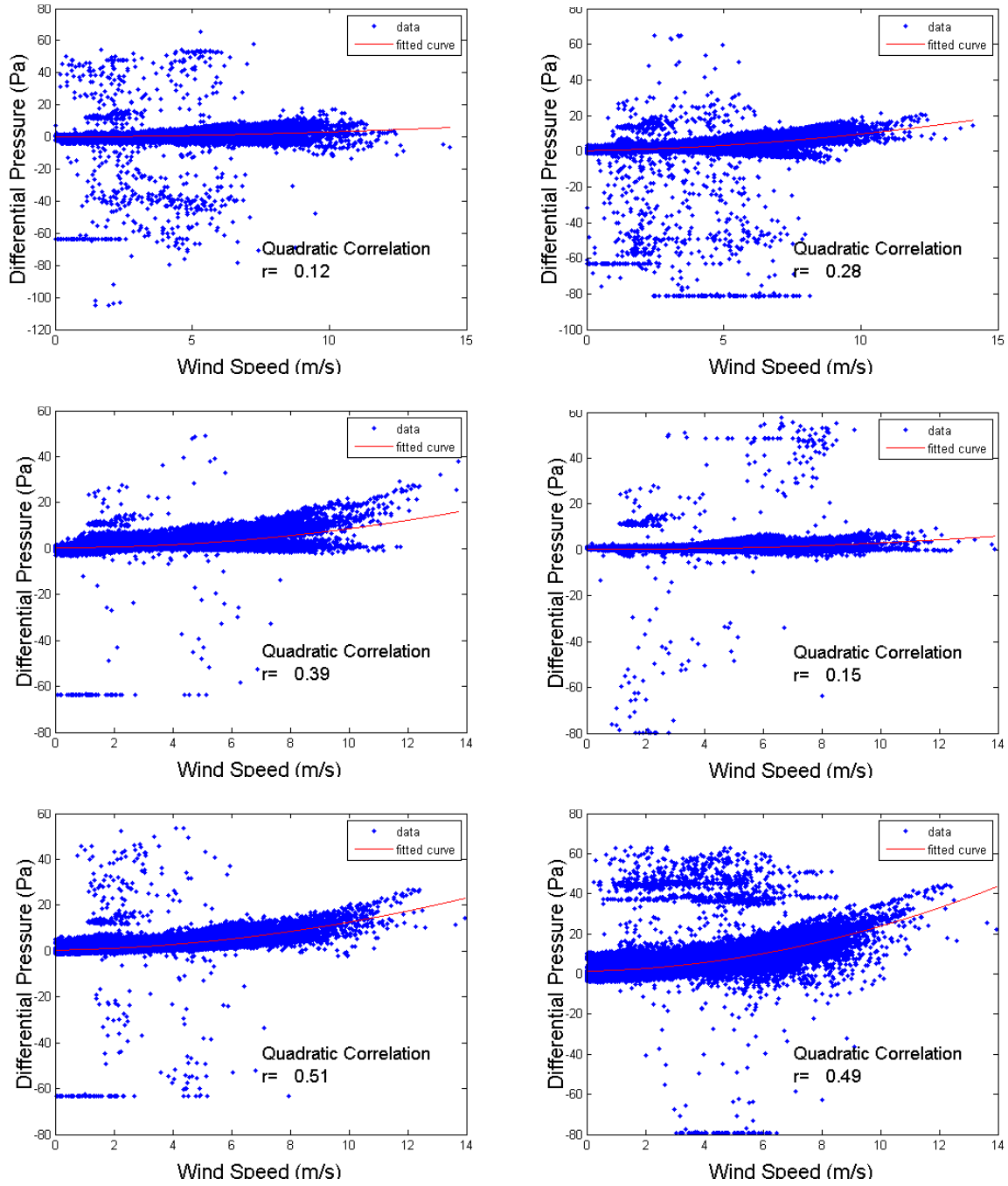

Figure A-31 – Correlation plot for wind speed versus differential external pressure. 10 minute data at a) W1 b) W2 c) W3 d) N1 e) N2 and f) N3

Correlation plots for wind speed – internal differential pressure

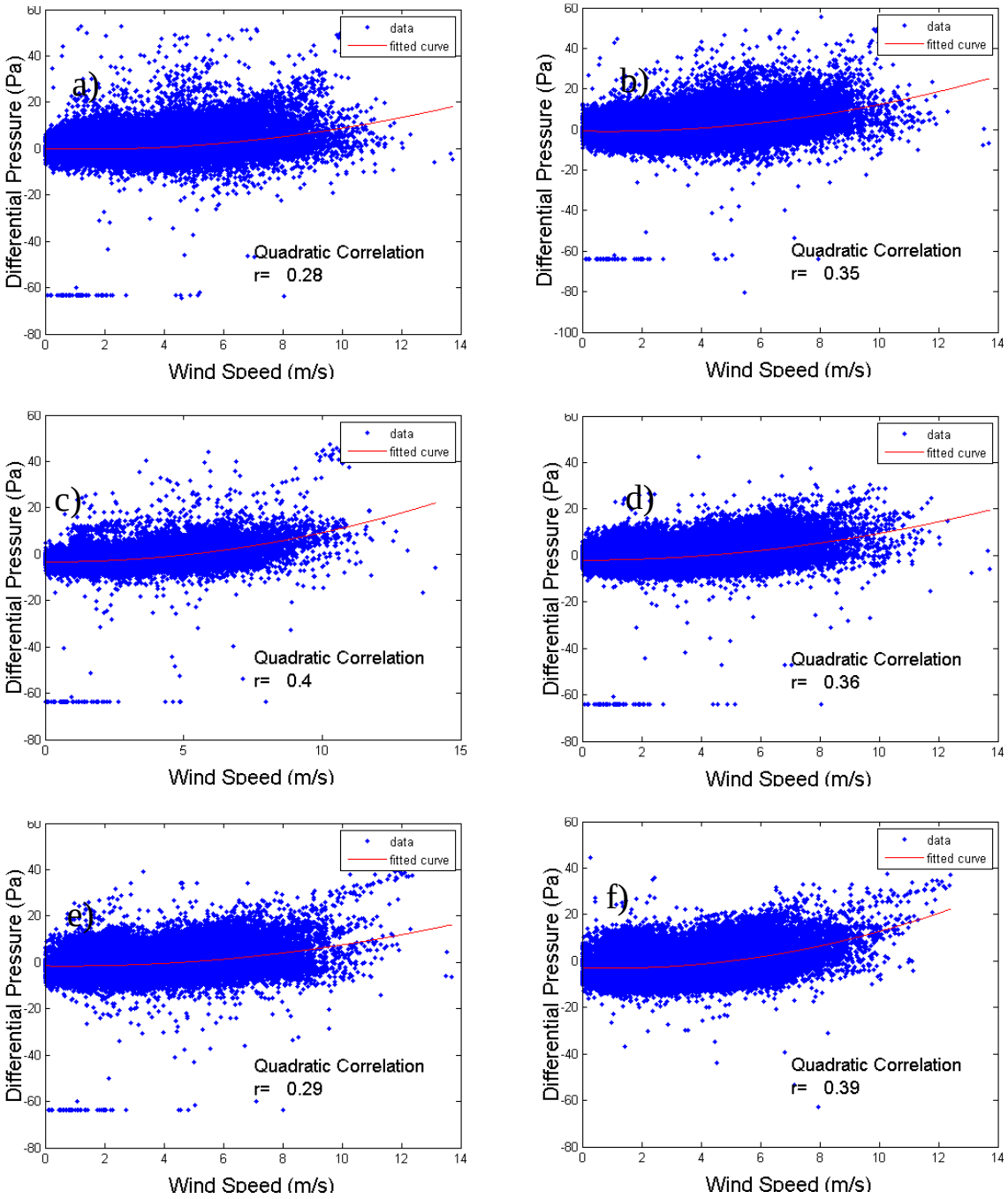

Figure A-32 – Correlation plot for wind speed versus differential internal pressure. 10 minute data at a) BH2011-3-1-1.7m b) BH2011-3-1-4.2m c) BH2011-3-1-6.7m d) BH2011-3-1-9.2m e) BH2011-3-1-11.7m and f) BH2011-3-1-14.2m

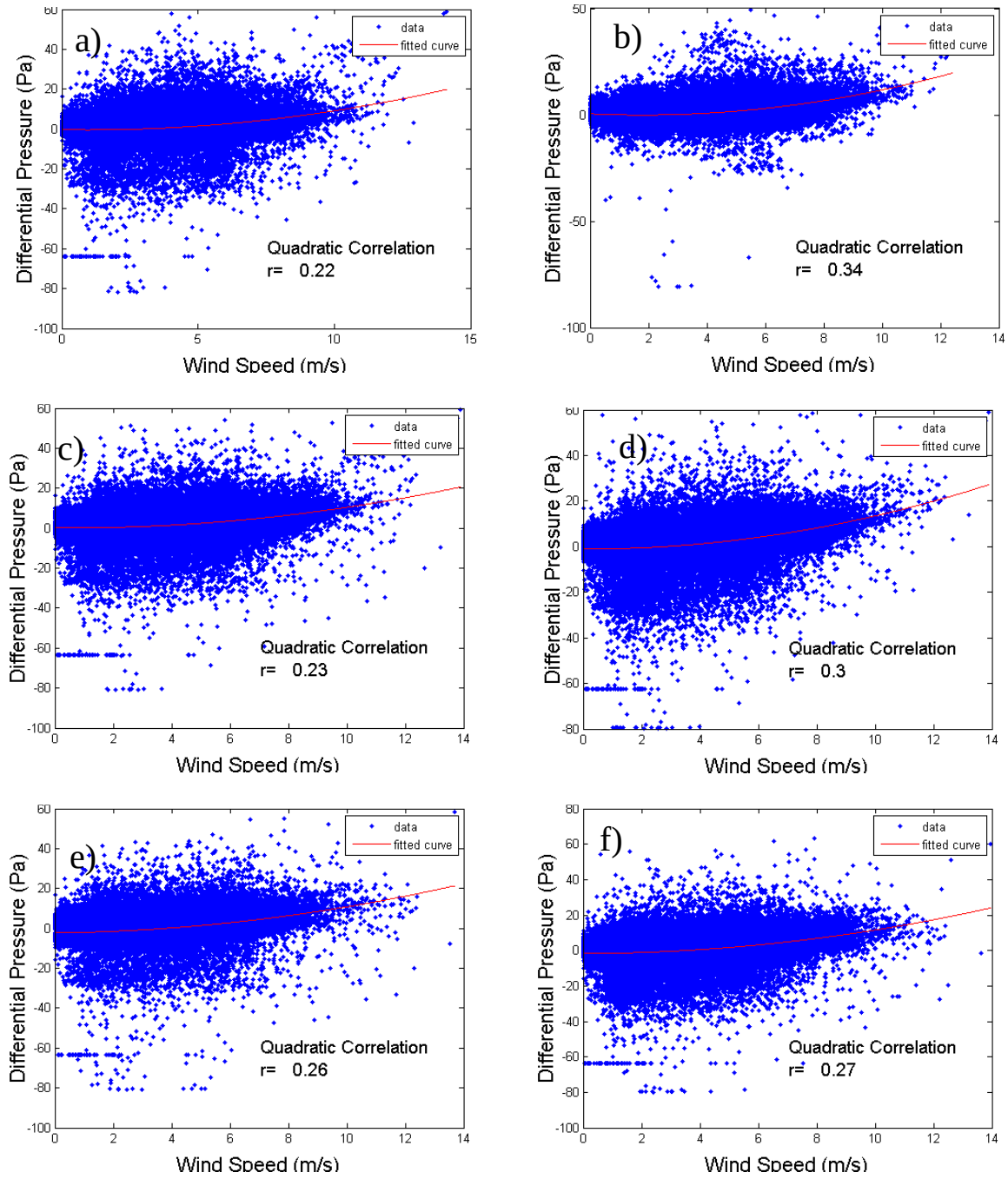

Figure A-33 – Correlation plot for wind speed versus differential external pressure. 10 minute data at a) BH2011-3-2-2.5m b) BH2011-3-2-5m c) BH2011-3-2-7.5m d) BH2011-3-2-10m e) BH2011-3-2-12.5m and f) BH2011-3-2-15m

Correlation plots for external differential pressure – internal differential pressure

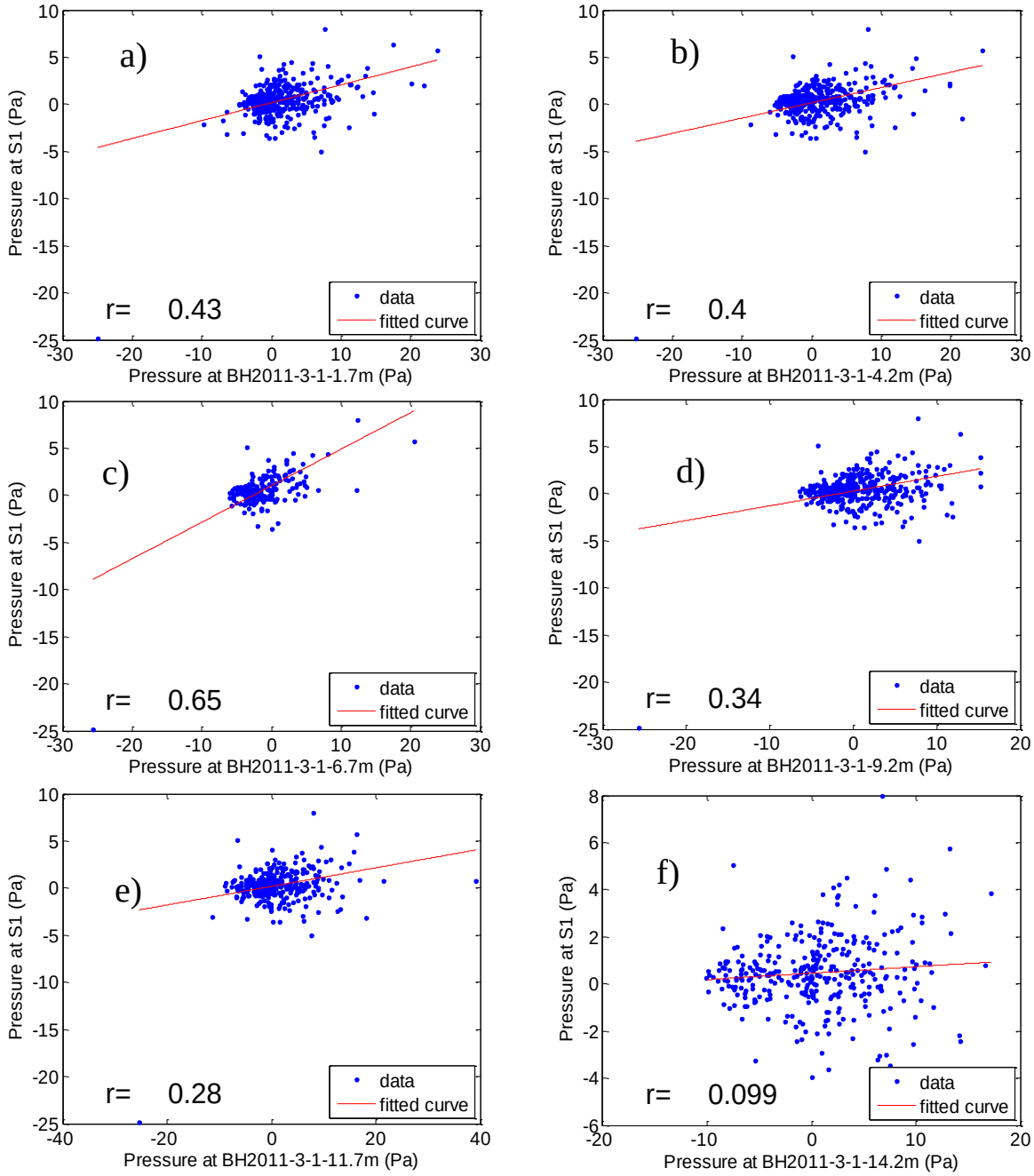

Figure A-34 – Correlation plot for differential external pressure versus differential internal pressure. Daily data at S1 and a) BH2011-3-1-1.7m b) BH2011-3-1-4.2m c) BH2011-3-1-6.7m d) BH2011-3-1-9.2m e) BH2011-3-1-11.7m and f) BH2011-3-1-14.2m

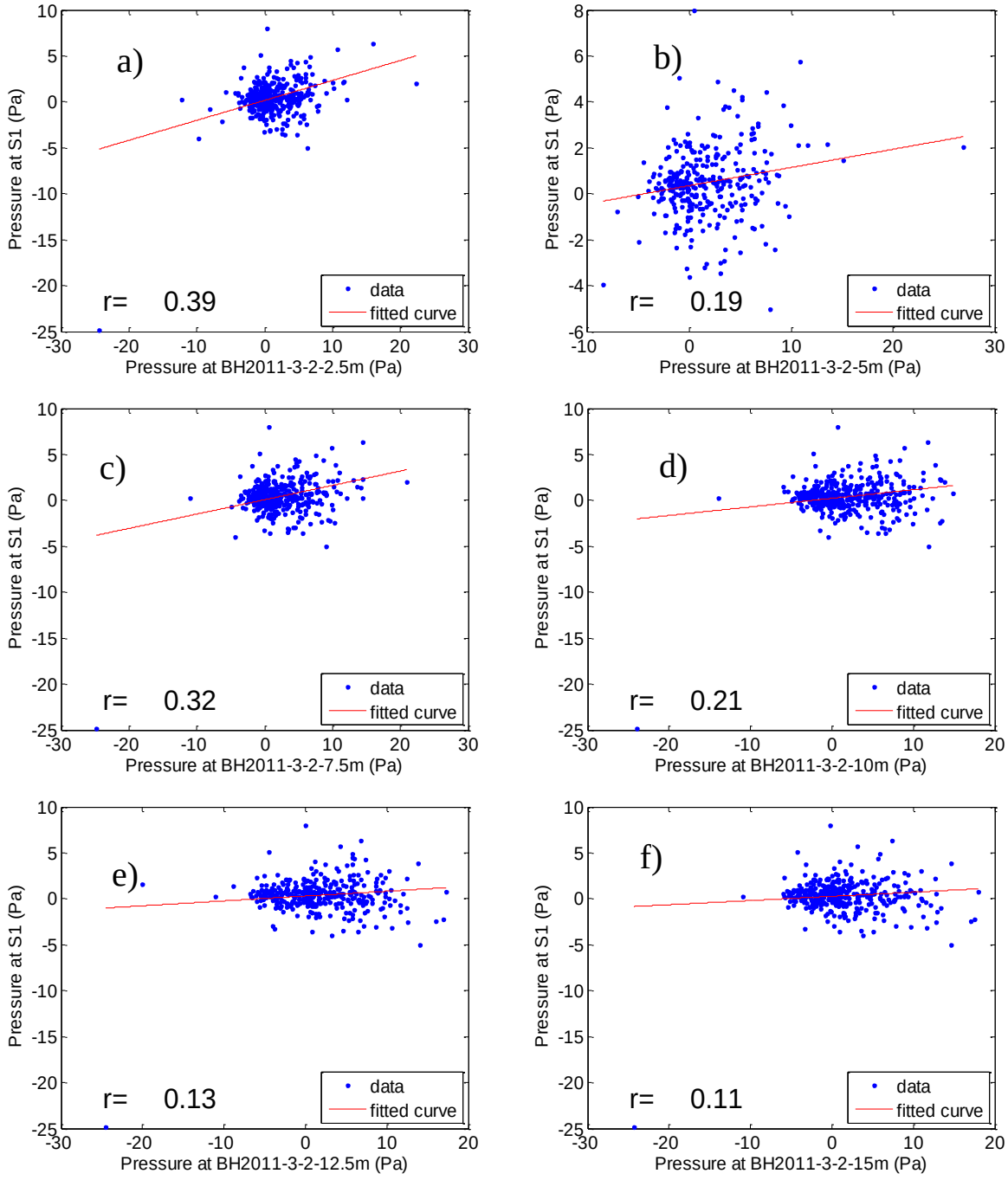

Figure A-35 – Correlation plot for differential external pressure versus differential internal pressure. Daily data at S1 and a) BH2011-3-2-2.5m b) BH2011-3-2-5m c) BH2011-3-2-7.5m d) BH2011-3-2-10m e) BH2011-3-2-12.5m and f) BH2011-3-2-15m

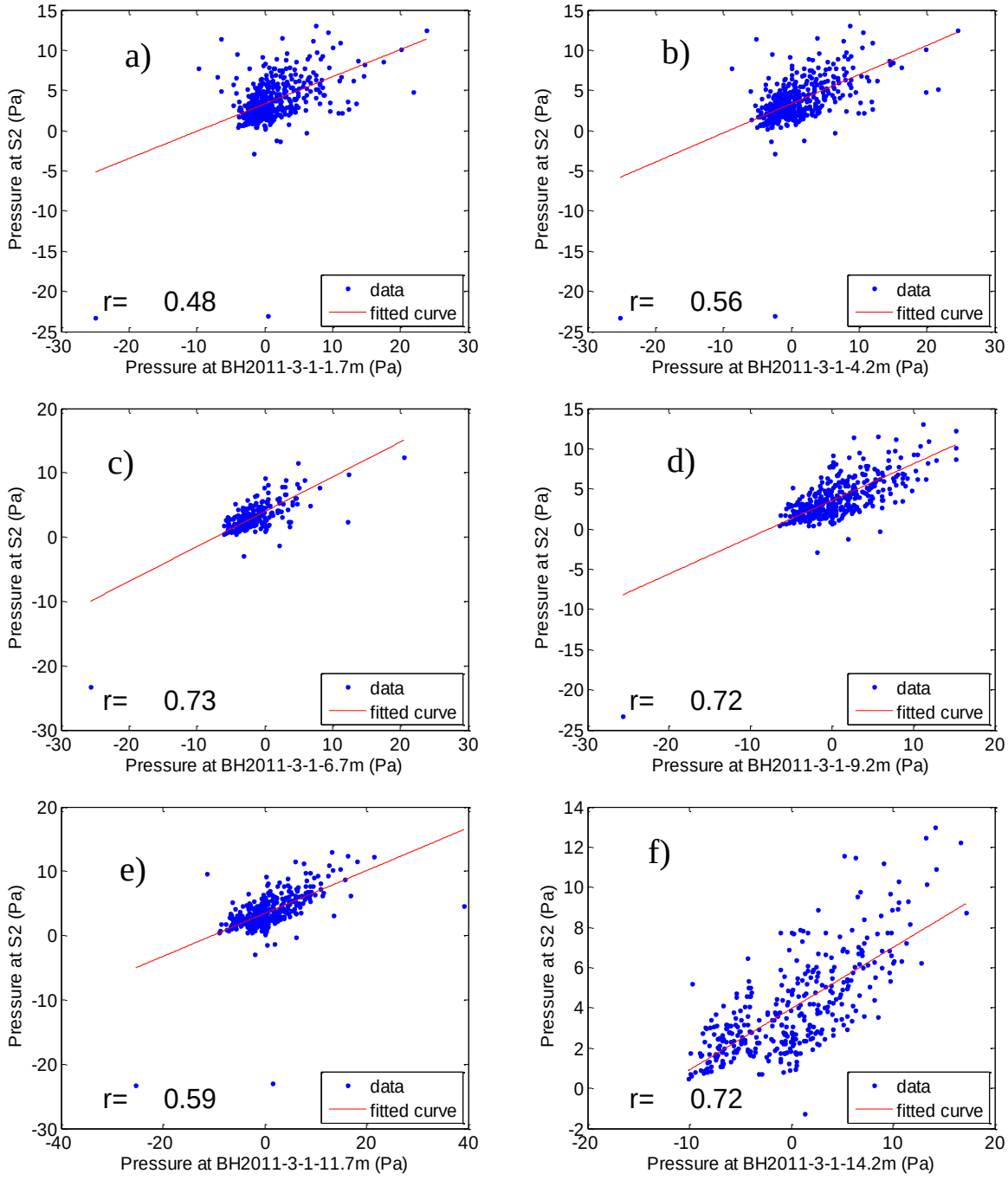

Figure A-36 – Correlation plot for differential external pressure versus differential internal pressure. Daily data at S2 and a) BH2011-3-1-1.7m b) BH2011-3-1-4.2m c) BH2011-3-1-6.7m d) BH2011-3-1-9.2m e) BH2011-3-1-11.7m and f) BH2011-3-1-14.2m

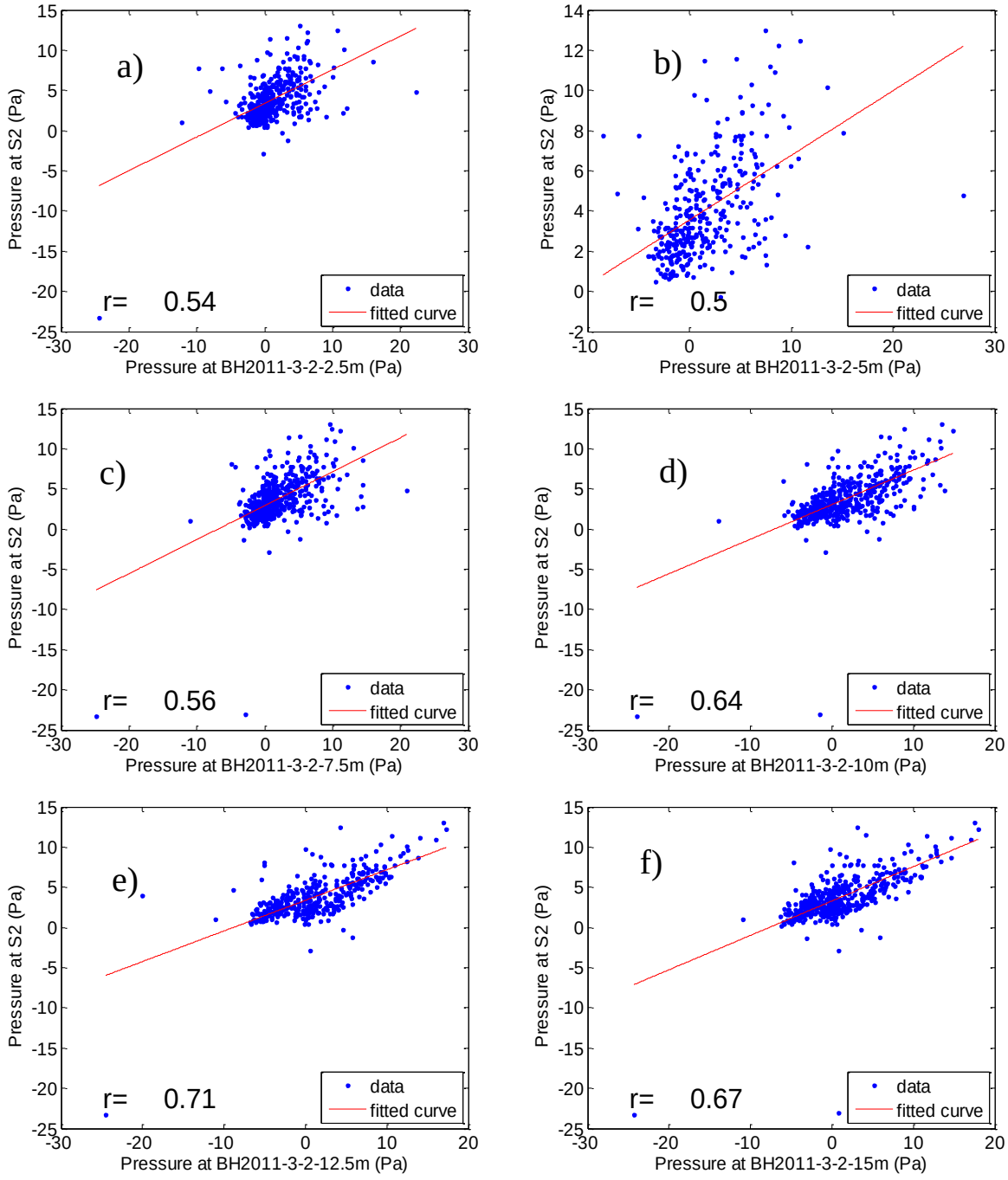

Figure A-37 – Correlation plot for differential external pressure versus differential internal pressure. Daily data at S2 and a) BH2011-3-2-2.5m b) BH2011-3-2-5m c) BH2011-3-2-7.5m d) BH2011-3-2-10m e) BH2011-3-2-12.5m and f) BH2011-3-2-15m

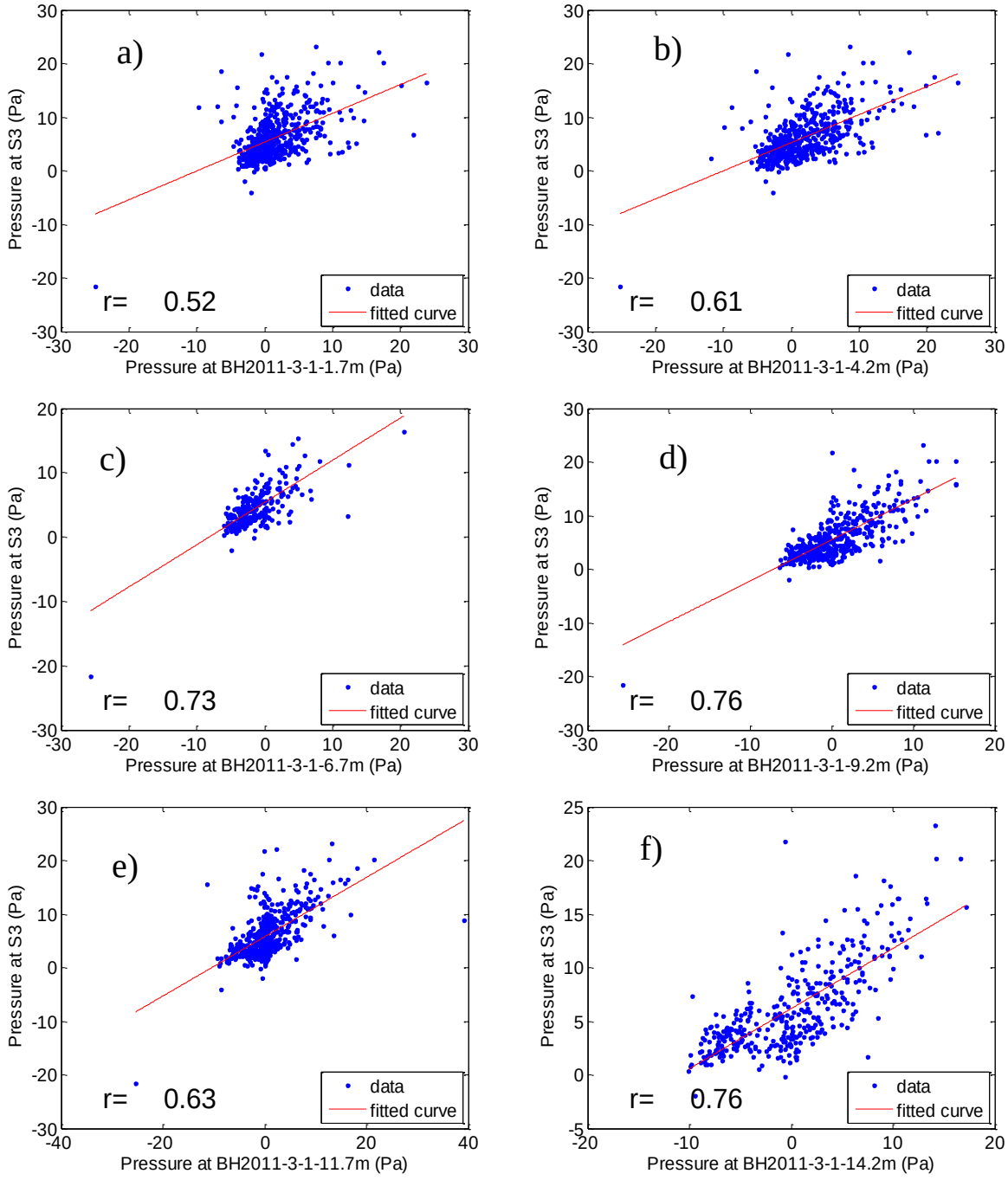

Figure A-38 – Correlation plot for differential external pressure versus differential internal pressure. Daily data at S3 and a) BH2011-3-1-1.7m b) BH2011-3-1-4.2m c) BH2011-3-1-6.7m d) BH2011-3-1-9.2m e) BH2011-3-1-11.7m and f) BH2011-3-1-14.2m

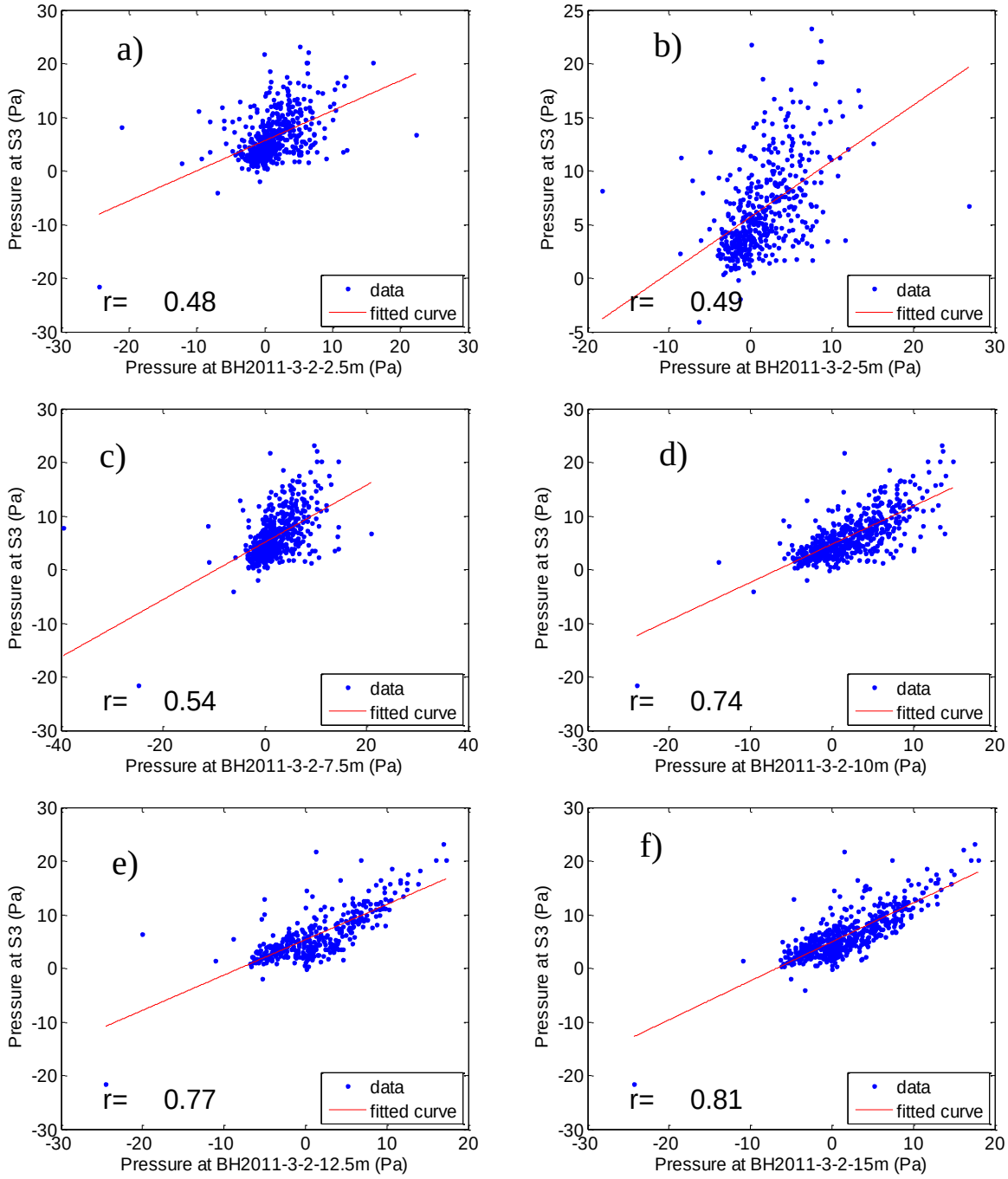

Figure A-39 – Correlation plot for differential external pressure versus differential internal pressure. Daily data at S3 and a) BH2011-3-2-2.5m b) BH2011-3-2-5m c) BH2011-3-2-7.5m d) BH2011-3-2-10m e) BH2011-3-2-12.5m and f) BH2011-3-2-15m

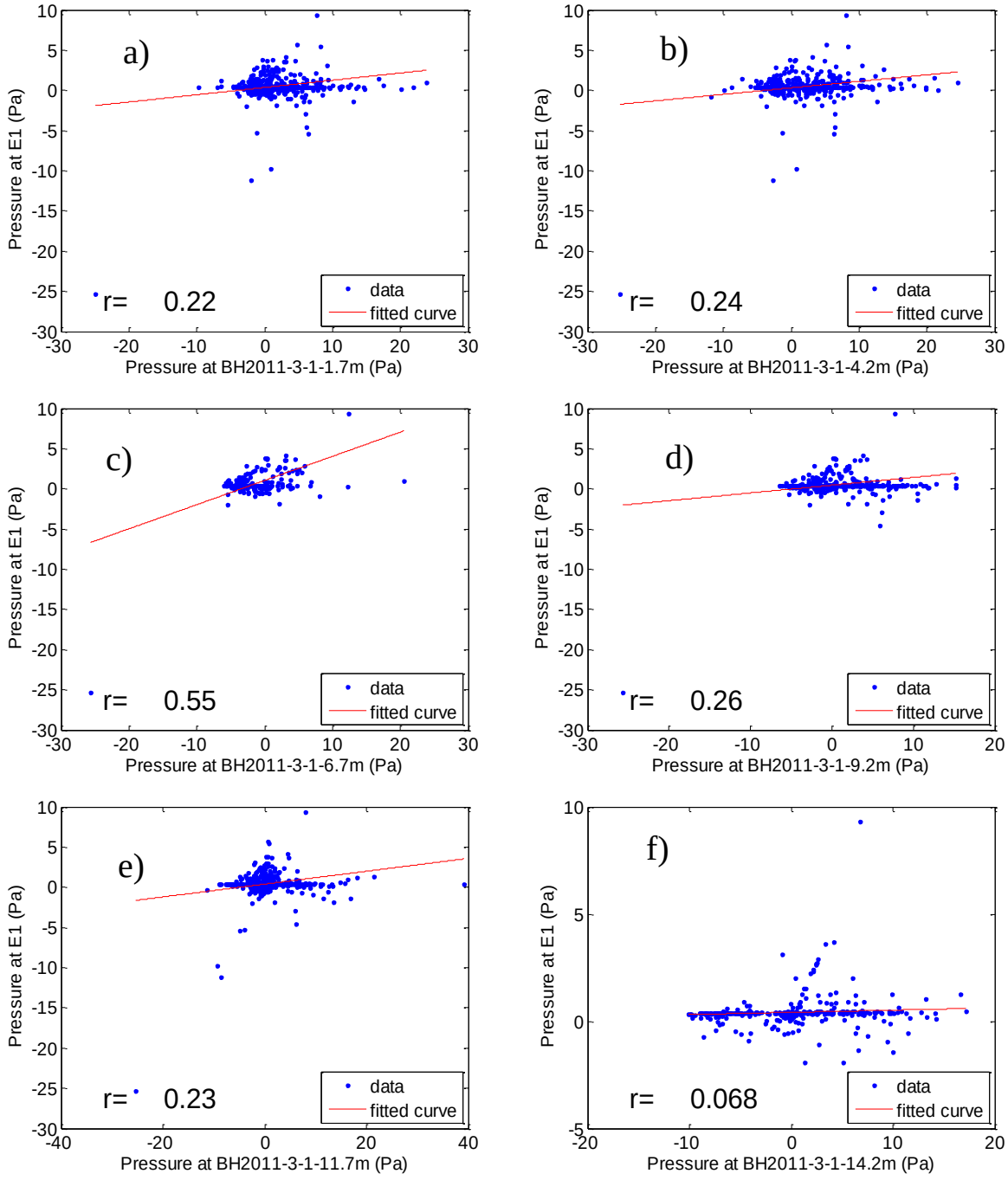

Figure A-40 – Correlation plot for differential external pressure versus differential internal pressure. Daily data at E1 and a) BH2011-3-1-1.7m b) BH2011-3-1-4.2m c) BH2011-3-1-6.7m d) BH2011-3-1-9.2m e) BH2011-3-1-11.7m and f) BH2011-3-1-14.2m

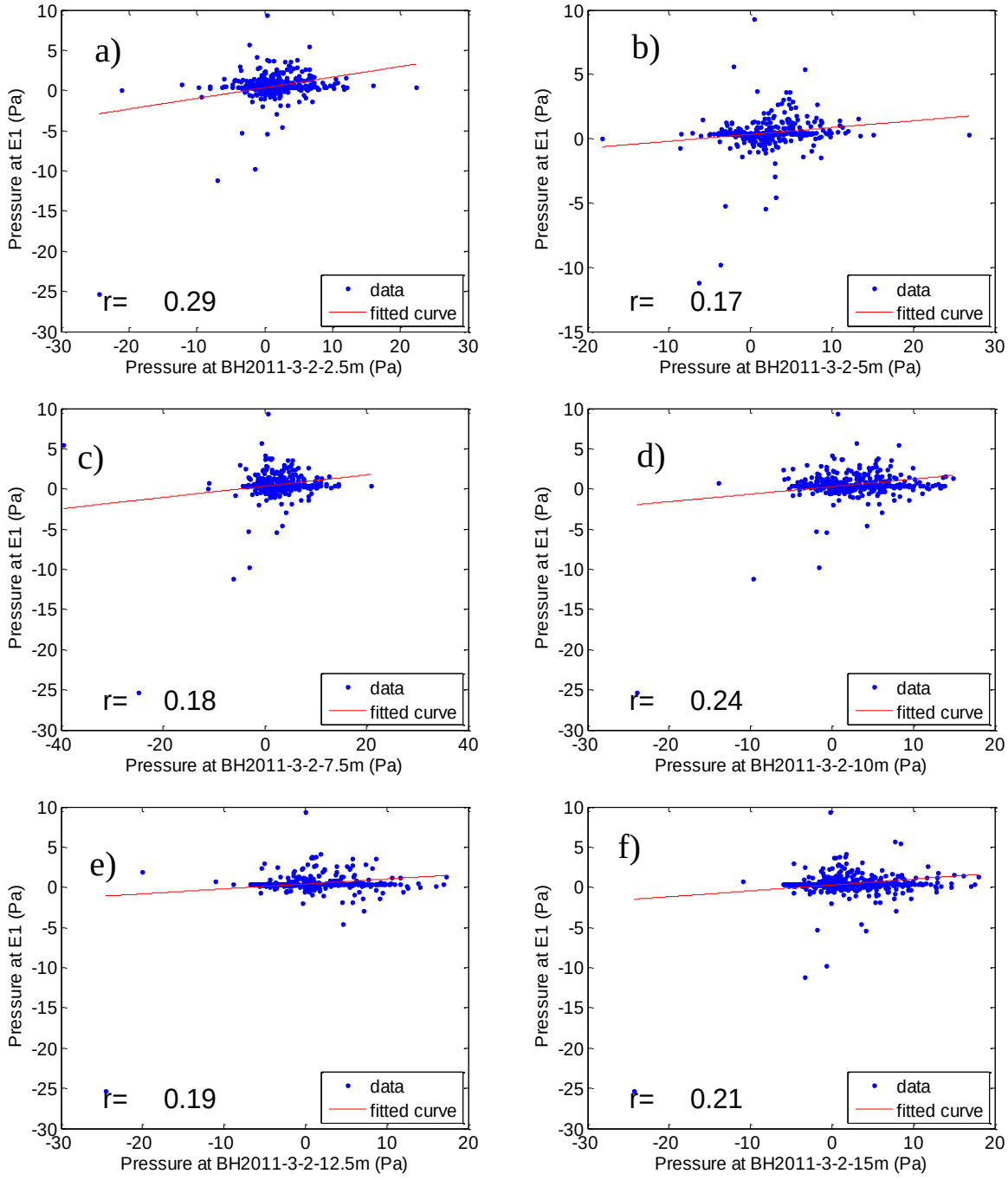

Figure A-41 – Correlation plot for differential external pressure versus differential internal pressure. Daily data at E1 and a) BH2011-3-2-2.5m b) BH2011-3-2-5m c) BH2011-3-2-7.5m d) BH2011-3-2-10m e) BH2011-3-2-12.5m and f) BH2011-3-2-15m

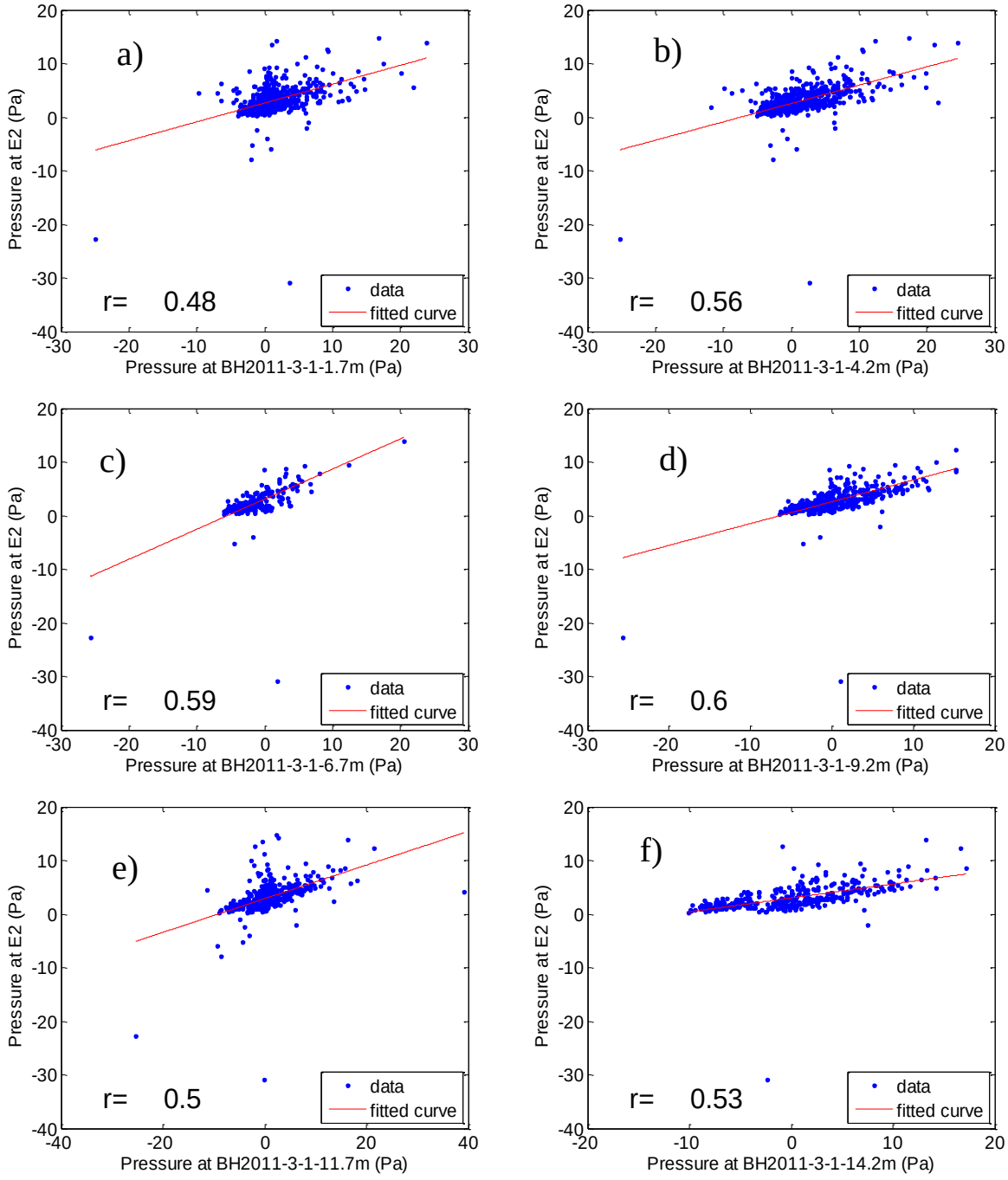

Figure A-42 – Correlation plot for differential external pressure versus differential internal pressure. Daily data at E2 and a) BH2011-3-1-1.7m b) BH2011-3-1-4.2m c) BH2011-3-1-6.7m d) BH2011-3-1-9.2m e) BH2011-3-1-11.7m and f) BH2011-3-1-14.2m

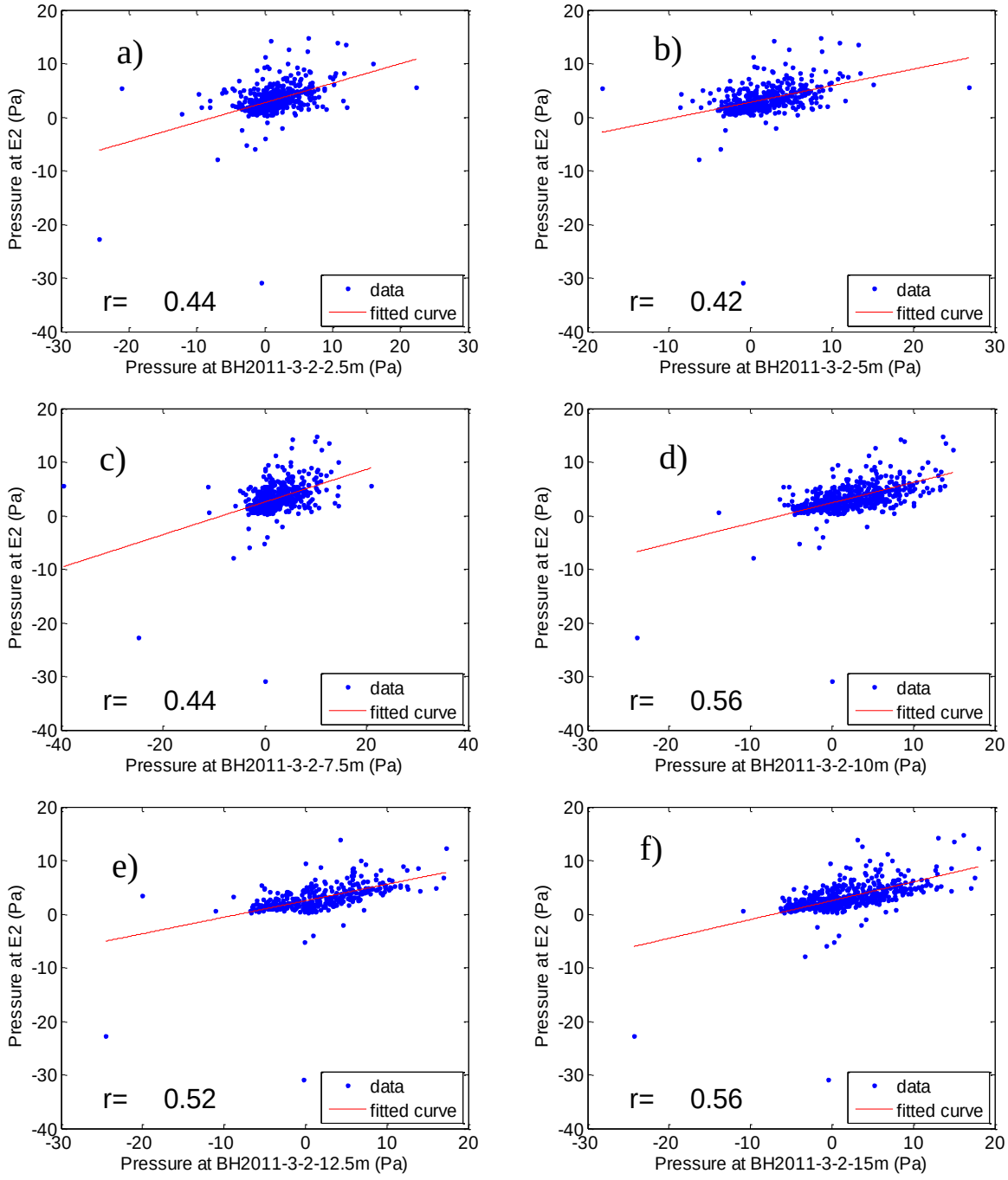

Figure A-43 – Correlation plot for differential external pressure versus differential internal pressure. Daily data at E2 and a) BH2011-3-2-2.5m b) BH2011-3-2-5m c) BH2011-3-2-7.5m d) BH2011-3-2-10m e) BH2011-3-2-12.5m and f) BH2011-3-2-15m

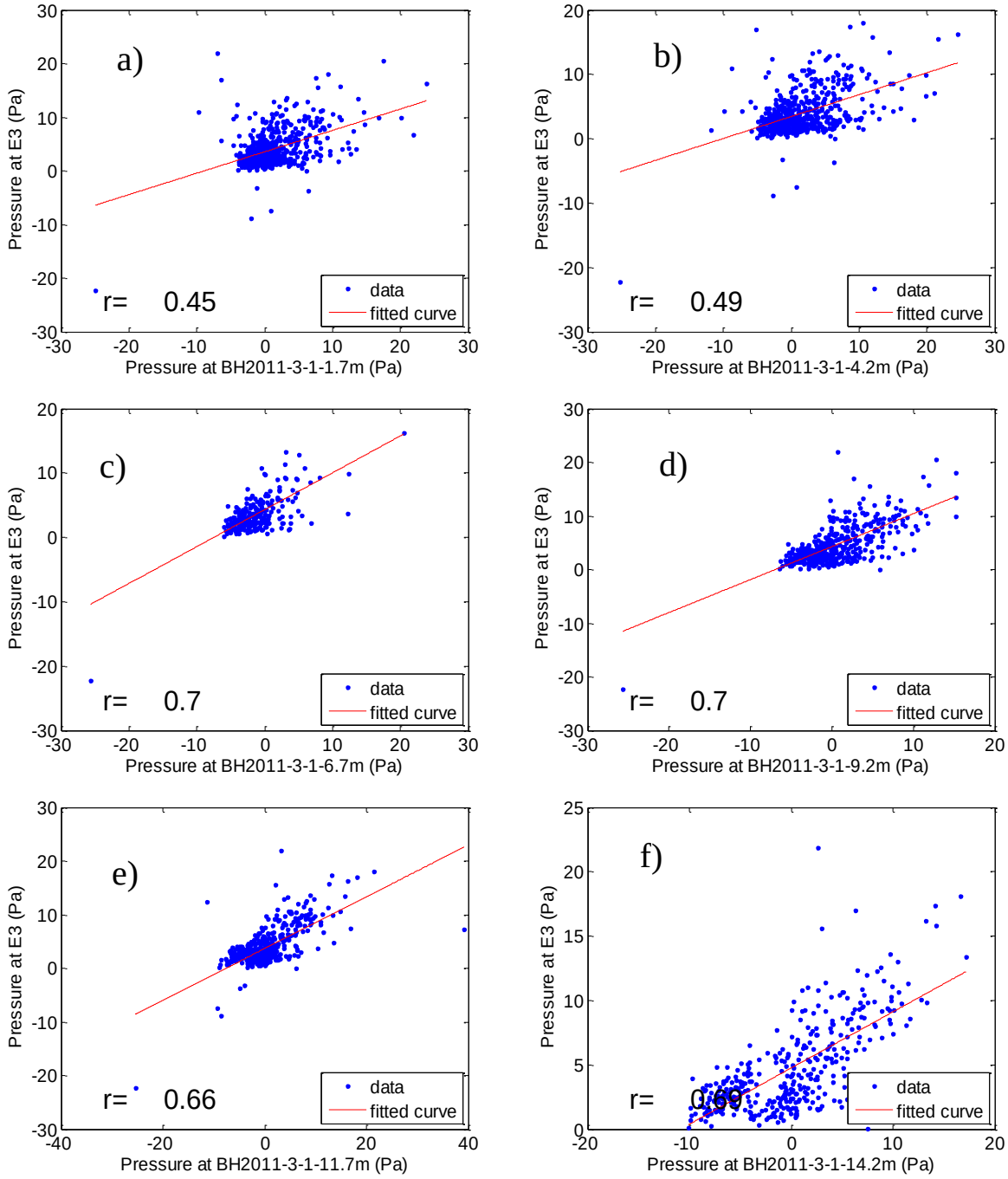

Figure A-44 – Correlation plot for differential external pressure versus differential internal pressure. Daily data at E3 and a) BH2011-3-1-1.7m b) BH2011-3-1-4.2m c) BH2011-3-1-6.7m d) BH2011-3-1-9.2m e) BH2011-3-1-11.7m and f) BH2011-3-1-14.2m

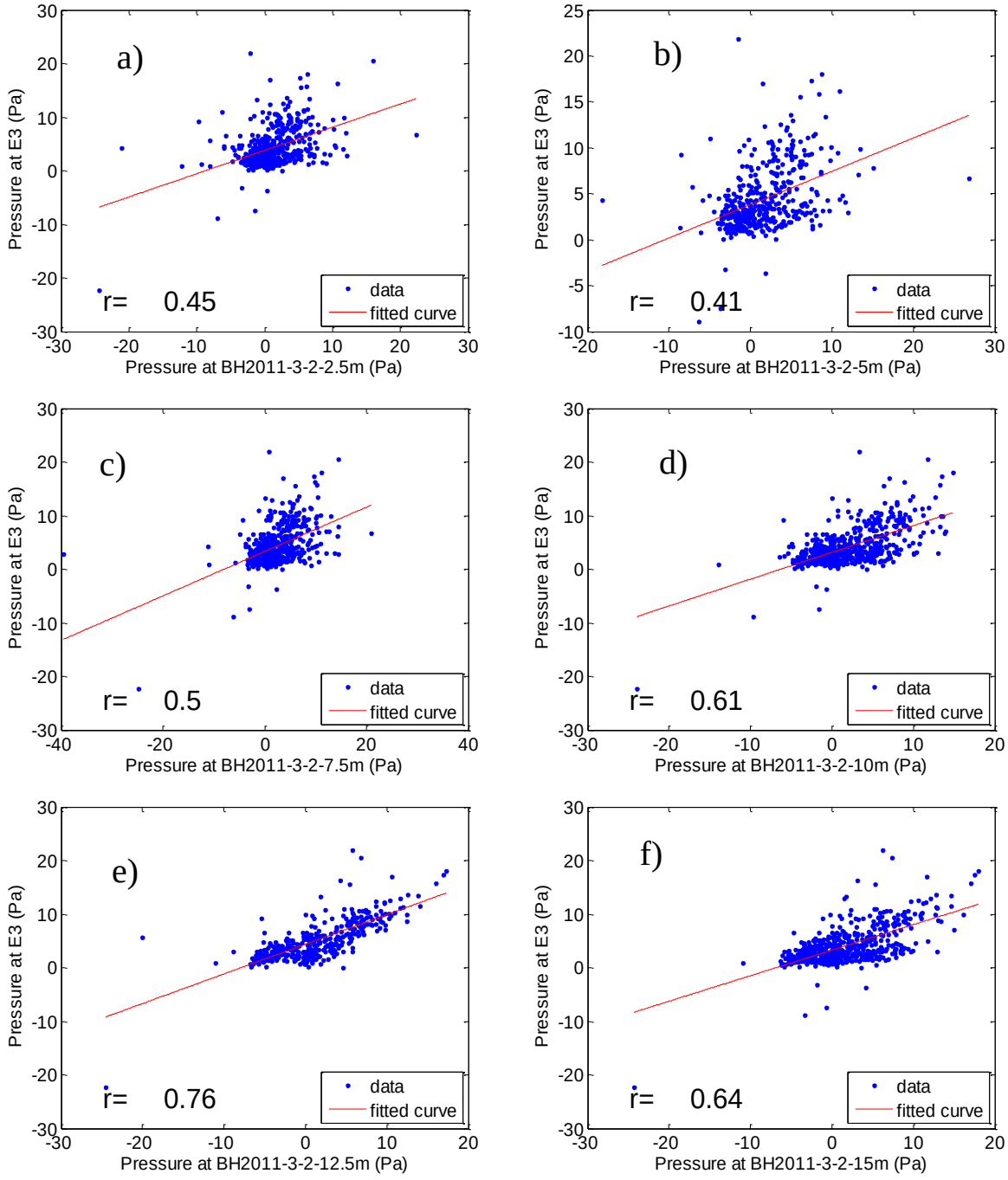

Figure A-45 – Correlation plot for differential external pressure versus differential internal pressure. Daily data at E3 and a) BH2011-3-2-2.5m b) BH2011-3-2-5m c) BH2011-3-2-7.5m d) BH2011-3-2-10m e) BH2011-3-2-12.5m and f) BH2011-3-2-15m

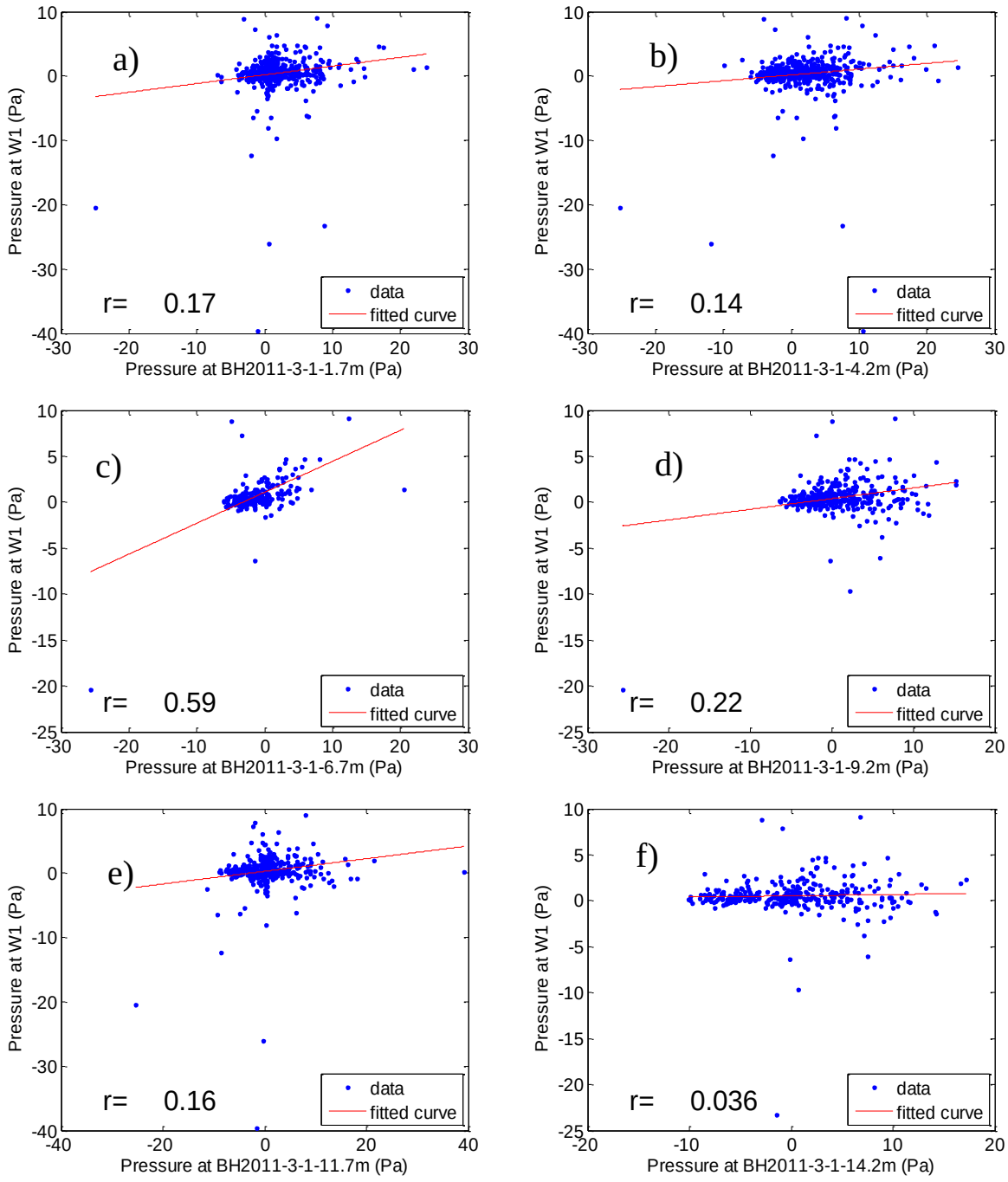

Figure A-46 – Correlation plot for differential external pressure versus differential internal pressure. Daily data at W1 and a) BH2011-3-1-1.7m b) BH2011-3-1-4.2m c) BH2011-3-1-6.7m d) BH2011-3-1-9.2m e) BH2011-3-1-11.7m and f) BH2011-3-1-14.2m

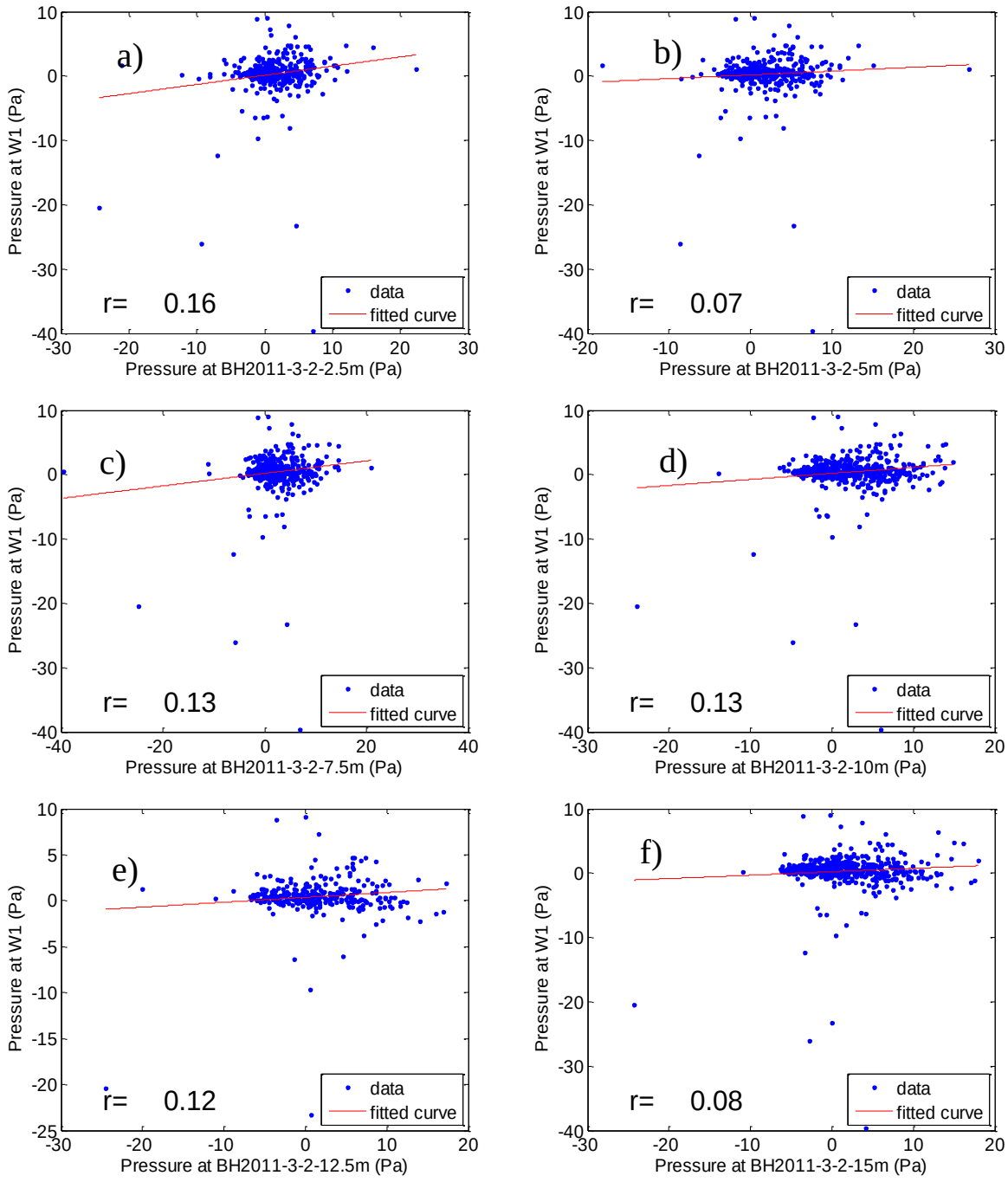

Figure A-47 – Correlation plot for differential external pressure versus differential internal pressure. Daily data at W1 and a) BH2011-3-2-2.5m b) BH2011-3-2-5m c) BH2011-3-2-7.5m d) BH2011-3-2-10m e) BH2011-3-2-12.5m and f) BH2011-3-2-15m

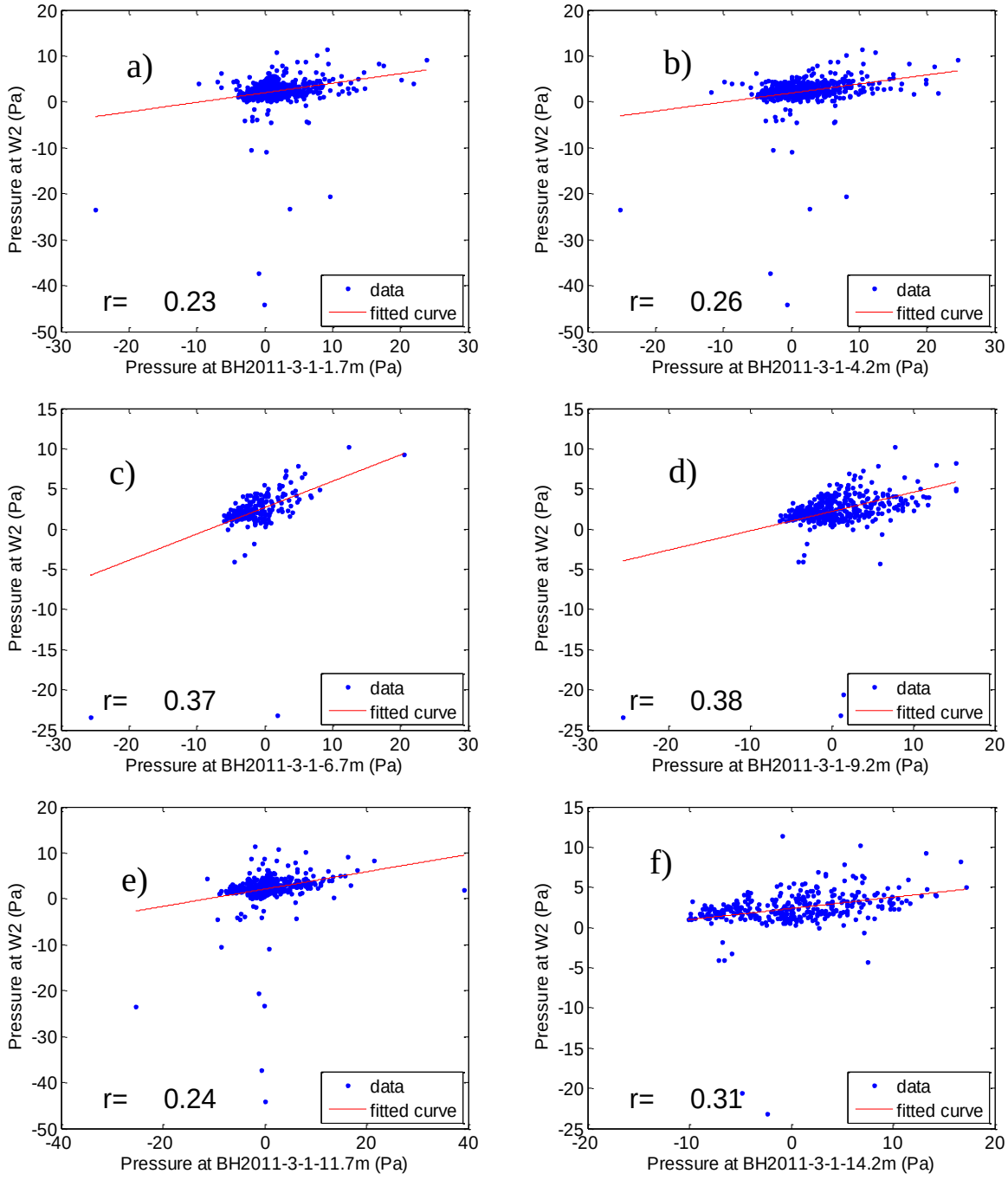

Figure A-48 – Correlation plot for differential external pressure versus differential internal pressure. Daily data at W2 and a) BH2011-3-1-1.7m b) BH2011-3-1-4.2m c) BH2011-3-1-6.7m d) BH2011-3-1-9.2m e) BH2011-3-1-11.7m and f) BH2011-3-1-14.2m

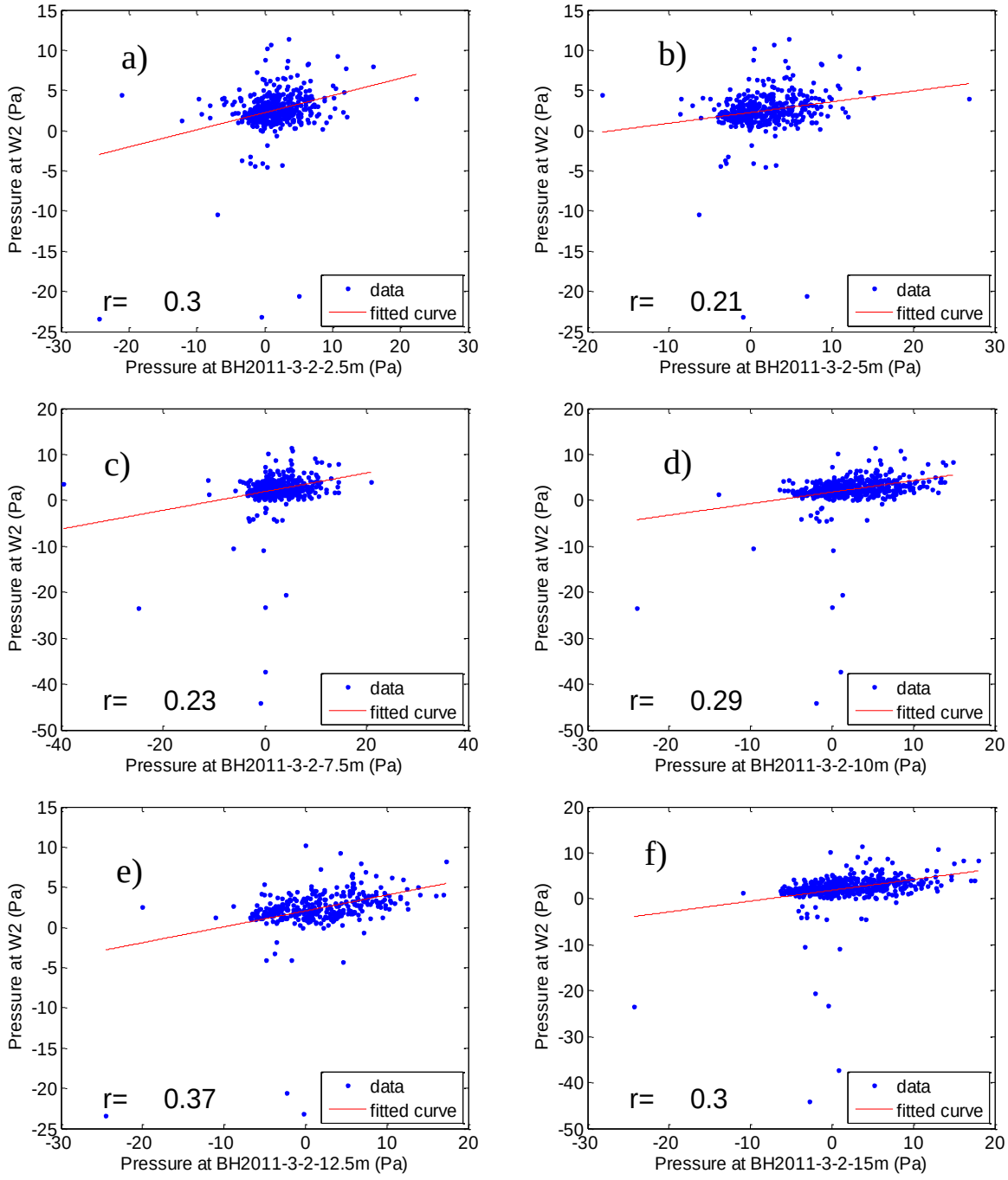

Figure A-49 – Correlation plot for differential external pressure versus differential internal pressure. Daily data at W2 and a) BH2011-3-2-2.5m b) BH2011-3-2-5m c) BH2011-3-2-7.5m d) BH2011-3-2-10m e) BH2011-3-2-12.5m and f) BH2011-3-2-15m

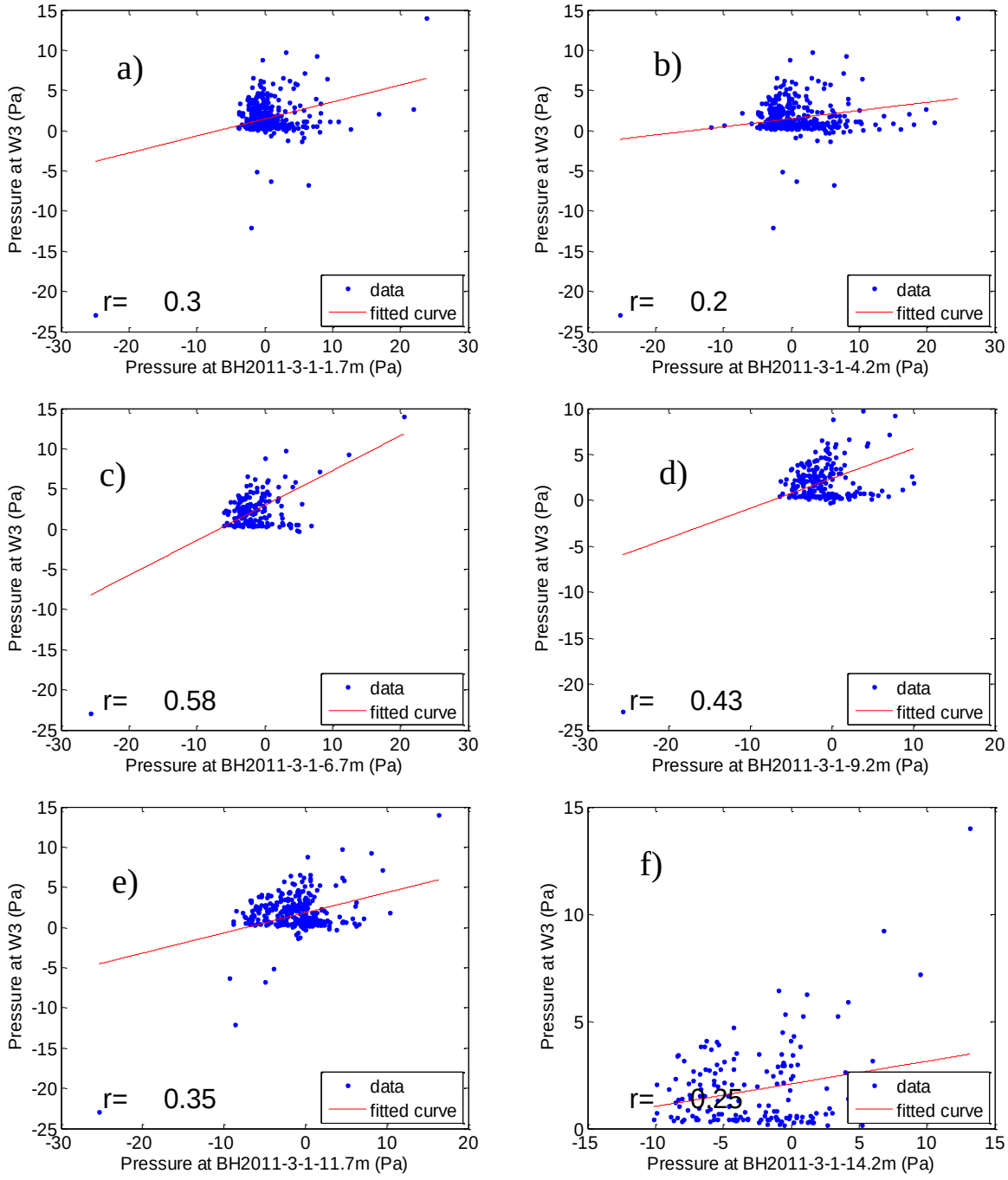

Figure A-50 – Correlation plot for differential external pressure versus differential internal pressure. Daily data at W3 and a) BH2011-3-1-1.7m b) BH2011-3-1-4.2m c) BH2011-3-1-6.7m d) BH2011-3-1-9.2m e) BH2011-3-1-11.7m and f) BH2011-3-1-14.2m

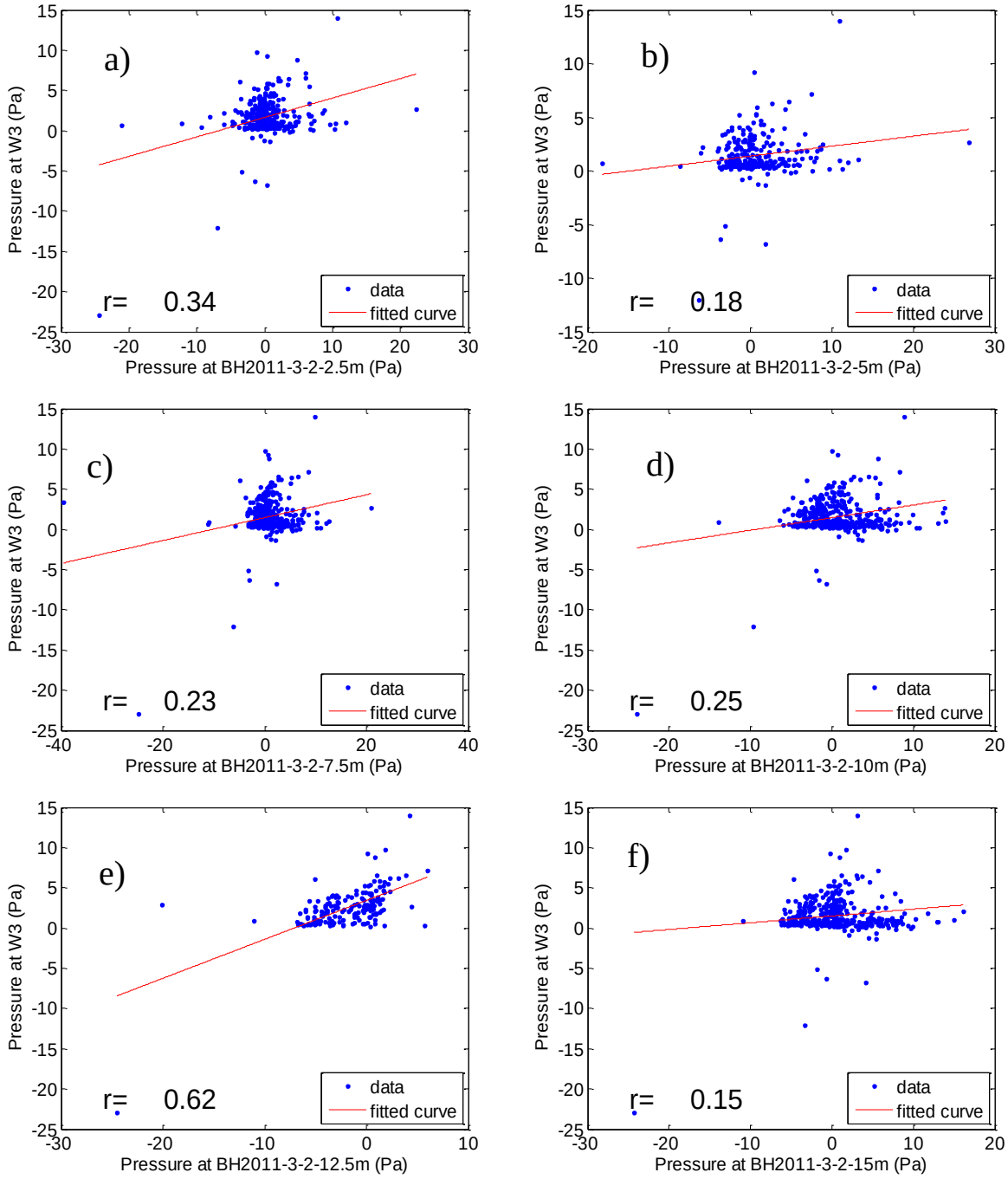

Figure A-51 – Correlation plot for differential external pressure versus differential internal pressure. Daily data at W3 and a) BH2011-3-2-2.5m b) BH2011-3-2-5m c) BH2011-3-2-7.5m d) BH2011-3-2-10m e) BH2011-3-2-12.5m and f) BH2011-3-2-15m

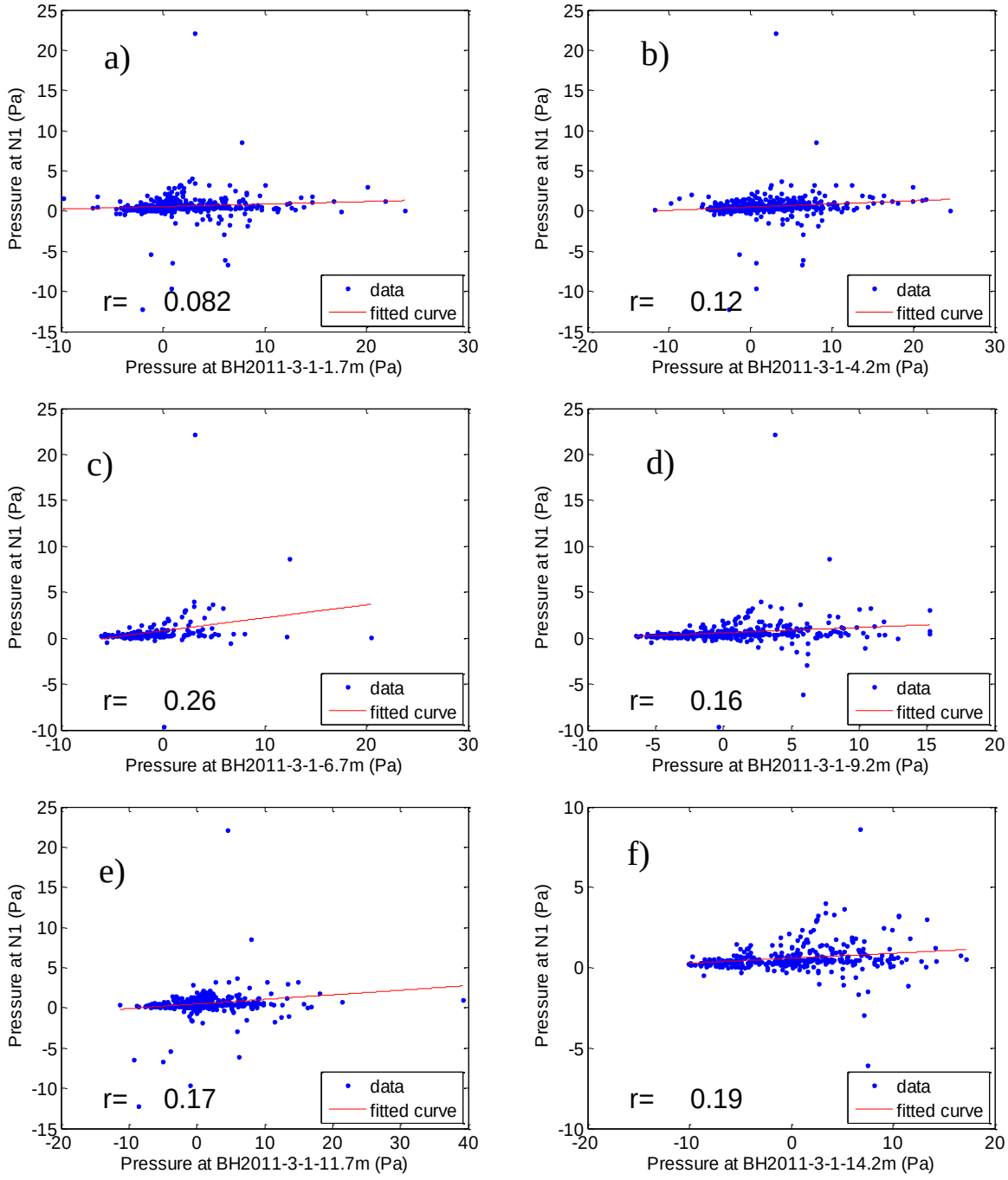

Figure A-52 – Correlation plot for differential external pressure versus differential internal pressure. Daily data at N1 and a) BH2011-3-1-1.7m b) BH2011-3-1-4.2m c) BH2011-3-1-6.7m d) BH2011-3-1-9.2m e) BH2011-3-1-11.7m and f) BH2011-3-1-14.2m

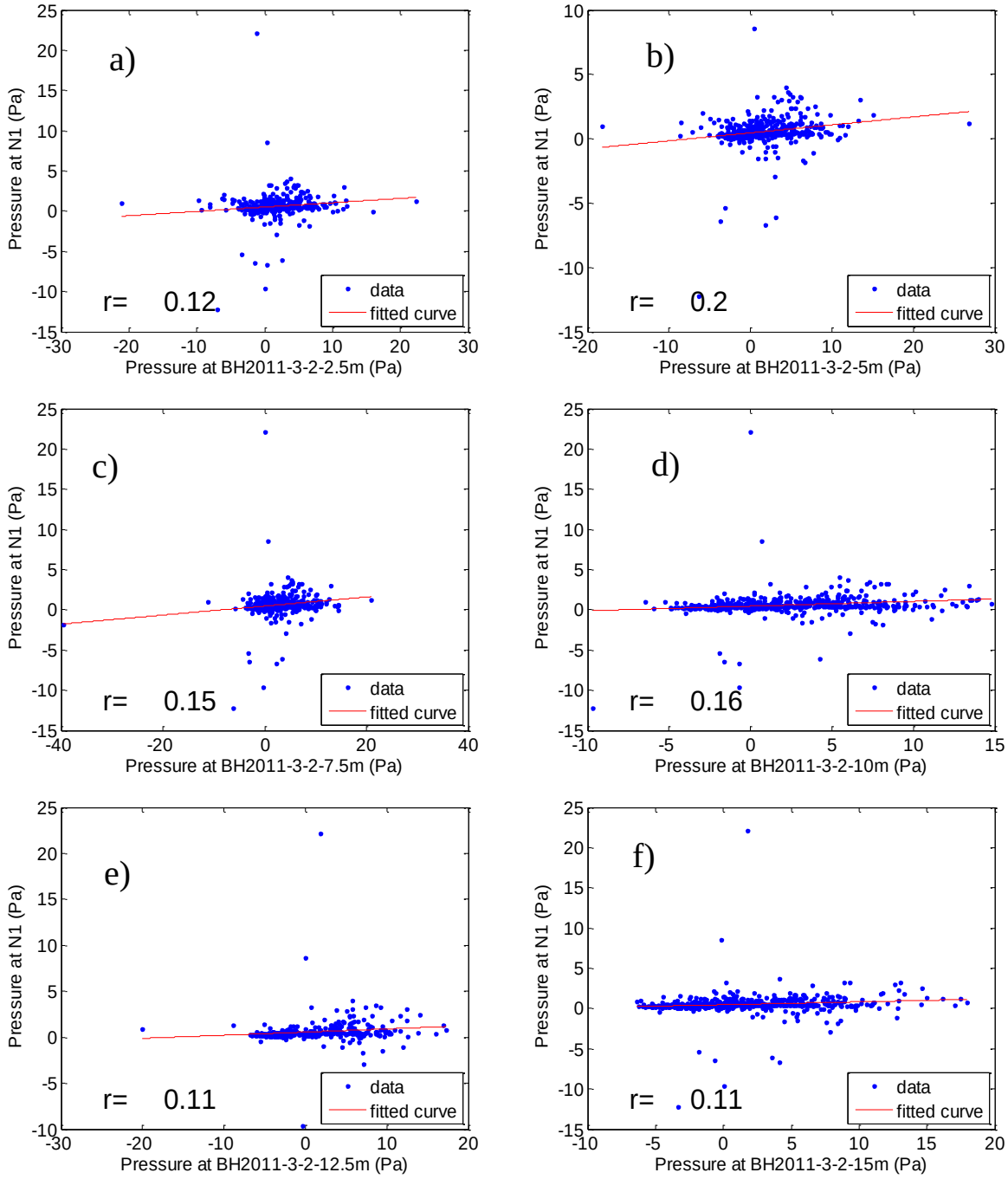

Figure A-53 – Correlation plot for differential external pressure versus differential internal pressure. Daily data at N1 and a) BH2011-3-2-2.5m b) BH2011-3-2-5m c) BH2011-3-2-7.5m d) BH2011-3-2-10m e) BH2011-3-2-12.5m and f) BH2011-3-2-15m

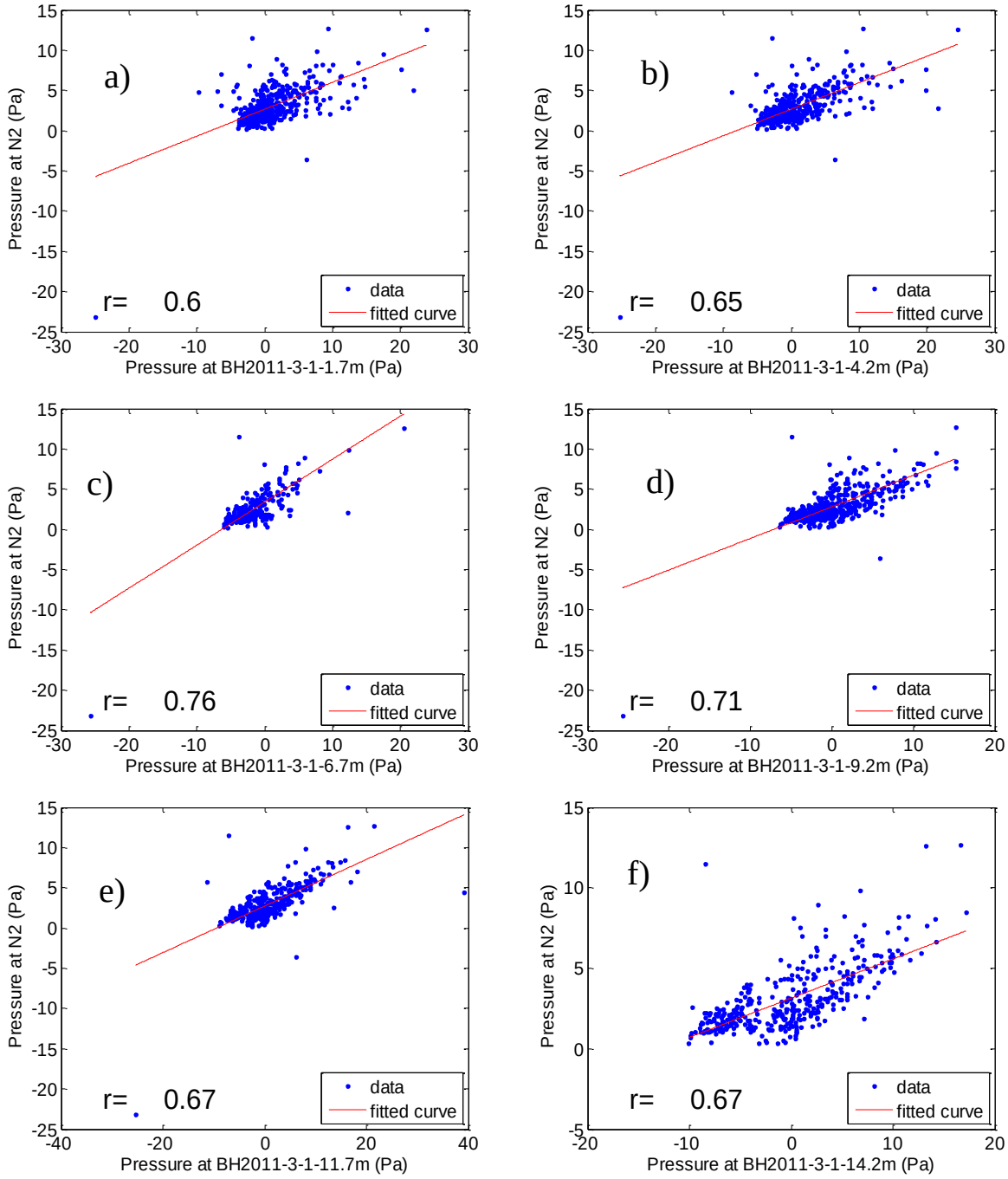

Figure A-54 – Correlation plot for differential external pressure versus differential internal pressure. Daily data at N2 and a) BH2011-3-1-1.7m b) BH2011-3-1-4.2m c) BH2011-3-1-6.7m d) BH2011-3-1-9.2m e) BH2011-3-1-11.7m and f) BH2011-3-1-14.2m

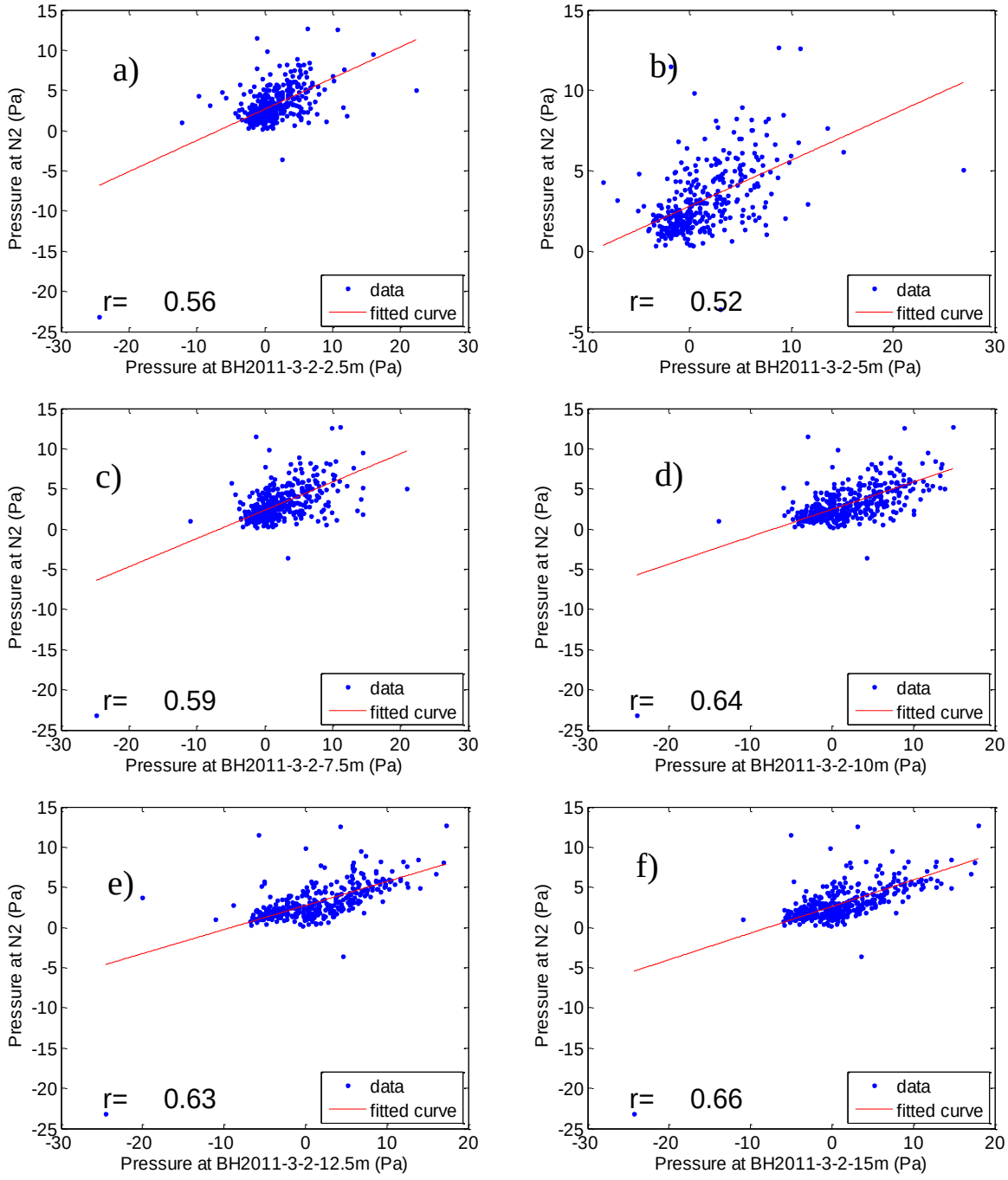

Figure A-55 – Correlation plot for differential external pressure versus differential internal pressure. Daily data at N2 and a) BH2011-3-2-2.5m b) BH2011-3-2-5m c) BH2011-3-2-7.5m d) BH2011-3-2-10m e) BH2011-3-2-12.5m and f) BH2011-3-2-15m

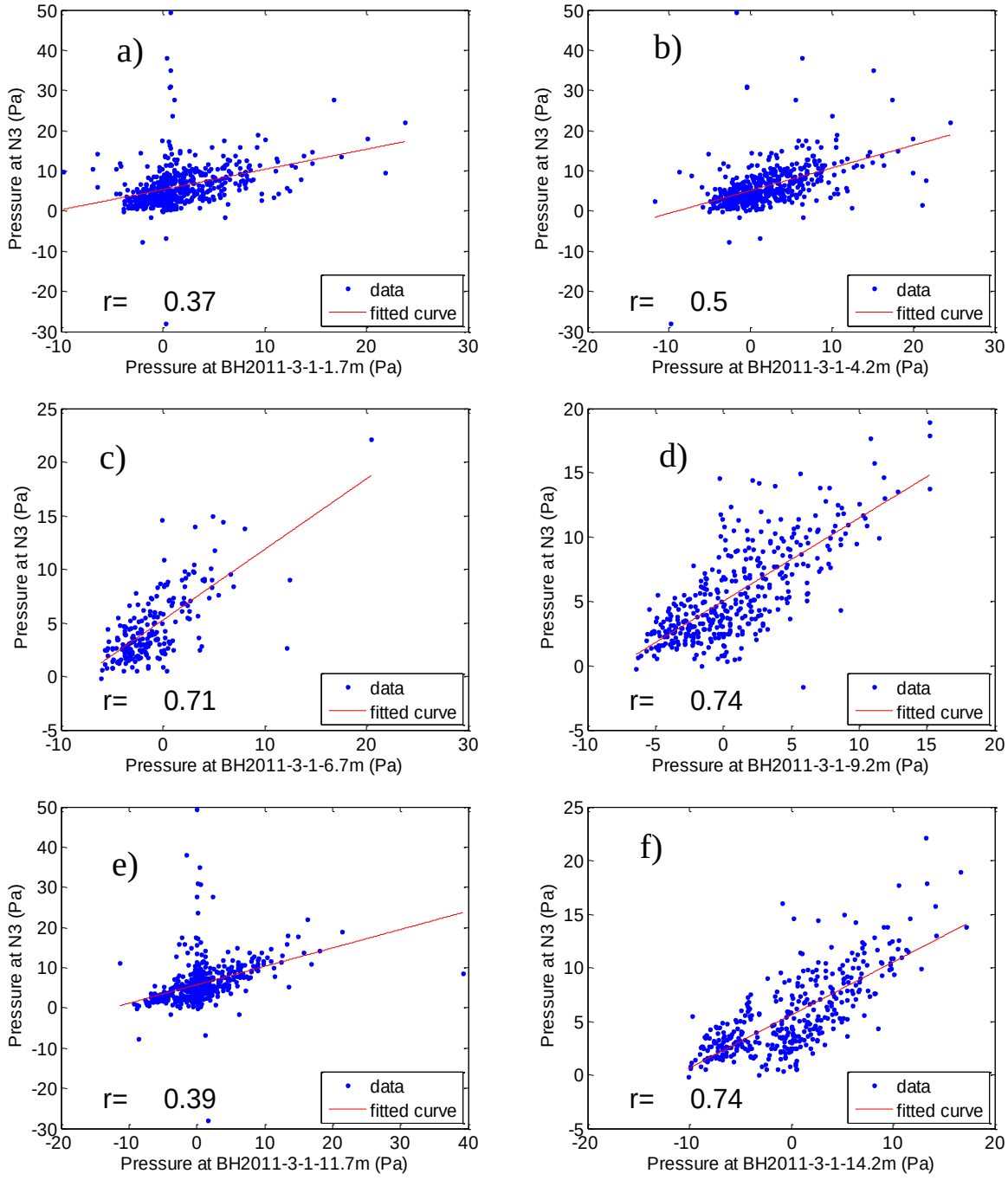

Figure A-56 – Correlation plot for differential external pressure versus differential internal pressure. Daily data at N3 and a) BH2011-3-1-1.7m b) BH2011-3-1-4.2m c) BH2011-3-1-6.7m d) BH2011-3-1-9.2m e) BH2011-3-1-11.7m and f) BH2011-3-1-14.2m

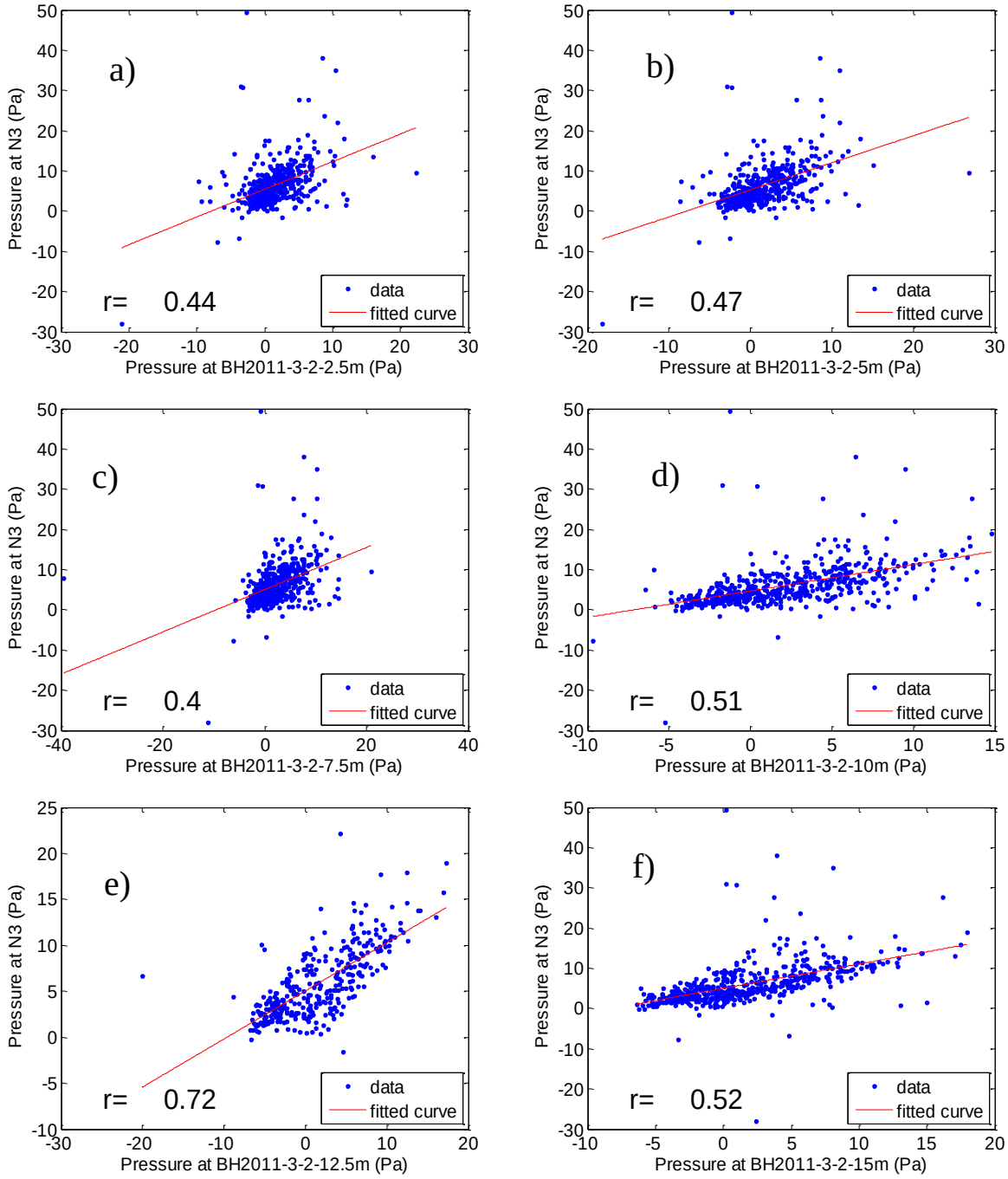

Figure A-57 – Correlation plot for differential external pressure versus differential internal pressure. Daily data at N3 and a) BH2011-3-2-2.5m b) BH2011-3-2-5m c) BH2011-3-2-7.5m d) BH2011-3-2-10m e) BH2011-3-2-12.5m and f) BH2011-3-2-15m

Correlation plots for internal differential pressure – internal differential pressure for the location above

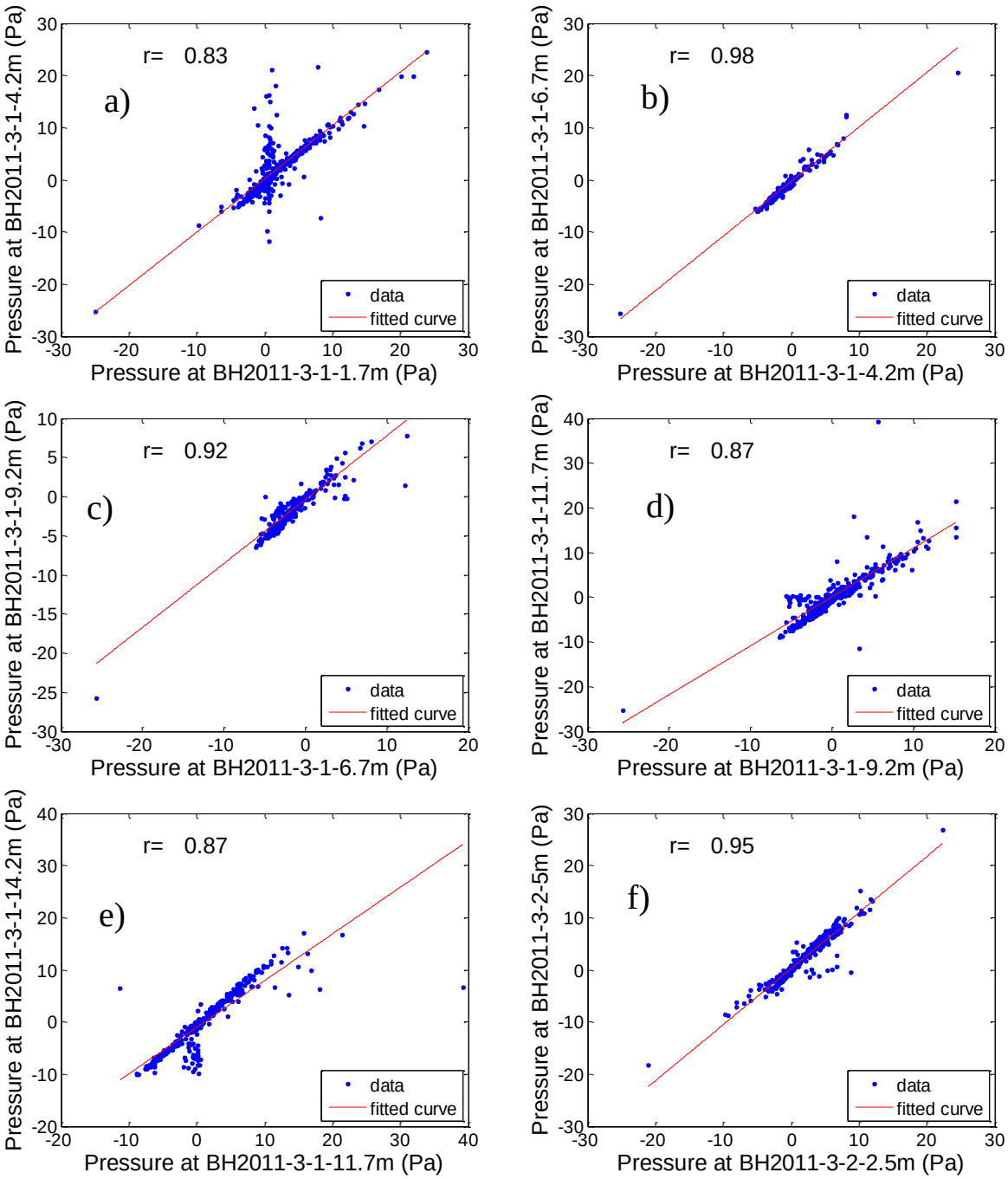

Figure A-58 – Correlation plot for differential internal pressure versus the location below. Daily data at a) BH2011-3-1-1.7m and BH2011-3-1-4.2m b) BH2011-3-1-4.2m and BH2011--6.7m c) BH2011-3-1-6.7m and BH2011-3-1-9.2m d) BH2011-3-1-9.2m and BH2011-3-1-11.7m e) BH2011-3-1-11.7m and BH2011-3-1-14.2m and f) BH2011-3-2-2.5m and BH2011-3-2-5m

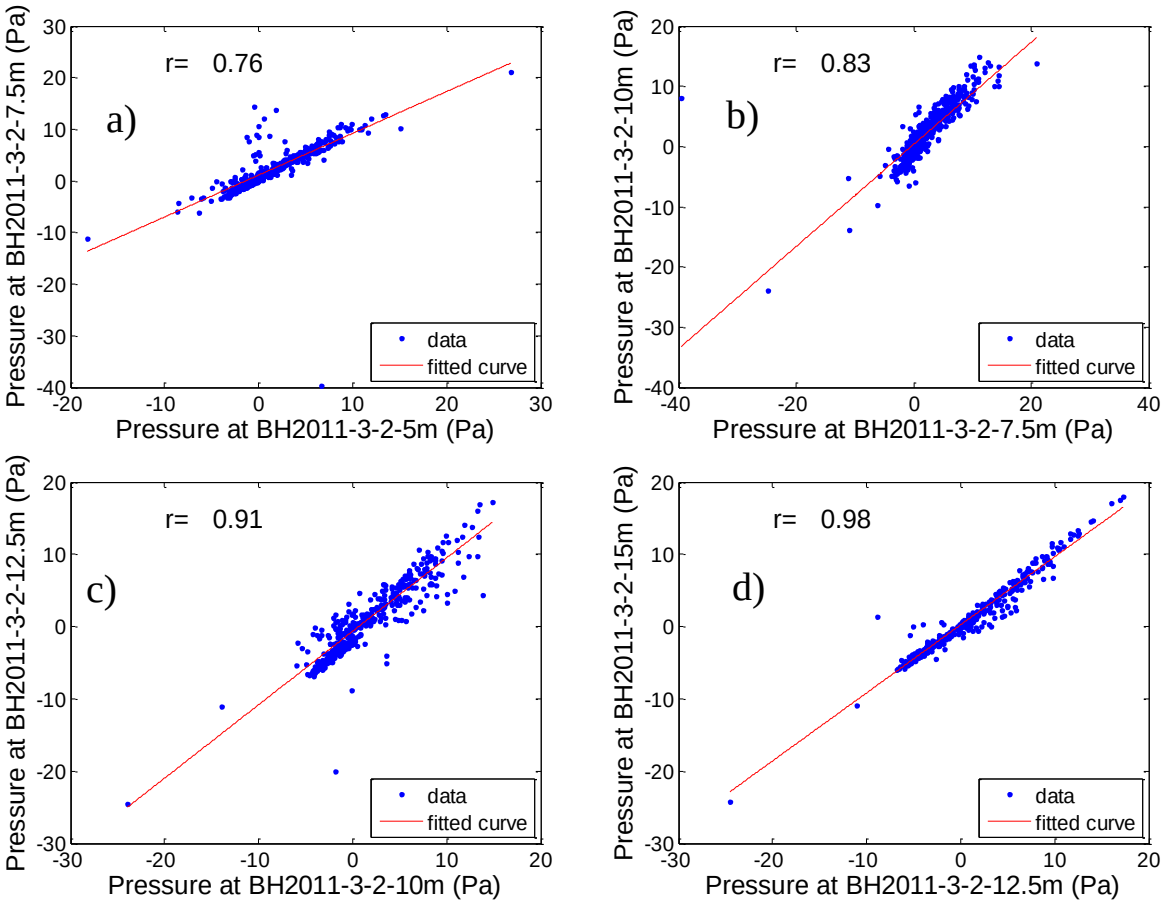

Figure A-59 – Correlation plot for differential internal pressure versus the location below. Daily data at a) BH2011-3-2-5m and BH2011-3-2-7.5m b) BH2011-3-2-7.5m and BH2011-3-2-10m c) BH2011-3-2-10m and BH2011-3-2-12.5mm d) BH2011-3-1-12.5m and BH2011-3-1-15m

Correlation plots for internal differential pressure – internal differential pressure for the location laterally across

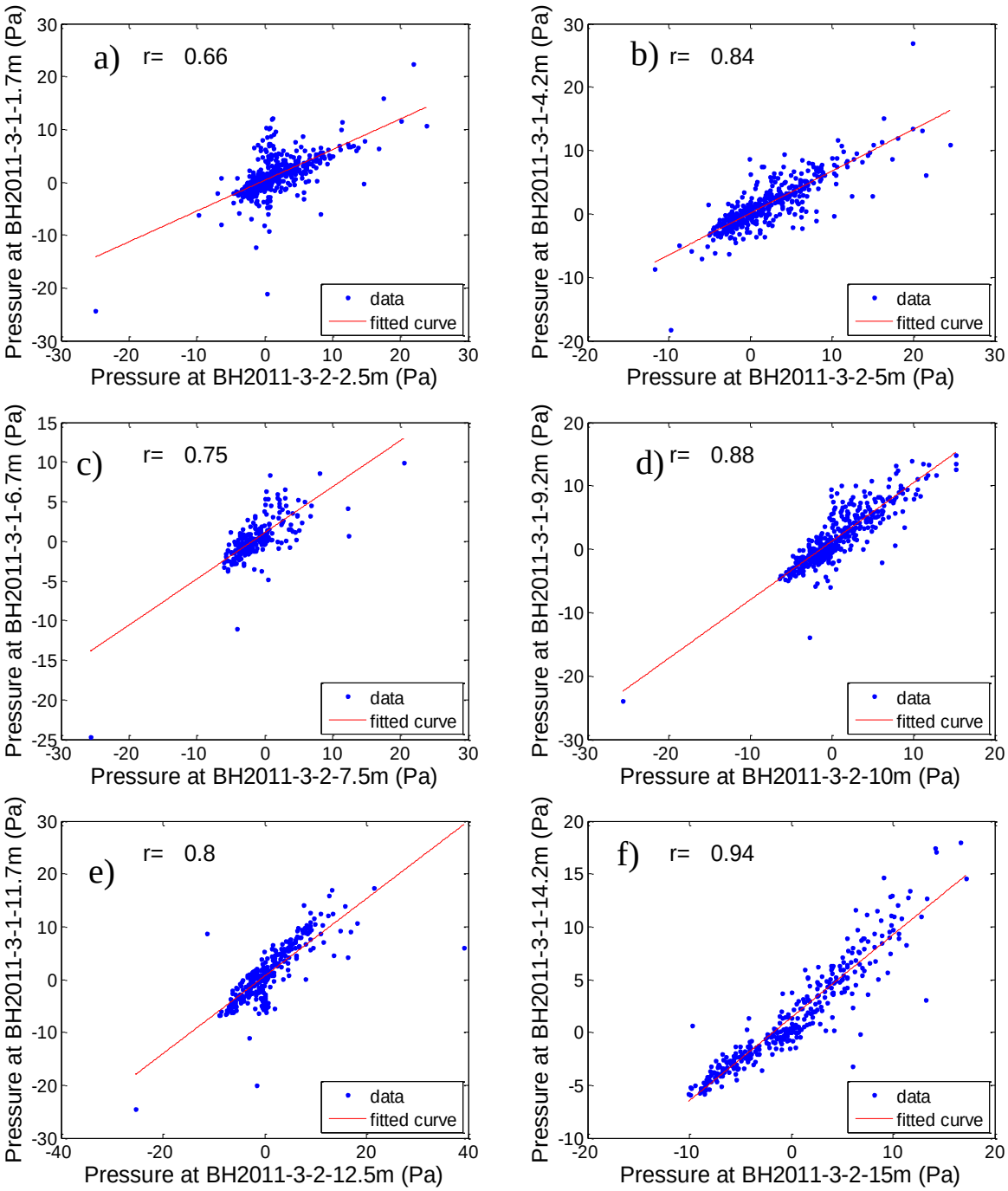

Figure A-60 – Correlation plot for differential internal pressure versus the location horizontally adjacent. Daily data at a) BH2011-3-1-1.7m and BH2011-3-2-2.5m b) BH2011-3-1-4.2m and BH2011-3-2-5m c) BH2011-3-1-6.7m and BH2011-3-2-7.5m d) BH2011-3-1-9.2m and BH2011-3-2-10m e) BH2011-3-1-11.7m and BH2011-3-2-12.5m and f) BH2011-3-1-14.2m and BH2011-3-2-15m

Correlation plots for ambient temperature – internal temperature

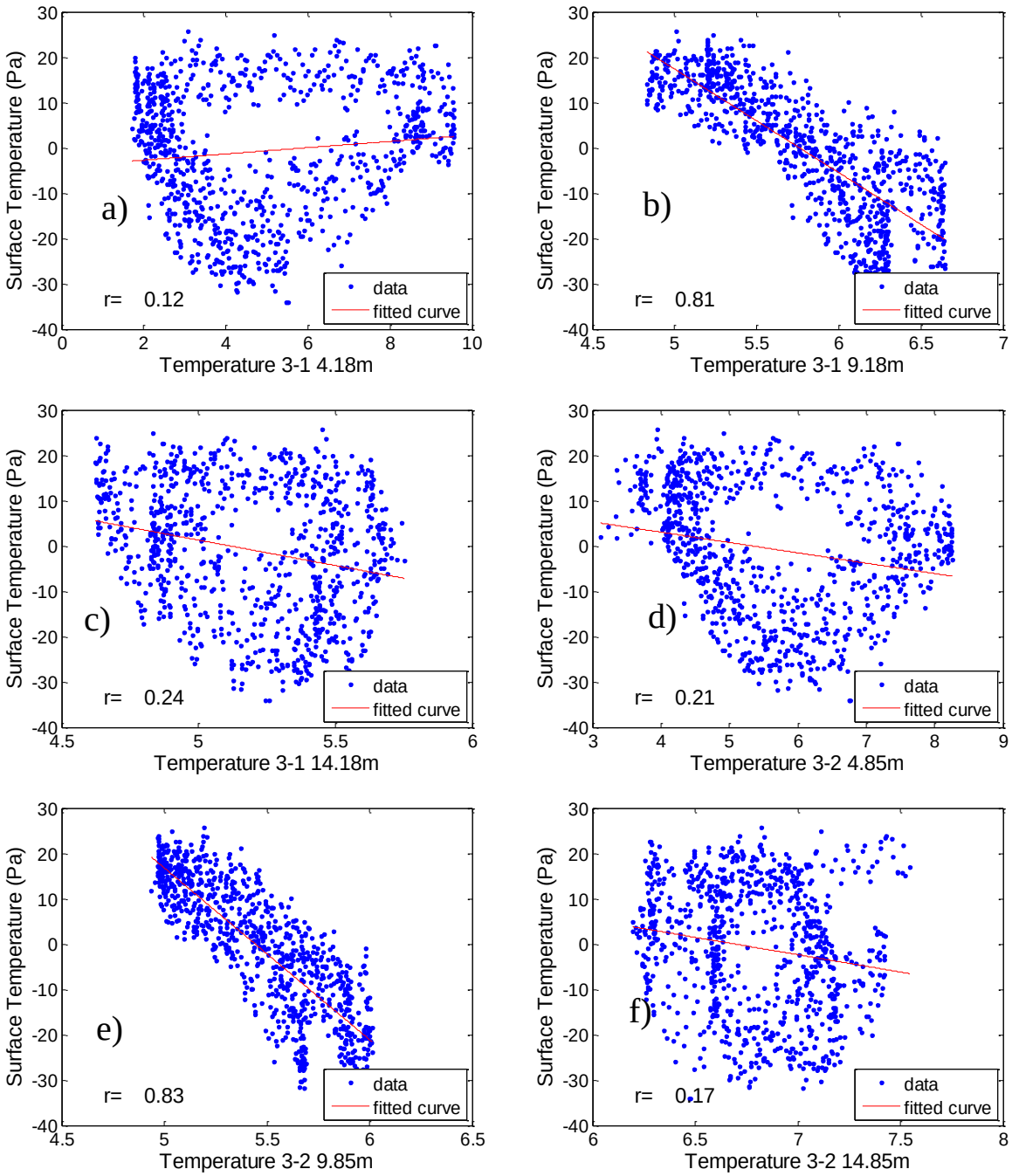

Figure A-61 – Correlation plot for ambient temperature versus internal temperature. 6 hour data at a) BH2011-3-1-4.18m b) BH2011-3-1-9.18m c) BH2011-3-1-14.18 d) BH2011-3-2-4.85m e) BH2011-3-2-9.85m and f) BH2011-3-2-14.85m

Correlation plots for pore gas O_2 content – pore gas O_2 content for location directly below

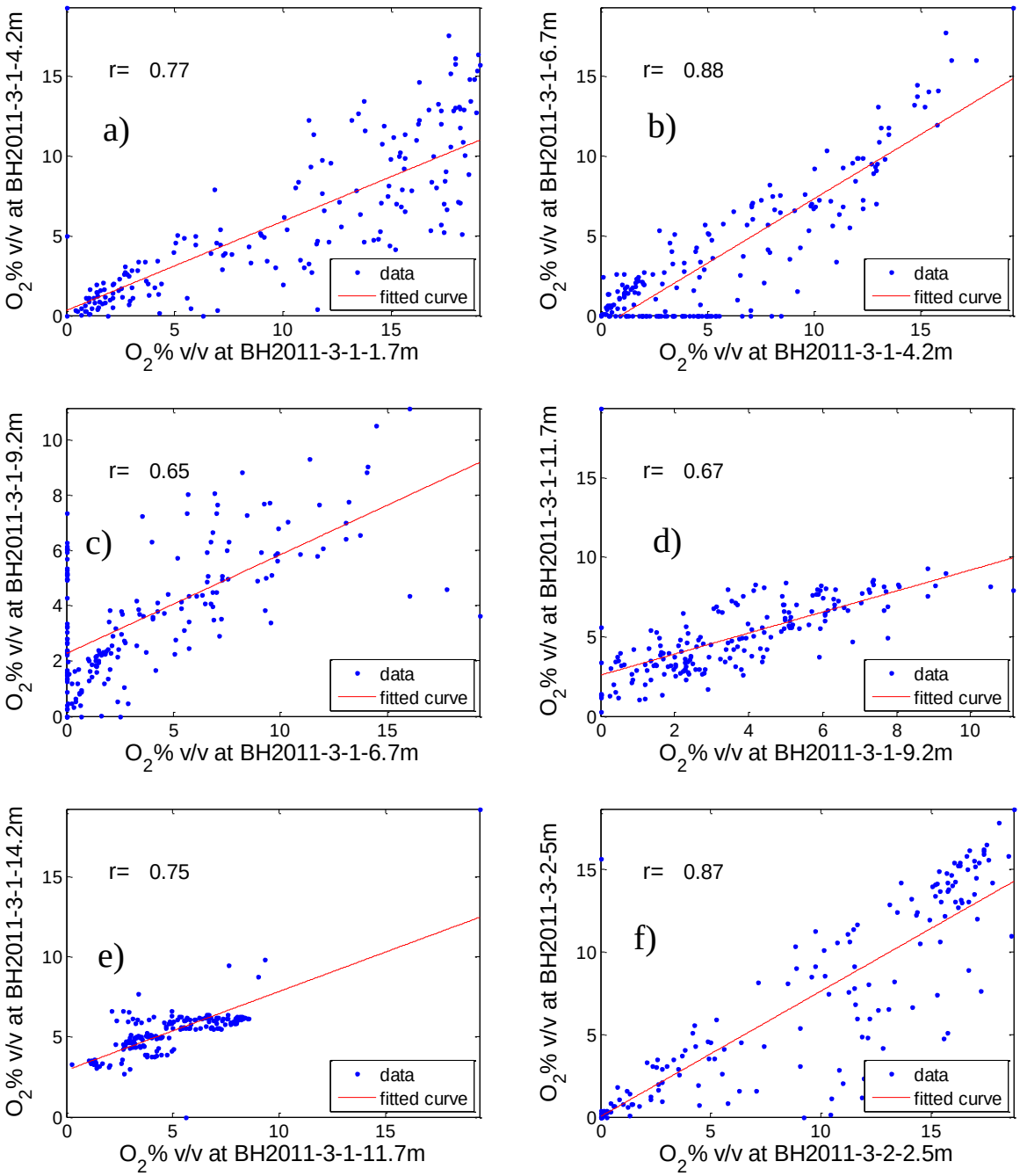

Figure A-62 – Correlation plot for pore gas O_2 content versus the location below. Daily data at a) BH2011-3-1-1.7m and BH2011-3-1-4.2m b) BH2011-3-1-4.2m and BH2011---6.7m c) BH2011-3-1-6.7m and BH2011-3-1-9.2m d) BH2011-3-1-9.2m and BH2011-3-1-11.7m e) BH2011-3-1-11.7m and BH2011-3-1-14.2m and f) BH2011-3-2-2.5m and BH2011-3-2-5m

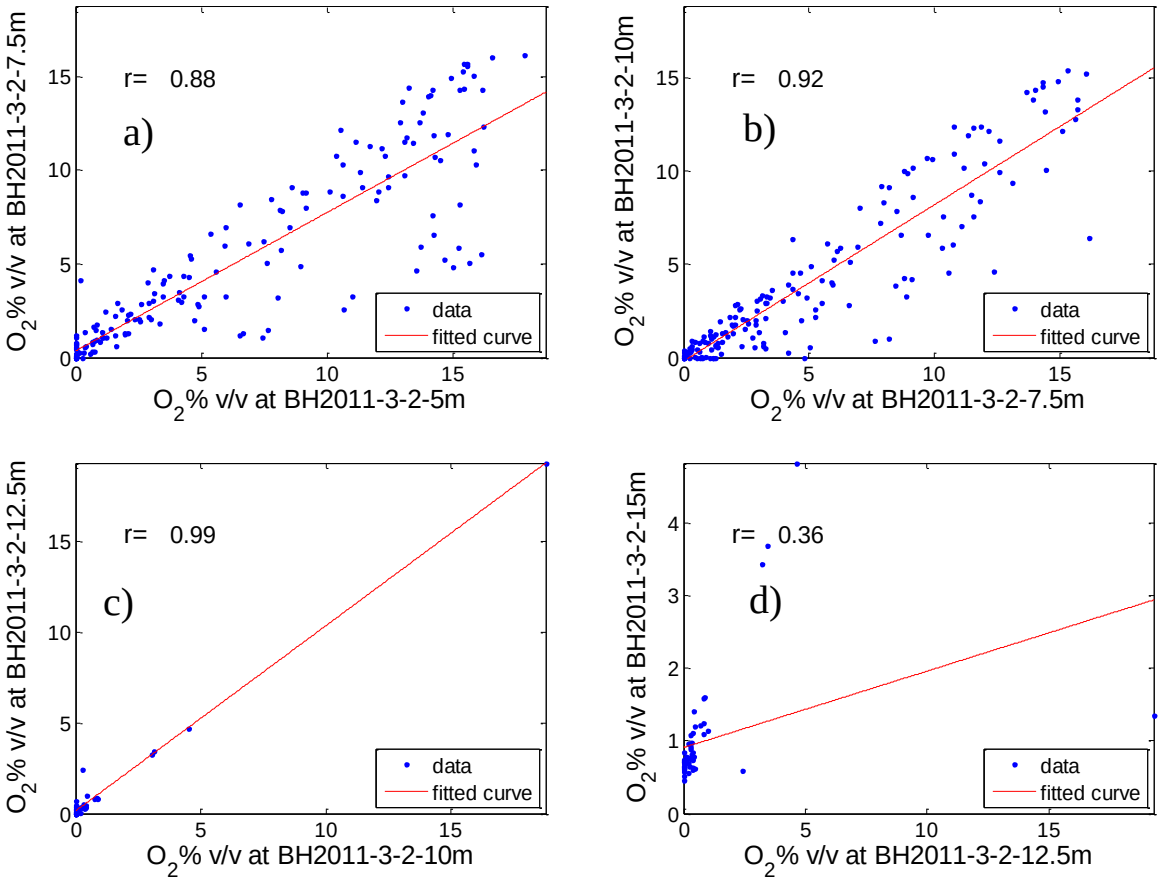

Figure A-63– Correlation plot for pore gas O_2 content versus the location below. Daily data at a) BH2011-3-2-5m and BH2011-3-2-7.5m b) BH2011-3-2-7.5m and BH2011-3-2-10m c) BH2011-3-2-10m and BH2011-3-2-12.5mm d) BH2011-3-1-12.5m and BH2011-3-1-15m

Correlation plots for pore gas O_2 content – pore gas O_2 content for location laterally across

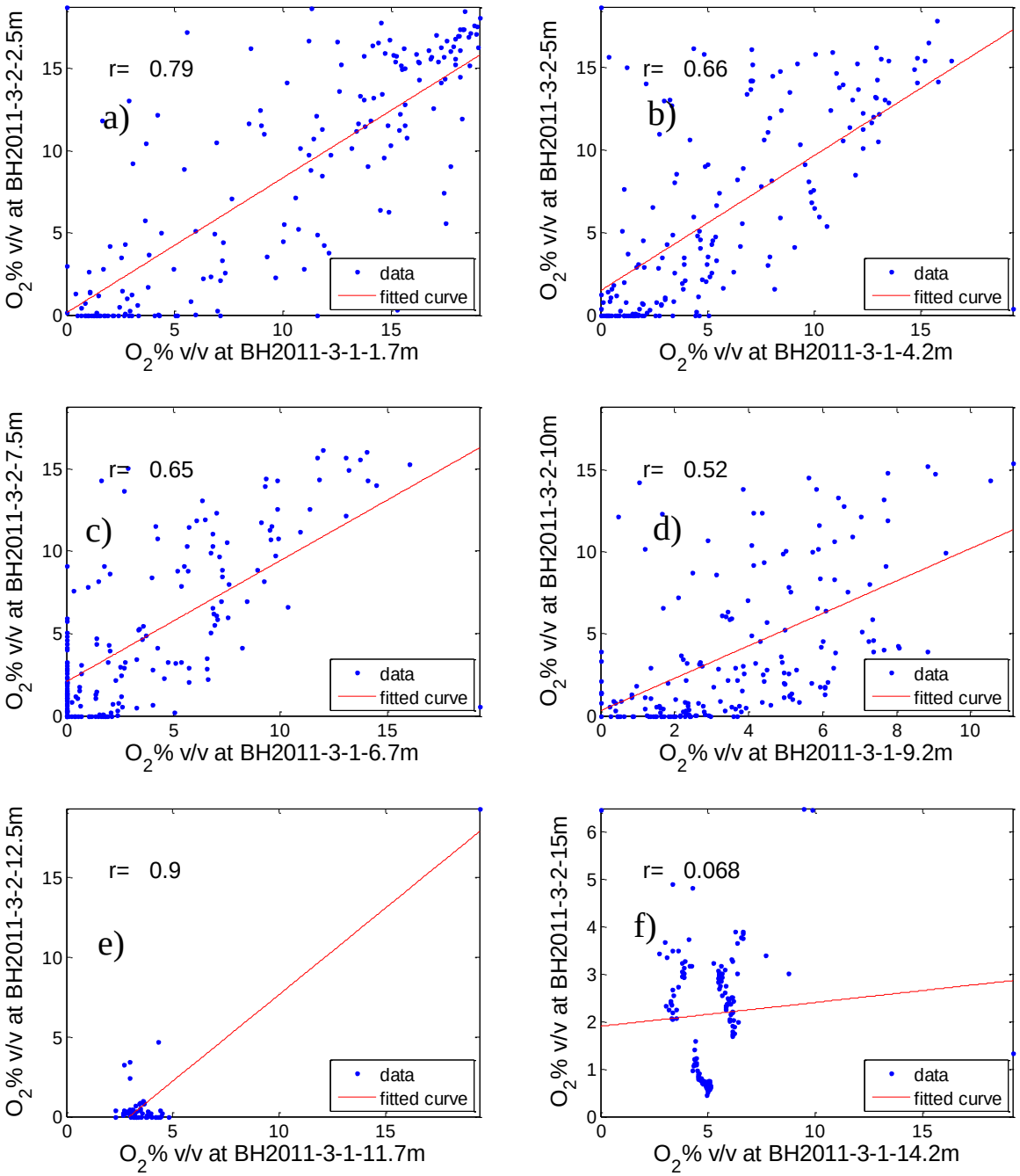

Figure A-64– Correlation plot for pore gas O_2 content versus the location laterally across. Daily data at a) BH2011-3-1-1.7m and BH2011-3-2-2.5m b) BH2011-3-1-4.2m and BH2011-3-2-5m c) BH2011-3-1-6.7m and BH2011-3-2-7.5m d) BH2011-3-1-9.2m and BH2011-3-2-10m e) BH2011-3-1-11.7m and BH2011-3-2-12.5m and f) BH2011-3-1-14.2m and BH2011-3-2-15m

Correlation plots for pore gas O_2 content – pore gas CO_2 content

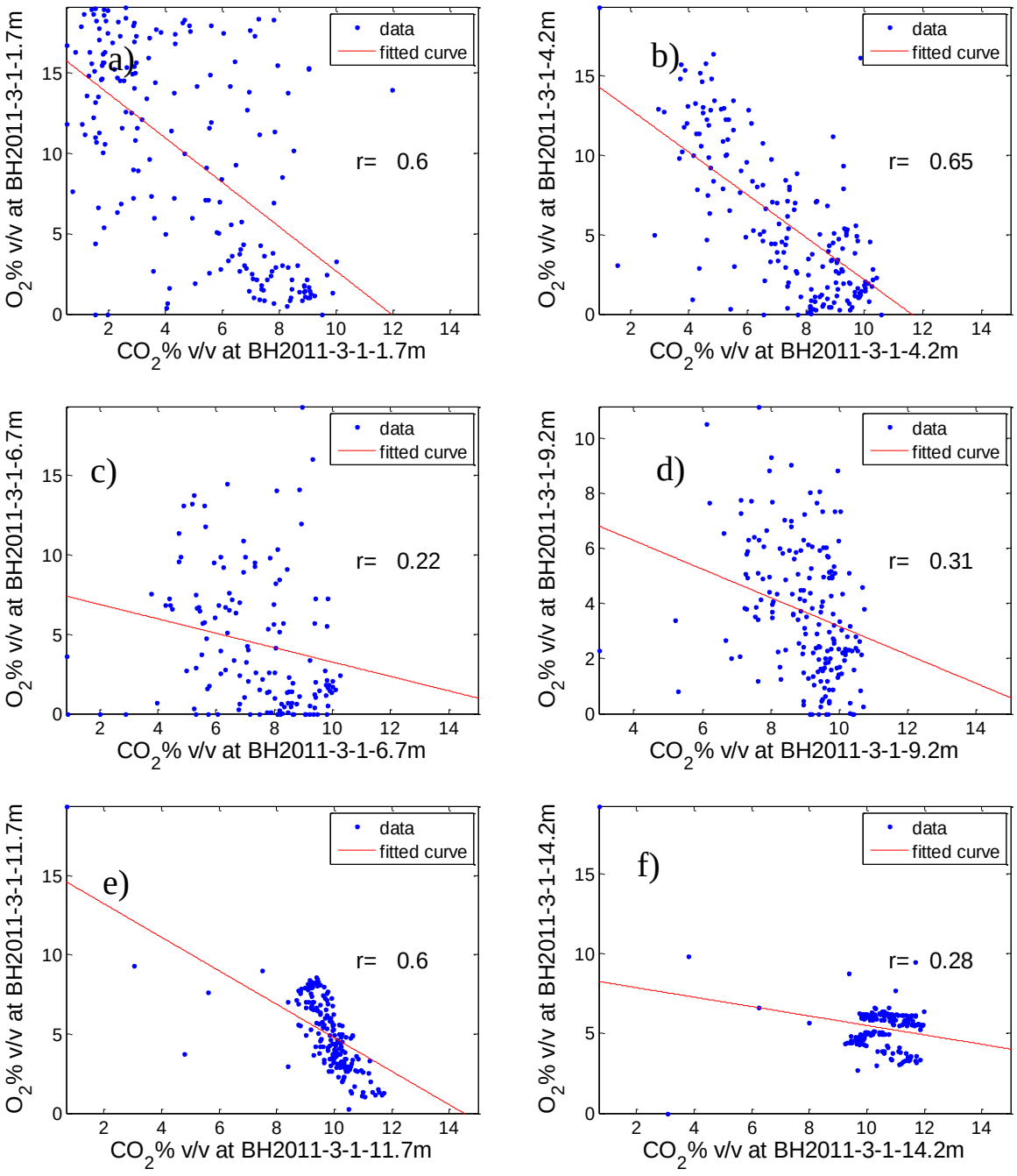

Figure A-65– Correlation plot for pore gas O_2 content versus CO_2 content. Daily data at a) BH2011-3-1-1.7m b) BH2011-3-1-4.2m c) BH2011-3-1-6.7m d) BH2011-3-1-9.2m e) BH2011-3-1-11.7m and f) BH2011-3-1-14.2m

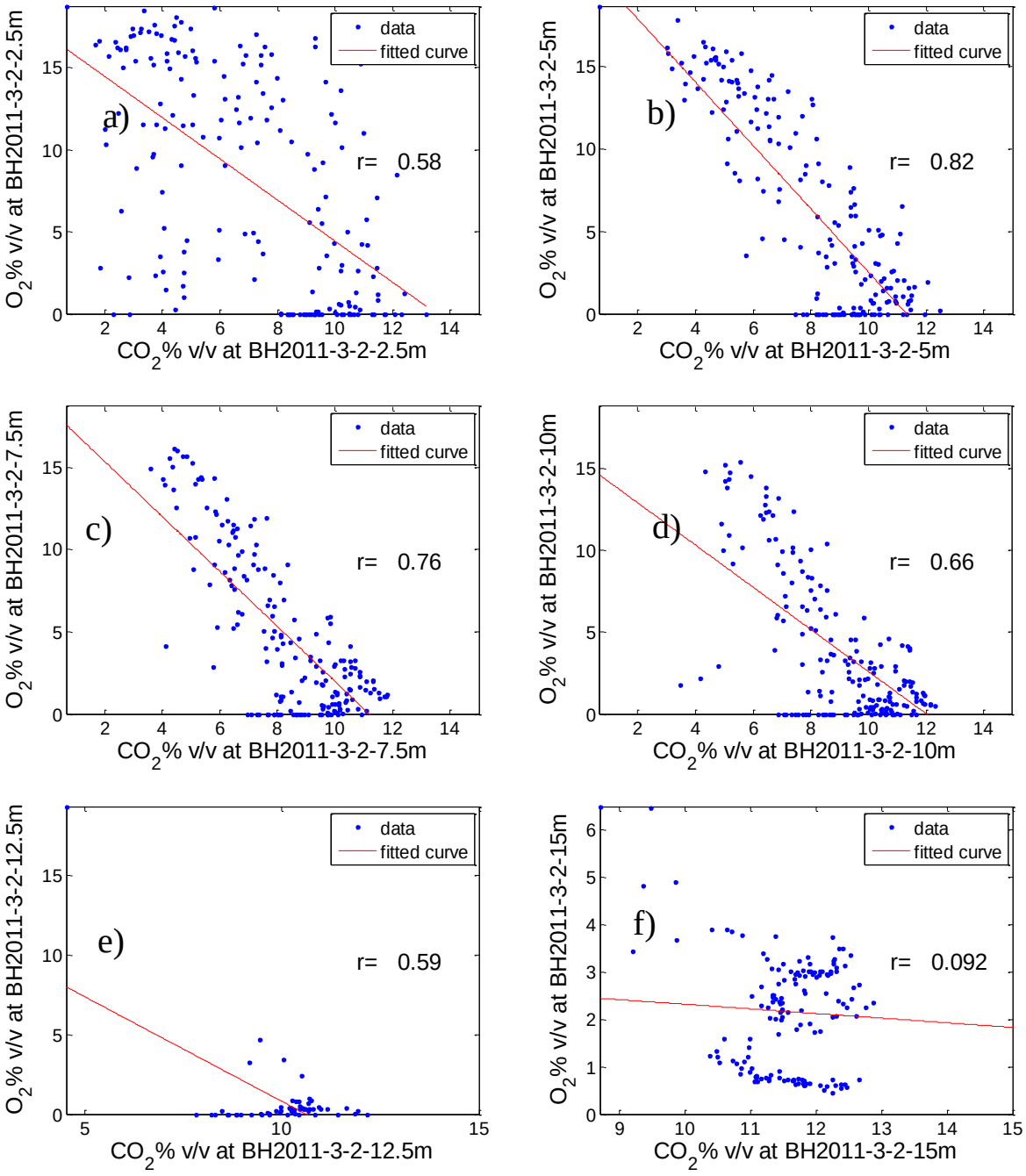

Figure A-66– Correlation plot for pore gas O_2 content versus CO_2 content. Daily data at a) BH2011-3-2-2.5m b) BH2011-3-2-5m c) BH2011-3-2-7.5m d) BH2011-3-2-10m e) BH2011-3-2-12.5m and f) BH2011-3-2-15m

Appendix B

Sulfur and Iron XANES Plots

Appendix B contains the results of the linear combination analysis plots of S and Fe XANES discussed in Chapter 3. Example plots were included in the main text. The following plots are included:

- Figure B2 – B7a : S XANES for grain 1;
- Figure B7b – B16a : S XANES for grain 2; and
- Figure B16b – B21 : Fe XANES for grain 2.

For reference, the location of the external and internal monitoring locations are shown on Figure B-1a to c.

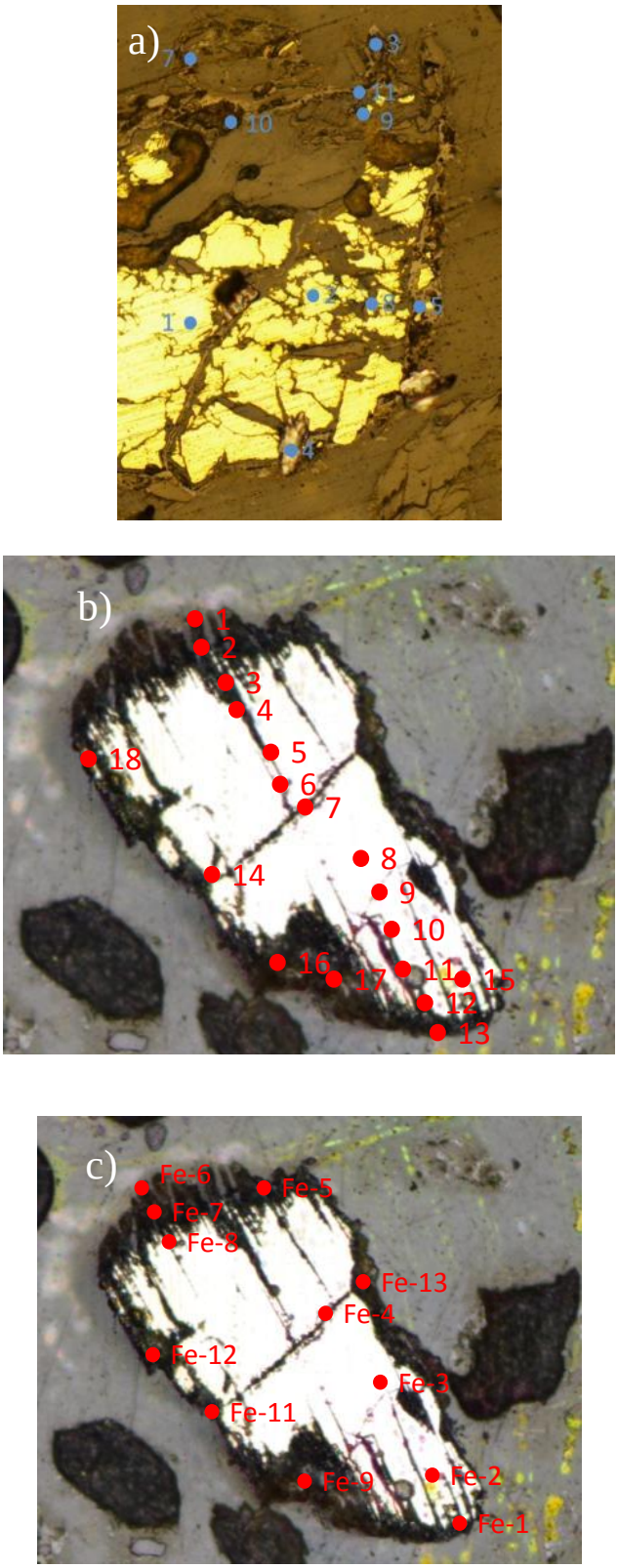

Figure B-66– Location of XANES collection for a) S – grain 1, b) S – grain 2 and c) Fe – grain 3

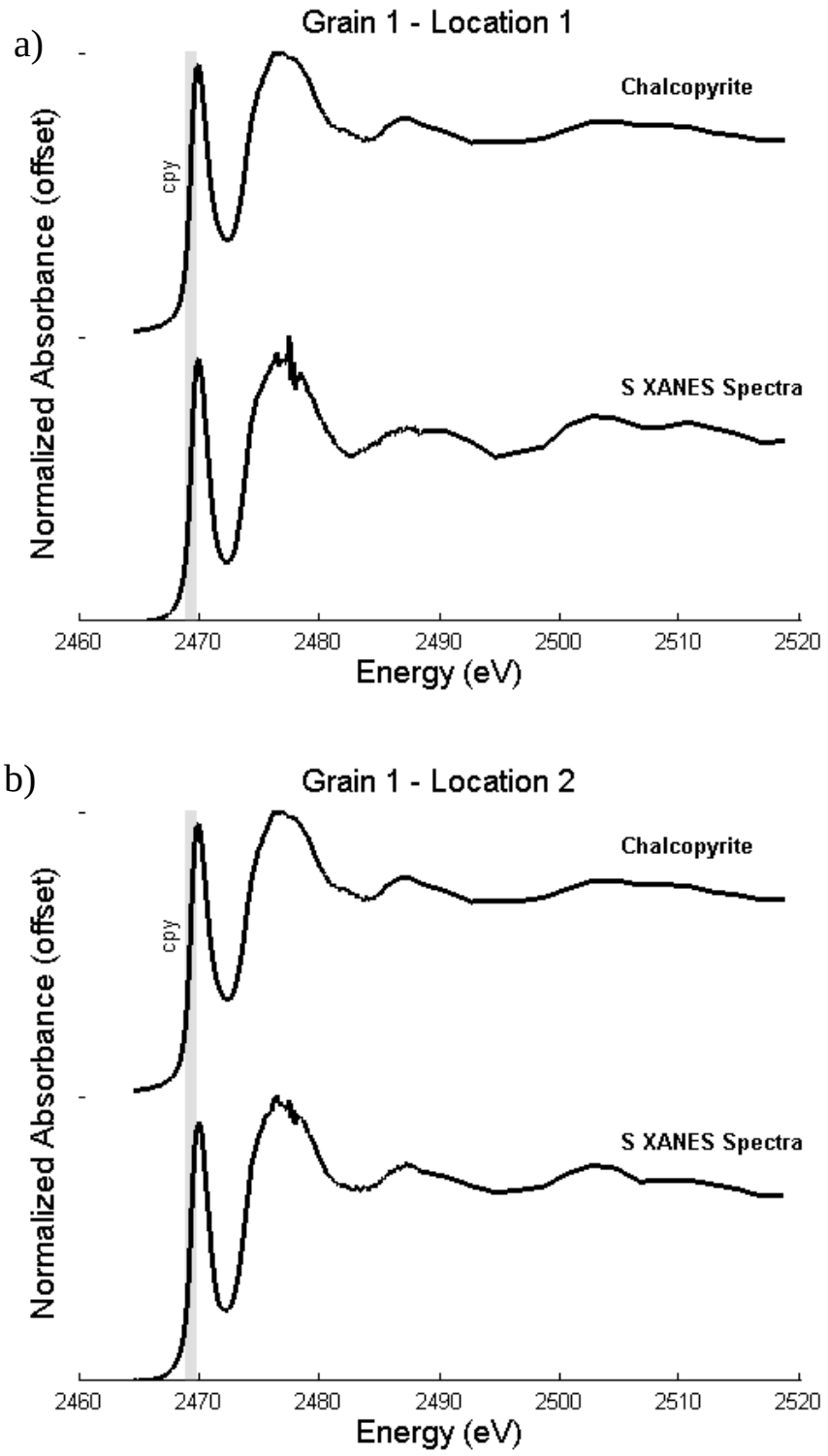

Figure B-2 –S XANES for Grain 1 at a) location 1 and b) location 2. The XANES for the standards of the species that were identified through linear combination analysis are superimposed. The grey bar lines indicate the reference e0 values for the standards

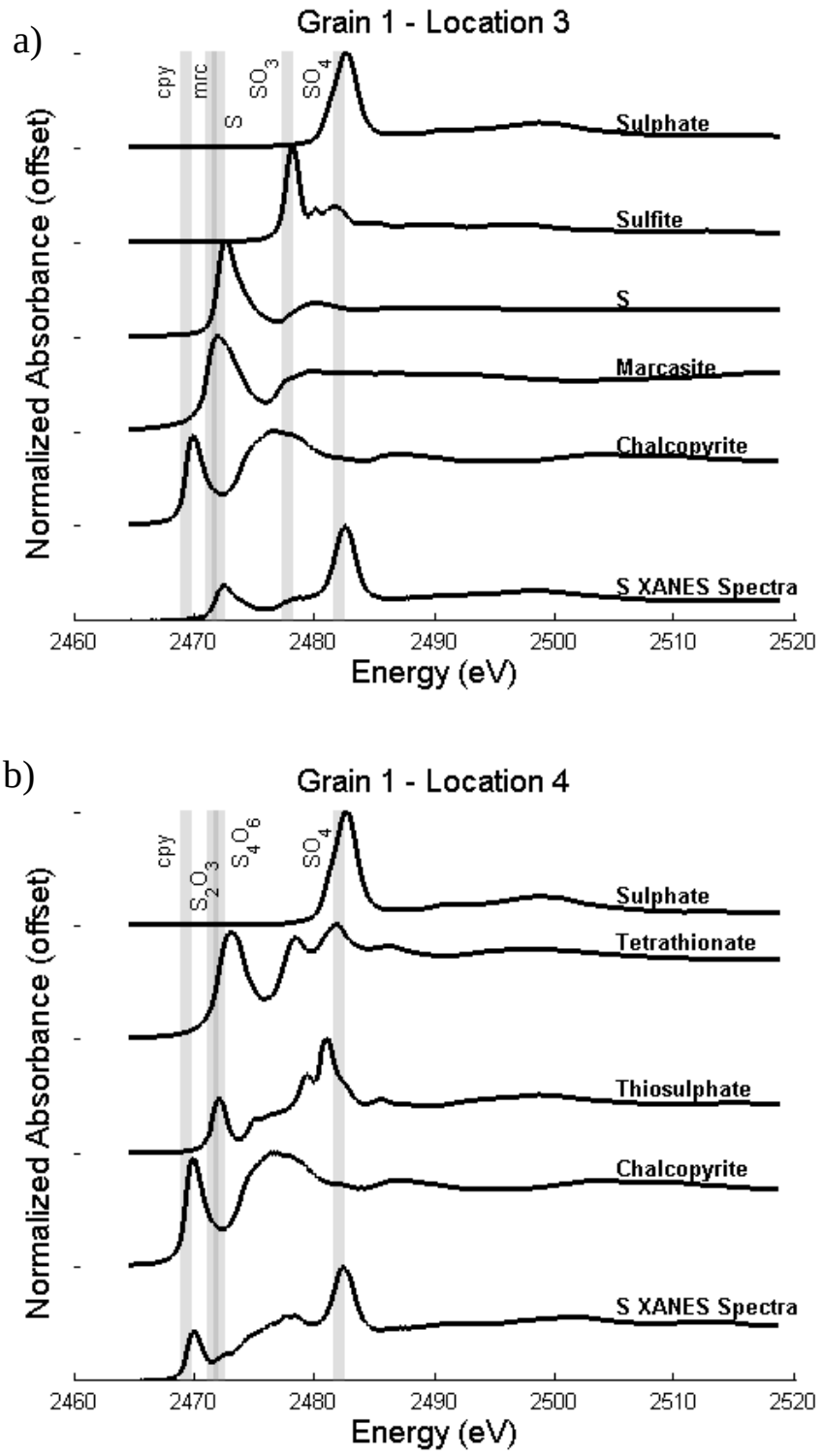

Figure B-3 –S XANES for Grain 1 at a) location 3 and b) location 4. The XANES for the standards of the species that were identified through linear combination analysis are superimposed. The grey bar lines indicate the reference e0 values for the standards

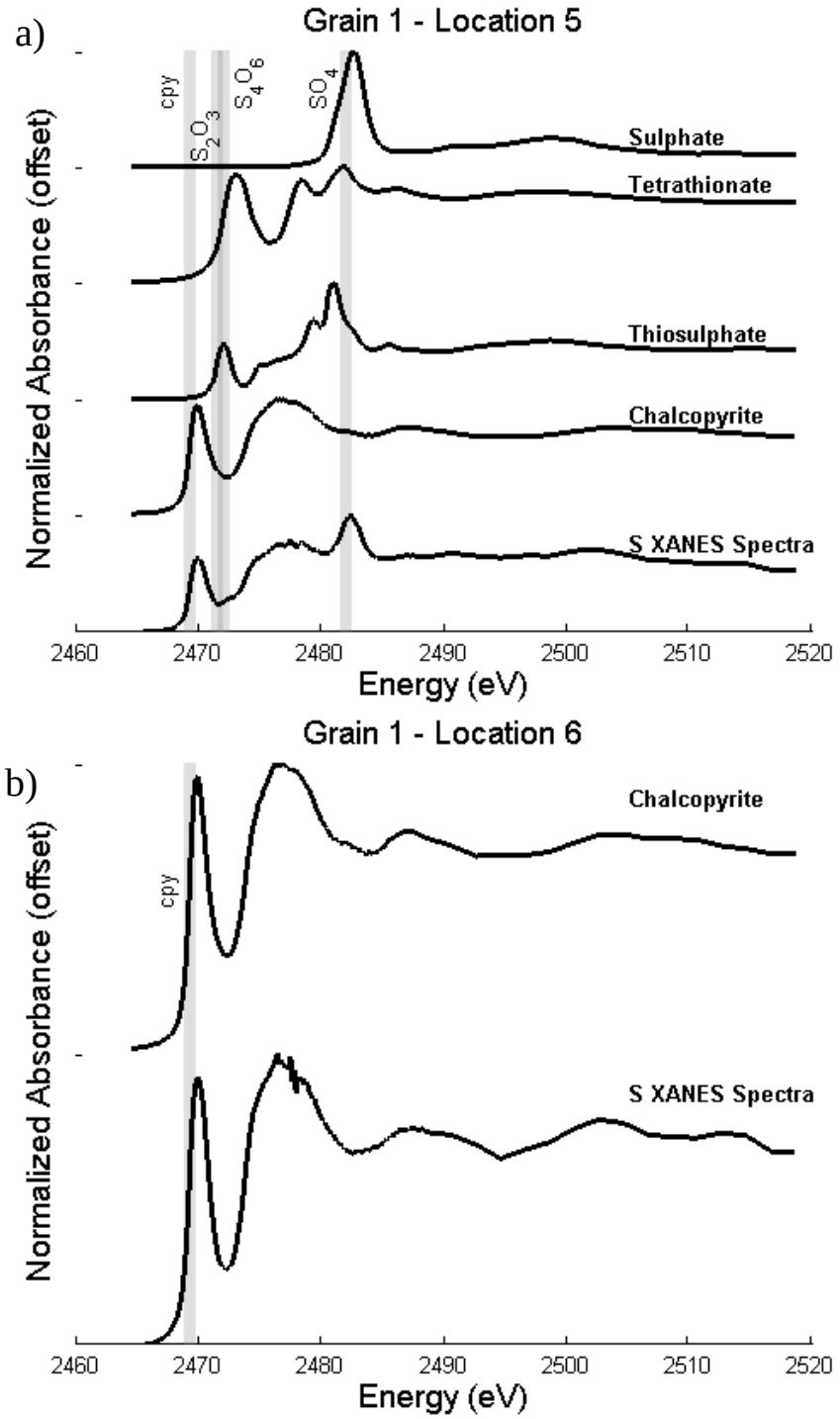

Figure B-4 –S XANES for Grain 1 at a) location 5 and b) location 6. The XANES for the standards of the species that were identified through linear combination analysis are superimposed. The grey bar lines indicate the reference e0 values for the standards

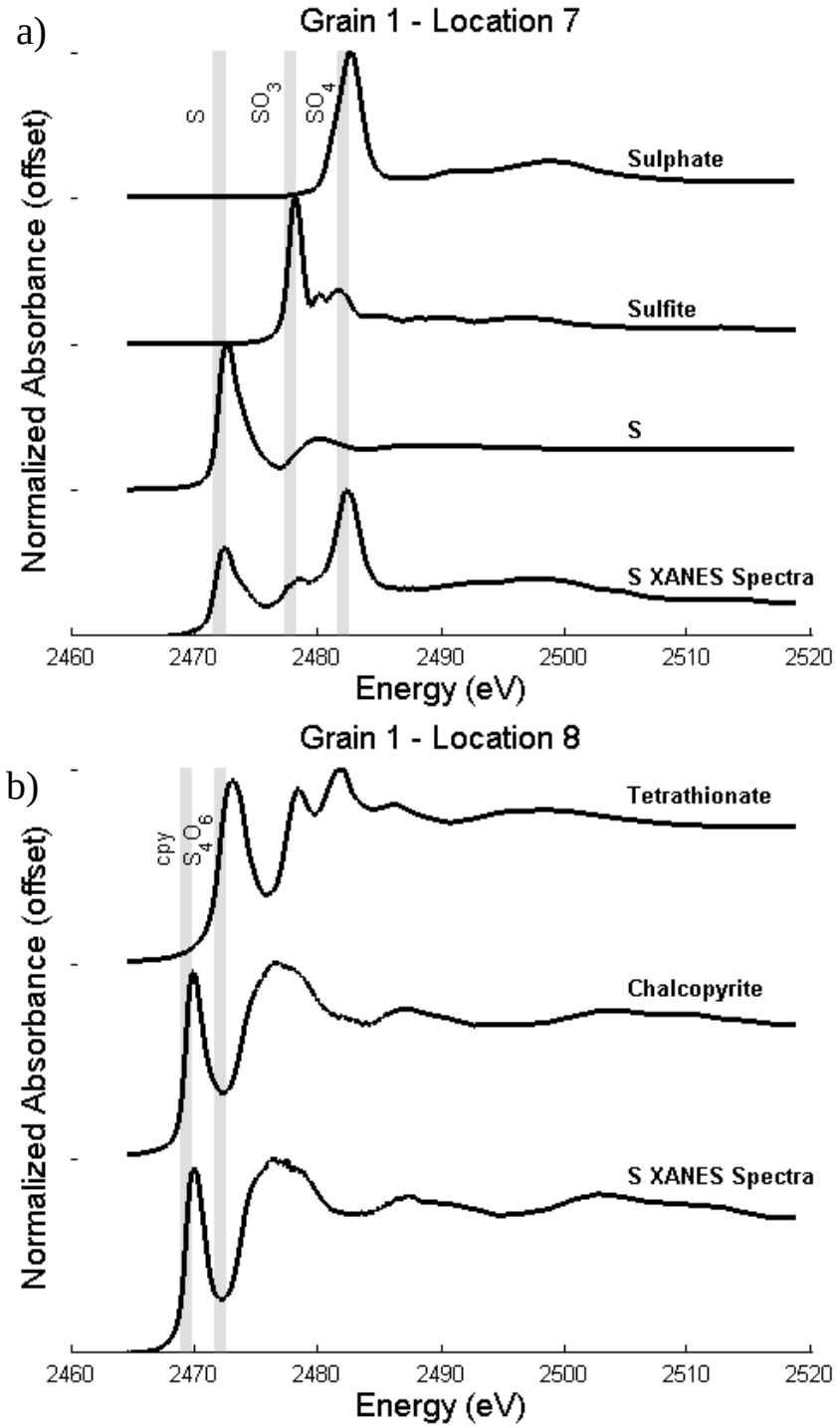

Figure B-5 –S XANES for Grain 1 at a) location 7 and b) location 8. The XANES for the standards of the species that were identified through linear combination analysis are superimposed. The grey bar lines indicate the reference e0 values for the standards

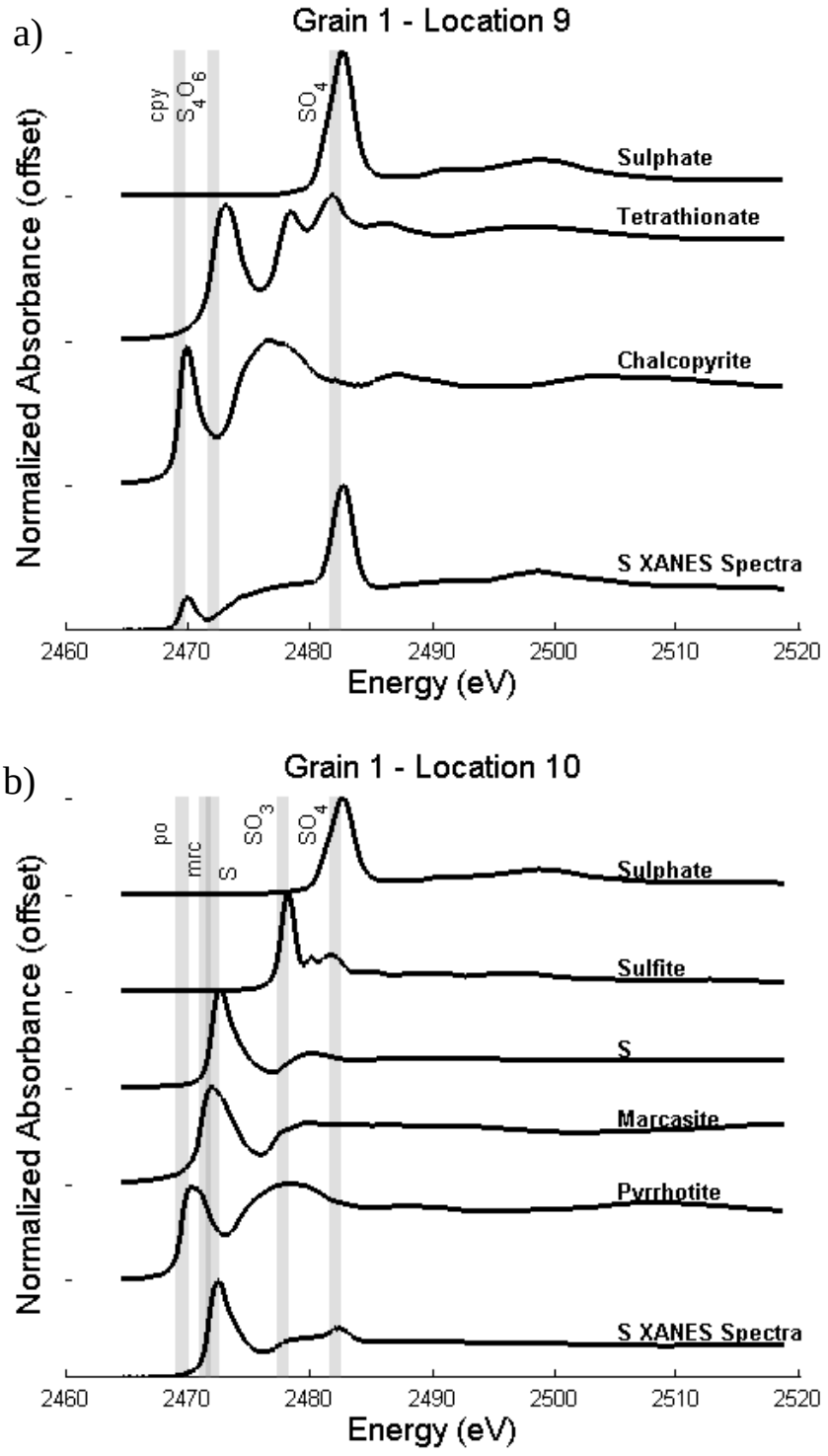

Figure B-6 –S XANES for Grain 1 at a) location 9 and b) location 10. The XANES for the standards of the species that were identified through linear combination analysis are superimposed. The grey bar lines indicate the reference e0 values for the standards

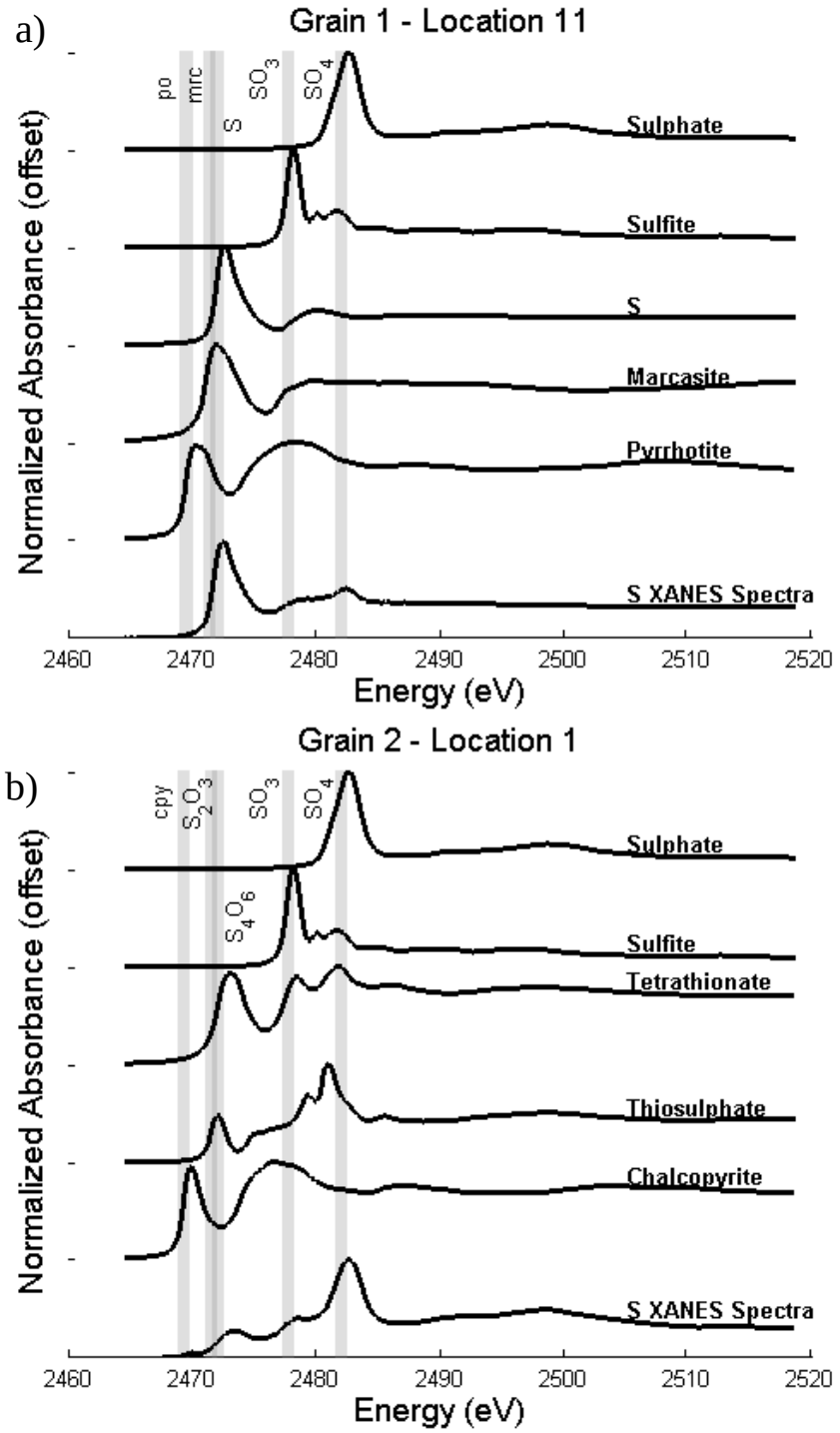

Figure B-7 –S XANES for Grain 1 at a) location 11 and Grain 2 at b) location 1. The XANES for the standards of the species that were identified through linear combination analysis are superimposed. The grey bar lines indicate the reference e0 values for the standards

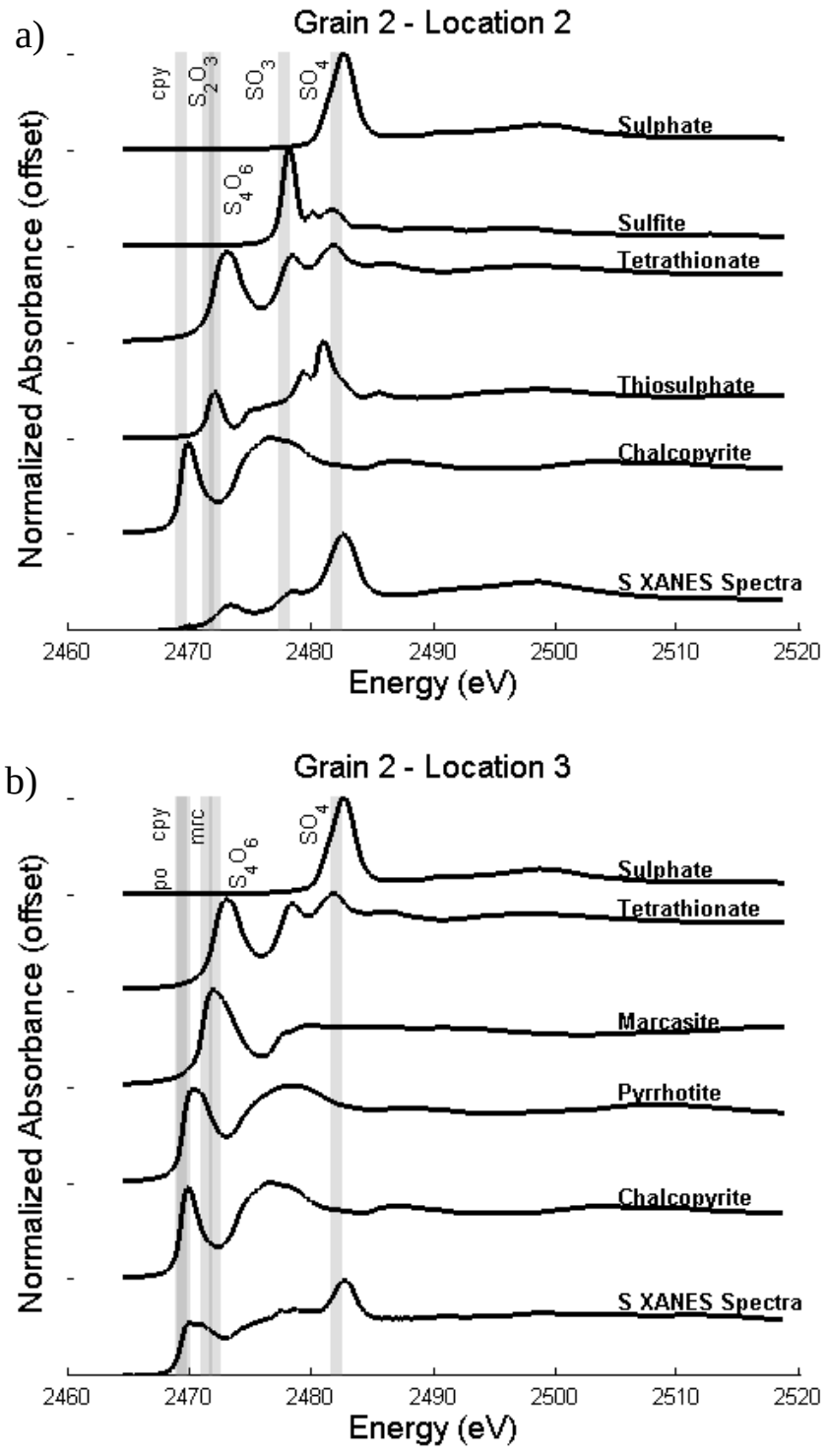

Figure B-8 –S XANES for Grain 2 at a) location 2 and b) location 3. The XANES for the standards of the species that were identified through linear combination analysis are superimposed. The grey bar lines indicate the reference e0 values for the standards

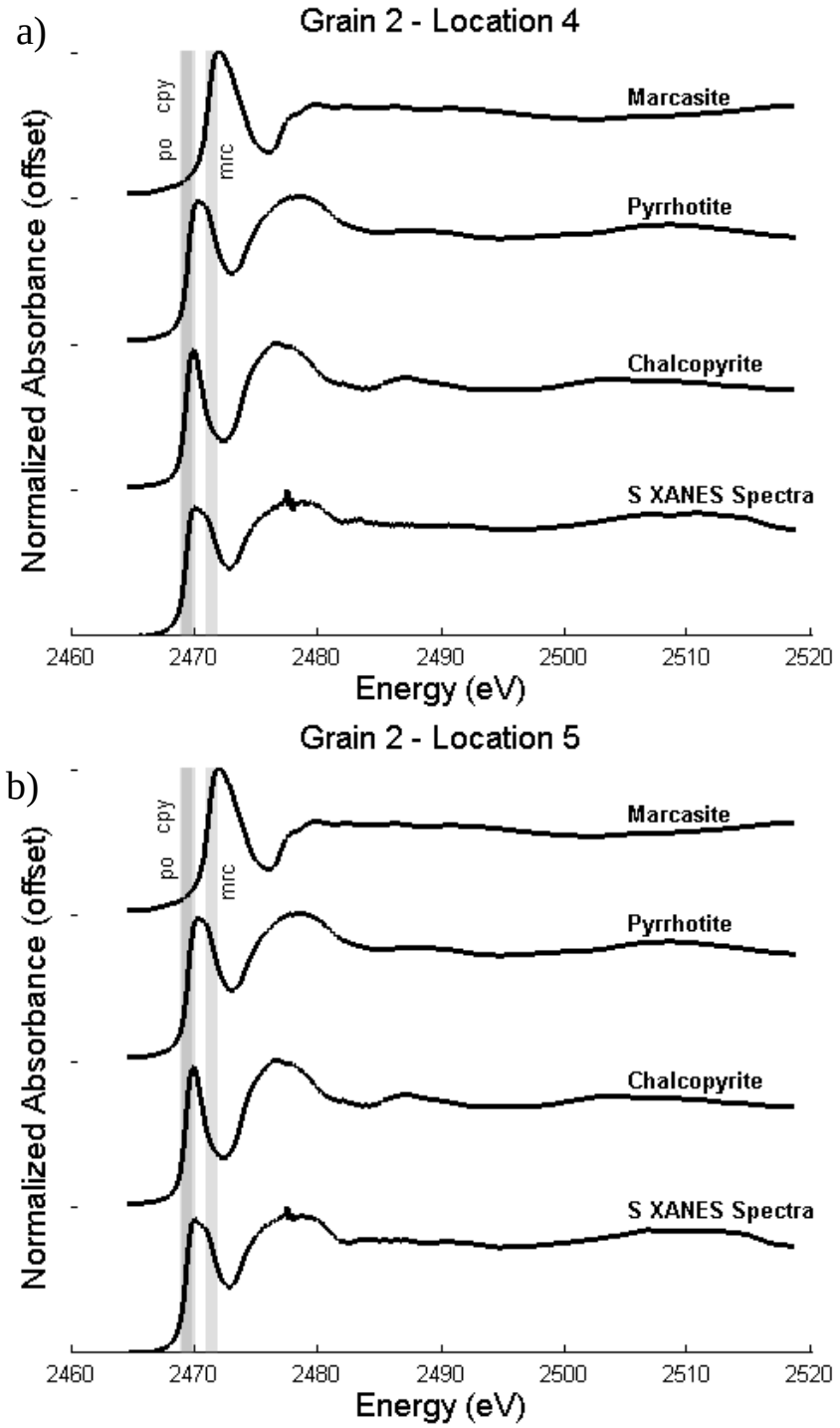

Figure B-9 –S XANES for Grain 2 at a) location 4 and b) location 5. The XANES for the standards of the species that were identified through linear combination analysis are superimposed. The grey bar lines indicate the reference e0 values for the standards

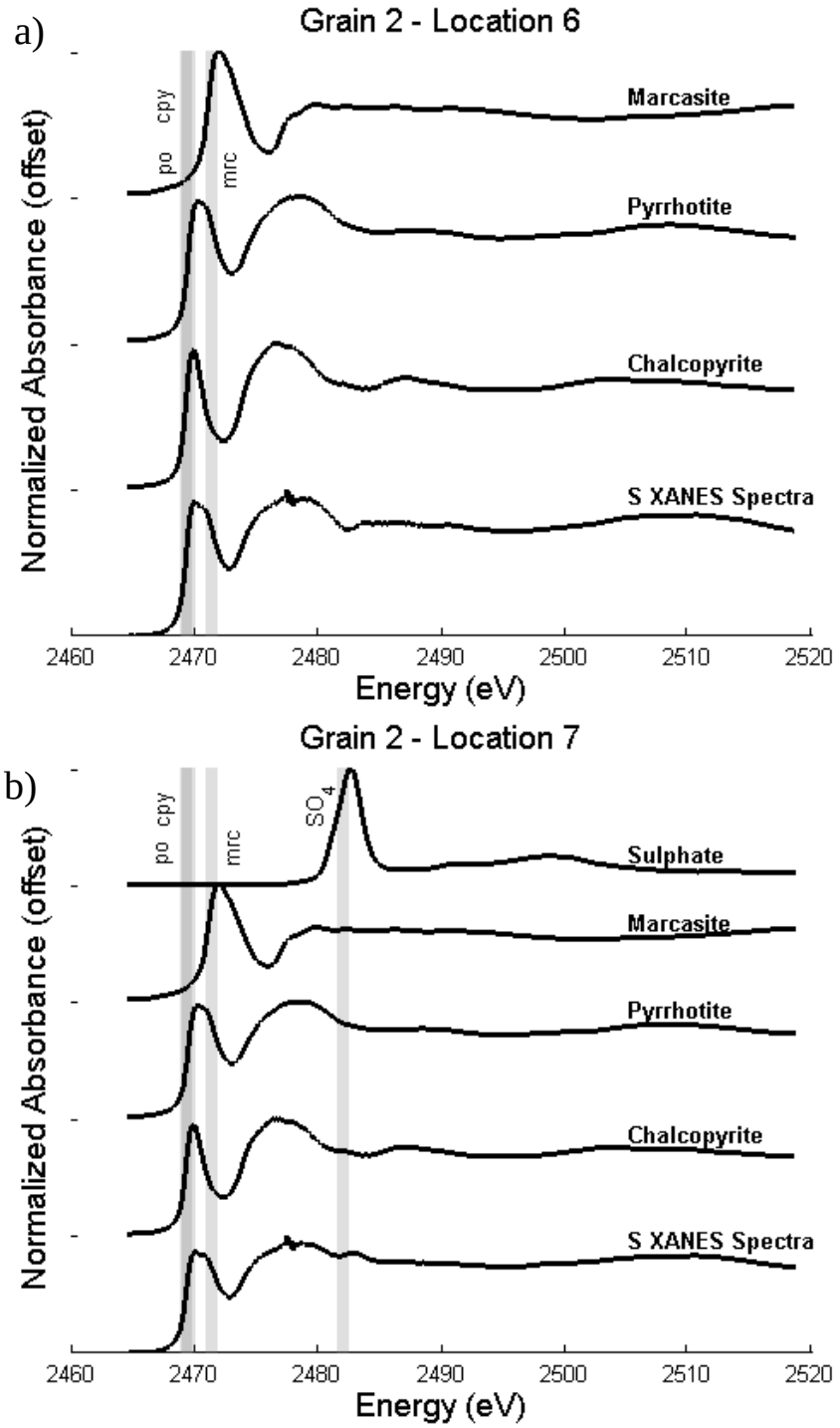

Figure B-10 –S XANES for Grain 2 at a) location 6 and b) location 7. The XANES for the standards of the species that were identified through linear combination analysis are superimposed. The grey bar lines indicate the reference e0 values for the standards

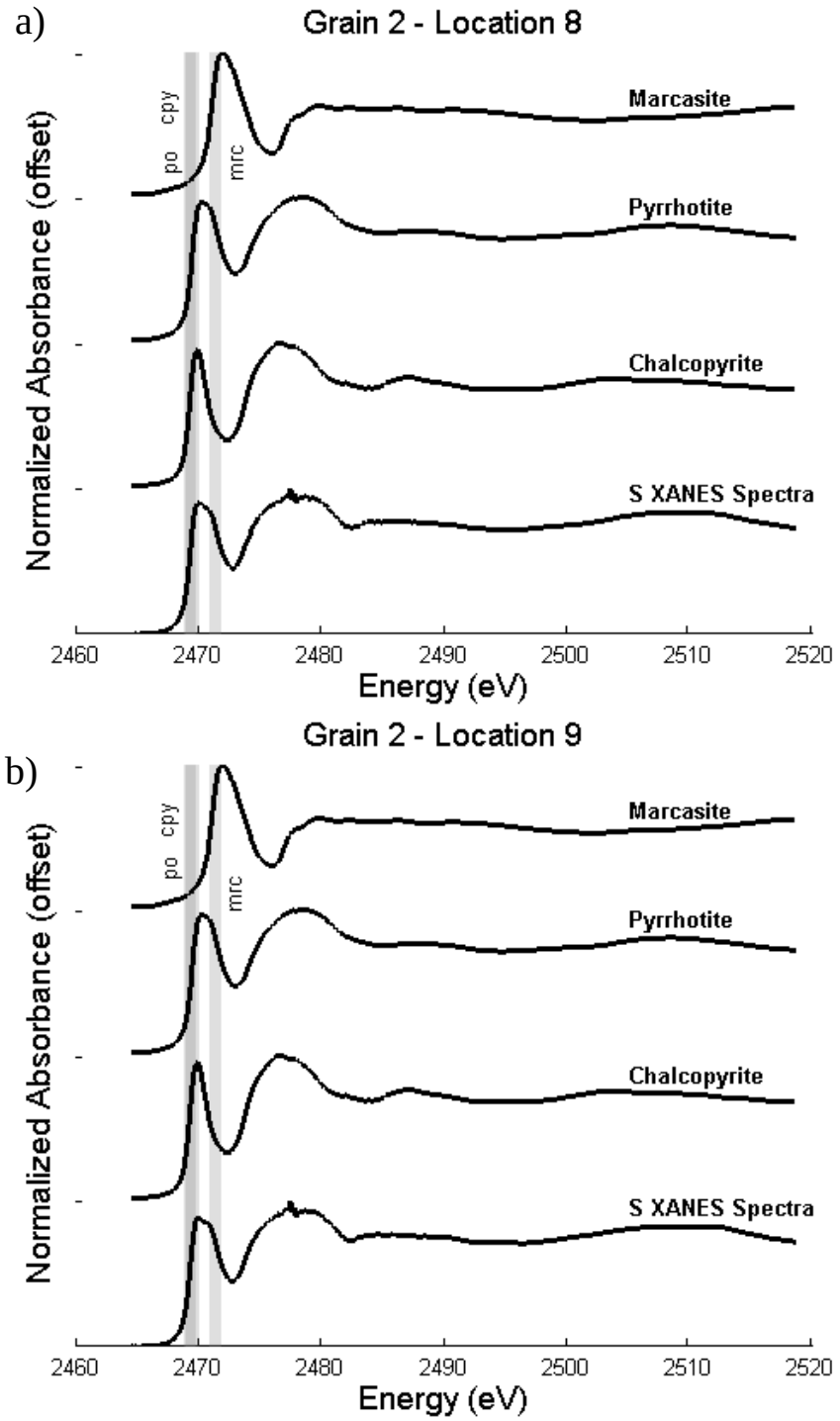

Figure B-11 –S XANES for Grain 2 at a) location 8 and b) location 9. The XANES for the standards of the species that were identified through linear combination analysis are superimposed. The grey bar lines indicate the reference e0 values for the standards

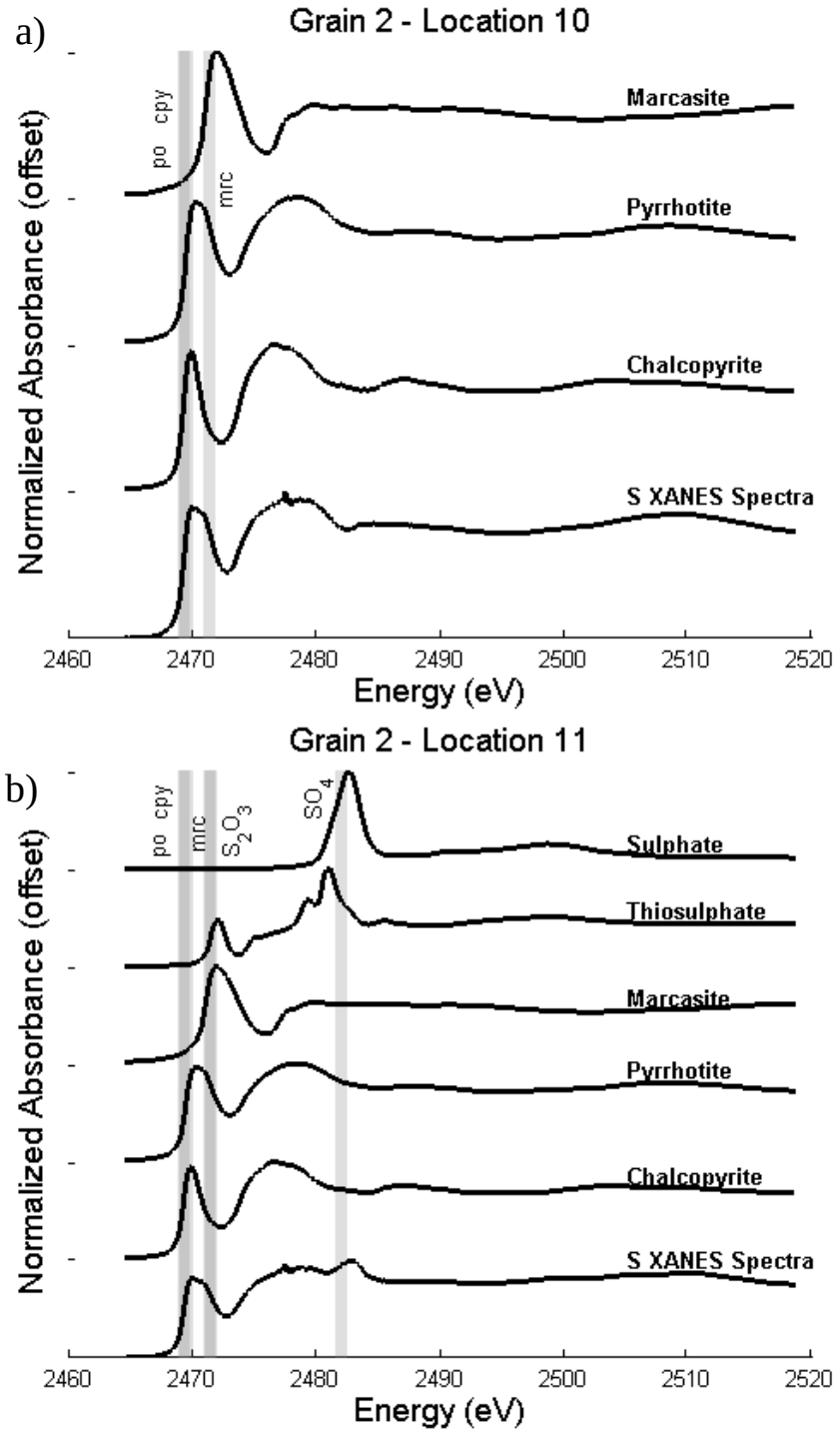

Figure B-12 –S XANES for Grain 2 at a) location 10 and b) location 11. The XANES for the standards of the species that were identified through linear combination analysis are superimposed. The grey bar lines indicate the reference e0 values for the standards

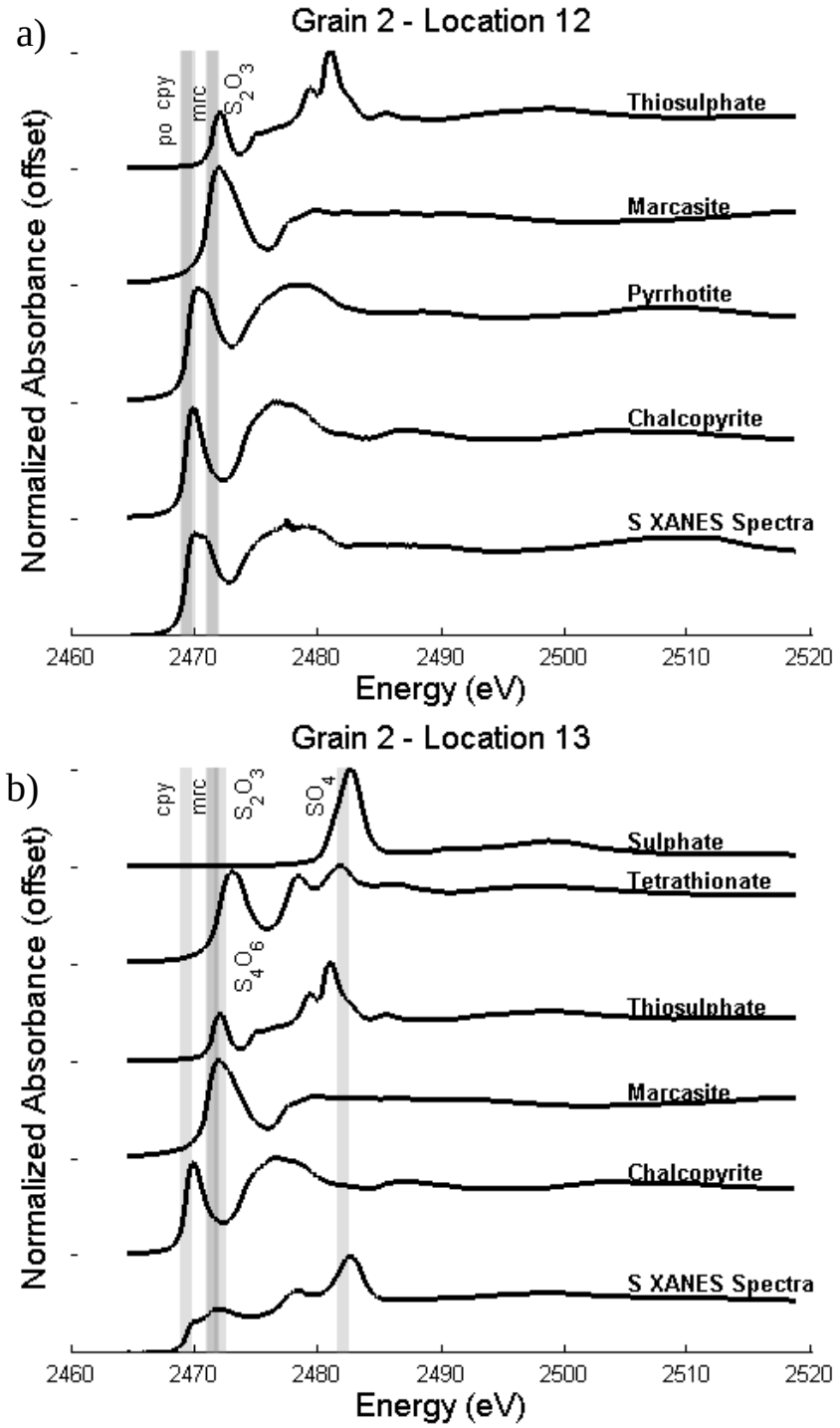

Figure B-13 –S XANES for Grain 2 at a) location 12 and b) location 13. The XANES for the standards of the species that were identified through linear combination analysis are superimposed. The grey bar lines indicate the reference e0 values for the standards

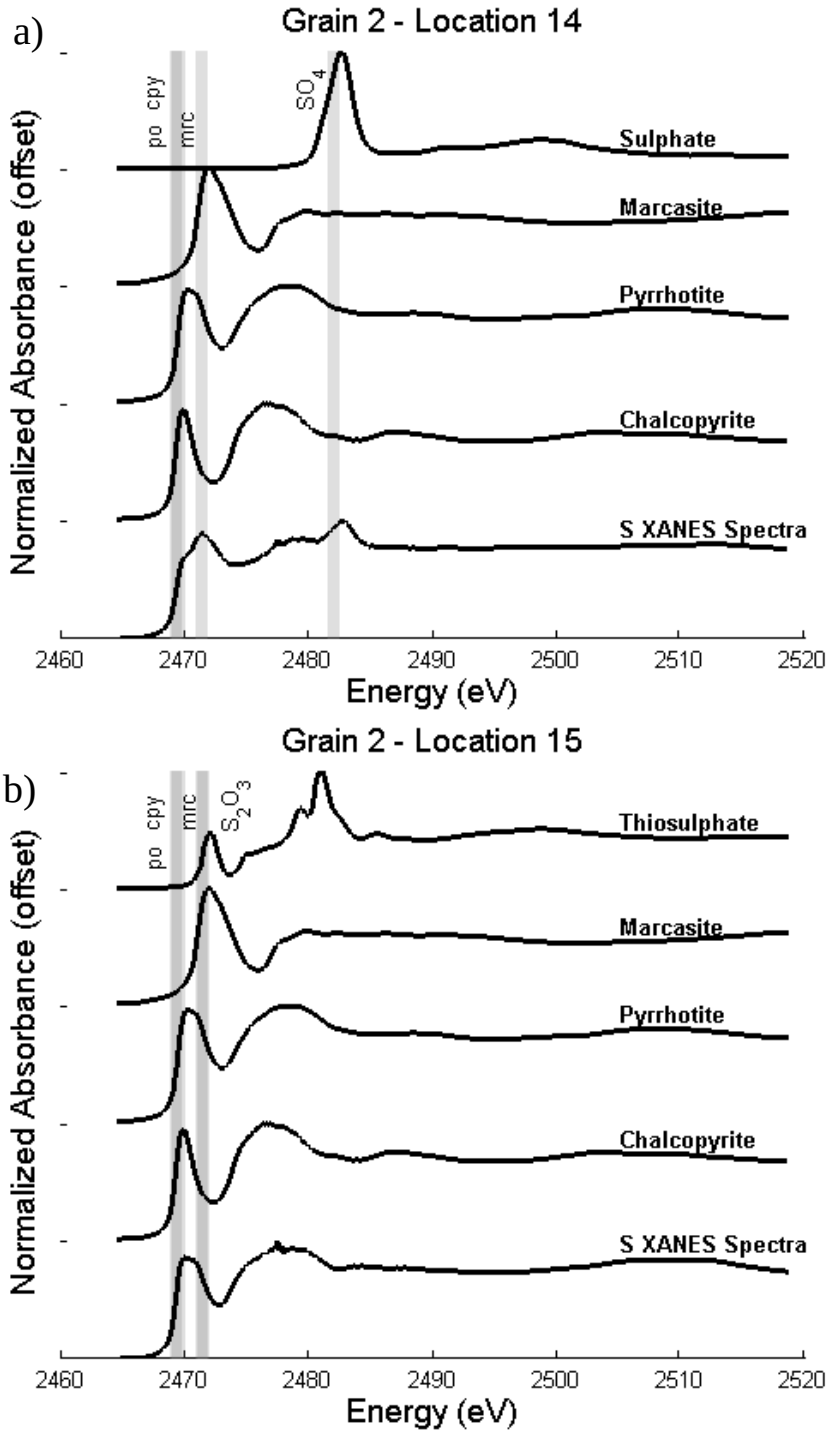

Figure B-14 –S XANES for Grain 2 at a) location 14 and b) location 15. The XANES for the standards of the species that were identified through linear combination analysis are superimposed. The grey bar lines indicate the reference e0 values for the standards

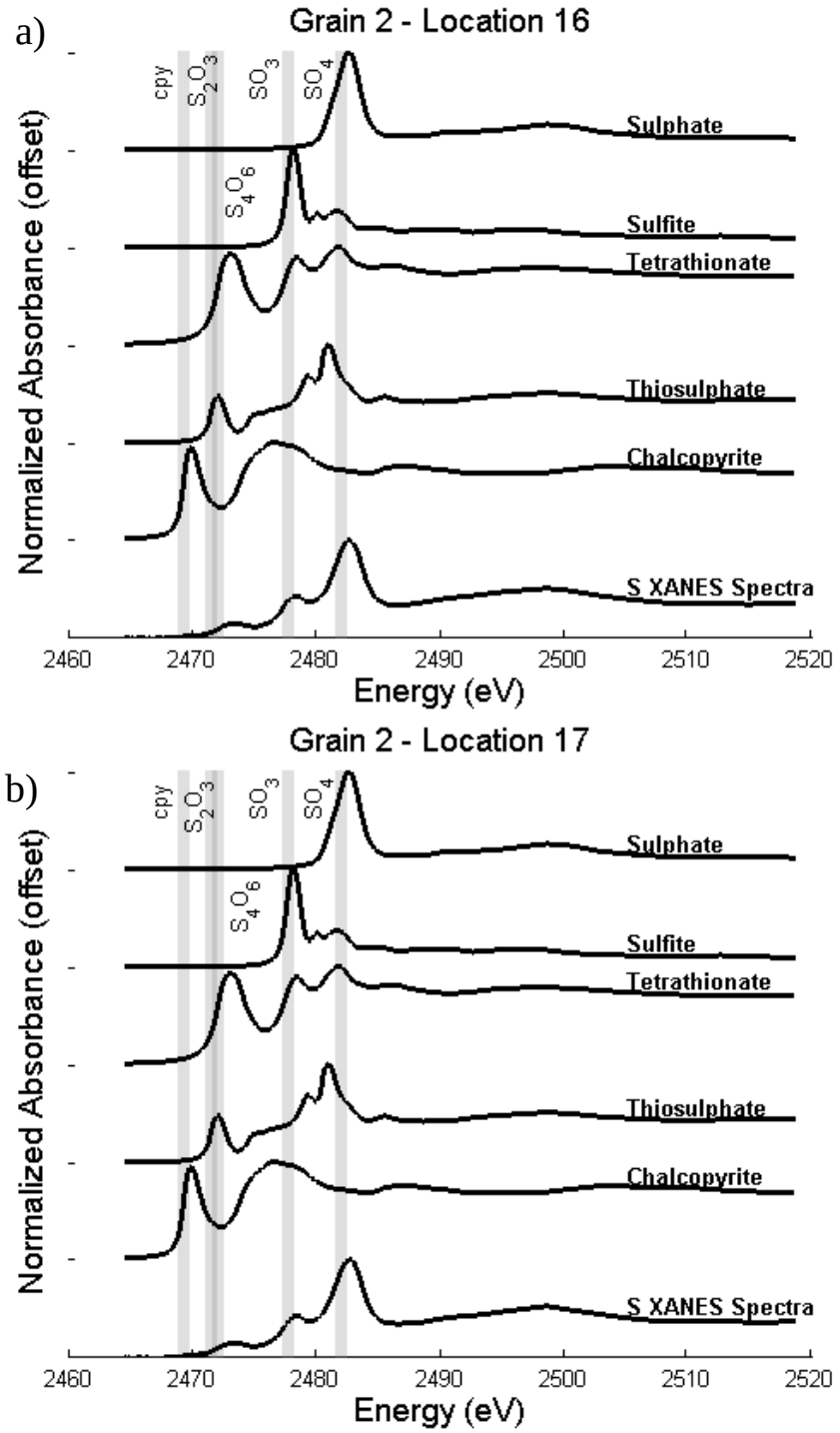

Figure B-15 –S XANES for Grain 2 at a) location 16 and b) location 17. The XANES for the standards of the species that were identified through linear combination analysis are superimposed. The grey bar lines indicate the reference e0 values for the standards

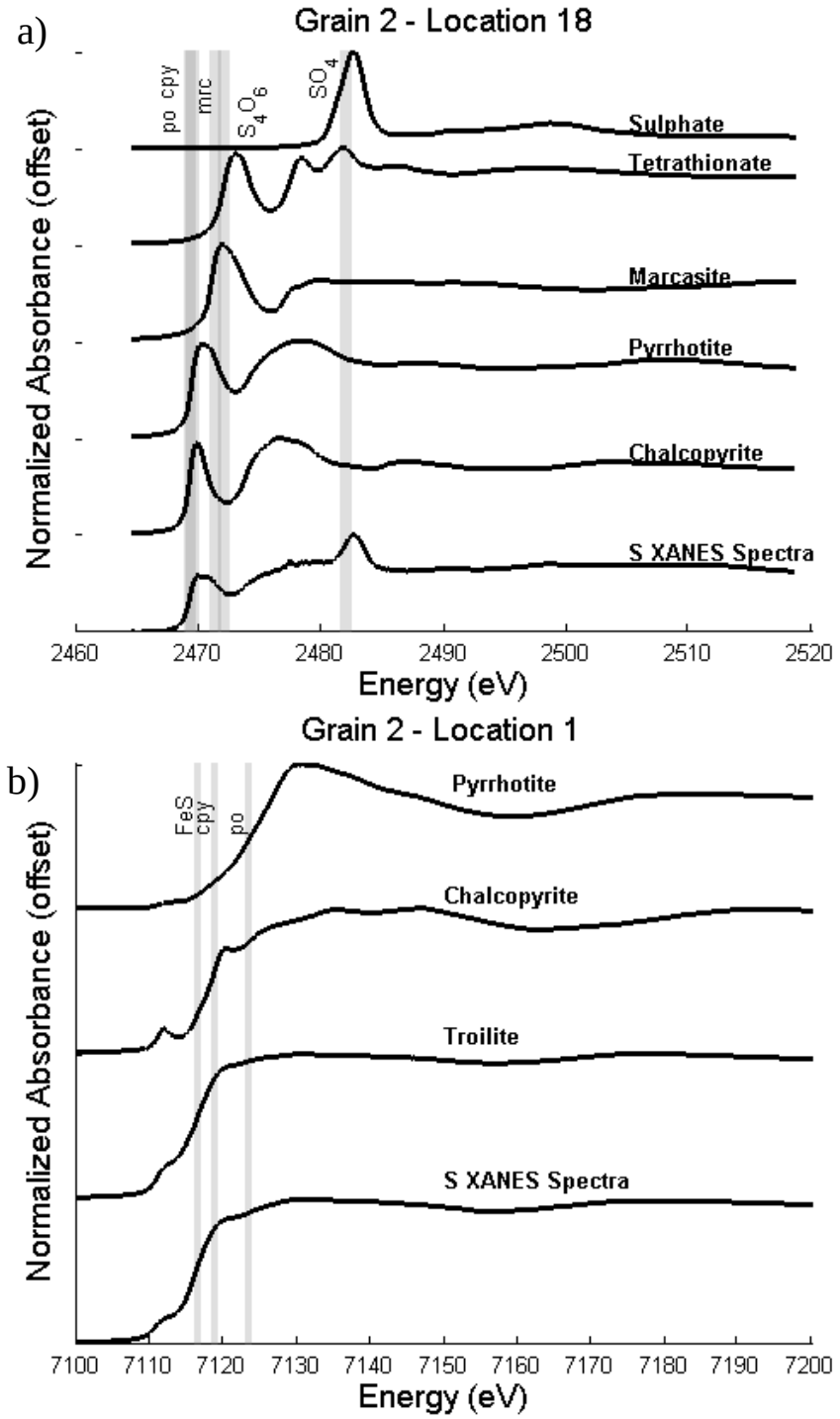

Figure B-16 –S XANES for Grain 2 at a) location 18 and Fe XANES at b) location 1. The XANES for the standards of the species that were identified through linear combination analysis are superimposed. The grey bar lines indicate the reference e0 values for the standards

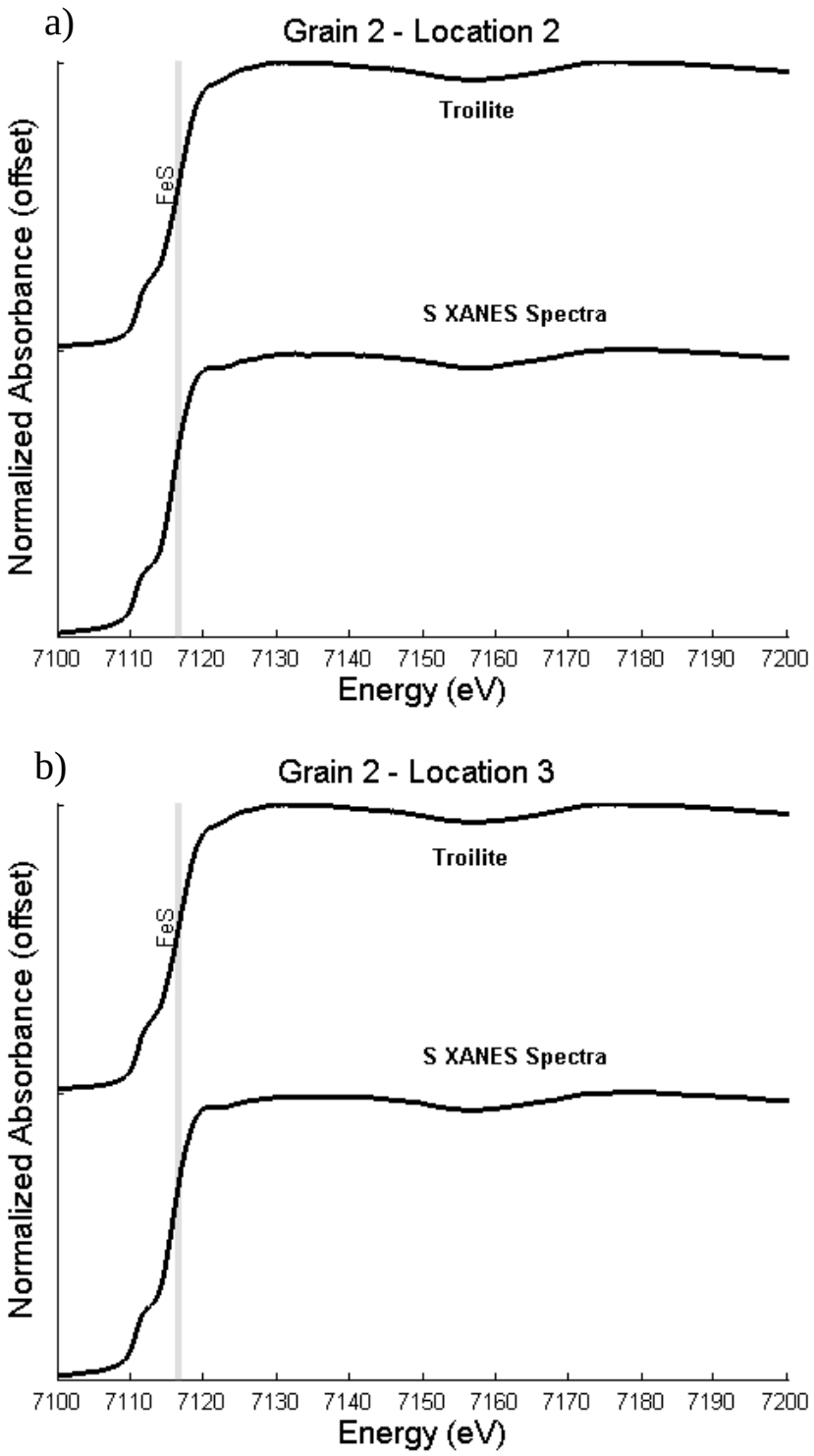

Figure B-17 –Fe XANES for Grain 2 at a) location 2 and b) location 3. The XANES for the standards of the species that were identified through linear combination analysis are superimposed. The grey bar lines indicate the reference e0 values for the standards

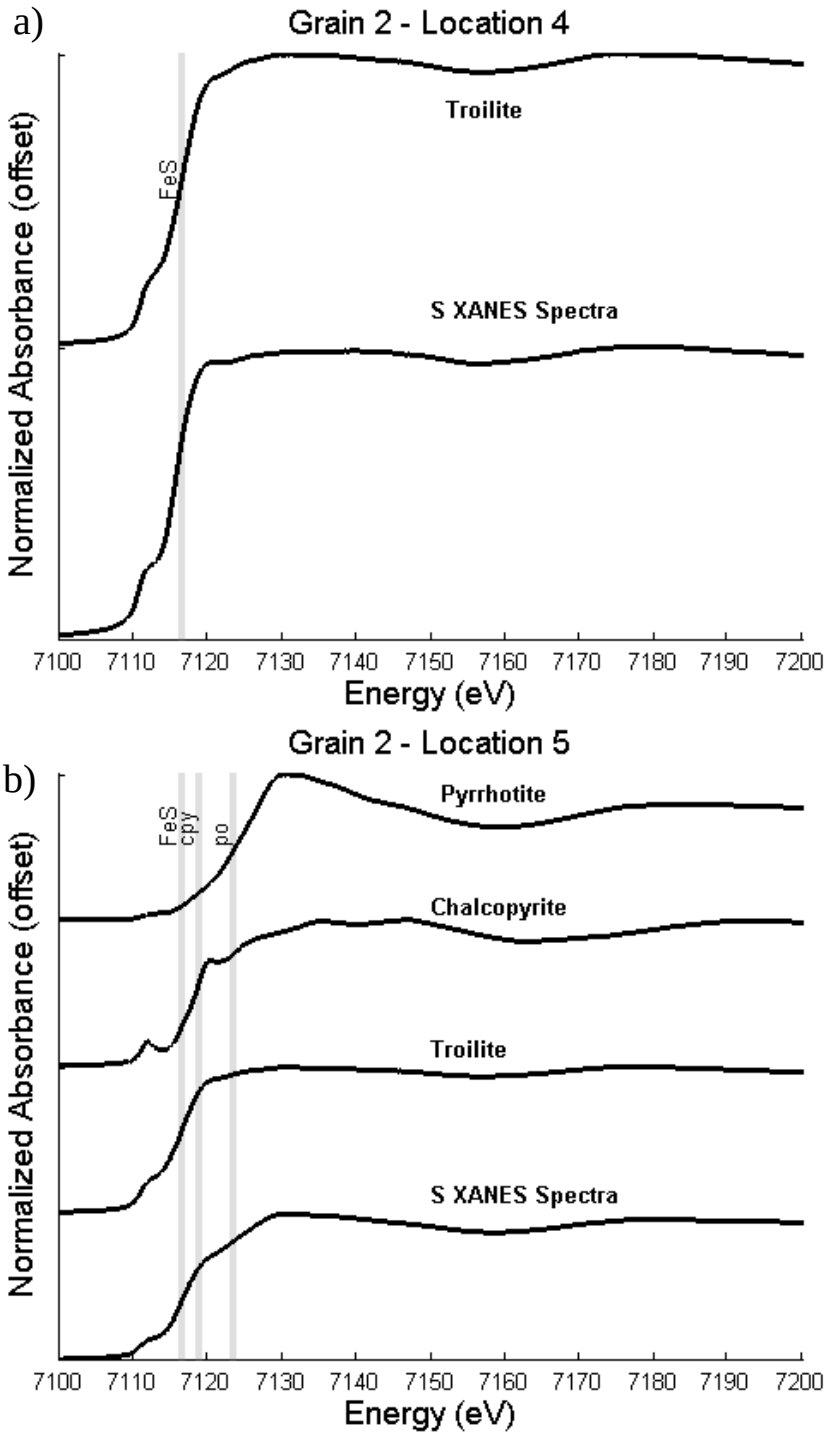

Figure B-18 –Fe XANES for Grain 2 at a) location 4 and b) location 5. The XANES for the standards of the species that were identified through linear combination analysis are superimposed. The grey bar lines indicate the reference e0 values for the standards

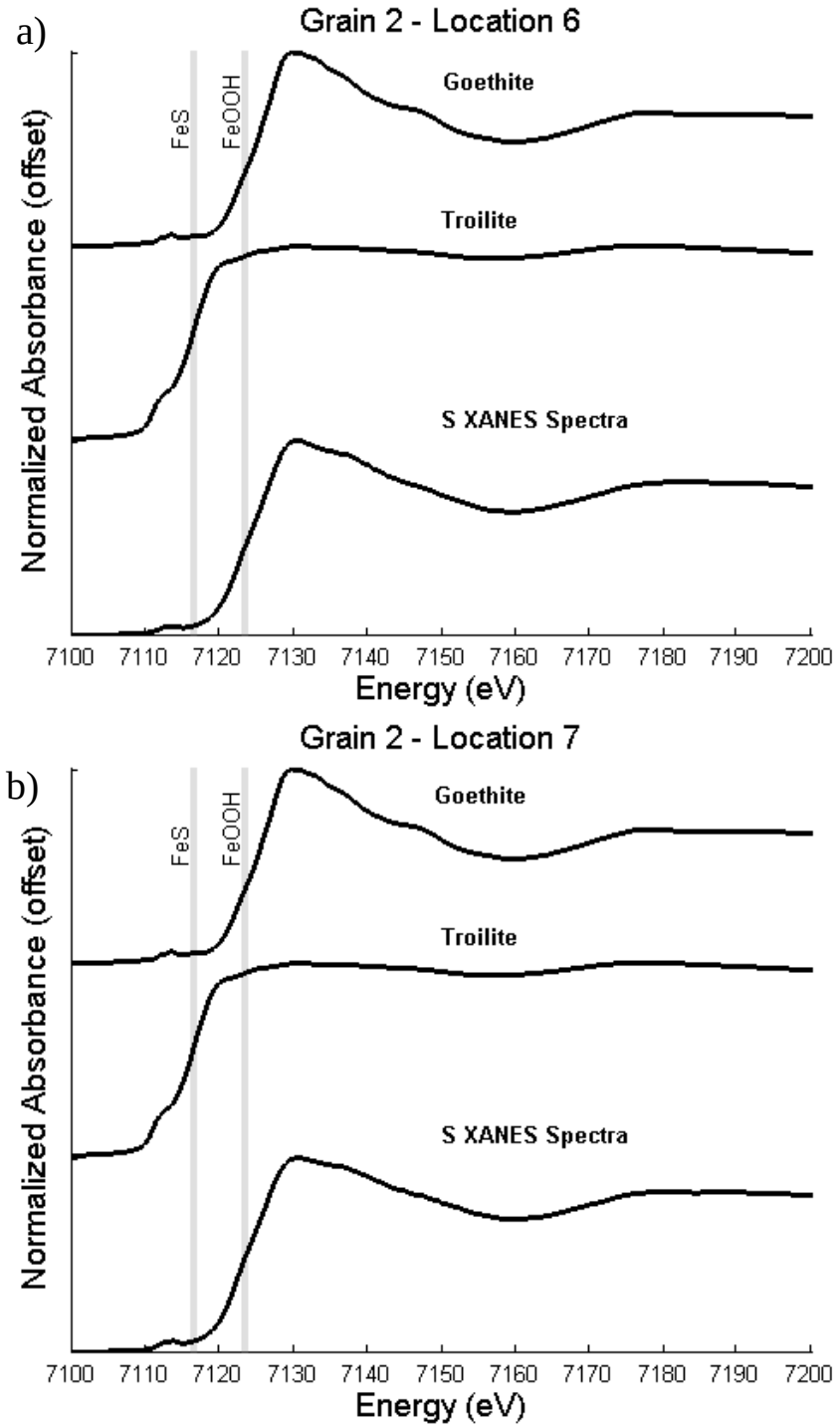

Figure B-19 –Fe XANES for Grain 2 at a) location 6 and b) location 7. The XANES for the standards of the species that were identified through linear combination analysis are superimposed. The grey bar lines indicate the reference e0 values for the standards

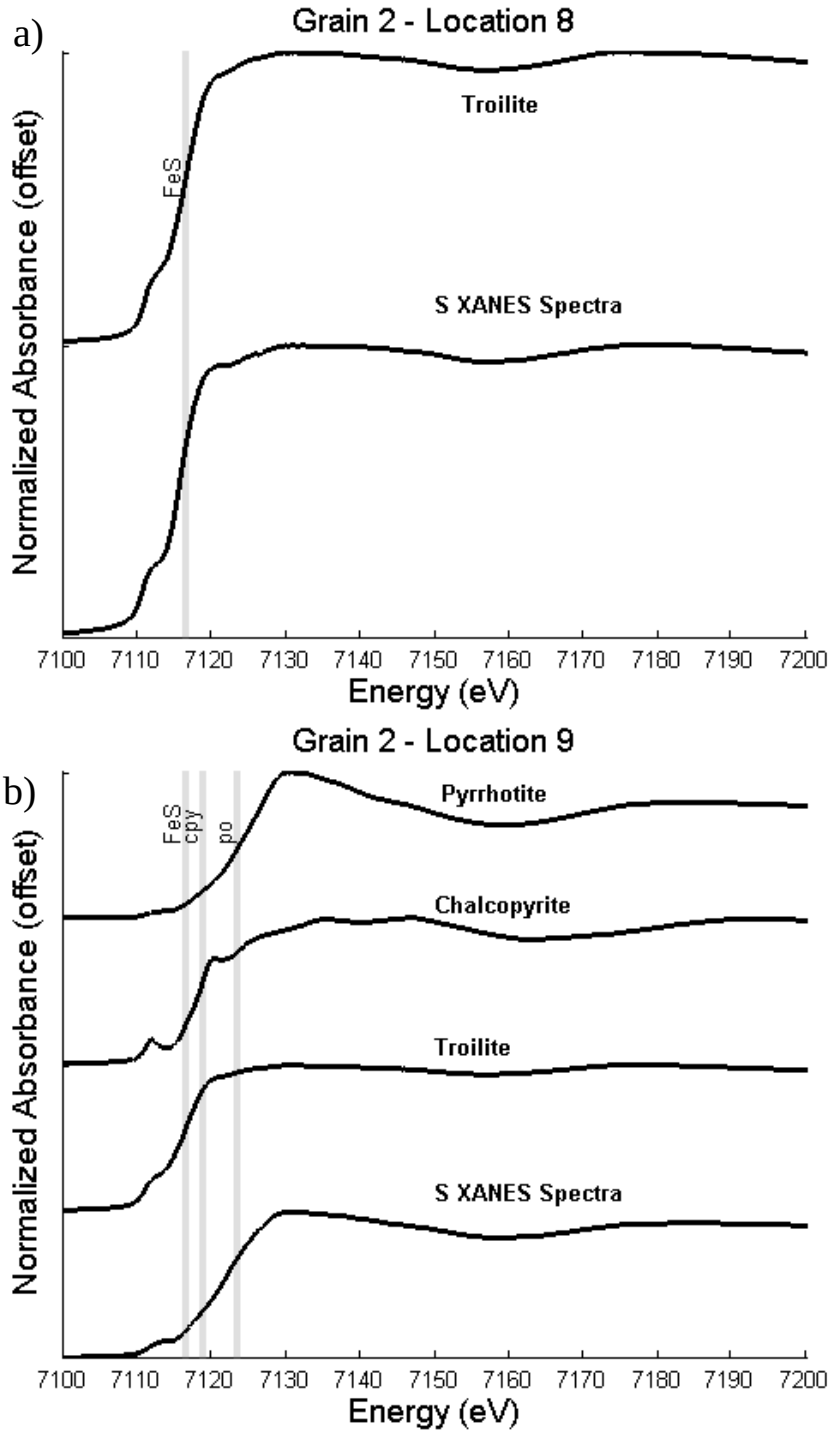

Figure B-20 –Fe XANES for Grain 2 at a) location 8 and b) location 9. The XANES for the standards of the species that were identified through linear combination analysis are superimposed. The grey bar lines indicate the reference e0 values for the standards

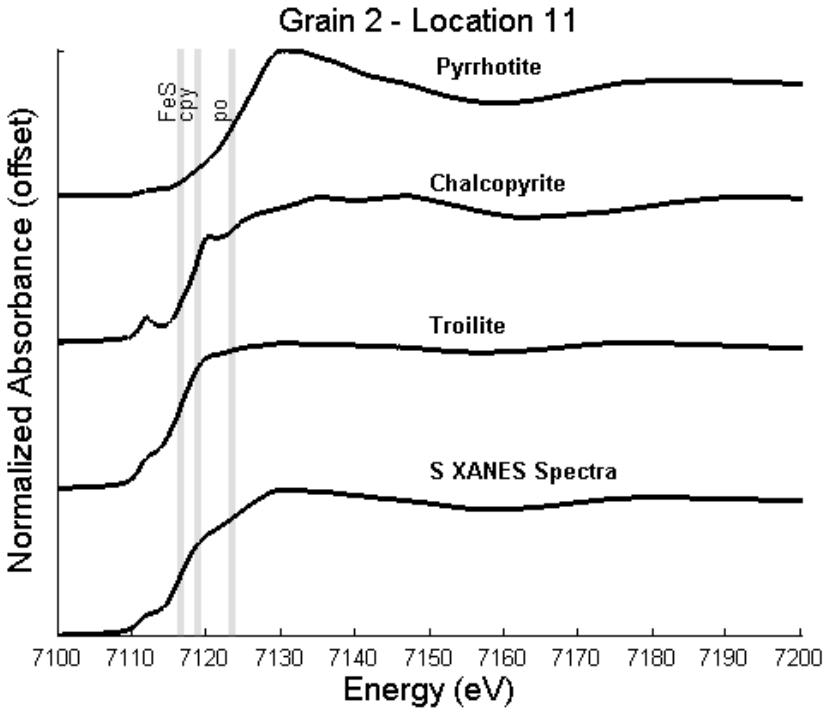

Figure B-21 –Fe XANES for Grain 2 at location 11. The XANES for the standards of the species that were identified through linear combination analysis are superimposed. The grey bar lines indicate the reference e0 values for the standards